ONDAS DE CHOQUE TIPO J CON PRECURSORES MAGNETICOS

Salvador Curiel Ramírez

Instituto de Astronomía

Universidad Nacional Autónoma de México

TESIS QUE PRESENTA

A LA FACULTAD DE CIENCIAS DE LA

UNIVERSIDAD NACIONAL AUTONOMA DE MEXICO

PARA OBTENER EL GRADO DE

DOCTOR EN CIENCIAS

(FISICA)

Enero 1992

Director de tesis: Dr. John Charles Raymond

Harvard-Smithsonian, Center for Astrophysics

Codirector de tesis: Dr. Jorge Cantó Illa

Instituto de Astronomía, UNAM

INDICE

J-Shock Waves with Magnetic Precursors

ABSTRACT

Standard models of inter-stellar shocks produce either strong H_2 emission (magnetically controlled C-shocks) or strong optical and UV emission (J-shocks), but not both. Following a brief review of infrared and radio molecular emission of Herbig-Haro objects, a model for a J-shock with a magnetic precursor, which is produced when a shock wave propagates through a magnetized molecular medium, is presented. As part of these calculations, the level population and emission of molecular hydrogen, as well as its destruction by chemical reactions with other particles and dissociation by collision with atomic and molecular hydrogen and electrons, are taken in consideration. In this type of shocks, the H_2 emission (infrared and ultraviolet) arises from the magnetic precursor, while the optical lines are emitted mainly by the gas behind the shock front. The results of this model show that hydrogen molecules radiate a considerably fraction of the total available energy in infrared lines, and that if H_2 molecules reach the J-shock before being dissociated within the precursor, excitation of the Lyman and Werner bands by hot electrons could carry away an amount of energy comparable to that radiated by H_2 infrared lines.

Applying this plane-parallel model to the HH7 Herbig-Haro Object, it is found that this single model seems to explain most of the existing infrared observations of this object. A bow-shaped shock wave model is constructed using several plane-parallel J-shocks with magnetic precursors. This model reproduces with some detail not only the infrared and optical line intensities but also the line profiles, position-velocity diagrams and morphology obtained at optical and infrared wavelengths. Some predictions are made about the intensites, profiles and emission distribution of a number of lines which are likely to be corroborated in future observations. Finally, the plane-parallel models are used to investigate the infrared emission observed in the Cygnus Loop Supernova Remnant.

Ondas de Choque tipo J con Precursores Magnéticos

RESUMEN

Los modelos típicos de onda de choque en el medio interestelar producen ya sea una fuerte emisión de H_2 en el infrarrojo (choques tipo C) ó una fuerte emisión en el óptico y en el ultravioleta (choques tipo J), pero no ambos. Después de una breve revisión de la emisión molecular infrarroja y de la de radio de los objetos Herbig-Haro, se presenta un modelo para ondas de choque tipo J con precursores magnéticos los cuales son producidos cuando una onda de choque se propaga a través de un medio molecular con un campo magnético considerable. En este modelo se han tomado en cuenta tanto la población de los niveles de energía y la emisión de la molécula de hidrógeno, así como la destrucción de esta molécula debida a reacciones químicas con otras partículas y su disociación debida a colisiones con hidrógeno atómico y molecular y electrones. En este tipo de onda de choque, la emisión de H_2 (infrarroja y ultravioleta) es producida en el precursor magnético mientras que las líneas ópticas son emitidas principalmente en el gas atrás del frente de choque. Los resultados de este modelo muestran que una fracción considerable de la energía disponible total es radiada por el hidrógeno molecular en forma de líneas en el infrarrojo, y que si las moléculas llegan al frente de choque antes de ser disociadas en el precursor, la excitación de las bandas de Lyman y de Werner, debida a colisiones con electrones energéticos, podría llevar consigo una cantidad de energía comparable a la emitida en el infrarrojo por la molécula de H_2.

Aplicando este modelo plano-paralelo al objeto Herbig-Haro HH7, se encuentra que este modelo sencillo parece explicar la mayoría de las observaciones en el infrarrojo de este objeto. Usando varios choques tipo J con precursores magnéticos plano-paralelos se construye un modelo de onda de choque con simetría en forma de proa. Este modelo reproduce con cierto detalle no sólo las intensidades de las líneas ópticas e infrarrojas sino tambien, los perfiles de las líneas, los diagramas de posición-velocidad y la morfología observados en longitudes de onda en el óptico y el infrarrojo. Se hacen predicciones sobre las intensidades, perfiles y distribución de emisión de un número de líneas, las cuales podrían ser corroboradas en observaciones futuras. Finalmente, se utilizan modelos plano-paralelos para investigar la emisión infrarroja observada en el Remanente de Supernova conocido como el Aro del Cisne (*The Cygnus Loop*).

RESUMEN

ONDAS DE CHOQUE TIPO J CON PRECURSORES MAGNETICOS

I. INTRODUCCION

Durante muchos años se ha sabido que las fuentes de emisión de líneas ópticas conocidas como objetos Herbig-Haro (HH) marcan la posición en la cual vientos energéticos de estrellas jóvenes interaccionan con gas denso estático de las nubes moleculares circundantes. A la fecha se ha establecido claramente la naturaleza de onda de choque de los objetos HH a partir de: sus movimientos propios frecuentemente altos, su asociación con flujos moleculares bipolares y su proximidad a estrellas jóvenes altamente enrojecidas (ver Schwartz [1983] para una revisión). Debido a que los objetos HH presentan una amplia variación en morfología (ver Strom *et al.* 1986), la geometría especifica de los choques ha sido objeto de debate. Se han propuesto varios modelos para explicar la excitación de este tipo de objetos: nubecillas ambientes en un viento estelar supersónico (Schwartz 1978), gas turbulento a lo largo de las paredes de una cavidad o jet estelar (Cantó 1980; Mundt *et al.* 1987), expulsiones discretas de masa estelar o balas ("bullets") (Norman and Silk 1979), y "superficies de trabajo" en la cabeza de jets (chorros) estelares (Mundt 1985; Mundt *et al.* 1987; Raga 1988; Hartigan 1989).

Normalmente, la estrella excitadora de los objetos HH únicamente se puede localizar a través de observaciones en radio o en el infrarrojo, ya que se encuentra altamente obscurecida a longitudes de onda en el óptico. La extinción puede también sesgar el estudio de los objetos HH mismos, favoreciendo la detección de objetos corridos hacia el azul (es decir, aquellos que se alejan de la nube molecular huésped hacia el observador). Observaciones recientes en el ultravioleta, el infrarrojo y en longitudes de onda milimétricas y centimétricas han revelado que los objetos HH son también fuentes de emisión de líneas moleculares. Utilizando los nuevos detectores infrarrojos es posible obtener imágenes de alta resolución comparables a las obtenidas en el óptico con CCDs. Esta nueva posibilidad ofrece la oportunidad de realizar una comparación detallada de indicadores

de gas molecular, atómico e ionizado en los frentes de choque de los objetos HH. La relación espacial entre las emisiones molecular y atómica podría indicar el tipo de choque y la geometría en objetos HH individuales. Observaciones de indicadores de alta densidad (tales como el HCO^+ y el NH_3) en longitudes de onda milimétrica y centimétrica han mostrado pequeñas condensaciones de gas molecular denso ($\gtrsim 10^4$ cm^{-3}) que se encuentran frecuentemente en la periferia de objetos HH. Aunque parece claro que existe una asociación entre estas condensaciones y los objetos HH, su origen es aún incierto.

La región espectral en el cercano infrarrojo contiene un número de líneas en emisión de hidrógeno molecular las cuales constituyen criterios de diagnóstico de importancia para la componente molecular del gas en objetos HH. La línea IR mas fuerte y más comúnmente estudiada es la línea del H_2 v=1-0 S(1) en 2.12 μ. En principio, esta línea se detectó y estudió en objetos HH utilizando técnicas con un solo haz, y más recientemente, por medio de detectores de arreglos bidimensionales. La emisión de H_2 se ha buscado y detectado en numerosos objetos HH, incluyendo HH1-2 (Harvey *et al.* 1986; Hartigan *et al.* 1991), HH7-11 (Zealey *et al.* 1984; Lightfoot y Glencross 1986; Hartigan *et al.* 1989; Burton *et al.* 1989; Garden *et al.* 1990; Stapelfeldt *et al.* 1991), HH32 (Zealey *et al.* 1986), HH43 (Schwartz *et al.* 1988b), HH52/53/54 (Sandell *et al.* 1986), HH6 y HH12 (Lane y Bally 1986; Stapelfeldt *et al.* 1991), Cep A/GGD 37 (Bally y Lane 1991), y varias fuentes adicionales en estudios realizados por Elias (1980), Schwartz *et al.* (1987) y Wilking *et al.* (1990) (ver también la revisión de Lane [1989]). Doyon y Nadeau (1988), Zinnecker *et al.* (1989), Brand *et al.* (1989) y Carr (1990) obtuvieron observaciones de líneas de H_2 de alta resolución en el infrarrojo en varios objetos HH. Un resultado general de estas observaciones es que las líneas de H_2 son mucho más angostas que las ópticas. En particular, el ancho de la línea S(1) es típicamente de sólo la mitad de el de la línea Hα en los mismos objetos, y las velocidades centrales observadas en las líneas de H_2 son asimismo menores que las ópticas (Zinnecker *et al.* 1989).

Las transiciones vibracionales y rotacionales de la molécula de H_2 pueden ser excitadas ya sea por choques (via excitación colisional en gas calentado a unos cuantos miles de grados por los choques), o bien, por absorción de radiación ultravioleta (UV) (en las bandas de Lyman y Werner con una subsecuente cascada a niveles inferiores). Debido a que las intensidades de las líneas producidas por los procesos colisionales y por fluorescencia son significativamente diferentes, es posible distinguir entre estos mecanismos

comparando la intensidad de las líneas de distintos niveles, tales como las transiciones v=1-0S(1) y v=2-1S(1) en 2.122 μ y 2.247 μ, respectivamente. Wolfire y Königl (1991) dan una descripción general de las características esperadas en la emisión de H_2 excitada en situaciones diferentes. Las simulaciones numéricas predicen que el cociente esperado para estas líneas (1-0S(1)/2-1S(1)) en gas chocado es del orden de 10, mientras que en gas fotoexcitado es de ~ 2 (*e.g.*, Black y vanDichoeck 1987). Los cocientes de líneas moleculares medidos en varios objetos HH son de ~ 10 (*e.g.*, Schwartz *et al.* 1987, 1988a), lo cual es consistente con las predicciones de modelos de ondas de choque no-disociativas y de baja velocidad (*e.g.*, Shull y Hollenbach 1978). En general, la emisión de H_2 parece indicar ondas de choque de baja velocidad (con velocidades de 10 a 40 km s^{-1}), mientras que la emisión óptica indica choques mucho más rápidos (con velocidades típicas de alrededor de 100 km s^{-1}, o más). Sin embargo, existe evidencia en el sentido de que hay otros mecanismos de excitación que intervienen en algunos de los casos. Por ejemplo, en algunos objetos HH de baja excitación, tales como HH43 y HH47 (Schwartz 1983), se han observado líneas UV que han sido identificadas como emisión de la banda de Lyman de H_2. Asimismo, el contínuo UV que se ha detectado en varios objetos HH (tales como HH1 y 2) y que previamente se había atribuído a emisión de dos fotones de hidrógeno atómico (*e.g.*, Dopita *et al.* 1982; Brugel *et al.* 1982), podría producirse, al menos en parte, a través de fotodisociación de H_2 (Böhm *et al.* 1987). Brugel (1989) presentó recientemente una revisión detallada de observaciones en UV de objetos HH. En el caso de HH1-2, los cocientes de líneas (Elias 1980; Harvey *et al.* 1986) se encuentran entre los esperados en fotoexcitación y excitación colisional. Wolfire y Königl (1991) propusieron recientemente que la emisión de línea en estos objetos se debe principalmente a fotoexcitación. Sin embargo, la distribución espacial de la emisión óptica e infrarroja (ver Capítulo 1[1]), sugiere que al menos en este caso, la emisión de línea de H_2 es debida a excitación colisional aunque con una componente importante de fotoexcitación (la cual podría explicar el exceso en el contínuo UV).

Debido a que las líneas ópticas y de H_2 son indicadoras de componentes diferentes del gas chocado, la comparación de la distribución espacial de emisión óptica e infrarroja en objetos HH podría proporcionar información esencial sobre la estructura del flujo. Con el reciente desarrollo de los nuevos detectores infrarrojos (IR) ahora es posible estudiar la distribución de la emisión de H_2 con resoluciones comparables a las obtenidas con imágenes

[1] Los capítulos y citas bibliográficas a los que se hace referencia en este texto corresponden a los de la Tesis Principal, ver Indice.

ópticas. Dichos estudios se han llevado a cabo por Schwartz *et al.* (1988), Hartigan *et al.* (1989), Garden *et al.* (1990), Stapelfeldt *et al.* (1991) y Lane (1989), y han demostrado que la emisión de línea en objetos HH presenta una amplia y compleja gama de morfologías. Aunque la distribución a gran escala de la emisión de H_2 es similar a la observada en longitudes de onda ópticas, hay diferencias sutiles que pueden ser importantes en la interpretación del origen de la emisión. Con el objeto de ilustrar estas diferencias, en el Capítulo 1 se presenta una descripción general de la morfología de tres objetos (HH1-2, Cepheus A y HH7-11), y se sugiere una posible interpretación para la emisión en cada objeto.

En el Capítulo 2, calculamos en detalle las poblaciones de los niveles rotacionales-vibracionales del estado electrónico base de la molécula de hidrógeno, tomando en cuenta varios mecanismos de excitación, entre ellos, la excitación colisional de los estados electrónicos $B\Sigma$ y $C\Pi$ por medio de electrones térmicos energéticos. Asimismo, se estudia el mecanismo de enfriamiento debido a la excitación colisional de las moléculas de hidrógeno. Los resultados de este Capítulo se utilizan en los Capítulos 4 y 5 para calcular la emisión en el óptico, el UV y el IR producida por ondas de choque tipo J plano-paralelas y de proa, con precursores magnéticos. En el Capítulo 3, presentamos imágenes tomadas casi simultáneamente "a la luz" de Hα, [SII], y H_2 S(1). Asimismo, se discute el procedimiento de calibración así como posibles interpretaciones para estas observaciones y otros datos ya existentes de esta región. En este Capítulo, se aplican resultados del Capítulo 4 con el objeto de explicar la estructura en forma de proa que se observa en HH7, así como los flujos de las distintas líneas que se obtienen. En el Capítulo 4, calculamos la emisión en el óptico, el UV y el IR producida por ondas de choque tipo J con precursores magnéticos, asumiendo una estructura muy simplificada para el precursor magnético y calculando en detalle la región post-choque. La estructura dinámica simplificada nos permite calcular no solamente la intensidad de las líneas de H_2 emitidas por el precursor, sino también la pérdida de energía en esta región, la cual juega un papel importante en la excitación del espectro emitido por la región post-choque. En este Capítulo, aplicamos este modelo plano-paralelo a HH7 (también ver Capítulo 3) y al filamento MH1 del Aro del Cisne (The Cygnus Loop). La simplicidad del modelo presentado en el Capítulo 4, nos permite construir ondas de choque de proa en el Capítulo 5. Con base en estos modelos, predecimos las morfologías infrarrojas y ópticas, y los perfiles de líneas y espacialmente resueltos de un jet (o bala) que se mueve a través de un medio molecular magnetizado. En el Capítulo

5, se calculan las intensidades y los perfiles de las línea, así como diagramas de posición-velocidad y mapas de contorno, para varias líneas ópticas e infrarrojas. Los resultados de este modelo de proa se comparan con resultados observacionales de objetos HH, así como con otros modelos teóricos. En particular, se comparan las predicciones de este modelo con observaciones de alta resolución (tanto espectrales como angulares) de HH7. Por último, presentamos algunas predicciones para intensidades y perfiles de líneas, diagramas de posición-velocidad, y mapas de contornos y de velocidades de líneas en el óptico y el infrarrojo para un choque de proa, los cuales podrían ser comparados con observaciones.

II. MODELO

a) Tasas de Enfriamiento de la Molécula de Hidrógeno

En algunos escenarios astrofísicos, tales como ondas de choque tipo J con precursores magnéticos y choques tipo C (Draine 1980, Draine *et al.* 1983), la temperatura de los electrones puede ser mayor que la de las partículas neutras. En dicho caso, la excitación de las moléculas de hidrógeno a niveles electrónicos superiores puede ser una fuente importante de enfriamiento. Más aún, como la mayoría de estas excitaciones van seguidas por desexcitaciones radiativas a niveles rotacionales-vibracionales excitados en el estado electrónico base, una cantidad substancial de radiación IR y UV puede ser emitida antes de que las moléculas sean disociadas. Este tipo de escenario podría explicar el contínuo UV observado en algunos objetos HH (*e.g.*, Brugel 1989), y la emisíon de líneas infrarrojas de H_2 asociadas con filamentos ópticos en el Aro del Cisne (Graham *et al.* 1991). Sin embargo, hasta ahora no se ha estudiado la excitación de niveles electrónicos superiores de H_2 por colisiones con electrones calientes. Con el objeto de estudiar la importancia de este mecanismo en el enfriamiento de un medio chocado y sus efectos en la producción de emisión infrarroja y UV, en el Capítulo 2 calculamos en detalle la población de niveles rotacionales-vibracionales del estado base electrónico de H_2. En estos cálculos, consideramos varios mecanismos de excitación, entre ellos, la excitación colisional de los estados electrónicos $B\Sigma$ y $C\Pi$ por electrones energéticos. En el Capítulo 2 se presenta un estudio de las tasas de enfriamiento debidas a colisiones con electrones, así como una comparación con las tasas de enfriamiento radiativas y disociativas. En el Capítulo 4 se presenta una discusión de la emisión IR y UV.

i) Población de Niveles de Energía Rotacionales-Vibracionales

En el caso del hidrógeno molecular, en el cual las transiciones cuadrupolares rotacionales-vibracionales son ópticamente delgadas y las líneas emitidas pueden viajar a través de la región de emisión sin ser absorbidas, la población de niveles depende únicamente de los parámetros físicos locales del gas. Por lo tanto, la población de los niveles fraccionales puede obtenerse resolviendo el sistema de ecuaciones de equilibrio estadístico.

ii) Enfriamiento y Calentamiento por H_2

Uno de los principales medios de enfriamiento del gas interestelar bajo una variedad de circunstancias (e.g. Shull y Beckwith, 1982) es por emisión de radiación del hidrógeno molecular. El H_2 puede jugar un papel significativo en el balance térmico de las nubes interestelares tanto en nubes frías difusas ($\sim 100K$) como en nubes moleculares chocadas ($\sim 200K$). En particular, la emisión de hidrógeno molecular puede proveer el enfriamiento primario de ondas de choque interestelar (Field et al 1968, Aannestad 1973 a,b) producidas por colisión de nubes moleculares, o el encuentro entre éstas y vientos estelares, regiones HII o supernovas. La función de enfriamiento de H_2 ha sido calculada para diferentes densidades y temperaturas utilizado una serie de aproximaciones (e.g. Shull y Hollenbach 1978; Lepp y Shull 1983). Estos cálculos se han llevado a cabo incluyendo varios procesos de excitación y desexcitación, y tomando en cuenta con cierto detalle la población de los niveles de energía de la molécula de hidrógeno. Debido a que queremos calcular la emisión de línea en el IR, el UV y el contínuo producido por un precursor magnético que precede a un choque fuerte de tipo J (ver Capítulo 4), calculamos en detalle la población de los 255 niveles de energía rotacionales-vibracionales del estado base $X\Sigma$ de la molécula de hidrógeno, tomando en cuenta la excitación de los estados electrónicos superiores $B\Sigma$ y $C\Pi$ (incluyendo 240 niveles rotacionales-vibracionales para el estado $B\Sigma$ y 100 para el estado $C\Pi$). En el Capítulo 2, calculamos la tasa de enfriamiento neto de la molécula de hidrógeno, incluyendo los siguientes procesos de enfriamiento y calentamiento:

a) Enfriamiento: emisión radiativa cuadrupolar debida a la excitación colisional y el bombeo colisional de las moléculas de H_2, emisión dipolar debida a la excitación de estados electrónicos superiores por electrones y disociación colisional.

b) Calentamiento: desexcitación colisional de moléculas de H_2 bombeadas colisionalmente, disociación radiativa espontánea de H_2, y formación molecular.

b) MODELO PARA ONDAS DE CHOQUE TIPO J CON PRECURSORES MAGNETICOS

Los modelos estándares de choques interestelares, producen ya sea emisión intensa de H_2 (choques tipo C magnéticamente controlados) o emisiones intensas en el óptico y el UV (choque tipo J), pero no ambos. Los choques tipo J con precursores magnéticos tienen la ventaja de producir emisión fuerte en el óptico, UV e IR a partir de la misma onda de choque; las líneas ópticas y UV se emiten principalmente en la región post-choque mientras que las líneas de H_2 surgen del precursor. Sin embargo, hasta ahora, esta posibilidad no se ha explorado. En el Capítulo 4, calculamos la emisión en el óptico, UV e IR producida por dichas ondas de choque asumiendo una estructura muy simplificada para el precursor magnético, y calculando la región post-choque en detalle. La estructura dinámica simplificada nos permite calcular no solamente la intensidad de líneas de H_2 emitidas a partir del precursor magnético, sino también calcular la pérdida de energía en esta región, la cual juega un papel importante en la excitación del espectro emitido por la región post-choque. Es más, como se muestra en el Capítulo 5, la simplicidad de este modelo nos permite construir ondas de choques con forma de proa, y a partir de ellas, predecir la morfología de un jet que se mueve a través de un medio molecular magnetizado en el IR y el óptico, así como sus perfiles de líneas integrados y espacialmente resueltos. En el Capítulo 4 se presentan las intensidades de líneas atómicas en el óptico y el IR así como aquéllas para líneas de H_2 en el IR esperadas a partir de modelos de choque tipo J con precursor magnético.

i) Precursor Magnético

Los modelos de onda de choque con precursor magnético fueron inicialmente desarrollados por Draine (1980). Cuando el gas ambiente es en su mayor parte neutro y la velocidad del choque es menor que la magnetosónica, un precursor de campo magnético comprimido y con partículas cargadas eléctricamente acopladas, se mueve a través del gas delante de la transición principal del choque. Las interacciones equivalentes a la fricción entre las partículas ionizadas y las neutras transfieren momento y energía de las primeras a las últimas. Mientras las moléculas enfríen suficientemente al gas, el calentamiento y la compresión de éste dan lugar a líneas espectrales infrarrojas con longitudes de onda cercanas a 2 μ. Cerca del choque tipo J, los electrones calientes pueden excitar bandas

de Lyman y Werner produciendo una cantidad substancial de emisión ultravioleta de H_2. Por último, cuando la temperatura se eleva lo suficiente para destruir moléculas de H_2, la eficiencia del enfriamiento disminuye drásticamente, la temperatura se eleva rápidamente y se dá una transición rápida en las condiciones de choque. Bajo estas condiciones la emisión del H_2 surge del precursor magnético mientras que las líneas ópticas son emitidas principalmente por el gas atrás del frente de choque.

ii) Estructura del Precursor Magnético

En el Capítulo 3 se calcula la estructura del precursor magnético siguiendo la formulación analítica de Draine (1980). Se asume un choque fuerte tipo J con $\rho v^2 \gg B_0^2/8\pi$, una densidad iónica significativamente menor que la neutral, una velocidad de choque menor que la de Alfvén, con lo cual, la escala de longitud caractéristica en la cual se comprime el campo magnético es la longitud de frenado L,

$$L \approx \frac{(\mu_i + \mu_n)B_0^2}{\pi \rho_i \rho_n < \sigma v >_{in} v_s} \; cm, \tag{1}$$

donde μ_i es la masa de los iónes y μ_n es la masa de las partículas neutras, B_0 es el campo pre-choque, v_s es la velocidad del choque, ρ_i y ρ_n son las densidades de masa de los iónes y neutros antes de ser chocados, y $< \sigma v >_{in}$ especifica la tasa de transferencia de momento entre iones y partículas neutras (Draine 1980).

La temperatura se incrementa en el precursor de manera estable a lo largo de la longitud L hasta cierta fracción de la temperatura post-choque, de manera que puede haber una columna substancial de H_2 excitado vibracionalmente por delante del choque. La tasa de calentamiento (o tasa de disipación de energía) del gas de partículas neutras por unidad de volumen debida a dispersión entre iones y partículas neutras Γ es

$$\Gamma \approx \frac{\rho_i \rho_n < \sigma v >_{in} v_s^2}{2(\mu_i + \mu_n)} \; erg \; cm^{-3} s^{-1}, \tag{2}$$

y la tasa de disipación de energía por unidad de área de choque ΓL es

$$\Gamma L \approx \frac{B_0^2 v_s}{2\pi}\ erg\ cm^{-2}s^{-1}. \tag{3}$$

La temperatura máxima del gas neutro se puede calcular asumiendo que el cambio en temperatura se debe a la diferencia entre el calentamiento Γ y el enfriamiento Λ, los cuales actúan a lo largo de una distancia L (o escala de tiempo de calentamiento L/v_s), i.e.,

$$\frac{\rho_n v_s}{\mu_n}\left[\frac{3}{2}k(T_{n,max}-T_{n0})\right] \approx L\left[\Gamma-\Lambda(T_{n,max})\right]\ erg\ cm^{-2}s^{-1}. \tag{4}$$

Esta expresión proporciona una ecuación implícita para la temperatura máxima $T_{n,max}$ en el precursor magnético:

$$T_{n,max} \approx T_{n0} + \frac{2\mu_n L}{3\rho_n v_s k}\left[\frac{B_0^2 v_s}{2\pi L} - \Lambda(T_{n,max})\right]\ K. \tag{5}$$

Esta ecuación trascendental se puede resolver cuando se conoce la tasa de enfriamiento como función de la densidad y temperatura. Ya que únicamente se están tomando en cuenta choques moleculares, se puede utilizar la tasa de enfriamiento mencionada en el Capítulo 2 para calcular la temperatura máxima en el precursor.

Debido a que la desaceleración máxima (en un marco de referencia en el cual el choque tipo J está en reposo) y la compensación de las componentes ionizadas y neutras del flujo en el precursor sólo se pueden obtener por medio de cálculos detallados, se tiene que efectuar una suposición arbitraria. Nosotros adoptamos una fracción de compresión máxima de 2 en el precursor, la cual parece ser un valor representativo para campos magnéticos intensos y fracciones de ionización muy bajas (ver Draine 1980). La velocidad se puede obtener a partir de la ecuación de transferencia de masa $\rho v = \rho_o v_o$.

Normalmente la zona de transición del choque se considera infinitesimalmente delgada. Sin embargo, una fracción substancial de las moléculas puede ser disociada en el frente de choque produciendo emisión, por lo cual, se hace necesaria la inclusión de esta región en los presentes cálculos. El modelo de Mott-Smith (1951) proporciona una descripción aproximada de frentes de choque colisionales fuertes. En este modelo, dos

distribuciones Maxwellianas independientes con temperaturas fijas, que representan los flujos chocados y no chocados, interactúan vía colisiones, las cuales transfieren partículas de las distribuciones no chocadas a las chocadas. El ancho del choque Δ_s, es del orden de un camino libre medio,

$$\Delta_s \approx \frac{1}{n_s \sigma} , \tag{6}$$

donde n_s es la densidad del fluído chocado y σ es la sección recta efectiva. En un gas de baja ionización ($X(e) \lesssim 10^{-4}$) las colisiones neutro-neutro predominan sobre los procesos de intercambio de cargas. En este caso la sección recta de colisión para átomos de hidrógeno es $\sigma_c = \pi a_0^2 \sim 10^{16} cm^2$ (Clausius 1858), donde $a_0^2 \sim 0.5 \times 10^{-8}$ es la primera órbita de Böhr.

Con el objeto de investigar la emisión en el óptico, en el UV y en el IR producida por choques tipo J con precursor magnético, se adoptó un modelo de ondas de choque plano-paralelo muy simplificado. En el presente trabajo se consideraron tres regiones principales como parte de la onda de choque: 1) Precursor magnético, 2) Frente de choque, 3) Región post-choque. Para las dos primeras regiones se adoptó un modelo muy simplificado en el cual la temperatura aumenta linealmente a través del precursor partiendo de valores iniciales T_0, n_0 hasta alcanzar sus valores máximos n_m, T_m, y posteriormente se incrementan linealmente a través del frente de choque hasta alcanzar sus valores post-choque (T_s y n_s). En la región post-choque se utilizó el código de choques atómicos desarrollado por John Raymond (ver Raymond 1976; Raymond 1979) para seguir la evolución del gas hasta que éste alcanza una temperatura de alrededor de 600 K.

iii) Cálculo de la Intensidad de las Líneas

Con el propósito de calcular la intensidad de líneas de hidrógeno en el IR, se calculó en detalle la población de niveles vibracionales-rotacionales de esta molécula incluyendo colisiones con electrones e hidrógeno atómico y molecular, a través de las regiones del precursor magnético y del frente de choque. Los procesos incluidos en estos cálculos se describen en el Capítulo 2.

Los procesos de emisión de líneas de H_2 y de contínuo (ultravioleta e infrarrojo)

subsecuentes tanto a la excitación colisional del estado base $X\Sigma$ así como al bombeo colisional y a fluorescencia a través de los estados $B\Sigma$ y $C\Pi$, contribuyen a la emisión de las regiones del precursor y del frente de choque. En los presentes cálculos únicamente se han tomado en cuenta los procesos colisionales. Los procesos incluidos en el calculo de la población de los niveles vibracionales-rotacionales del H_2 se presentan en el Capítulo 2. Las longitudes de onda de las líneas de H_2 en el IR, en el UV y en el contínuo se calcularon según se describe en el Capítulo 2.

c) Modelo para Choques tipo J de Proa con precursores magnéticos.

Se han calculado perfiles de línea teóricos esperados en choques de proa ya sea para líneas ópticas (Hartigan, Raymond y Hartmann 1987), o bien para líneas de H_2 en el IR (Smith y Brand 1990), pero no simultáneamente para ambos. En el primer caso, el choque de proa se construyó utilizando ondas de choque atómicas plano-paralelas, mientras que en el último caso, se utilizan ondas de choque tipo C para la emisión molecular. De la misma manera, Raga y Böhm (1986) y Hartigan, Raymond y Meaburn (1990) calcularon diagramas teóricos de posición-velocidad para líneas ópticas de un choque de proa. El propósito del Capítulo 5 es calcular los espectros de líneas de emisión en el IR y el óptico de un choque de proa que se mueve a través de un medio molecular magnetizado. Estos cálculos se basan hasta cierto punto en la extensión de cálculos previos desarrollados por Hartigan, Raymond y Hartmann (1987), los cuales se restringen al caso de un choque de proa que se mueve a través de un medio atómico. En el Capítulo 5 se estudia el papel que juega la emisión de líneas de H_2 en el infrarrojo en un precursor magnético. Se calculan las intensidades y perfiles de línea así como los diagramas de posición-velocidad y los mapas de contorno para varias líneas ópticas y en el IR.

i) Descripción del Modelo de Choque de Proa

En el Capítulo 5 se calculan intensidades y perfiles de línea, diagramas de posición-velocidad, morfologías y perfiles de velocidad locales teóricos de emisiones de línea tanto en el óptico como en el IR de choques tipo J de proa. Se sigue el modelo de choque de proa desarrollado por Hartigan, Raymond y Hartmann (1987). Sin embargo, debido a que estos autores se concentraron en el estudio de líneas atómicas emitidas en la región post-choque, se han efectuado algunos cambios y extensiones para calcular la emisión en el IR de la región pre-choque (*i.e.*, del precursor magnético).

ii) Geometría

En el Capítulo 5 se presenta un diagrama esquemático de un choque en proa y los parámetros característicos que lo definen, la dirección del observador y la orientación adoptada para el campo magnético B, la cual se asume es perpendicular al eje principal de simetría. El observador ve al choque a un ángulo ϕ con respecto a su eje principal de simetría. En este marco de referencia, el gas pre-choque moviéndose a una velocidad v_s penetra al choque de proa a un angulo ξ con respecto a la vertical, el cual se determina una vez que se conoce el perfil del choque. La radiación emitida por la onda de choque de proa se calcula dividiendo el choque en un número de anillos concentricos (típicamente 200 anillos) con dξ constante. Cada anillo se divide a su vez en segmentos con un angulo azimutal Ψ, los cuales son considerados como choques plano-paralelos individuales con velocidad de choque constante $v_\perp$ y campo magnético $B_\parallel$. Estos modelos plano-paralelos se presentan en el Capítulo 4. Para calcular los perfiles de las líneas y los diagramas de posición-velocidad, se deben conocer la velocidad local v_2 y el angulo θ del gas emisor. Una vez que se conoce la velocidad, se toma la emisión de cada segmento como la de una onda de choque plano-paralela con velocidad $v_\perp$ y $B_\parallel$ pesada por el área del segmento, y se divide la contribución de cada segmento al perfil de la línea en intervalos de 5 km s^{-1} en el marco de referencia del observador. La velocidad cero corresponde a la velocidad de la nube molecular ambiental.

Los cocientes y perfiles de líneas predichos se obtienen sumando primero los segmentos de cada anillo y despues sumando los anillos a lo largo del choque de proa. Los diagramas de posición-velocidad se obtienen asumiendo que el choque de proa es observado con un espectrógrafo teórico con su rendija centrada y orientada paralelamente al eje de simetría del choque de proa. En este caso, la emisión de cada anillo se calcula sumando los segmentos dentro de la rendija. Despues de esto, se calculan los contornos de igual intensidad en el plano (z,v_y) interpolando las intensidades obtenidas para cada anillo en función de la velocidad. Finalmente, se construyen archivos IRAF tridimensionales para cada línea con la emisión integrada de cada segmento (integrando a lo largo de la línea de visión) y su contribución al perfil de las líneas. Las primeras dos dimensiones contienen información sobre la distribución espacial de la emisión mientras que la tercera contiene la distribución de velocidades de la línea. A continuación, se obtienen los mapas de contorno del choque de proa calculando contornos de igual intensidad en el plano (x,z), y los diagramas con los

perfiles locales de las líneas se construyen obteniendo el perfil de la línea en cada posición (x,z) dentro del área del choque de proa.

iii) Forma del choque de proa

Tal como lo sugiere la morfología observada en algunos objetos HH, los choques de proa son frecuentemente aproximados usando geometrías hiperbólicas o parabólicas. Choe, Böhm y Solf (1985), y Raga y Böhm (1986) han estudiado morfologías más complicadas para describir el choque, y posteriormente, Hartigan, Raymond y Hartmann (1987) utilizaron una forma simplificada de estas aproximaciones. En el Capítulo 5 se utiliza este último enfoque para calcular el perfil del choque de proa. La forma del choque está dada por $z(r) = \alpha r^2 + \alpha^3 \beta r^4$, donde α y β son constantes, y r es el radio de un anillo dado (Hartigan, Raymond y Hartmann 1987). Para obtener esta ecuación, el radio y la altura de la proa se normalizaron con una constante R_0 que puede corresponder al radio de una condensación de alta densidad (*e.g.*, en los modelos de "bullets" o "cloudlets"), o al radio del choque de proa (*e.g.*, en el modelo de "jet"), o en unidades de un segundo de arco para un caso más general. Bajo esta normalización, z=Z/R_0, r=R/R_0, y α y β dependen de la elección de la constante de normalización.

iv) Campo Magnético

Observaciones de HH7 en el IR han mostrado que la emisión de líneas de H_2 surge de todo el objeto con forma de proa, incluyendo su ápice. Un choque tipo J produce menor emisión de líneas de H_2 que la emitida por un precursor magnético (*e.g.*, Hollenback y McKee 1989), de manera que un campo magnético debe moderar el choque aún en la punta del choque de proa. En términos de un precursor magnético, este resultado observacional se podría explicar si un campo magnético se encuentra alineado principalmente en una dirección perpendicular al eje de simetría de este objeto. Esto se debe a que sólo la componente paralela del campo magnético (*i.e.*, orientado en una dirección paralela al plano del choque), $B_{\parallel}$, dá origen al precursor magnético de una onda de choque. El tamaño del precursor L y el número de Mach de Alfvén M_A ($M_A = v_s/v_A$, donde $v_A = (B^2/4\pi\rho_i)^{1/2}$ es la velocidad de Alfvén) son proporcionales a B^2/v_s^2 y v_s/B, respectivamente. Por lo tanto, sólo se puede esperar emisión en el IR de una region cercana al ápice del choque de proa (como se observa en HH7) si $B_{\parallel}$ es más fuerte cerca del ápice, donde los choques son menos oblícuos y por lo tanto más fuertes. De esta manera, las velocidades de los

choques permanecen sub-alfvénicas dando lugar a un precursor de tamaño considerable. Esto sugiere que si la emisión en el IR surge de un precursor magnético, el campo magnético debe de estar orientado casi o totalmente perpendicular al eje de simetría del choque de proa. Bajo estas circunstancias, el tamaño del precursor y el número de Mach de Alfvén permanecen aproximadamente constantes a través del choque de proa, *i.e.*, $v_\perp/B_\parallel = v_*/B$.

III. RESULTADOS Y DISCUSION

a) TASAS DE ENFRIAMIENTO DE HIDROGENO MOLECULAR

Se considera un medio parcialmente ionizado y mayormente molecular, donde la fracción de ionización $X(e) = 10^{-5} - 10^{-1}$, la fracción atómica $X(H) = 10^{-2} - 10^{-1}$, y la densidad $n_H = 10^0 - 10^6\, cm^{-3}$.

Las tasas de enfriamiento radiativa (Λ_{rad}), disociativa (Λ_{diss}) y por bombeo colisional (Λ_e) muestran diferentes comportamientos. La tasa de enfriamiento radiativa es dependiente de la densidad, debido a la desexcitación colisional de los niveles. A altas densidades ($n \gtrsim 10^6$) la mayor parte de los niveles vibracionales-rotacionales están poblados casi como en equilibrio térmico, y la tasa de enfriamiento por volumen es proporcional a n_H. Para densidades $n \lesssim 10^5$, una molécula en un nivel excitado radía antes de ser desexcitada colisionalmente, y $\Lambda_{rad} \propto n_H^2$. La tasa de enfriamiento disociativa escala como n_H^2, independientemente de la temperatura, densidad y fracción de ionización en el gas molecular. Este comportamiento es consecuencia directa del hecho de que sólo se han incluido en estos cálculos las tasas disociativas por colisiones con H y H_2. La tasa de enfriamiento por bombeo colisional depende levemente de la densidad y escala con la fracción de ionización. Por lo tanto, la tasa de enfriamiento por volumen va como $\Lambda_e \propto n_H X(e)$.

Las tasas de enfriamiento radiativas dominan completamente a los otros procesos de enfriamiento a temperaturas menores que 10^4 K para la mayor parte de los parámetros considerados en este trabajo. A temperaturas mayores, su predominancia depende en gran parte de la densidad y de la fracción de ionización. Para densidades entre 10^2 y $10^4\, cm^{-3}$ el enfriamiento radiativo contribuye a más del 50% de la tasa de enfriamiento total a temperaturas tan altas como 50000 K para $X(e) = 10^{-5}$, y 20000 K para $X(e) = 10^{-2}$.

Los otros tipos de tasas de enfriamiento se hacen más importantes a bajas temperaturas cuando $n_H < 10^2$ o $n_H > 10^4\ cm^{-3}$.

A altas temperaturas y densidades y bajas fracciones de ionización (T $\gtrsim$ 7000 K, $n_H \geq 10^4\ cm^{-3}$ y $X(e) \sim 10^{-5}$), el enfriamiento por disociación supera al enfriamiento radiativo y al enfriamiento por bombeo colisional de electrones (ver Capítulo 2). Por ejemplo, $\Lambda_{diss} \simeq \Lambda_{rad}$ a T $\simeq$ 7500 K cuando $n_H = 10^6\ cm^{-3}$ y $X(e) = 10^{-5}$. A bajas densidades, la excitación colisional de los estados electrónicos BΣ y CΠ constituye el proceso de enfriamiento más importante a temperaturas $\gtrsim$20000 K o $\gtrsim$80000 K para densidades $\sim 10^0$ o $10^3\ cm^{-3}$, respectivamente. Puesto que Λ_e escala con la fracción de ionización, Λ_e se hace más importante a bajas temperaturas, en el caso de aumente la fracción de ionización (ver Capítulo 2). Sin embargo, el enfriamiento por disociación puede todavia dominar sobre el enfriamiento por bombeo a altas densidades, debido a su dependencia n_H^2, mientras que $\Lambda_e \propto n_H$. Por lo tanto, el enfriamiento debido a electrones es importante principalmente para medios moleculares de bajas densidades ($n_H \lesssim 10^3\ cm^{-3}$), altas fracciones de ionización ($X(e) \gtrsim 10^{-3}$) y altas temperaturas electrónicas ($T_e \gtrsim$ 20,000 K).

b) MODELOS PARA ONDAS DE CHOQUE TIPO J CON PRECURSORES MAGNETICOS

i) Líneas Moleculares

En general, la línea 1-0S(1) es más fuerte que H_β en la mayoría de los modelos considerados en este trabajo. Como en el caso de H_β, esta línea decrece monotónicamente cuando se reduce la velocidad del choque. Sin embargo, el cociente H_β/1-0S(1) decrece con la velocidad para $v_s \sim$ 100 a 50 km s^{-1}, y aumenta para valores más bajos, indicando que esta línea infrarroja tiene una dependencia más fuerte con la velocidad del choque que H_β. Las líneas emitidas por estados vibracionales excitados exhiben un comportamiento similar al observado en la línea 1-0S(1), mientras que las líneas rotacionales aumentan monotónicamente cuando se reduce la velocidad del choque. El aumento en las intensidades de la líneas con respecto a H_β a velocidades menores que o similares a 50 km s^{-1} se debe al hecho de que el frente de choque ha sido tomado en cuenta en los cálculos presentes. De hecho, el bajo cociente de líneas 1-0S(1)/2-1S(1) a velocidades menores que 50 km s^{-1} refleja las altas temperaturas del frente de choque.

Cuando se comparan las líneas infrarrojas de H_2 con la línea 1-0S(1), ellas presentan dos comportamientos generales de sus energías de excitación con respecto al nivel del cual se emite la línea 1-0S(1) (v=1 y j=3). Las líneas de niveles de excitación inferiores tienden a aumentar monotónicamente en intensidad relativamente a la línea 1-0S(1) cuando se reduce la velocidad del choque, alcanzando un máximo valor y luego decreciendo con la velocidad. El punto donde cambia la pendiente para las líneas de alta excitación (asi como para las líneas de baja excitación) puede ocurrir a velocidades diferentes para líneas diferentes, dependiendo de su energía de excitación. Los cocientes de líneas predichas a velocidades mayores que la velocidad de cambio dependen fundamentalmente de la temperatura en el precursor magnético, mientras que para velocidades menores dependen fundamentalmente de la temperatura en el frente de choque y de la rapidez con que se disocian las moléculas de H_2. Estos resultados muestran que la inclusión de la región del frente de choque produce cambios considerables en la intensidad de la emisión de líneas infrarrojas de H_2, asi como en la intensidad relativa de las líneas rotacionales respecto a las vibracionales-rotacionales tales como 1-0S(1).

Los efectos sobre la emisión de líneas de H_2 debido a cambios en los parámetros pre-choque son diferentes y en general menos notables que los producidos en las líneas atómicas. En este caso, los flujos de las líneas de H_2 reflejan la dependencia de los parámetros característicos del precursor magnético, tal como la longitud de amortiguamiento L y la temperatura máxima $T_{n,max}$, en los parámetros del choque. La emisión ultravioleta de H_2 en líneas y contínuos esperada para esta clase de choque se ha calculado también. Los resultados indican que dentro del intervalo cubierto por los parámetros usados en los cálculos, la intensidad predicha es demasiado débil, por varios ordenes de magnitud, para ser detectable. La emisión UV predicha no puede explicar ni la emisión UV observada en objetos como HH1 y HH2, ni las líneas UV observadas en HH43 y HH47.

ii) Velocidad Equivalente del Choque y Pérdida de Energía en el Precursor Magnético

Cuando una onda de choque se mueve a traves de un medio molecular, una fracción considerable de la energía disponible en el choque se disipa por excitación y disociación de las moléculas (McKee y Hollenbach 1987). Si el choque no es lo suficientemente fuerte como para ionizar al gas, una fracción de la energía se disipa también por excitación e ionización del gas atómico (Cox y Raymond 1985). Esta pérdida de energía reduce la

excitación del espectro producido por el gas chocado. Por lo tanto, el resultado neto de esta pérdida de energía es que el espectro obtenido para una onda de choque moviéndose en un medio neutro con velocidad v_s, se aplica en realidad a un choque moviéndose en un gas molecular con una velocidad equivalente v_{eqv} (Cox y Raymond 1985; McKee y Hollenbach 1987), dada por

$$v_{eqv}^2 = v_s^2 + 2g_{H2}(0)v_{H2}^2, \tag{7}$$

donde las velocidades están dadas en km s^{-1}, $g_{H2}(0) = n(H_2)/n_H$, y v_{H2} está dado por

$$\left[\frac{v_{H2}}{km\ s^{-1}}\right] \simeq 9.78 \left[\frac{R_{H2} + I_{H2}}{eV}\right]^{1/2}. \tag{8}$$

Aqu´ i, $I_{H2} = 4.48$ eV es la energía requerida para disociar las moléculas de hidrógeno, y R_{H2} es la pérdida de energía por excitación de H_2. Para los parámetros considerados aqu´ i, v_{eqv} es t´ ipicamente 10–15% veces mayor que la velocidad del choque supuesta.

Estos resultados indican que el espectro característico observado en objetos HH de baja excitación y sus altas velocidades radiales pueden resultar de la pérdida de energía por radiación de moléculas en precursores magnéticos. Sin embargo, algunos objetos tales como HH7-11 exhiben altas velocidades radiales, $\sim$ -60 to -180 km s^{-1}, mientras que su espectro de muy baja excitación es característico de choques con velocidades de 20-30 km s^{-1}. La pérdida de energía en el precursor magnético no puede explicar el espectro de baja excitación y las altas velocidades radiales simultáneamente. Puesto que una onda de choque de proa tiene una variedad de ondas de altas y bajas velocidades, su espectro tendrá una mezcla de líneas de alta y baja excitación. Por lo tanto, una onda de choque de proa moviéndose en un medio molecular magnetizado podría explicar el espectro característico observado en objetos HH de baja excitación. Esta posibilidad es explorada en el Capítulo 5.

iii) APLICACION DEL MODELO A HH7 Y AL CYGNUS LOOP

Hartigan, Curiel y Raymond (1989; Capítulo 3) encontraron que HH7 tiene forma de proa en todas las imágenes (Hα, [SII] y H_2 1–0S(1)), donde las imágenes de H_2 y [SII]

coinciden en un segundo de arco. HH7 tiene un pico secundario brillante dentro de la proa en la imagen de [SII], que es también brillante en Hα, pero desaparece en H_2, por lo que es un objeto de mucha más alta excitación que el resto de HH7. HH 8 consiste de dos nudos distintos, con comparable brillo en Hα. Sin embargo, el nudo sureste es considerablemente más brillante que el noroeste en [SII] y H_2. Los nudos coinciden aproximadamente en el espacio excepto por HH 8SE, que está desplazado 2" hacia el este en [SII] (alejandose de la fuente de excitación) con respecto a sus fotocentros en Hα y H_2. Un claro gradiente en condiciones de excitación existe también en HH 10, con la componente norte brillante en Hα y la porción sur brillante en [SII]. La emisión en [SII] está también localizada al este de la emisión en H_2 en este objeto. HH 11 no posee emisión en H_2 aunque es el más brillante de todos los objetos en Hα. Este nudo tiene una velocidad radial mucho más alta que la de otros objetos HH, y tiene mas forma de punto (ver Solf y Böhm 1987).

El modelo plano-paralelo ha sido usado por Hartigan, Curiel y Raymond (1989; Capítulo 3) para explicar la intensidad de las líneas de H_2 observadas en HH7. Estos autores encuentran que una onda de choque de 100 km s^{-1} moviéndose en un medio molecular magnetizado puede explicar las intensidades de líneas de H_2 observadas. Ellos también proponen que la morfología de proa y los perfiles de líneas observados en este objeto en longitudes de onda ópticas e infrarrojas podrían ser explicados por este tipo de modelo. Esta interpretación ha sido apoyada recientemente por observaciones nuevas e independientes (Carr 1990; Stapelfeldt *et al.* 1991). Un modelo basado en estos resultados plano-paralelos se usa en el Capítulo 5 para estudiar las características morfológicas y de líneas esperadas de un choque de proa moviéndose en un medio molecular magnetizado, y los resultados son aplicados al caso de HH7.

Recientemente, Graham *et al.* (1990) detectaron líneas de emisión infrarrojas débiles de H_2 excitado vibracionalmente asociado con filamentos ópticos brillantes excitados por choques (radiativos y no radiativos) al NE del Cygnus Loop. Encuentran que la población de los niveles de H_2 deducidas de las líneas 1-0S(2), 1-0S(1), 1-0S(0) y 2-1S(1) son consistentes con una sola temperatura de excitación vibracional $T_{ex} \simeq 2500$ K. Este resultado implica que el mecanismo de excitación es colisional en una onda de choque (descartando la fluorescencia UV y formación de moléculas en el post-choque como otros posibles mecanismos). Graham *et al.* usaron un modelo similar al que se presenta aquí para explicar el brillo superficial observado en H_2, la población de los niveles, y la

relación a la emisión óptica en el Cygnus Loop. Asimismo, ellos proponen que un precursor magnético puede explicar también el ancho de 20-30 km s^{-1} de la componente delgada de Hα por choques no radiativos observada por Hester y Raymond (1988), inexplicable de otra manera. Usando parámetros similares a los usados por Graham *et al.* (1990), hemos obtenido brillos superficiales similares pero con algunas diferencias importantes. La Tabla 5 muestra una comparación entre el brillo superficial calculado y el observado en el filamento MH1 por Graham *et al.*. Esta tabla muestra que para la velocidad de choque de 87 km s^{-1} , ambos modelos predicen el mismo brillo superficial en 1-0S(1), mientras que el modelo de 173 km s^{-1} difiere por un orden de magnitud. Esta discrepancia puede deberse a diferencias en el cálculo. Por ejemplo, la tabla muestra que la temperatura máxima obtenida en el precursor por estos autores es substancialmente mayor que la obtenida en los cálculos presentes. Ellos sugieren que el modelo con 87 km s^{-1} parece ser apropiado para el filamento MH1 y que puede explicar la emisión en H_2 por un factor de aumento geométrico de cerca de 30. Los resultados presentes apoyan los cálculos de Graham *et al.*. Sin embargo, los cocientes de líneas obtenidas con estos cálculos son bastante diferentes a las observadas. Se requieren cálculos adicionales para explicar mejor los cocientes de líneas de H_2 en estos filamentos del Cygnus Loop.

c) MODELO PARA CHOQUES TIPO J DE PROA CON PRECURSORES MAGNETICOS

i) Perfiles de Líneas

Los perfiles de la línea Hα se calculan a varios ángulos de visión ϕ desde 0° a 90°, donde $\phi = 90°$ corresponde a un choque de proa moviéndose en el plano del cielo y $\phi = 0$ representa un choque de proa moviéndose hacia el observador. El perfil de la línea Hα es simétrico en velocidad con un ***plateau*** característico cuando el choque de proa se mueve en el plano del cielo ($\phi = 90°$). A medida que el ángulo de orientación ϕ decrece, el perfil se vuelve más y más asimétrico, con un pico principal de intensidad creciente a las más altas velocidades negativas, mientras que un segundo "pico" o plateau, a más bajas velocidades radiales, decrece en intensidad. El segundo pico desaparece a bajos ángulos ($\phi \lesssim 45°$), dejando al pico principal con un ala extendida. Cuando $\phi = 0°$, Hα tiene un único pico muy asimétrico, con velocidad radial similar a la del choque de proa, y alas que se extienden a velocidades cercanas a cero. Esta forma indica que la emisión con alta velocidad radial proviene de cerca del ápice, mientras que a menores velocidades es emitida

en las alas del choque de proa. El plateau observado cuando $\phi = 90°$ se debe al hecho de que en esta orientación, el frente y los lados del choque de proa tienen velocidades radiales opuestas pero tienen la misma intensidad, contribuyendo lo mismo a la emisión en la línea.

Para un ángulo de visión dado, las líneas atómicas de alta excitacioón muestran perfiles similares al de Hα pero con algunas diferencias importantes. Líneas de alta excitación, como [OII] y [CII], son significativamente más delgadas que Hα, siendo más evidentes a ángulos de visión ϕ pequeños. Esto indica que estas líneas provienen fundamentalmente de regiones más cercanas al ápice de la proa que Hα, donde los choques son más fuertes y entonces tienen temperaturas más altas. Por otra parte, las líneas de baja excitación, como [SII] y [FeII], presentan un patrón característico de dos picos, independientemente del ángulo de inclinación. Ambos picos tienen intensidad comparable y separación similar a ángulos diferentes. El pico más intenso corresponde a la velocidad mayor y negativa debido a los ángulos de orientación que hemos escogido ($0° \lesssim \phi \lesssim 90°$). En este caso, una fracción considerable de la emisión proviene de las alas del choque de proa, donde los choques son oblicuos y más débiles (por lo que tienen temperaturas post-choque menores y baja velocidad radial), dando origen al pico doble. Una característica general es que el ancho completo a intensidad cero (FWZI) de una línea permanece constante a medida que ϕ varía.

Los perfiles infrarrojos de H_2 no muestran una estructura de doble pico como las líneas atómicas. Estas líneas infrarrojas son mucho más delgadas y tienen menor asimetría que las líneas atómicas. Debido a que las líneas de H_2 se emiten durante la aceleración del gas molecular en el precursor magnético y la velocidad aumenta desde cero hasta una fracción de la velocidad del sonido local $v_\perp$, la separación esperada entre los picos sería solamente de unos km s^{-1}, dependiendo de la velocidad del gas molecular y de la distribución espacial de la emisión. Si la separación entre los picos es lo suficientemente pequeña, los dos picos podrían ser escondidos por el ensanchamiento térmico y/o por la resolución instrumental usada en los cálculos (*i.e.*, 25 km s^{-1} para todas las líneas mostradas). Este modelo predice que las líneas de H_2 tienen velocidades radiales desde 0 hasta $\sim$ 50 km s^{-1}, dependiendo del ángulo de inclinación del choque de proa. Como en el caso de las líneas ópticas, la mayor velocidad ocurre cuando el choque de proa se mueve hacia el observador (*i.e.*, $\phi = 0°$). Asi mismo, el ancho completo a intensidad cero de estas líneas permanece constante a medida que ϕ varía. Sin embargo, el ancho completo a

intensidad cero de las líneas de H_2 es mucho menor que los $\sim$160 km s^{-1} obtenidos para las líneas atómicas. Esta diferencia se debe al hecho que las líneas atómicas se emiten en la región post-choque donde la velocidad del gas es $\sim v_\perp$, mientras que el gas molecular en el precursor es acelerado solamente hasta una fracción de $v_\perp$ (en la región pre-choque, $v \lesssim v_\perp/2$).

ii) Diagrama Posición-Velocidad

Para las líneas ópticas e infrarrojas, los perfiles en los diagramas posición-velocidad son simétricos respecto a la posición del ápice cuando $\phi = 0°$ (con una forma de bumerang), como se espera de un choque de proa axialmente simétrico como el considerado aqu´ i. Los perfiles son simétricos en velocidad cuando $\phi = 90°$, y tienen una forma triangular que es más evidente en las líneas de baja excitación. Esta forma característica se debe al hecho que, en esta orientación, el gas que se mueve a ambos lados de la proa a lo largo de la línea de visión tiene velocidades radiales opuesta de igual magnitud. A ángulos intermedios, la forma del perfil cambia, con una forma de anzuelo a $\sim 45°$. Una característica general es que las líneas de baja excitación (por ejemplo, [SII], [FeII]) aparecen más extendidas hacia la cola/alas del choque de proa, mientras que las líneas de alta excitación (por ejemplo,[OII], CII]) están más restringidas a regiones cercanas al ápice. Similarmente, las líneas rotacionales aparecen más extendidas hacia las alas que las líneas vibracionales.

iii) Mapas de Contorno Teóricos

Es evidente que la morfología predicha cambia drásticamente con el ángulo de orientación del choque de proa. Dos cambios importantes que se observan cuando ϕ cambia son la variación en posición del pico principal y del tamaño de las alas observables. En el Capítulo 5 se muestra que el choque de proa exhibe una morfología circular cuando $\phi = 0°$, como se espera de un choque de proa axialmente simétrico. A medida que el ángulo aumenta, la fuente aparece más y más elongada hasta que alcanza una forma parabólica con una cola cuártica empinada (es decir, una morfología cometaria) cuando $\phi = 90°$. El pico de la emisión aparece en el centro del objeto cuando $\phi = 0°$, y se mueve más cerca de la punta a ángulos mayores.

Para un ángulo dado, líneas diferentes muestran un comportamiento similar, pero tienen alas con extensión y distribución de emisión diferente. Las líneas de baja excitación

y las líneas de H_2 excitado rotacionalmente tienen colas largas y relativamente intensas, mientras que las líneas de alta excitación y las líneas de H_2 excitado vibracionalmente aparecen más compactas y con alas más débiles. Las líneas de alta excitación provienen de las regiones de más alta velocidad (alrededor del ápice del choque de proa), mientras que las líneas de baja excitación se extienden a velocidades mucho más bajas. Asimismo, este tipo de modelo predice que la emisión óptica y de H_2 presentará morfología similar y coincidirá espacialmente. Una consecuencia importante de este comportamiento morfológico es que la excitación del objeto decrece desde el ápice hacia las alas del choque de proa (esto es, el cociente [SII]/Hα aumenta en esta dirección), reflejando la menor excitación predicha para las menores velocidades de las alas (*e.g.*, Hartigan *et al.* 1987; Capítulo 4). Asimismo, el cociente entre H_2 y las líneas de Balmer (por ejemplo, el cociente 1-0S(1)/Hα) aumenta en la misma dirección, como predicen los modelos plano-paralelos (ver también el Capítulo 4).

iv) Cocientes de Líneas Teóricas

Los resultados muestran una mezcla de líneas de alta y baja excitación, como se espera de un objeto que contiene una variedad de velocidades de choque. Puesto que los modelos de choques de proa incluyen sólo velocidades $\leq$100 km s^{-1}, no se esperan líneas de muy alta excitación, como [OIII] λ5007, y otras líneas, como λ1206,1896, [CIII] λ1908 aparecen muy débiles. Líneas de excitación moderada, como [OII] λ3726,3729 y CII] λ2325 aparecen realtivemente fuertes, de intensidad comparable a Hβ. Por otra parte, líneas de baja excitación, como [SII] λ6716,6731 y [OI] λ6300, asi como las líneas infrarrojas de [FeII], [OI] y [SiII] aparecen con intensidad similar o mayor que Hβ. Estos resultados también muestran que un choque de proa tipo J con un precursor magnético produce líneas rotacionales y vibracionales de H_2 relativamente fuertes, varias de ellas más fuertes que Hβ.

v) Comparación con Observaciones y con otros Modelos

El modelo choque de proa tipo J con un precursor magnético predice un ancho completo a máximo medio (FWHM) de $\sim$100 km s^{-1} para las líneas atómicas y de $\sim$50 km s^{-1} para las líneas infrarrojas de H_2, anchos que son similares a los observados en objetos HH. Asimismo, las velocidades radiales predichas están en el rango de 0 a cerca de $-$100 km s^{-1} para las líneas ópticas y entre 0 y $-$50 km s^{-1} para las líneas de H_2

(dependiendo del ángulo de visión), que son también similares a las observadas en objetos HH. Este modelo también predice que una onda de choque de proa moviéndose en un medio molecular magnetizado presentará morfologías óptica e infrarroja de forma de proa similares si se observa a un ángulo diferente que alineado a lo largo de la línea de visión (a este ángulo presentará morfología circular), con una forma mejor definida para ángulos cercanos a 90° (ver Capítulo 5). Del mismo modo, el objeto tendrá sus picos principales en el óptico y en el infrarrojo coincidiendo espacialmente y tendrá una cola extendida pero más débil en ambas longitudes de onda. Estas características han sido observadas en algunos objetos HH. Algunas observaciones ópticas e infrarrojas de objetos HH han revelado que la emisión en H_2 exhibe una amplia variedad de morfologías, similares a las observadas a longitudes de onda ópticas, pero con algunas diferencias (ver revisión presentada en el Capítulo 1; Curiel 1992). En algunos casos, como en HH43 (Schwartz *et al.* 1988) y HH7 (Hartigan, Curiel y Raymond 1989; Stapelfeldt *et al.* 1991) las emisiones óptica e infrarroja coinciden espacialmente, mientras que en otros tales como HH1 y Cefeo A (ver Capítulo 1) la emisión en H_2 proviene de las alas/cola del objeto óptico en forma de proa. La onda de choque de proa tipo J con un precursor magnético puede explicar las formas y la distribución espacial de las emisiones óptica e infrarroja observada en objetos tales como HH7 y HH43, pero no las observadas en HH1 y Cefeo A/GGD 37. Sin embargo, si los fuertes choques cercanos al ápice produjeran suficiente emisión UV como para disociar las moléculas de H_2 antes de llegar al frente de choque, el precursor magnético no se formaría cerca del ápice, y por lo tanto, la emisión de H_2 sería observada sólo en las alas del choque de proa, como se observa en HH1 y Cefeo A.

En el Capítulo 5 se muestra que un choque de proa predice naturalmente un decrecimiento en el nivel de excitación (por ejemplo, el cociente [SII]/Hα aumenta) y un aumento del cociente H_2/Hα (por ejemplo, 1-0S(1)/Hα) desde el ápice hacia las alas de la proa, debido a que las menores velocidades de las alas producen un espectro de menor excitación (Hartigan *et al.* 1987) y líneas de H_2 más fuertes en relación a Hβ (ver Capítulo 4). Un comportamiento similar ha sido observado en HH43 por Schwartz *et al.* (1988), donde el cociente [SII]/Hα decrece desde la posición NO del objeto hacia la SE, mientras que el cociente 1-0S(1)/Hα aumenta en la misma dirección. La estructura de nudos múltiples observada en este objeto sugiere que el choque de proa puede estarse rompiendo en muchas piezas, como parece estar ocurriendo en HH2.

IV. Aplicación del Modelo de Choque de proa a HH7

a) Mapas de Contorno

A pesar de que los mapas de contorno observados y los predichos por el modelo son bastante similares, el perfil observado varía de línea a línea mientras que los calculados exhiben básicamente la misma forma, tal como se esperaría de un modelo tan idealizado. El modelo no predice el segundo pico brillante dentro de la proa que aparece en las imágenes de [SII]. Sin embargo, se ha propuesto que este segundo pico, podría ser debido al gas de un jet enfriandose detrás del disco de Mach del jet (Hartigan, Curiel y Raymond 1989; Capítulo 3, and Capítulo 5), lo cual no se ha tomado en cuenta en los presentes cálculos.

b) Perfiles de Líneas y Diagramas de Posición-Velocidad

Los resultados del modelo muestran una similitud notable entre los perfiles de línea y los diagramas de posición-velocidad calculados y los observados. En particular, las velocidades radiales obtenidas para las tres líneas así como el ancho de la línea 1–0S(1) concuerdan bastante bien con lo observado. Una diferencia importante entre los perfiles calculados y los observados es que el perfil de la línea de [SII] predicho tiene un pico secundario de baja velocidad que no aparece en el perfil observado. Esta diferencia se puede deber a que la emisión de la segunda componente brillante que se observa en las imágenes de [SII], y que parece corresponder a un disco de Mach, podría aumentar la intensidad del pico primario con respecto al segundo pico en el perfil de la línea. Es más, tal como Hartigan (1987) hace notar, en un jet estelar tanto el choque de proa como el disco de Mach deberían de poseer brillos comparables, y por lo tanto, la distribución de velocidades de la emisión del último juega un papel importante en la forma del perfil final de las líneas observadas. Otra de las diferencias principales es el ala de alta velocidad negativa que aparece en la línea 1–0S(1) y que no se predice en este modelo. Carr (1990 propuso que la componente de alta velocidad podría ser emitida detrás del frente tipo J, donde el gas se mueve a velocidades comparables a las del choque. Esta segunda componente podría explicar la emisión de alta velocidad que se observa en el perfil de la línea y en el diagrama de posición-velocidad.

c) Cocientes de Líneas

Un cierto número de cocientes de línea en el óptico, UV e IR fueron obtenidos integrando sobre una rendija téorica con anchos similares a los obtenidos en las

observaciones. Los valores más notables en las tablas que se dan en el capítulo 5 son los flujos altos que se obtienen para las líneas de [OII], [NII], MgII, [FeII] y de H_2 y los flujos relativamente bajos para las otras líneas. Las líneas intensas en el UV y el óptico concuerdan con los flujos observados mientras que las líneas de baja excitación tales como [OI], [CI] y [SII] son substancialmente más debiles que las observadas. Este resultado dista mucho de explicar la naturaleza de la extrema baja excitación de este objeto que se deriva de los cocientes de líneas ópticas (*e.g.*, Böhm y Solf 1990; Solf y Böhm 1987).

Los cocientes calculados para las líneas IR concuerdan con los observados. En particular, la línea 1–0S(1) es una de las calculadas con menor exactitud. El flujo calculado para esta línea es de aproximadamente el 70% del observado utilizando una rendija de 5" de ancho, y esta diferencia aumenta cuando los flujos son obtenidos con una rendija más ancha. Es importante hacer notar que el cociente de las líneas 1–0S(1)/2–1(S1) calculado es de alrededor de 4, mientras que el valor observado es de alrededor de 10. El bajo cociente de las líneas calculado se debe a: a) Una cantidad considerable de la emisión de H_2 proviene de regiones cercanas al ápice, donde los choques son más fuertes y por lo tanto con temperaturas más elevadas, y b) La mayor parte de la emisión de H_2 se produce cerca del frente de choque tipo J donde la temperatura es mayor.

d) Mapas de Velocidades

Recientemente se ha obtenido un mapa detallado de velocidades de la línea H_2 1–0S(1) de HH7 con una resolución espacial del orden de 1", combinando un arreglo de detectores infrarrojos bidimensional (utilizando IRCAM en UKIRT) con un espectrofotómetro Fabry-Perot (Carr 1990). El perfil de la línea 1–0S(1) se calculó en diferentes puntos a lo largo del choque de proa con el objeto de compararlo con la distribución espacial observada. Aunque existen algunas diferencias entre los mapas de velocidad observados y los calculados, en el capítulo 5 se muestra que la distribución espacial y los perfiles de las líneas calculados son similares a los que se observan en este objeto, lo cual apoya la idea de que HH7 es un choque de proa. En ambos casos, las líneas más anchas e intensas se observan cerca del ápice de la proa. Las líneas son más debiles en las alas y disminuyen en intensidad en las regiones más alejadas de ápice. Los perfiles de las líneas detrás del ápice a lo largo del eje principal de simetría estan dominados por la emisión proveniente de las regiones con mayores velocidades (*i.e.*, el lado más cercano al observador contribuye en mayor medida a la línea de emisión. Por último, los perfiles a lo largo del contorno del choque (shock

limb) son más angostos y presentan velocidades centrales menores.

Debido a que esta técnica puede ser utilizada no sólo en el IR sino también en el óptico, se presentan mapas de perfiles de líneas locales (mapas de velocidades) para un número de líneas en el óptico y el IR (ver capítulo 5). Las líneas escogidas han sido detectadas previamente y en principio podrían ser mapeadas. En el capítulo 5 se muestra que se espera una distribución de perfiles similares para distintas líneas. Las características descritas anteriormente para la línea 1–0S(1) son aún más notorias en las líneas de baja excitación como [SII], [CI] y [FeII]. En estas líneas, el rasgo de pico doble predicho para el perfil de la línea integrada tambien aparece en los perfiles de líneas locales. La intensidad relativa entre ambos picos cambia a lo largo de la proa y como se mencionó anteriormente, la componente de baja velocidad es más prominente a lo largo del contorno del choque, mientras que las alas, de alta velocidad, dominan atrás del ápice a lo largo del eje principal.

Este nuevo tipo de observaciones será muy útil para establecer el tipo de choque y la geometría de objetos HH y jets ópticos individuales. El mapeo de líneas de baja excitación parece ser un metodo particularmente útil para definir una geometría de choque de proa, debido al rasgo característico de doble pico predicho para este tipo de líneas. En particular, se podría utilizar [SII] en el óptico y [FeII] en el infrarrojo en los casos en que estas líneas sean lo suficientemente intensas para ser mapeadas.

Por último, se podría probar la existencia del disco de Mach propuesto en HH7 obteniendo mapas de velocidades de alta resolución de líneas de baja excitación tales como [SII] y [FeII], y comparándolos con las líneas que se espera sólo sean emitidas por el choque de proa tales como H_2 1–0S(1) y Hα. Un estudio detallado de los cambios sistemáticos en los perfiles de estas líneas a través de este objeto HH, y su comparación con las predichas para un choque de proa podría conducir a la identificación del disco de Mach.

V. RESUMEN Y CONCLUSIONES

Choque Plano-Paralelo

Se presentó un modelo plano-paralelo para una onda de choque tipo J con un precursor magnético, y se mostró que este tipo de ondas de choque puede producir una cantidad considerable de emisión en líneas tanto de H_2 como atómicas. Así mismo, se

mostró que produce emisión de líneas de H_2 en el IR de intensidad comparable o mayor a la de líneas ópticas atómicas tales como Hβ.

Al tomar en cuenta la región del frente de choque, las líneas de H_2 en el IR pueden ser considerablemente más intensas de lo esperado cuando esta region no se toma en cuenta. De la misma manera, los cocientes de las líneas de H_2 con respecto a la línea 1–0S(1) pueden cambiar al considerar el frente de choque.

La energía emitida por las moléculas de hidrógeno reduce considerablemente la excitación de la onda de choque, *i.e.*, el espectro atómico será equivalente al de una onda de choque de menor velocidad. Sin embargo, esto por sí solo no es suficiente para explicar la naturaleza de la extremadamente baja excitación de HH7.

Las intensidades de las líneas que este modelo predice pueden explicar las intensidades de las líneas de H_2 observadas en HH7. En el caso del Cygnus Loop se requiere de un factor geométrico de aumento de alrededor de 30 para explicar las intensidades observadas en el filamento MH1.

Choque de proa

Se presentó un modelo para ondas de choque de proa tipo J con precursores magnéticos. Se calcularon intensidades y perfiles de líneas teóricos, así como diagramas de posición-velocidad y mapas de contornos y velocidades para varias líneas ópticas e infrarrojas. Esta es la primera vez que se han llevado a cabo simulaciones numéricas para predecir líneas de emisión en el óptico y en el IR simultáneamente a partir de ondas de choque en proa. Los resultados principales del modelo se enumeran a continuación:

Espectro. Los resultados indican que en un choque de proa tipo J con precursor magnético se espera una combinación de líneas de alta y baja excitación así como líneas de H_2 relativamente intensas.

El modelo predice un decremento en el nivel de excitación del ápice hacia las alas del choque de proa (*i.e.*, el cociente [SII]/Hα aumenta en esta dirección). Se espera una correlación similar en la intensidad relativa de líneas de H_2 con respecto a Hβ (*i.e.*, el cociente H_2/Hβ aumenta del ápice hacia las alas). La pérdida de energía en el precursor

magnético reduce considerablemente la excitación del espectro predicho. Sin embargo, este espectro aún dista mucho del observado en objetos HH de baja excitación.

Perfiles de Líneas y Diagramas de Posición-Velocidad. Los perfiles de las líneas y los diagramas de posición-velocidad predichos presentan formas que cambian con la orientación del choque de proa. Las líneas de baja excitación exhiben un rasgo característico de doble pico, mientras que las líneas de alta excitación exhiben sólo un pico principal con un ala extendida de baja velocidad. La velocidad radial predicha tambien cambia con el ángulo, siendo similar a la velocidad del choque cuando se mueve hacia el observador. A un ángulo dado, el FWHM es distinto para líneas de alta y baja excitación, y es similar para líneas dentro de cada categoría, mientras que el FWZI es similar para todas las líneas atómicas. Por otro lado, los perfiles de las líneas de H_2 exhiben un pico único y son más angostas que las líneas ópticas, con FWHM de $\sim$50 km s^{-1}, anchos a un 10% del pico de $\sim$80 km s^{-1}, y velocidades radiales que varían de 0 a 50 km s^{-1}. El ensanchamiento instrumental no cambia apreciablemente los anchos de las líneas ópticas e infrarrojas, lo cual indica que éstas se deben principalmente a dispersión de velocidades y a ensanchamiento térmico.

Mapas de Contornos. El modelo predice morfologías similares para la emisión óptica y de H_2 para un choque de proa, y que éstas coinciden espacialmente. Se encontró que en el caso de líneas rotacionales del H_2 y atómicas de baja excitación, la emisión presenta alas extendidas y relativamente intensas mientras que en el caso de líneas vibracionales de H_2 y atómicas de alta excitación la emisión es mas compacta y de alas mas débiles. Este resultado indica que el objeto presentaría una disminución en la excitación del ápice hacia las alas.

Con el desarrollo reciente de detectores bidimensionales ópticos e infrarrojos, es posible estudiar la morfología de los objetos HH y su distribución de perfiles de líneas locales combinando los detectores bidimensionales con espectrofotómetros Fabry-Perot. La comparación de resultados de este nuevo tipo de observaciones con los obtenidos a partir de modelos teóricos, como el aquí presentado, será un metodo muy efectivo para establecer el tipo de choque y la geometría de objetos HH y jets ópticos individuales. El modelo predice una distribución de perfiles de línea característica para un choque de proa que podría identificarse observacionalmente. Se encontró que las líneas más intensas con perfiles más anchos y velocidades radiales más altas se encuentran cercanas al ápice, mientras que las líneas más débiles con velocidades radiales bajas aparecen a lo largo

del contorno del choque, y las líneas a lo largo del eje de simetría están dominadas por la emisión del lado del choque más cercano al observador. El mapeo de líneas de baja excitación puede ser particularmente útil para definir la geometría de un choque en proa, debido al rasgo característico de doble pico predicho para este tipo de líneas. En particular, se podría utilizar [SII] en el óptico y [FeII] en el IR siempre y cuando estas líneas sean lo suficientemente intensas para ser detectadas.

HH7. Los resultados que aquí se presentan indican que un choque en proa tipo J con precursor magnético puede reproducir la mayoría de los resultados observacionales del objeto HH7. Se encontró que un choque de proa que se mueve con $v_s \sim 100$ km s^{-1} a través de un medio molecular magnetizado de $n_H \sim 300$ cm^{-3}, y con un ángulo de inclinación de $\sim 60°$ con respecto a la línea de observación, reproduce con bastante precisión no sólamente los perfiles de líneas en el óptico y el infrarrojo y las velocidades radiales, sino también los diagramas de posición-velocidad, y los mapas de contornos y de velocidad observados en este objeto. Sin embargo, el espectro óptico calculado aún dista mucho de explicar el espectro de baja excitación extrema que se observa en este objeto. Se propone que un choque de proa con alas más extendidas, campos magnéticos aún más intensos, mayor pérdida de energía por otras moléculas, o la emisión proveniente de un disco de Mach podría explicar dicho espectro. Asimismo, el ala de alta velocidad negativa observada en el perfil de la línea 1-0S(1) no se reproduce en este modelo. Sinémbargo, se propone que esta componente de alta velocidad puede deberse a emisión producida en el frente de choque, en el cual, las altas temperaturas y velocidades pueden producir un ala negativa extendida. Esta posibilidad no se incluyó en los cálculos presentes. Es importante hacer notar que este modelo a pesar de ser simple, puede reproducir la mayoría de las observaciones de HH7 y varios resultados observacionales de otros objetos HH.

Aunque los choques tipo J con precursores magnéticos podrían ser un tipo importante de ondas de choque, se ha realizado muy poco trabajo al respecto. Este tipo de choque parece ser una manera muy prometedora de explicar la coincidencia espacial de la emisión óptica e infrarroja, así como los perfiles de líneas observados en HH7 y otros objetos. En el futuro, se requerirá de calculos más detallados para mejorar los resultados de este modelo básico.

CHAPTER 1

INTRODUCTION

MOLECULAR STUDIES OF HERBIG-HARO OBJECTS

ABSTRACT.

Recent ultraviolet, infrared, millimeter and centimeter-wavelength observations have revealed that HH objects are also sources of molecular line emission. With the new infrared array detectors, it is now possible to study the H_2 emission distribution at resolutions comparable to that of optical images. This type of observations have shown that H_2 line emission in HH objects presents a wide and complex variety of morphologies, and that although the overall distribution of the H_2 emission is similar to that observed at optical wavelengths, they have subtle but important differences. Infrared and optical observations combined with further calculations may provide fundamental information about the physical conditions in the gas that yield both H_2 and optical emission from the same HH objects. New high-angular resolution radio observations of molecular lines have revealed that small high-density condensations are frequently found at the border of HH objects. The study of the association and interaction between these cloudlets and the HH objects will provide important clues about the origin of these condensations and the HH objects themselves.

I. INTRODUCTION

It has been known for several years that the optical line emission sources known as Herbig-Haro (HH) objects mark the location where energetic winds from young stellar objects confront the dense quiescent gas of surrounding molecular clouds. It is now well established: the shock wave nature of HH objects, their often large proper motions, their association with bipolar molecular outflows, and their proximity to highly reddened young stars (see Schwartz 1983 for a review). Because HH objects exhibit a wide variety in morphology (see Strom *et al.* 1986), their specific shock geometries have been a matter of some debate.

Several models have been proposed to explain the excitation of this type of objects: ambient cloudlets in a supersonic stellar wind (Schwartz 1978), turbulent gas along the walls of a cavity or a stellar jet (Cantó 1980, Mundt *et al.* 1987), discrete stellar mass ejections or "bullets" (Norman and Silk 1979), and "working surfaces" at the head of stellar jets (Mundt 1985; Mundt *et al.* 1987; Raga 1988; Hartigan 1989).

The exciting star of HH objects can usually be located only by infrared or radio observations since they are highly obscured at optical wavelengths. Extinction may also bias our view of the HH objects themselves, favoring the detection of blueshifted objects (*i.e.*, those moving out from the host molecular cloud toward us). Recent ultraviolet, infrared, millimeter and centimeter wavelength observations have revealed that HH objects are also sources of molecular line emission. With new infrared array detectors, it is now possible to obtain high-resolution images comparable to those at optical wavelengths. This new possibility offers the opportunity for a detailed comparison of the molecular, atomic, and ionized gas tracers of the Herbig-Haro object shock fronts. The spatial relationship between the molecular and atomic emission should be indicative of the shock type and geometry within an individual HH object. Millimeter and centimeter-wavelength observations of high density tracers (such as HCO^+ and NH_3) have shown that small clumps of dense ($\geq 10^4$ cm^{-3}) molecular gas are frequently found at the border of HH objects. Although the association between these molecular condensations and the HH objects seems to be clear, their origin is still uncertain.

Below, a brief review of molecular emission in HH objects will be presented. It will be discussed that HH objects have a wide variety of morphologies at optical and infrared wavelengths, and that the line characteristics, morphology and spatial distribution between optical, infrared and radio line emission may provide important clues about the origin of HH objects.

II. H_2 EMISSION ASSOCIATED WITH HH OBJECTS

The near-infrared spectral region contains a number of emission lines of molecular hydrogen, which have been proven to be important diagnostics for the molecular component of the gas in HH objects. The strongest and most commonly studied infrared line is the v=1–0 S(1) H_2 line at 2.12 μm. This line was first detected and mapped in HH objects

using single beam techniques, and recently, using two–dimensional array detectors. H_2 emission has been searched for and detected in many Herbig-Haro objects, including HH1-2 (Harvey *et al.* 1986; Hartigan, *et al.* 1991), HH 7-11 (Zealey *et al.*1984; Lightfoot and Glencross 1986; Hartigan *et al.* 1989; Burton *et al.* 1989; Garden *et al.* 1990; Stapelfeldt *et al.* 1991), HH32 (Zealey *et al.* 1986), HH43 (Schwartz *et al.* 1988b), HH52/53/54 (Sandell *et al.* 1986), HH 6 and HH 12 (Lane and Bally 1986; Stapelfeldt *et al.* 1991), Cep A/GGD 37 (Bally, and Lane 1991), and several additional sources in surveys by Elias (1980), Schwartz *et al.* (1987), and Wilking *et al.* (1990); see also the review by Lane (1989). High-resolution infrared spectra of H_2 lines, from several HH objects, have been obtained by Doyon and Nadeau (1988), Zinnecker *et al.* (1989), Brand *et al.* (1989) and Carr (1990). A general result of these observations is that H_2 lines are much more narrow than optical lines. In particular, the width of the S(1) line is typically only half of the width of the Hα line in the same objects, and the observed central velocities of the H_2 lines are also lower than those of the optical lines (Zinnecker *et al.* 1989).

The vibrational and rotational transitions of the H_2 molecule can be excited either by shocks (via collisional excitation in gas heated by the shocks to a few thousand degrees) or by absorption of ultraviolet radiation (in the Lyman and Werner bands with subsequent cascade to lower levels). Because the line strengths produced by the collisional and the fluorescent processes are significantly different, it is possible to distinguish between these mechanisms by comparing the line strength of lines from different levels such as the v=1–0 and v=2–1 S(1) transitions at 2.122 μm and 2.247 μm, respectively. A general description of the characteristics expected for H_2 emission excited in several different situations is given by Wolfire and Königl (1991). Numerical simulations predict that the expected line ratio of these lines from shocked gas is of the order of 10, whereas in photo excited gas it is ~ 2 (*e.g.*, Black and van Dishoeck 1987). Molecular line ratios measured in several HH objects are ~ 10 (*e.g.*, Schwarts *et al.* 1987, 1988a), which are consistent with the predictions of nondissociative, low velocity shock wave models (*e.g.*, Shull and Hollenbach 1978). In general, the H_2 emission seems to trace low velocity shock waves (with velocities around 10 to 40 km s^{-1}), while the optical emission traces much faster shocks (with typical velocities of about 100 km s^{-1}, or more). However, there is some evidence that other molecular excitation mechanisms may be at work in some of the objects. For instance, ultraviolet lines identified as H_2 Lyman band emission have been observed in some low-excitation HH objects such as HH 43 and HH 47 (Schwartz 1983). Likewise, the UV continuum that has

been detected in several HH objects (such as HH 1 and 2) and previously attributed to atomic hydrogen two-photon emission (*e.g.*, Dopita *et al.* 1982; Brugel *et al.* 1982) may arise, at least in part, from H_2 photodissociation (Böhm *et al.* 1987). A detailed review of UV observation of HH objects has been recently presented by Brugel (1989). In the case of HH1-2, for instance, the measured infrared line ratios (Elias 1980; Harvey *et al.* 1986) lie between those expected by UV continuum pumping and collisional excitation. Wolfire and Königl (1991) have recently proposed that the H_2 line emission in these objects is mostly due to photo-excitation. However, the spatial distribution of the optical and infrared emission (see below) suggests that at least in this case, the H_2 line emission is excited collisionally, but having a significant contribution from photo excitation (which may also take account of the excess in the UV continuum).

III. COMPARISON OF OPTICAL AND IR EMISSION IN HH OBJECTS

Since H_2 lines and optical lines trace different components of the shocked gas, a comparison of the spatial distribution of optical and infrared emission in HH objects may provide essential clues to their flow structure. With the new infrared array detectors, it is now possible to study the H_2 emission distribution at resolutions comparable to optical images. Such studies have been performed by Schwartz *et al.* (1988), Hartigan *et al.* (1989), Garden *et al.* (1990), Stapelfeldt *et al.* (1991), and Lane *et al.* (1991). The technique and new results are discussed in a recent review by Lane (1989). These studies have shown that the H_2 line emission in HH objects presents a wide and complex variety of morphologies. Although the overall distribution of the H_2 emission is similar to that observed at optical wavelengths, they have subtle but important differences. To illustrate these differences, we will present a general description of the morphology of three regions; HH 1-2, Cepheus A, and HH 7-11.

a) HH1-2. Large proper motions and wide optical lines have been observed in this region indicating that high velocity (up to ~200 km s^{-1}; Hartmann and Raymond 1984) shock waves are taking place. However, H_2 line profiles exhibit narrow linewidths (of about 40 km s^{-1}; Zinnecker *et al.*1989), suggesting that H_2 molecules are excited by weaker shock waves. Figure 1 shows a comparison of an infrared H_2 line image with optical H_α and [SII] images of the HH1-2 region obtained by Hartigan *et al.* (1991). Although HH1 and HH2 share a common energy source, they exhibit different morphologies at both,

infrared and optical wavelengths. HH1 is a clear example of a well defined bow shaped optical object where the H_2 lines are emitted from the wings (away from the apex) of the bow shock. This morphology is consistent with a jet model (or a bullet model) with a bow shock at its end. In this model, the external H_2 molecules entering the bow shock will be dissociated near its apex (where the shock velocity is generally greater than 100 km s^{-1}) and H_2 line emission will therefore predominantly arise from the wings of the bow shock (where the shocks are oblique and thus, weaker), having small radial velocities (compared with optical lines). The fact that the H_2 emission is observed mainly along the edge of one side of the optical object may be due to a geometrical projection (being favored the regions in the wings of the shock wave where, viewed from an angle, the molecular column density along the line-of-sight is greater) or to inhomogeneities in the ambient gas (*e.g.*, if the flow is hitting the edge of a molecular condensation such as that detected in this region by Davis *et al.* [1990]; see below). On the other hand, HH 2 has a more complicated optical structure, with several knots and extended emission connecting them. A similar morphology is observed at infrared wavelengths but with less evident extended emission. When infrared images are superimposed to optical images (see Figure 1), the H_2 emission seems to be produced predominantly upstream with respect to the H_α and [SII] lines (*i.e.*, toward the energy source of the system). However, most of the optical knots seem to have an H_2 counterpart, suggesting a common origin for the H_2 and optical lines.

b) Cepheus A/GGD 37. A particularly intriguing case is the Cepheus A region (*e.g.*, Hartigan *et al.* 1986, Lenzen 1988), which has been mapped at arcsecond resolution (Lane 1989, Bally and Lane 1991). This HH object presents large proper motions (110–250 km s^{-1}) and extremely broad optical lines indicating shock velocities up to almost 500 km s^{-1}. On the other hand, the H_2 lines are much narrower with linewidths of 25–45 km s^{-1} (Doyond and Nadeau 1988), suggesting that the H_2 molecules are excited by much less energetic shock waves. Figure 2 shows a comparison of a mosaic of H_2 emission with a [SII] image (Bally and Lane 1991; Lane *et al.* 1991). The GGD 37 HH object has an overall bow shock morphology, with complex bow shaped substructures. A similar morphology is seen in molecular hydrogen, but in this case the arcs are softer and less protruding. As in the case of HH1, it appears that the H_2 lines are emitted mainly from the wings of the bow shocks, where the shocks are oblique and thus much weaker (Bally and Lane 1991). The morphology and spectroscopic characteristics of this object seem to be consistent with a model of a bow shock formed around an interstellar "bullet" moving

through a molecular medium and viewed from an angle (Hartigan *et al.*1986; Lane 1989; Bally and Lane 1991).

c) HH7-11. HH7-11 is a nearly collinear system of optical emission knots in the L1450 molecular cloud near NGC 1333 (see Strom *et al.* 1986). These objects have optical radial velocities (–200 to –40 km s^{-1}) and line profiles indicative of shock velocities $\sim$ 100 km s^{-1} (Solf and Böhm 1987), but the spectra show strong [OI] and [SII] lines characteristic of a low-velocity ($\sim$ 30 km s^{-1}) shock. The H_2 1–0S(1) emission line is centered at much lower radial velocities of –60 to 0 km s^{-1} (Zinnecker *et al.* 1989), an important fact to shock models of the region. Figure 3 shows a comparison of an infrared H_2 line image with optical H_α and [SII] images of this region obtained by Hartigan *et al.* (1989). Intense H_2 emission is observed in three of the HH objects (HH7, HH8, and HH10), while weak emission is observed in HH9 and no emission is associated with HH11. HH7 is a particularly interesting object which has a bow-shaped morphology at both, optical and infrared-wavelengths, with the H_2 and [SII] images coinciding within an arcsecond. Recent results indicate that in the case of HH7 the H_2 emission seems to arise from a "magnetic precursor" in front of a J–shock (Hartigan *et al.* 1989; Carr 1990; and Stapelfeldt *et al.* 1991). In this model, since the ion–magnetic speed is greater than the shock velocity, a "magnetic precursor" propagates ahead of the shock, compressing and heating the gas before it goes through the main shock (see, *e.g.*, Draine 1980, and Draine *et al.* 1983 for a more detailed discussion). Therefore, a jet moving through a magnetized molecular medium will produce a substantial amount of H_2 emission from the precursor (even at high velocities close to the apex of the bow shock). In this case, the H_2 lines will be broader and have higher radial velocities than those expected in bow shock models without a magnetic precursor, and the H_2 and optical emission should nearly coincide spatially, having a similar bow-shaped morphology. Although J–shocks with magnetic precursors may be an important class of shock wave, little work has been done (*e.g.*, Draine 1980; Hartigan *et al.* 1989) in this direction. Detailed calculations will be needed to establish if such kind of precursors may actually exist in shock waves with shock velocities of about 100 km s^{-1} or even higher (as suggested by observations). In HH8 and HH10, the H_2 emission seems to be produced upstream with respect to the H_α and [SII] lines (*i.e.*, toward the energy source of the system). In these two objects, the spatial and velocity characteristics of the emitting gas reveal a geometry more complex than that of a simple bow shock or planar shock. HH11 remains an enigma, and could represent a second ejection from SVS

13 (the presumed energy source of the system). The low–excitation spectrum observed in this object is particularly difficult to explain since HH 11 has no visible H_2 emission.

Recently, detailed H_2 velocity mapping with spatial resolution of the order of 1″ has been obtained combining two-dimensional infrared detector arrays, such as IRCAM at UKIRT, with Fabry-Perot spectrophotometers (*e.g.*, Carr 1990). This new type of observations will be very useful to establish the shock type and geometry of individual HH objects and optical jets. Likewise, further information can be obtained by calculating infrared line intensities and profiles from bow-shaped shock waves with magnetic precursors, similar to those calculated for optical lines by Hartigan *et al.* (1987). This type of model has been used by Carr (1990) to calculate the H_2 1–0S(1) line profile for a bow shock geometry, for which he obtained a profile very similar to the spatially integrated line profile for HH7. In Figure 4, we compare the integrated H_2 flux map and spatial line profiles obtained for HH7 by Carr (1990) with those calculated for a bow-shaped shock wave with a magnetic precursor, using a shock velocity of 100 km s^{-1}, and an inclination angle of 40° with respect to the line-of-sight. The adopted shock is a very simplified jet model in which both the temperature and velocity increase linearly from an initial value to their maximum values in the precursor (see Hartigan *et al.* 1989 for more detail). It is important to notice how the local line profiles and the global morphology predicted by this simple model resemble those observed. This type of shock wave seems to be a very promising way to explain the spatial coincidence of optical and infrared emission, and the line profiles observed in HH7 and other HH objects.

IV. HCO^+ AND NH_3 EMISSION ASSOCIATED WITH HH OBJECTS

Recent high-angular resolution observations of molecular lines, carried out with the VLA, Hat Creek, NMA and JCMT radio telescopes, have shown that small high-density condensations are frequently found at the border of HH objects and aligned with the outflow direction. The most commonly studied lines are those of $HCO^+(J=1\rightarrow0)$ and $(J=3\rightarrow2)$ at millimeter wavelengths, and $NH_3(1,1)$ and (2,2) at centimeter wavelengths. HCO^+ clumps have been detected in association with HH 7-11 (Rudolph and Welch 1988), and with HH 1-2 (Davis *et al.* 1990). Ammonia condensations have been observed toward HH 25-26 (Torrelles *et al.* 1989), and HH 2 (Torrelles *et al.* 1991, private communication); see also the review by Torrelles (1990). These NH_3 and HCO^+ condensations or clumps

have typical densities of $n(H_2) \simeq 10^5$ cm^{-3}, radial velocities similar to those of the ambient molecular cloud and typical sizes of a few arcseconds. Although the number of reported cases is still comparatively small, the high detection rate suggests that this emission may be a common feature of HH objects.

An important characteristic observed in the HCO^+ and NH_3 condensations is that their main peak appears offset (typically a few arcseconds) downstream with respect to the optical emission (*i.e.*, the optical emission appears closer to the energy source of the system), an important fact to be taken into account for the interpretation of these HH objects. Figures 1 and 3, for instance, show the spatial distribution of NH_3 and HCO^+ with respect to the optical and infrared emission in HH1–2 and HH7–11, respectively. In HH7, where there are no associated HCO^+ or NH_3 condensations, the optical and infrared observations suggest that the emission is produced in a bow shock (see discussion above), consistent with what is expected for a jet model. On the other hand, objects such as HH2, HH8, and HH10, where NH_3 and/or HCO^+ emission has been detected, are much more complex since the spatial distribution, and optical and infrared line characteristics can not be explained by a simple model. A number of models have been proposed to explain the association of high-density clumps with HH objects, all of them assuming a cloudlet model (*e.g.*, Rudolph and Welch 1988; and Zinnecker *et al.* 1989).

The association of HH objects with molecular condensations suggests that at least these HH objects could be ambient dense gas shocked by a wind. If this is the case, the observed high-density clumps associated with the HH objects would be ambient cloudlets (perhaps uniformly distributed in the molecular cloud) that have been compressed by a shock wave, enhancing the density by at least a factor of ~ 100 in order to be detectable with molecular tracers of high-density gas such as NH_3 and HCO^+ (*e.g.*, Rudolph and Welch 1988, and Torrelles 1990). However, the compression of the ambient molecular gas would also imply an acceleration of the molecular gas to velocities different to the ambient molecular cloud velocity. For instance, a compression of ~ 100 would imply a bulk velocity of ~ 10 km s^{-1} for a stellar wind velocity of ~ 100 km s^{-1}. At present, such acceleration has not been observed in the high-density condensations associated with HH objects. The molecular lines observed typically have radial velocities of only ~ 1 km s^{-1} and widths of ≤ 1 km s^{-1}. Another possible explanation to this association is that the uv radiation emitted by the shock waves (that may travel ahead of the HH objects)

excite and heat ambient high–density cloudlets nearby. In this case, the cloudlets would have radial velocities similar to that of the molecular cloud velocity, and line widths given by thermal broadening. However, calculations will be needed to establish if the radiation emitted by shock waves is capable of exciting HCO^+ and NH_3 in molecular condensations to the observed levels.

Finally, if the molecular clumps observed in the vicinity of HH objects are indeed shocked molecular cloudlets, one would expect to find small condensations moving with velocities significantly different to the molecular cloud velocity. These high-velocity cloudlets could be detected with high angular resolution (a few arcseconds) observations sensitive to high-density molecular gas ($n(H_2) \geq 10^4$ cm^{-3}) and covering a wide range in velocities ($\Delta v \sim 10$ km s^{-1}, or more) with respect to the ambient gas velocity. Observing simultaneously different transitions (*e.g.*, $NH_3(1,1)$ and $(2,2)$), it would be possible to study the heating produced in the cloudlet by the shock wave. These type of observations will provide further insight about the nature of the excitation of these molecular condensations and the HH objects themselves.

V. Outline for the Thesis

In Chapter 2, we calculate the population of the rotational-vibrational levels of the ground electronic state of the hydrogen molecule in detail, taking into account a number of excitation mechanisms, among them, collisional excitation of the $B\Sigma$ and $C\Pi$ electronic states by energetic thermal electrons. In this Chapter, we study the cooling due to collisional excitation of hydrogen molecules. The results of this Chapter are used in Chapters 4 and 5 to calculate the optical, UV, and infrared emission produced by plane-parallel and bow-shaped J-shock waves with magnetic precursors.

In Chapter 3, we present images of HH 7-11 taken nearly simultaneously in the light of Hα, [S II], and H_2 S(1). We discuss the calibration procedure as well as possible interpretations for this observations and other existing data of this region. Finally, in this Chapter we apply results of Chapter 4 to explain the bow-shaped structure observed in HH 7, as well as the line fluxes obtained.

In Chapter 4, we calculate the optical, UV, and infrared emission produced by J-shock waves with magnetic precursors, assuming a very simplified structure for the magnetic

precursor and calculating the post-shock region in detail. The simplified dynamical structure allows us to compute not only the intensity of H_2 lines emitted from the magnetic precursor but also to calculate the energy loss in this region, which plays an important role in the excitation of the spectrum emitted by the post-shock region. We apply this plan-parallel model to the HH 7 object (see also Chapter 3) and the MH1 filament of the Cygnus Loop.

The simplicity of the model presented in Chapter 4 allows us to construct bow-shaped shock waves in Chapter 5. Based on these models, we predict the infrared and optical morphology, and the spatially resolved and integrated line profiles for a jet (or bullet) moving through a magnetized molecular medium. In Chapter 5, line intensities and profiles, as well as position-velocity diagrams and contour maps are calculated for a number of optical and infrared lines. The results of this bow-shock model are compared to observational results of HH objects, as well as other theoretical models. In particular, the predictions of this model are compared to high-resolution observations (both spectral and angular) of HH 7. Finally, we present a number of predictions for integrated line profiles, position-velocity diagrams, morphologies, and a characteristic line profile distribution in the optical and infrared for a bow shock that could be identified observationally.

–I am grateful to A.P. Lane and B. Reipurth who kindly provided some excelent images which I used during the presentation of this work in the IAU Symposium No. 150, in Brazil.. I am also grateful to J.M. Torrelles for comments on an early version of this manuscript and for providing the unpublished NH_3 contour map used in Fig. 1.

REFERENCES

Bally, J., and Lane, A.P. 1991, in Astrophysics with Infrared arrays, ASP vol. 14, ed. R. Elston, p. 273-278.

Black, J.H., and van Dishoeck 1987, *Ap. J.*, **322**, 412.

Böhm, K.H., Bührke, Th., Raga, A.C., Brugel, E.W., Witt, A.N., and Mundt, R. 1987, *Ap. J.*, **316**, 349.

Brand, P.W.J.L., Toner, M.P., Geballe, T.R., and Webster, A.S. 1989, *MNRAS*, **237**, 1009.

Brugel, E.W. 1989, in ESO-Workshop on Low Mass Star Formation and Pre-Main Sequence Objects, ed. Bo Reipurth, p. 311-329.

Bugel, E.W., Shull, J.M., and Seab, C.G. 1982, *Ap. J.*, **262**, L35.

Burton, M.G., Brand, P.W.J.L., Geballe, T.R., and Webster, A.S. 1989, *MNRAS*, **236**, 409.

Cantó, J. 1980 *Astr. Ap.*, **86**, 327.

Carr, J.S. 1990, *Bull. AAS*, **21**, 1086.

Davis, C.J., Dent, W.R.F., and Bell Burnell, S.J. 1990, *MNRAS*, **244**, 173.

Dopita, M.A., Binette, L., and Schwartz, R.D. 1982, *Ap. J.*, **261**, 183.

Doyon, R., and Nadeau, D. 1988, *Ap. J.*, **334**, 883.

Draine, B.T. 1980, *Ap. J.*, **241**, 1021.

Draine, B.T., Roberge, W.G., and Dalgarno, A. 1983, *Ap. J.*, **264**, 485.

Elias, J.H. 1980, *Ap. J.*, **241**, 728.

Garden, R.P., Russell, A.P.G., and Burton, M.G. 1990, *Ap. J.*, **354**, 232.

Hartigan, P. 1989, *Ap. J. (Letters)*, **339**, 987.

Hartigan, P., Curiel, S., and Raymond, J. 1989, *Ap. J. (Letters)*, **347**, L31.

Hartigan, P., Curiel, S., and Raymond, J. 1991, in preparation.

Hartigan, P., Lada, C.J., Stocke, J., and Tapia, S. 1986, *A. J.*, **92**, 1155.

Hartigan, P., Raymond, J., and Hartmann, L. 1987, *Ap. J.*, **316**, 323.

Hartmann, L., and Raymond, J. 1984, *Ap. J.*, **276**, 560.

Harvey, P.M., Joy, M., Lester, D.F., and Wilking, B.A. 1986, *Ap. J.*, **301**, 346.

Lane, A.P, 1989, in ESO-Workshop on Low Mass Star Formation and Pre-Main Sequence Objects, ed. Bo Reipurth, p. 331-348.

Lane, A.P., and Bally, J. 1986, *Ap. J.*, **310**, 820.

Lane, A.P., Bally, J., and Hartigan, P. 1991, in preparation.

Lenzen, R. 1988, *Astr. Ap.*, **190**, 269.

Lightfoot, J.F., and Glencross, W.M. 1986, *MNRAS*, **221**, 993.

Mundt, R. 1985, Protostars and Planets II, ed. D.C. Black and M.S. Mathews (Tucson; University of Arizona Press), p. 414.

Mundt, R., Brugel, E.W., and Buhrke, T. 1987, *Ap. J.*, **319**, 275.

Norman, C., and Silk, J. 1979, *Ap. J.*, **228**, 197.

Raga, A. 1988, *Ap. J.*, **335**, 820.

Rudolph, A., and Welch, W.J. 1988, *Ap. J. (Letters)*, **326**, L31.

Sandell, G., Zealey, W.J., Williams, P.M., Taylor, K.N.R., and Strey, J.V. 1987, *Astr. Ap.*, **182**, 237.

Schwartz, R.D. 1983, *Ann. Rev. Astr. Ap.*, **21**, 209.
Schwartz, R.D. 1978, *Ap. J.*, **223**, 884.
Schwartz, R.D., Cohen, M., and Williams, P.M. 1987, *Ap. J.*, **322**, 403.
Schwartz, R.D., Cohen, M., and Williams, P.M. 1988a, *Ap. J.*, **333**, 1035.
Schwartz, R.D., Williams, P.M., Cohen, M., and Jennings, D.G. 1988b, *Ap. J. (Letters)*, **334**, L99.
Shull, J.M., and Hollenbach, D.J. 1978, *Ap. J.*, **220**, 525.
Solf, J., and Böhm, K.H. 1987, *A. J.*, **93**, 1172.
Stapelfeldt, K.R., Beichman, C.A., Hester, J.J., Scoville, N.Z., and Gautier III, T.N. 1991, *Ap. J. (Letters)*, , in press.
Strom, K.M., Strom, S.E., Wolff, S.C., Morgan, J., and Wenz, M. 1986, *Ap. J. Suppl.*, **62**, 39.
Torrelles, J.M. 1990, in Atoms, Ions, and Molecules: New Results in Spectral Line Astrophysics, ASP vol. 16, eds. A.D. Haschick and P.T.P. Ho, p. 257-268.
Torrelles, J.M., Ho, P.T.P., Rodríguez, L.F., Cantó, J., and Verdes-Montenegro, L. 1989, *Ap. J.*, **346**, 756.
Wilking, B.A., Schwartz, R.D., Mundy, L.G., and Schultz, A.S.B. 1990, *A. J.*, **99**, 344.
Wolfire, M.G., and Königl, A. 1991, Ap. J., in press.
Zealey, W.J., Williams, P.M., and Sandell, G. 1984, *Astr. Ap.*, **140**, L31.
Zealey, W.J., Williams, P.M., Taylor, K.N.R., Storey, J.W.V., and Sandell, G. 1986, *Astr. Ap.*, **158**, L9.
Zinnecker, H., Mundt, R., Geballe, T.R., and Zealey, W.J. 1989, *Ap. J.*, **342**, 337.

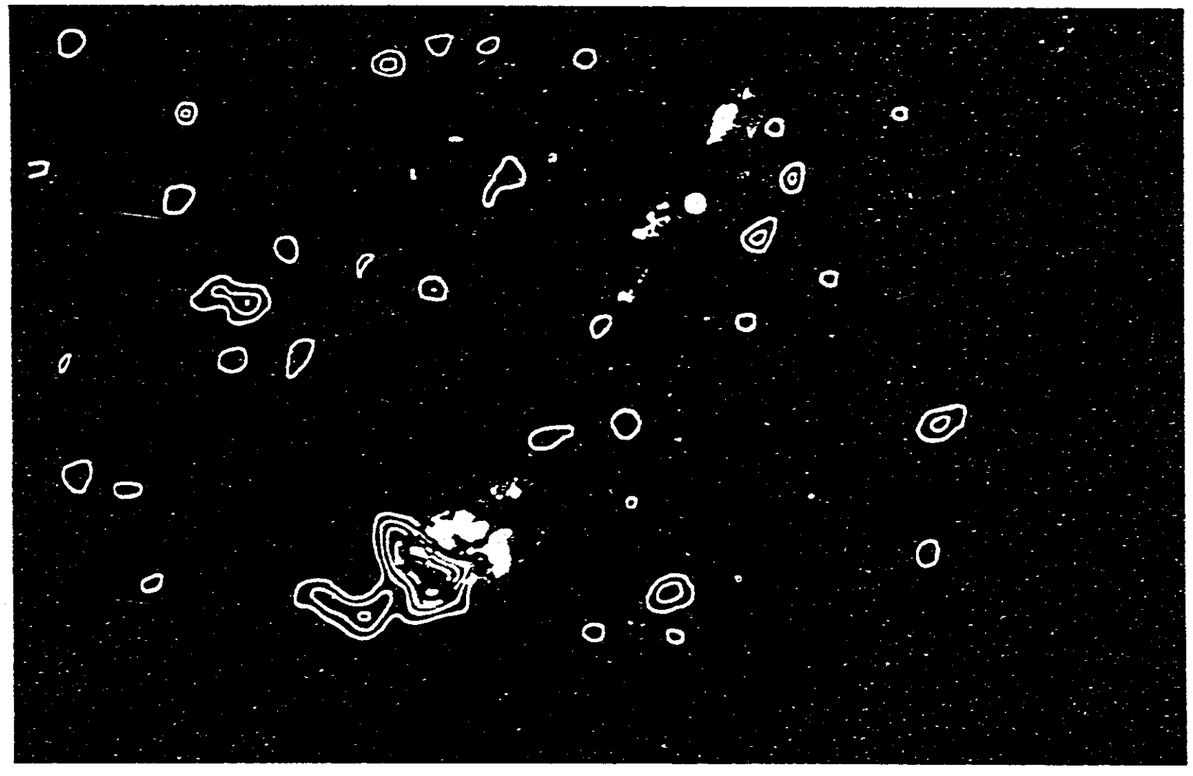

Figure 1. Comparison of an infrared H_2 line (red), optical H_α (blue) and [SII] (green) images of the HH1-2 region obtained by Hartigan *et al.*(1991). This figure also shows the spatial distribution of NH_3 condensations detected by Torrelles *et al.* (1992; private communication) with respect to the optical and infrared emission.

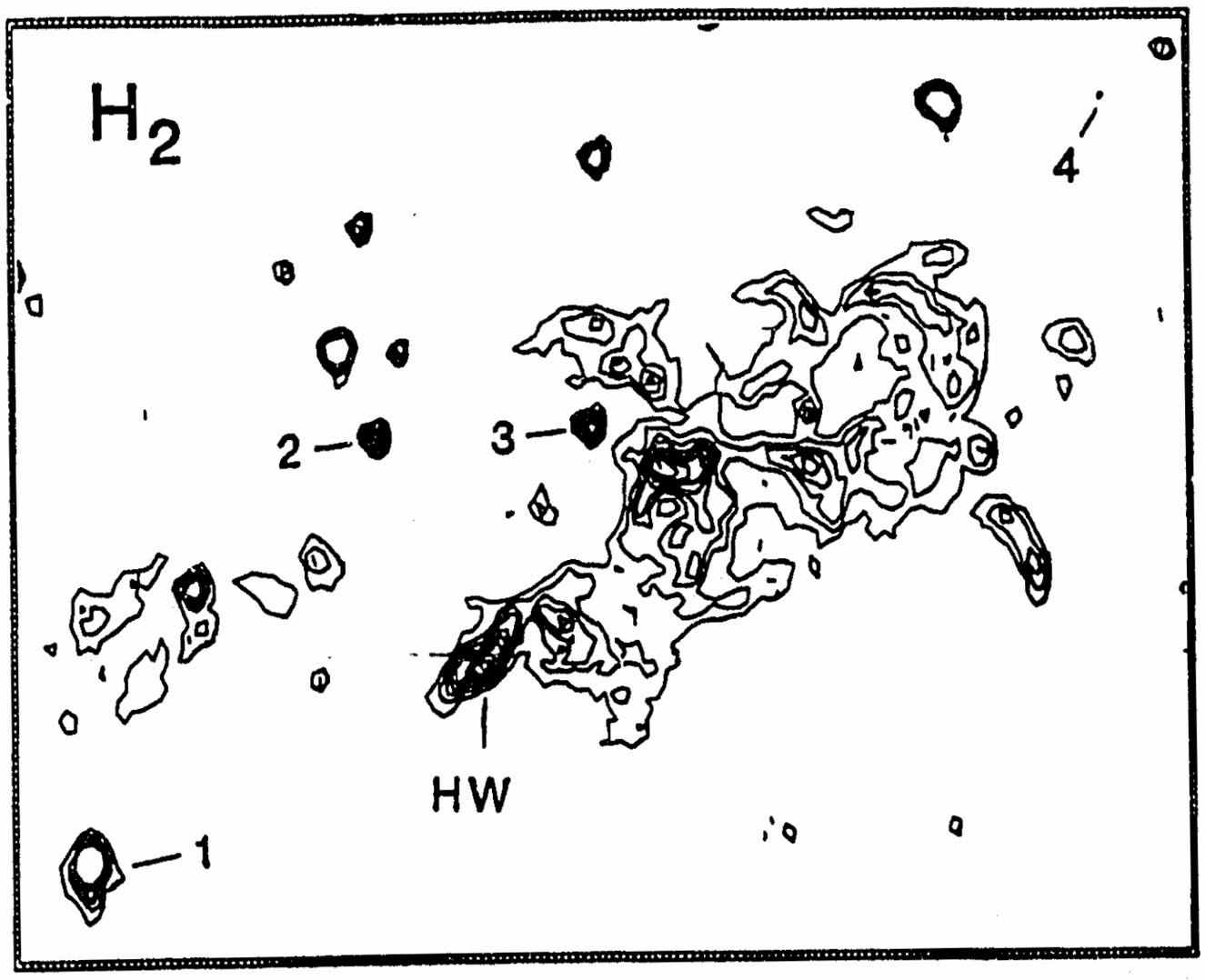

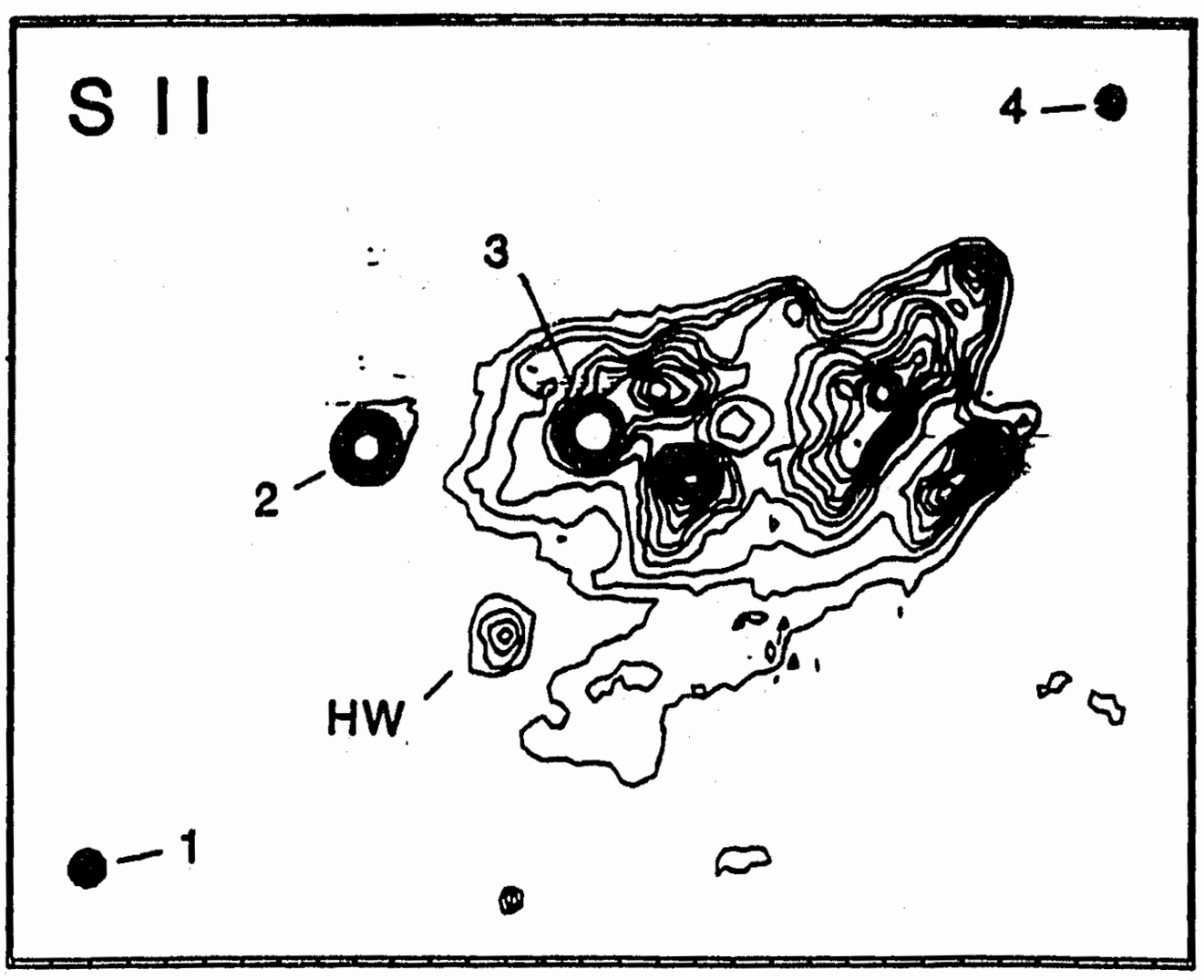

Figure 2. Contour maps of the optical [SII] λ6716/6731 and the infrared H_2 1–0S(1) at 2.1μ line emissions from Cepheus A/GGD 37. Both frames are 120"×88" in size, and are aligned. Figure taken from Lane (1989).

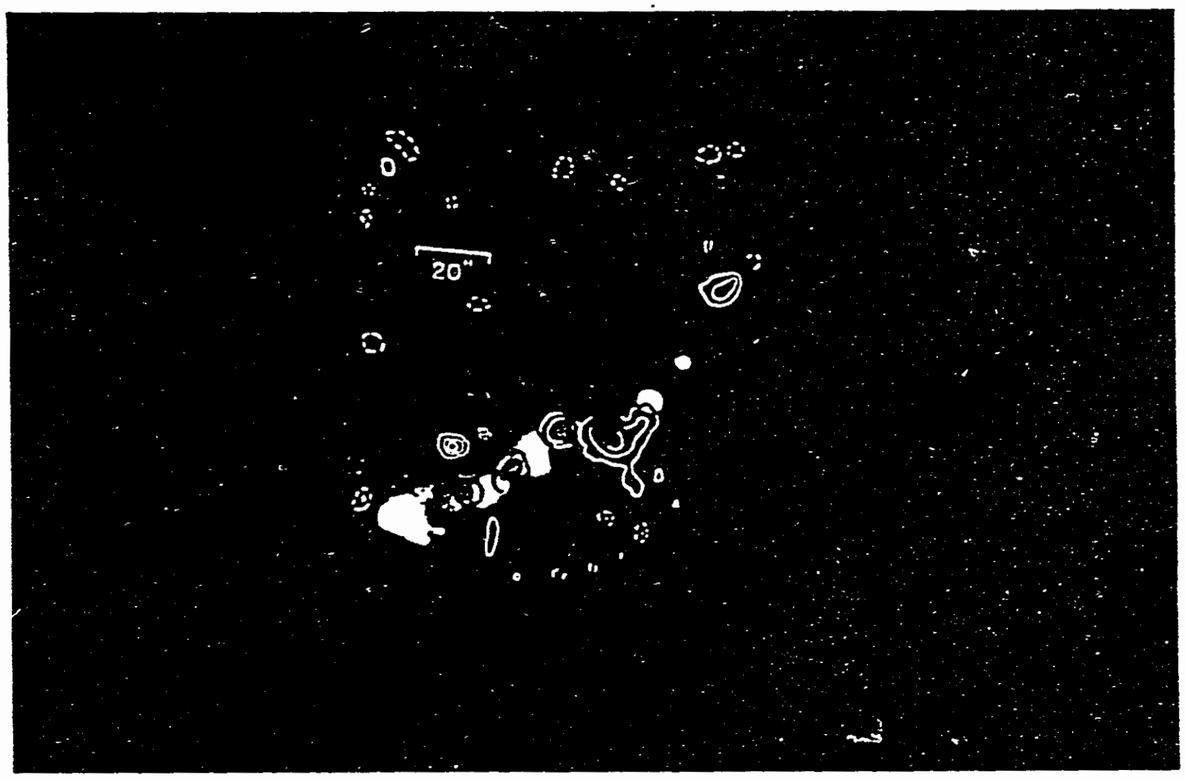

Figure 3. Comparison of an infrared H_2 line (red), optical H_α (blue) and [SII] (green) images of the HH7-11 region obtained by Hartigan, Curiel and Raymond (1989). This figure also shows the spatial distribution of HCO^+ condensations detected by Rudolph and Welch (1988) with respect to the optical and infrared emission.

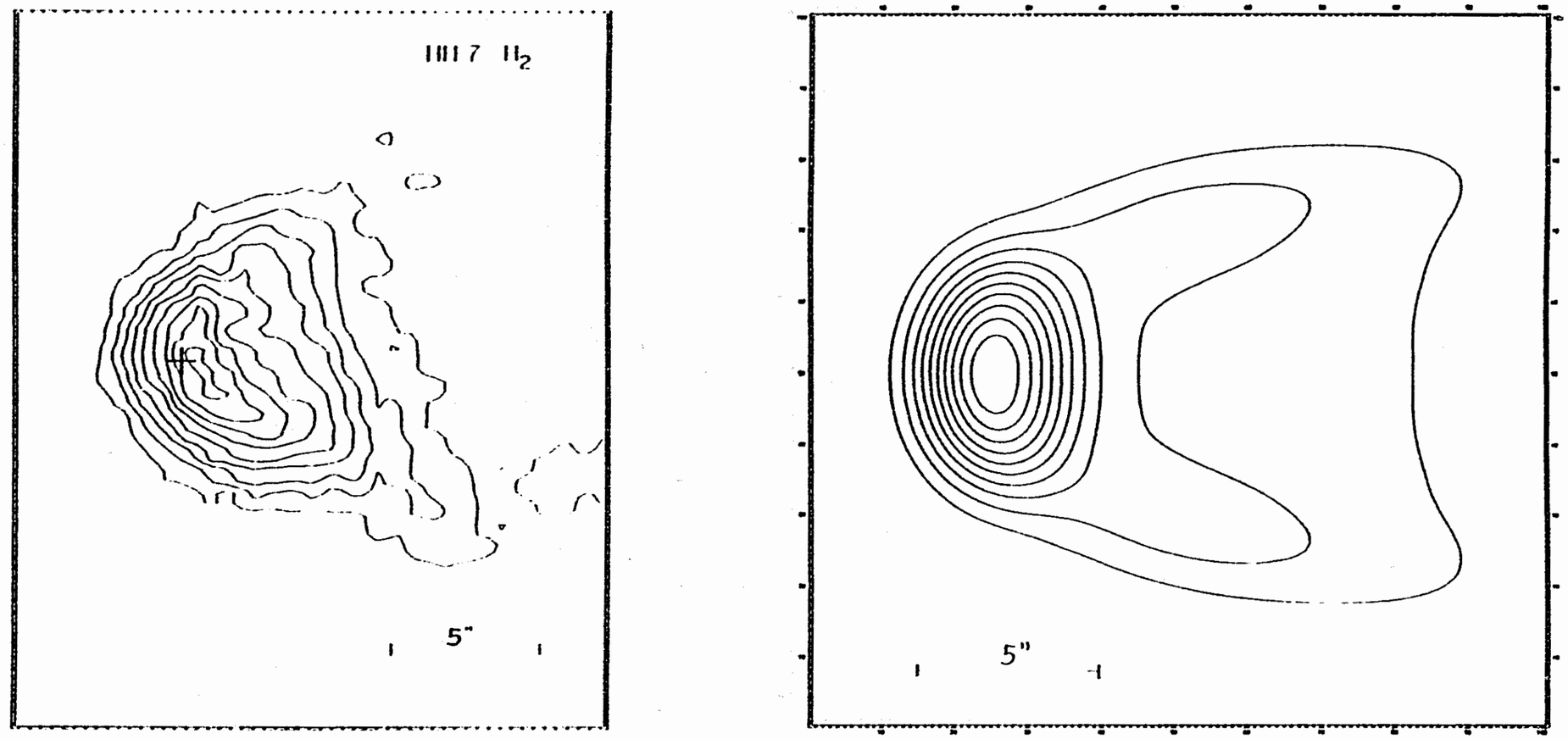

Figure 4. Top: Comparison of the integrated 1-0S(1) H_2 flux map of HH7 (left) obtained by Hartigan, Curiel and Raymond (1989) and that calculated for a bow-shaped shock wave with a magnetic precursor (right), using a shock velocity of 100 km s^{-1}, and an inclination angle of 60^0 with respect to the line-of-sight. Bottom: Comparison of the 1-0S(1) H_2 velocity map of HH7 (left) obtained by Carr (1990) and that calculated for a bow-shaped shock wave with a magnetic precursor (right), using the same parameters as above.

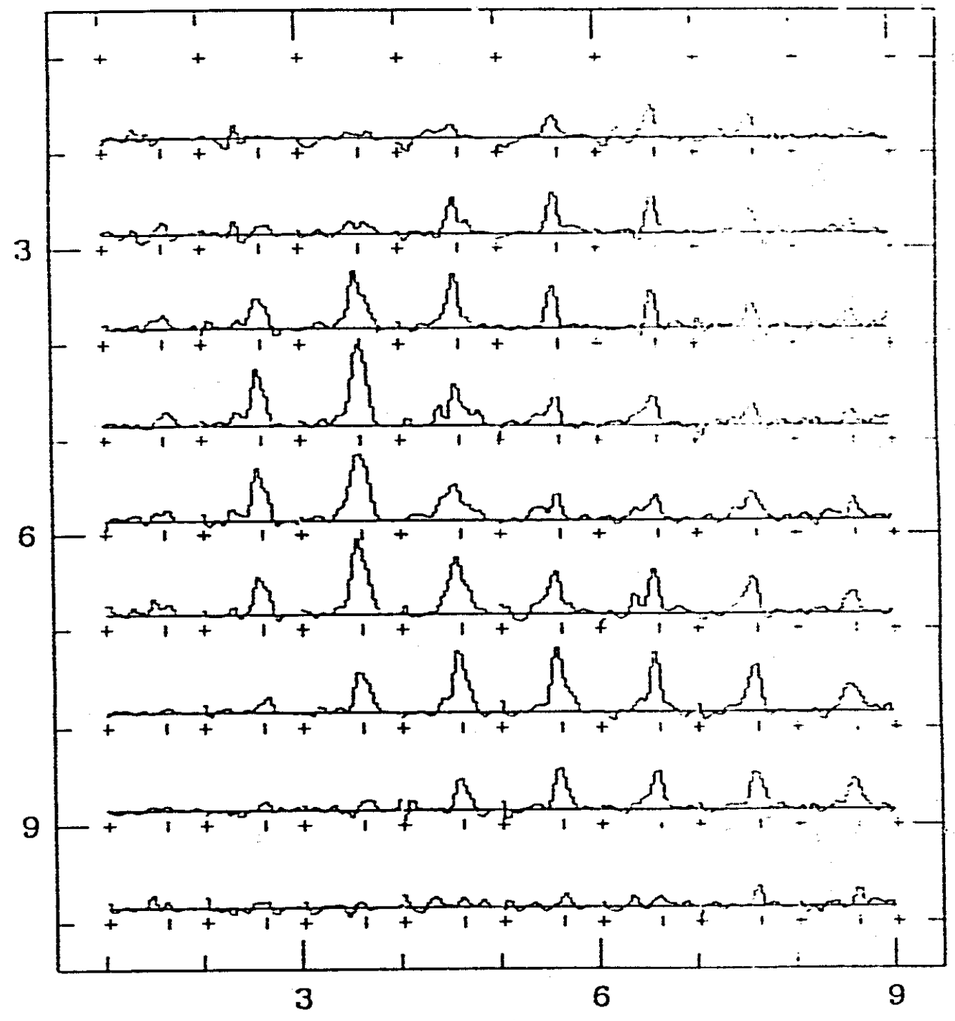
3
6
9
3
6
9

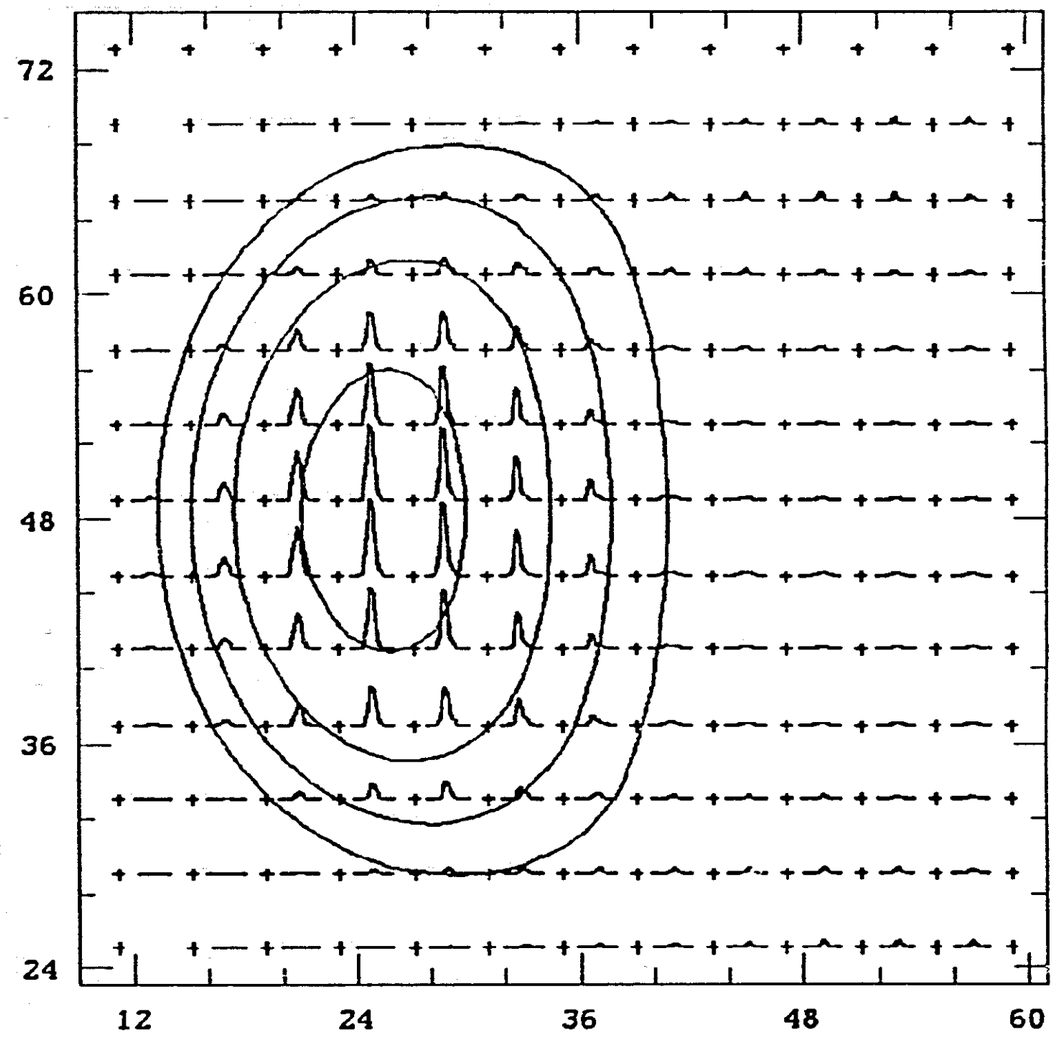
72
60
48
36
24
12
24
36
48
60

CHAPTER 2

MOLECULAR HYDROGEN COOLING RATES

I. Introduction

Since molecular hydrogen (H_2) is homonuclear, lacking of dipole moment, and its energy levels are more widely spaced than many other molecules, its vibrational-rotational excitation must be treated differently than that of other molecules. With no dipole moment, the main rotational-vibrational transitions are quadrupolar ($\Delta J = 2$) with spontaneous de-excitation probabilities with typical values of $\sim 3 \times 10^{-7}$ s^{-1}. As a consequence of this, collisional de-excitation of vibrational states is important for densities $\gtrsim 10^6$ cm^{-3}. Furthermore, since photoabsorption cross sections are also small, radiative trapping is negligible for column densities $N \lesssim 3 \times 10^{23}$ cm^{-2}. A proper treatment of H_2 requires a detailed calculation of the population of each of its individual excited levels.

In a high density ($n \gtrsim n_{crit} = A/<\sigma v> \approx 3 \times 10^5$ cm^{-3}) molecular shock, the characteristic cooling time t_c is longer than the inelastic collision time t_i. Therefore, Boltzmann (LTE) level populations, are quickly established among the H_2 levels, and the radiative cooling may be computed by assuming an LTE level population. On the other hand, for a low density ($n < n_{crit}$) molecular shock, the inelastic collisions determine the level population and hence the cooling rates (*i.e.*, $t_c \approx t_i$). In this case, the evolution of the shocked molecular gas must be treated by computing the time-dependent H_2 level population and the radiative cooling simultaneously.

In some astrophysical scenarios, such as J-shock waves with magnetic precursors and C-shocks (Draine 1980, Draine *et al.* 1983), the temperature of the electrons may be greater than that of the neutrals. In this case, excitation of upper electronic levels of hydrogen molecules by collisions with electrons may be an important source of cooling. Furthermore, since most of these excitations are followed by radiative de-excitation to excited rotational-vibrational levels in the ground electronic state, a substancial amount of IR and UV radiation may be emitted before the molecules are dissociated. This type of scenario might explain the UV continuum observed in some HH objects (*e.g.*, Brugel

1989), and the infrared H_2 line emission associated with optical filaments in the Cygnus Loop (Graham *et al.* 1991). However, collisional excitation of the H_2 upper electronic levels by collisions with hot electrons has not been studied before. In order to further study the importance of this mechanism in the cooling of a shocked medium and its effect in the production of IR and UV emission, we have calculated in detail the population of the rotational-vibrational levels of the ground electronic state. We have taken into account a number of excitation mechanisms, among them, collisional excitation of the $B\Sigma$ and $C\Pi$ electronic states by hot electrons. In this work, a study of the cooling rates due to collisions with electrons is presented, as well as a comparison with radiative and dissociative cooling rates. The discussion of the IR and UV emission will be presented elsewhere.

II. Population of H_2 Rotational-Vibrational Energy Levels

When cooling plays an important role, the level populations n_i are determined by the difference between the number of transitions per second per cm^{-3} departing from this level and the corresponding number getting into that level. If $(R_{ji})_Y$ is the probability per unit of time that a particle in level j undergoes a transition to level i as a result of process Y, the level populations are determined by,

$$\frac{dn_i}{dt} = -n_i \sum_Y \sum_j (R_{ij})_Y + \sum_Y \sum_j n_j \times (R_{ji})_Y, \qquad (1)$$

where the summations extend over all physical processes Y and over all other levels j. Under steady-state conditions, the number density n_j of particles in a level j is constant with time, and the number of transitions per second per cm^{-3} into level j must equal the corresponding number out of that level. In this case, the set of equations (1) becomes,

$$n_i \sum_Y \sum_j (R_{ij})_Y = \sum_Y \sum_j n_j \times (R_{ji})_Y. \qquad (2)$$

In general, if there are M separate levels, the set of equations (2) provides M–1 linearly independent equations, which determine the M–1 ratios of the population densities

n_i to each other. If the probability rates $(R_{ij})_\gamma$ are known, the solution is in principle straightforward and in practice feasible.

The specific form of equation (2) depends on the types of excitation, de-excitation, molecular formation and dissociation, ionization, and recombination processes that are being considered. For a collisionally excited atom or molecule, the fractional population in the ith level, f_i, is given by the equation of statistical equilibrium, which may be written as:

$$f_i \sum_j (C_{ij} + A_{ij}\beta_{ij}) = \sum_j f_j (C_{ji} + A_{ji}\beta_{ji}), \tag{3}$$

where C_{ij} are the probabilities per unit time for collision to induce transitions between levels i and j, A_{ij} are defined as zero for $j \geq i$, and β_{ij} are the probabilities that photons emitted anywhere in the emitting region escape the medium. This set of equations, together with the total number of atoms or molecules $\sum_i n_i = n$, can be solved to obtain the density population in each level.

In the simplest case, when the high density limit is applicable, the spontaneous radiative transition probabilities, A_{ij}, are negligible compared to the collisional rates, Q_{ij}, and the fractional level populations (f_i) attain their LTE values:

$$f_i = \frac{g_i \exp(-E_i/kT)}{\sum_j g_j \exp(-E_j/kT)}, \tag{4}$$

where g_j and E_j are the statistical weight and the energy of the j^{th} level respectively.

The next simplest case is that in which the level populations are non-thermal but the transition optical depths are small so that the escape probabilities, β_{ij}, are everywhere equal to unity. In that case, the fractional level population depends only on the local temperature and on the local density of whatever particles (usually H, and H_2 or electrons) are responsible for collisionally exciting the emitting molecule or atom.

Finally, the radiative transition probability may be non-negligible compared to the

collisional de-excitation rates but the emission lines may be optically thick. In this case, the fractional level populations depend on the escape probabilities, β_{ij}, which themselves depend on the level populations, so that an iterative solution is required (*e.g.*, Neufeld and Melnick 1987).

In the case of the molecular hydrogen, where the quadrupole rotational–vibrational transitions are optically thin and the emitted lines may travel throughout the emitting region without being absorbed, the level population depends only on the local physical parameters of the gas. The fractional level populations may therefore be obtained by solving the system of equations (3), taking β_{ij} equal to unity.

For the molecular hydrogen equation (3) can be given as:

$$
\begin{aligned}
& x_{vj} \sum_{v'j'} \left[A(vj \rightarrow v'j') + \sum_i n_i Q_i(T; vj \rightarrow v'j') \right] \\
& \quad + x_{vj} \left\{ \sum_{v^*j^*} n_e P_e(T; vj \rightarrow v^*j^*) + \sum_k n_k Q_k(T; vj \rightarrow f) \right\} \\
& = \sum_{v'j'} x_{v'j'} \left[A(v'j' \rightarrow vj) + \sum_i n_i Q_i(T; v'j' \rightarrow vj) \right] \\
& \quad + \sum_{v'j'} x_{v'j'} \sum_{v^*j^*} n_e P_e(T; v'j' \rightarrow v^*j^*) b(v^*j^* \rightarrow vj) \\
& \quad + R(T) \beta(vj) n_H X(H),
\end{aligned}
\tag{5}
$$

where n_e is the electron density, $x_{vj} \equiv n_{vj}/n(H_2)$, and $X(H) \equiv n(H)/n(H_2)$, whith n_{vj}, $n(H_2)$ and $n(H)$ being, respectively, the volume density of excited H_2 levels and the total molecular and atomic volume hydrogen densities. The total density of hydrogen nuclei is given by $n_H = n(H) + 2n(H_2)$. In these equations, $Q_i(T; vj \rightarrow v'j')$ are the temperature-dependent excitation rate coefficients for collisions with particles of density n_i that induce transitions from levels vj to $v'j'$. $Q_k(T; vj \rightarrow f)$ are the dissociation rate coefficients to the continuum. $P_e(T; vj \rightarrow v^*j^*)$ are the temperature-dependent collisional excitation rates out of level vj of the ground electronic state to level v^*j^* of an excited electronic state by collisions with electrons. The various rate coefficients that we have adopted for

the important processes of rotational-vibrational excitation and de-excitation, and ortho-para conversion are presented in Appendix A. The electronic excitation by collisions with electrons is presented with some detail in Appendix B. The parameters $b(v^*j^* \rightarrow vj)$ are the branching ratios of the transitions between levels v^*j^* and vj of the excited and ground electronic states (see Appendix B). $R(T)$ is the temperature-dependent molecular formation rate coefficient (see Appendix C), and $\beta(vj)$ are the fractions of molecules formed in levels vj. The molecular formation model which we have adopted in the present calculations is presented in Appendix C.

III.- Cooling and Heating by H_2

Emission from molecular hydrogen is one of the principal means by which the interstellar gas cools under a variety of circumstances (*e.g.*, Shull and Beckwith 1982). H_2 can play a significant role in the thermal balance of interstellar clouds; both in cool ($\sim$ 100 K) diffuse clouds and in shocked molecular clouds ($\sim$ 2000 K). In particular, molecular hydrogen emission may provide the primary coolant for interstellar shock waves (Field *et al.* 1968, Aannestad 1973a,b) produced when molecular clouds collide, or when stellar winds, HII regions or supernovae encounter these clouds. A number of approaches have been taken to calculate the H_2 cooling function (*e.g.*, Shull and Hollenbach 1978; Lepp and Shull 1983) for different temperatures and densities. These calculations have been carried out including several excitation and de-excitation processes, and taking into account with some detail the population of the energy levels of the hydrogen molecule. Since we want to calculate the infrared line emission and ultraviolet line and continuum emission produced by a magnetic precursor preceding a strong J-shock (see chapter 4), we calculate in detail the level population of the 255 rotational–vibrational energy levels of the $X\Sigma$ ground state of the hydrogen molecule, taking into account the excitation to the two upper $B\Sigma$ and $C\Pi$ electronic states (including 240 rotational–vibrational levels for the $B\Sigma$ state and 100 levels for the $C\Pi$ state).

In the present work, we calculate the net cooling rate of the hydrogen molecule, including the following cooling and heating processes:

a) Cooling: quadrupole radiative emission following collisional excitation and collisional-pumping of the H_2 molecules, dipole emission following collisional excitation

of upper electronic states by electrons, and collisional dissociation.

b) Heating: collisional de-excitation of collisionally-pumped H_2 molecules, spontaneous radiative dissociation of H_2, and molecular formation.

The net cooling (or heating) rate due to these processes is given by:

$$\Lambda_{H_2} = \sum_i \Lambda_i - \sum_j \Gamma_j, \tag{6}$$

where Λ_i and Γ_j are the cooling and heating rates, respectively, and the summations extend over all processes that cool or heat the gas. The rates included in the calculations are described below. The excitation, de-excitation, dissociation and formation rates used to calculate the cooling and heating rates are given in Appendices A, B and C.

Inelastic collisions convert kinetic energy into internal molecular energy (the opposite direction of this process is also feasible). Collisional excitation followed by quadrupole decay cools the gas. The cooling rate due to radiative energy loss is:

$$\Lambda_{rad} = \sum_{vj} n_{vj} \sum_{v'j'<vj} A(vj \rightarrow v'j') \times (E_{vj} - E_{v'j'}) \ \ ergs\ cm^{-3} s^{-1}, \tag{7}$$

where n_{vj} is the density of H_2 in level vj, $A(vj \rightarrow v'j')$ is the spontaneous radiative transition probability from level vj to $v'j'$ given by Turner, Kirby-Docken and Dalgarno (1977), and E_{vj} is the energy of level vj.

The molecular gas can also be cooled by exciting upper electronic levels by collisions with energetic electrons. The cooling rate due to collisional-pumping is:

$$\Lambda_P = \sum_i \sum_{vj} n_{vj} \sum_{v^*j^*} n_e P_i(T; vj \rightarrow v^*j^*) \times (E_{v^*j^*} - E_{vj}) \ \ ergs\ cm^{-3} s^{-1}, \tag{8}$$

where $P_i(T; vj \rightarrow v^*j^*)$ are the collisional-pumping rates to levels v^*j^* in the $B\Sigma$ and $C\Pi$

energy states (see Appendix B). A fraction of these excitations is followed by radiative de-excitations to excited rotational–vibrational levels in the ground electronic state. The cooling (or heating) rate due to collisional-pumping excitation is given by:

$$\Lambda_{P_{exc}} = \sum_i \sum_{vj} n_{vj} \sum_{v^*j^*} \sum_{v'j'} n_e P_i(T; vj \rightarrow v^*j^*) b(v^*j^* \rightarrow v'j') \times (E_{vj} - E_{v'j'}) \ \ ergs\ cm^{-3} s^{-1}, \tag{9}$$

where $v'j' < vj$ for cooling and $v'j' > vj$ for heating. The other fraction of these collisional-pumping excitations is followed by spontaneous radiative dissociation of H_2, which heats the gas producing energetic hydrogen atoms. The average kinetic energies $< E_{v*} >$ (typically 0.4 eV) of the H atoms produced by spontaneous radiative dissociation out of the vibrational levels of the $B\Sigma$ and $C\Pi$ states have been calculated by Stephens and Dalgarno (1973). The resulting collisional-pumping dissociation heating rate is:

$$\Gamma_{P_{diss}} = \sum_i \sum_{vj} n_{vj} \sum_{v^*j^*} n_e P_i(T; vj \rightarrow v^*j^*) \eta(v^*j^*) < E_{v^*j^*} > \ \ ergs\ cm^{-3} s^{-1}, \tag{10}$$

where $\eta(v^*j^*)$ are the dissociation fractions out of level v^*j^* given by Stephens and Dalgarno (1972). The dissociation fractions and the average kinetic energies are independent of the rotational j^* level (Stephens and Dalgarno 1972, 1973). Therefore, the net cooling rate due to collisions with electrons is:

$$\Lambda_e = \Lambda_P + \Lambda_{P_{exc}} - \Gamma_{P_{exc}} - \Gamma_{P_{diss}}, \ ergs\ cm^{-3} s^{-1} \tag{11}$$

Another important cooling mechanism is that due to dissociation of molecular hydrogen, resulting from collisional excitation of the H_2 into the vibrational continuum ($v > 14$), which lies 4.48 eV ($\sim$ 52,000 K) above the ground state. At sufficiently high-temperature, this process may become the dominant cooling mechanism in the shocked molecular gas (*e.g.*, Shull and Hollenbach 1978). The resulting H_2 dissociative cooling rate can be given by:

$$\Lambda_{diss} = \sum_{vj} n_{vj} q_f(T; vj \rightarrow f) \times \Delta E_{th} \quad ergs\ cm^{-3} s^{-1}, \tag{12}$$

where ΔE_{th} = E_f - E_{vj} is the dissociation threshold energy for levels vj, E_f = 4.48 eV is the energy level of the continuum, and $q_f(T; vj \rightarrow f)$ are the dissociation rates for collisions with both H and H_2 (see Appendix A).

H_2 heating by (re)formation may be a specially important heat source at high densities behind dissociative J-shocks (Hollenbach and McKee 1989). An uncertain fraction of the energy released during the formation of H_2 is converted into kinetic energy of the newly formed molecule (Hollenbach and Salpeter 1971; Hunter and Watson 1972; Duley and Williams 1986). In the present calculations we have assumed that one-third of the available energy is converted into kinetic energy. The heating rate due to formation of H_2 is:

$$\Gamma_{fm} = R(T) n_H n(H) < E_{fm} > \quad ergs\ cm^{-3} s^{-1}, \tag{13}$$

where $< E_{fm} >$ = 2.39×10^{-12} ergs, and $R(T)$ is the H_2 formation rate coefficient (see Appendix C).

IV.- Results and Discussion

We have computed the H_2 level population in both Boltzmann (LTE) and in non-LTE steady-state equilibria. In the first case, we have used the set of equations (4) to calculate the population of the levels in LTE while in the second case, we have calculated the steady-state populations determined by solving the equations of statistical equilibrium (5) using a matrix inversion technique. The energy of the rotational-vibrational levels in the $X\Sigma$, $B\Sigma$ and $C\Pi$ states used in this calculation as well as selection rules for radiative and collisional transitions are presented in Appendix D. We consider a partially ionized and mostly molecular medium, where the ionization fraction $X(e) = 10^{-5}$–10^{-1} and the atomic fraction $X(H) = 10^{-2}$–10^{-1}. Since the quadrupole rotational-vibrational transitions of H_2 are optically thin, the level populations are solved for equilibrium at each temperature, for

densities $n_H = 10^0$–10^6 cm^{-3}. Contributions from rotational levels J = 0–20 in the first 8 vibrational levels (v= 0–7) and from J= 0–18 for v = 8, J= 0–16 for v = 9, J= 0–14 for v = 10, J= 0–12 for v = 11, J= 0–10 for v = 12, J= 0–7 for v = 13, and J= 0–3 for v = 14 vibrational levels, have been included. Contributions from rotational levels up to 20 and vibrational levels up to 14 (see Turner, Kirby-Docken and Dalgarno 1977), have been included.

Our results are shown in Figures 1, 2 and 3. Figure 1 shows the volume H_2 radiative (Λ_{rad}), dissociative (Λ_{diss}) and collisional-pumping (Λ_e) cooling rates ($ergs\ cm^{-3}s^{-1}$) for temperatures between 50 and 10^6 K. Λ_{rad} and Λ_{diss} are not sensitive to either the ionization or the atomic fractions in the molecular gas, while Λ_e is not sensitive to the atomic fraction and scales with the ionization fraction. However, Λ_{rad} appears slightly sensitive to $n(H)$ at temperatures around 2000, 5000 and 8000 K for high, intermediate and low densities, respectively. These temperatures correspond to gas temperatures at which upper vibrational levels are being excited.

Figure 1 shows different behaviors for the radiative, dissociative and collisional-pumping cooling rates. The radiative cooling rate is density-dependent, due to the collisional de-excitation of the levels. At high densities ($n \gtrsim 10^6$) most rotational-vibrational levels are populated in near-thermal equilibrium, and the volume cooling rate is proportional to n_H. For densities $n \lesssim 10^5$ a molecule in an excited level radiates before being collisionally de-excited, and $\Lambda_{rad} \propto n_H^2$. The dissociative cooling rate scales as n_H^2, independently of the temperature, density and ionization fraction in the molecular gas. This behavior is a direct consequence of the fact that only dissociative rates for collisions with H and H_2 have been included in these calculations. The collisional-pumping cooling rate is barely dependent on the density and scales with the ionization fraction. Therefore, the volume cooling rate $\Lambda_e \propto n_H X(e)$.

The cooling rates used to obtain Figure 1 are given in tables 1, 2 and 3. These rates may be very useful in calculating, for instance, the thermal structure of a non-dissociative shock wave, molecular (re)forming shocked gas, or photo-dissociation regions. Radiative, dissociative and collisional-pumping cooling rates at any temperature, density and ionization fraction are easily obtained by interpolating the values given in these tables (at least within the intervals of parameters considered in this work), and in the case of cooling by electrons (Λ_e), scaling it with the ionization fraction.

Figure 2 shows the fraction of the total cooling rate, Λ_{H2}, due to each one of these processes, while Figure 3 compares the three cooling fractions for high, intermediate and low densities. Radiative cooling rates completely dominate the other cooling processes at temperatures lower than 10^4 K for most of the parameters considered in this work. At higher temperatures, their predominance highly depends on the density and ionization fraction (see Figure 2 and 3). For densities between 10^2 and 10^4 cm^{-3}, radiative cooling contributes with more than 50% of the total cooling rate at temperatures as high as 50,000 K for $X(e) = 10^{-5}$, and 20,000 K for $X(e) = 10^{-2}$. The other types of cooling rates become more important at lower temperatures when $n_H < 10^2$ or $n_H > 10^4$ cm^{-3}.

At high temperatures and densities, and low ionization fractions (T $\gtrsim$ 7000 K, n_H $\geq$ 10^4 cm^{-3} and $X(e) \sim 10^{-5}$), dissociative cooling overpowers radiative cooling and collisional-pumping cooling by electrons (see Figure 1 and 3). For instance, $\Lambda_{diss} \simeq \Lambda_{rad}$ at T $\simeq$ 7500 K when $n_H = 10^6$ cm^{-3} and $X(e) = 10^{-5}$. For low densities, collisional excitation of the BΣ and CΠ electronic states becomes the most important cooling process at temperatures $\gtrsim$ 20000 K or $\gtrsim$ 80000 K for densities $\sim 10^0$ or 10^3 cm^{-3}, respectively. Since Λ_e scales with the ionization fraction, Λ_e becomes more important at lower temperatures when the ionization increases (see Figure 2). However, dissociative cooling may still dominate over collisional pumping at high densities, due to its n_H^2 dependence while Λ_e $\propto$ n_H. Therefore, cooling due to electrons is important mainly for molecular media with low densities ($n_H \lesssim 10^3$ cm^{-3}), high ionization fractions [$X(e) \gtrsim 10^{-3}$], and high electron temperatures ($T_e \gtrsim$ 20,000 K).

V.- Conclusions

Radiative, dissociative and collisional-pumping cooling rates have been calculated for a variety of densities, temperatures, and atomic and ionization fractions. The importance of these processes depends strongly on the physical conditions in the molecular medium. In particular, cooling due to quadrupole radiation dominates at temperatures lower than $\sim$ 10,000 K, while the other two processes predominate at higher temperatures. The most important characteristics of these cooling rates can be summarized as follows:

a) Radiative cooling predominates over the other processes at temperatures lower than 10^4 K, for most of the densities and ionization fractions considered in this work. At

these temperatures, Λ_{rad} is independent from the ionization and atomic fractions in the gas.

b) Dissociative cooling becomes relevant when the temperature is greater than $\sim$ 7000 K. This process is particularly important in a high density medium ($n_H \gtrsim 10^4\ cm^{-3}$) with a very low ionization fraction [$X(e) \lesssim 10^{-3}$). For higher ionization fractions, it is overcome by the collisional-pumping cooling when the temperature is greater than $\sim$ 30,000 K (or even lower temperatures at lower densities).

c) Cooling due to excitation of $B\Sigma$ and $C\Pi$ electronic states scales with the ionization fraction and is mainly independent from the density. This cooling process is, generally the less relevant of the three. Although it is not predominant at high densities, its importance rises at intermediate densities and ionizations fractions, and overates dissociative cooling at low densities, relatively high ionization fractions and very high electron temperatures. This result suggests that in a low density molecular gas with a relatively high ionization fraction, rotational-vibrational energy levels of the hydrogen molecules may be excited via collisional-pumping by collisions with electrons, emitting a substantial amount of UV and IR emission before being dissociated.

Appendix A
Mechanisms that Populate the Energy Levels

Changes in the internal energy of hydrogen molecules can be induced by inelastic collisions with protons, electrons, hydrogen atoms, and other hydrogen molecules. The main processes controlled by inelastic collisions are ortho-para conversions and rotational-vibrational excitation and de-excitation. Limited theoretical and experimental rate coefficients for such collisions are available, and in order to explore the effects of collisions on the cooling by hydrogen molecules and on the infrared spectra (we will defer this part to chapter XX) of a shocked molecular medium, we have taken into account the following rate coefficients.

A.1.- Neutral–Neutral Collisional Excitation

For collisions that induce only rotational transitions ($\Delta v = 0$), we have adopted the rate coefficients given by Shull and Hollenbach (1978), and Shull and Beckwith (1982). For H_2-H_2 and H-H_2 collisions the de-excitation rate coefficients are:

$$q(T; v, j+2 \rightarrow v, j) = \sigma_0 v \left(1 - \frac{1}{b}\right)\left(1 - \frac{1}{b} + \frac{E_{th}}{kT}\right), \qquad (A1)$$

where $\bar{v} = (8kT/\pi\mu)^{1/2}$, $b = 1 + (akT/E_{th})$, $kT \geq 0.3\ E_{th}$, $\sigma_0 \approx 10^{-16}$ cm^2, $E_{th} = E_{v,j+2} - E_{v,j}$, $a \approx 0.1$, and μ is the reduced mass of the colliding particles. We do not take into account collisions that induce pure rotational transitions other than $\Delta j = \pm 2$ since they are at least one order of magnitude smaller.

For collisions that induce changes in the vibrational quantum number we have adopted the rate coefficients proposed by Shull and Beckwith (1982). The de-excitation rate coefficient for H_2–H_2 collisions is given by

$$\begin{aligned} q_{H_2}(T; vj \rightarrow v'j') &= \sigma_0 v \exp\left[-\lambda_v \left(\frac{\Delta E}{kT}\right)\right] cm^3 s^{-1} \\ &= 1.45 \times 10^{-12} T^{1/2} \exp\left[-4.2 \left(\frac{\Delta E}{k(T+1190)}\right)\right] cm^3 s^{-1}, \end{aligned} \qquad (A2)$$

where $\Delta E = E_{vj} - E_{v'j'}$, and $\lambda_v = A/[B + (\Delta E_0/kT)]$, with A = 22.3, B = 5.32, and $\Delta E_0 = E_v - E_{v'}$. For collisions between H and H_2 the de-excitation rate coefficient (in $cm^3\ s^{-1}$) is given by

$$\begin{aligned} q_H(T; vj \rightarrow v'j') &= 1.4 \times 10^{-13} \exp\left[(T/125) - (T/577)^2\right]; T < 1635K \\ &= 1.0 \times 10^{-12} T^{1/2} \exp\left[-1000/T\right]; T > 1635K. \end{aligned} \qquad (A3)$$

Excitation rate coefficients q(T;$v'j' \rightarrow vj$) can be obtained by the detailed balance requirement that

$$q(T; v'j' \rightarrow vj) = \frac{g_{vj}}{g_{v'j'}} q(T; vj \rightarrow v'j') \exp\left(-\frac{\Delta E}{kT}\right), \qquad (A3')$$

where g_{vj} is the statistical weight of level vj, and $\Delta E \equiv E_{vj} - E_{v'j'}$; with the usual convention that vj lies above level $v'j'$. We used equation (A1) for rotational de-excitation within a given vibrational level ($\Delta v = 0$), and equation (A2) for de-excitations involving changes of v (*i.e.*, $\Delta v \geq 1$). We use the collisional selection rule $\Delta J = 0, \pm 2$, as suggested by the work of Zarur and Rabitz (1974). We have also included the transition J = 0→0, which is allowed, unlike in radiative decays, due to the existence of s-wave scattering. There is no restriction on v, other than the energetics of the "exponential gap" form.

A.2.- Ortho-Para Conversion

Ortho-para conversion is affected by H-atom interchange in hot gas (Schofield 1967) or by proton interchange in collisions with H^+ at low temperatures (Dalgarno, Black, and Weisheit 1973). In cold gas, reactive collisions with protons induce transitions for which Δj is odd (Dalgarno, Black, and Weisheit 1973). For $\Delta j = 1$ collisions we follow Black and Dalgarno (1977), adopting a rate coefficient of $1 \times 10^{-10}\ cm^3\ s^{-1}$ for the 1→0 transition and obtain the downward rate coefficient for higher lying rotational levels using the formula

$$q_{H^+}(j+2 \rightarrow j+1) = \frac{g(j+1)}{g(j+2)} q_{H^+}(j+1 \rightarrow j), \qquad (A4)$$

where g(j) is the statistical weight of level j. Upward rate coefficients are obtained from the requirement of detailed balance, and $\Delta j > 1$ transitions are excluded.

In warm gas the spin interchange that can occur during a reactive H–H_2 collision also contributes to the ortho-para conversion. Blais and Truhlar (1981) have calculated the state-to-state rates for this reaction. For ortho-para exchange due to collisions with H atoms, we follow Takayanagi, Sakimoto and Onda (1987), adopting a rate coefficient given by

$$q_H(T; j \rightarrow j+1) = 1.38 \times 10^{-17} \left(E_j \alpha^2\right) g(j+1) \left[E_K - (E_{j+1} - E_j)\right]^{1/2} \times \exp\left(-\lambda\, E_{j+1}/E_j\right) \quad cm^3 s^{-1}, \tag{A5}$$

where α is equal to the vibrational quantum number v (and is equal to 1 when $v = 0$), $\lambda = 2$, and E_j and E_K are the energy of the level j and the mean kinetic energy of the relative motion before reaction respectively, given in units of cm^{-1}. This excitation rate is equal to zero when the value under the square-root sign becomes negative. The de-excitation rate coefficients are obtained from the requirement of detailed balance, and as in the case of collisions with protons, $\Delta j > 1$ are excluded.

A.3.- Collisional Dissociation

The dissociation rates for each v level in H–H_2 collisions are calculated following the analytic expression given by Hollenbach and McKee (1989)

$$q_f = 9 \times 10^{-11} \left(\frac{E_f}{\Delta E_{th}}\right) \left(\frac{T}{4500K}\right)^{1/2} \times \exp\left[-1.25 \left(\frac{\Delta E_{th}}{kT}\right)\right] cm^3 s^{-1}, \tag{A6}$$

where $E_f = 4.48$ eV, and ΔE_{th} is the dissociation threshold energy from level v. To obtain the dissociation rate from the rotational levels, we assume that the same expression is valid using the rotational–vibrational threshold energy ($\Delta E_{th} = E_f - E_{vj}$) instead of the vibrational energy. We adopted the same dissociation rate for H_2–H_2 collisions.

Appendix B
Electron-Impact Excitation of Molecular Hydrogen

B1. Excitation of the B $^1\Sigma_u^+$ and C $^1\Pi_u$ Electronic States

The cross section for collisional excitation of the H_2 to upper electronic levels (B $^1\Sigma_u^+$ and C $^1\Pi_u$) may be a relevant value in some astrophysical scenarios. In C shocks for instance, the neutral fluid has warm temperatures T $< 10^4$ K while the electrons and ions can reach temperatures higher than 10^4 K (Draine *et al.* 1983). Hydrogen molecules can be dissociated by collisions with electrons which are produced in shocks with $v_s \gtrsim 30$ km s^{-1} and postshock temperatures $T_s \gtrsim 5 \times 10^4$ K (Hollenbach and McKee 1980). H_2-H_2 collisions are the main source of electrons for low electron fractional abundances ($X(e) \lesssim 10^{-3}$), while electron-H_2 collisions are the main source at higher $X(e)$.

The probability per unit time of collision induced transitions between electronic levels into excited vibrational-rotational levels is:

$$R = nq(T) = N \int_0^\infty \left(\frac{2E}{m_r}\right)^{1/2} \sigma(E) f(E) dE, \qquad (B1)$$

where n is the density of the colliding particles, q(T) is the rate coefficient for collisional excitation, $\sigma(E)$ is the collisional cross section for collisions with a particle of kinetic energy E = 1/2 $m_r v^2$, $f(E)$ is energy distribution, and $m_r = m_1 m_2/(m_1+m_2)$ is the reduced mass, where m_1 and m_2 are the masses of the molecular hydrogen and of the colliding electrons respectively. Here, we will consider electrons as the colliding particles but, an equivalent discussion can be made for other colliding particles. Assuming a Maxwellian electron energy distribution at temperature T, the energy distribution is given as

$$f(E)dE = \left(\frac{2E}{\sqrt{\pi}kT}\right) \exp\left[-\frac{E}{kT}\right] \frac{dE}{(kTE)^{1/2}}, \qquad (B2)$$

For a given transition between states i and j, the rate coefficient is:

$$q_{ij}(T) = \left(\frac{2}{kT}\right)\left(\frac{2}{\pi m_r kT}\right)^{1/2} \int_{E_{ij}}^{\infty} \sigma(E) E \exp\left(\frac{-E}{kT}\right) dE, \qquad (B3)$$

where E_{ij} is the excitation threshold energy between levels i and j, and the cross section, $\sigma(E)$, is given by the relation

$$\sigma(E) = \frac{\Omega_{ij}(X)}{\omega_i} \frac{1}{E}, \qquad (B4)$$

where ω_i is the state degeneracy for the lower electronic state, and Ω_{ij} is the dimensionless collision strength, which is given in terms of the scaled energy $X = E/E_{ij}$. Substituting equation (B4) into equation (B3), the excitation rate coefficient (in units of $cm^3\ s^{-1}$) can be written as

$$q_{ij}(T) = \frac{\Delta\ E_{ij}}{\omega_i (kT)^{3/2}} \int_1^{\infty} \Omega_{ij}(X) \exp\left(-\frac{E_{ij}}{kT} X\right) dX, \qquad (B5)$$

where $\Delta = 2(2/\pi m_r)^{1/2}$ is a constant whose value depends on the units used for the cross section, the energy, and the temperature. If we take the cross section in units of πa_0^2 (atomic units, where a_0 is the Bohr radius), the kinetic electron energy and the threshold energy in rydbergs (1 rydberg = 13.6 eV), and kT in electron volts, then $\Delta = 8.010 \times 10^{-8}$.

The downward rate coefficients $q_{ji}(T)$ can be obtained by the detailed balance requirement that

$$q_{ij}(T) = \frac{g_j}{g_i} q_{ji}(T) \exp\left(-\frac{E_{ij}}{kT}\right), \qquad (B6)$$

where g_j is the statistical weight of level j, and $E_{ij} \equiv E_j - E_i$; with the usual convention that j lies above level i, giving E_{ij} a positive value.

Shemansky, Ajello, and Hall (1985) proposed that for excitation of H_2 by electrons, the measured relative excitation function from threshold can be fit using a collision strength

of the form

$$\Omega_{ij}(X) = \left[C_0\left(\frac{1}{X^2}\right) + C_5\right]\left(1 - \frac{1}{X}\right) + \sum_{n=1}^{4} C_n (X-1)\exp(-\alpha n X) + C_7 lnX, \quad (B7)$$

where the C_n and α are constants. This fitting formula was chosen so that the rate coefficient integration can be carried out easily for the important transitions. The relative values of constants C_n with respect to C_7 were established by fitting the experimental excitation function using equations (B4) and (B7). Then, the absolute value of the collision strength can be fixed by the first Bohn approximation through the following relation (Shemansky, Ajello, and Hall 1985):

$$\begin{aligned} C_7 &= \omega_i \frac{8 m_e a_0^2}{\hbar^2} \frac{f_{ij}}{E_{ij}} \\ &= \omega_i (4.0003) \frac{f_{ij}}{E_{ij}}, \end{aligned} \quad (B8)$$

where a_0 is the Bohr radius, m_e is the electron mass, f_{ij} is the absorption oscillator strength (see bellow), and the statistical weight $\omega = 1$ for $X^1\Sigma_g^+$. The coefficients of equation (B7) and the threshold excitation energy of the H_2 B and C states are presented in Table B1. These values were taken from Shemansky, Ajello, and Hall (1985, 1987).

Integrating equation (B5), the rate coefficients can be written in the following analytical form:

$$q_{ij}(T) = \frac{8.010 \times 10^{-8}}{\omega_i (kT)^{1/2}} \left[D_0 e^{-Y} + \sum_{n=1}^{3} D_n Y E_n(Y) + D_4 E_1(Y) + \sum_{n=5}^{8} D_n \frac{\exp[-(\alpha(n-4)+Y)]}{[\alpha(n-4)+Y]^2}\right], \quad (B9)$$

where Y = E_{ij}/kT, kT is in electron volts, $D_0 = C_5$, $D_1 = -C_5$, $D_2 = C_0$, $D_3 = -C_0$, $D_4 = C_7$, and $D_n = C_{n-4}$ (for n= 5,6,7, and 8). E_n(Y) is the exponential integral of order n, defined as

$$E_n(t) = \int_1^\infty \frac{e^{-tx}}{x^n} dx. \qquad (B10)$$

From equations (B1) and (B9), the excitation rate of H_2 by energetic thermal electrons is given by

$$R_e = n_e P_e(T; vj \rightarrow v^* j^*) = n_e q_e(T; vj \rightarrow v^* j^*) \ \ s^{-1}, \qquad (B11)$$

where the excitation rate, q_e, is given by equation (B9) and n_e is the electron density.

B.2.- Collisional-Pumping Excitation

Most of the collisional pumping occurs through the bands of the B $^1\Sigma_u^+$–X $^1\Sigma_g^+$ Lyman system, and the C $^1\Pi_u$–X $^1\Sigma_g^+$ Werner system since B and C are the only energetically accessible electronic states from the rotational-vibrational levels of the ground state to electrons with temperatures $\sim 10^5$ k ($kT_e \sim 8.6$ eV).

The transitions of the Lyman system are of the $\Sigma - \Sigma$ type, processing P and R branches whereas the Werner system is of the $\Sigma - \Pi$ type, yielding P, Q, and R branches. The Π state is Λ-doublet, and the Q-branch connects the ground state with the Π^+ substate, while the P and R branches connect the ground state with the Π^- substate. Collisional pumping (as well as ultraviolet pumping) can therefore change the rotational quantum number by $\Delta j = 0, \pm 2$ with no restrictions on Δv. The oscillator strengths for the individual rotational-vibrational branch transitions can be obtained from the relation

$$f(vj \rightarrow v^* j^*) = f(v \rightarrow v^*) \frac{\lambda_{v^* v}}{\lambda_{j^* j}} \frac{S_j}{2j+1}, \qquad (B12)$$

given by Schadee (1967). Here, $f(v \rightarrow v^*)$ are the band oscillator strengths calculated by Allison and Dalgarno(1970), $\lambda_{v^*v} = c/\nu_0$, the wavelength of the fictitious transition when $j = j^* = 0$, λ_{j^*j} is the wavelength of the transition, and S_j are the Hönl-London factors given in Table B2. These factors satisfy the sum rule

$$\sum_j S_j = 2j + 1. \qquad (B13)$$

The branching ratios, that describe the probability that the particular rotational-vibrational transition $v^*j^* \rightarrow vj$ occurs, are given by

$$b(v^*j^* \rightarrow vj) = \frac{A(v^*j^* \rightarrow vj)}{\sum_{v^"j^"} A(v^*j^* \rightarrow v^"j^")}, \qquad (B14)$$

where $A_{v^*j^*,vj}$ is the spontaneous emission probability for the transition $v^*j^* \rightarrow v^"j^"$ which may be approximated by

$$A(v^*j^* \rightarrow vj) = \left[\frac{\omega_{vj}}{\omega_{v^*j^*}} \frac{k}{\lambda^2_{v^*v}} f(v \rightarrow v^*)\right] \times \left[\frac{S_j}{2j+1}\left(\frac{\lambda_{v^*v}}{\lambda_{j^*j}}\right)^3\right] \quad s^{-1}, \qquad (B15)$$

where $k = (8\pi^2\ e^2/m_e c)$ is equal to 0.66702 when λ_{v^*v} is in centimeters, where $k = 0.66702$ when λ_{v^*v} is in centimeters, and ω is the statistical weights of the levels, being equal to 1 for the X and BΣ levels, and equal to 2 for the CΠ level. The first term is the band emission probability for the transition between vibrational levels (Allison and Dalgarno 1970), and the second term denotes the correction factor due to the consideration of rotational-vibrational transitions.

Appendix C
Excitation by Molecular Formation

H_2 formation may be an important heat source in diffuse clouds (Jura 1976), dissociative fronts driven by the UV radiation from O stars (London 1978), and behind dissociative J-shocks (Hollenbach and McKee 1989). The dominant processes for molecular hydrogen formation are on the surfaces of the dust grains, and at the gas phase reaction $H^- + \mathrm{H} \rightarrow H_2 + e^-$. The former dominates at low temperatures and in particular at low ionization fractions, while the latter predominates at high temperatures and relatively high ionization fractions. In the present work, we are interested in calculating the cooling rate due to formation of hydrogen molecules in a medium with low ionization fraction, and its effects on the level population of this molecule. We include only H_2 formation on the surfaces of dust grains, adopting a molecular formation rate coefficient of

$$R(T) = 3 \times 10^{-18} T^{1/2} \quad cm^3 s^{-1}. \qquad (C1)$$

This expression is similar to that given by Hollenbach and McKee (1979) but in this case, we have not taken into account effects due to grain temperature.

Various conflicting suggestions have been made concerning the amount and distribution of binding energy that appears as internal excitation energy when molecular hydrogen is formed on grains (*e.g.*, Leonas and Pjarnpuu 1981; Duley and Williams 1986). In the calculations presented here, it has been assumed that one-third of the 4.48 eV binding energy is distributed statistically over all the rotational-vibrational levels (Black and Dalgarno 1976) so that the fraction of molecules formed in level vj is given by

$$\beta(vj) = \frac{g(vj)\exp(-E_{vj}/1.493)}{\sum_{vj} g_{vj}\exp(-E_{vj}/1.493)}, \qquad (C2)$$

where g is the statistical weight of the level vj, and E_{vj} is the energy of this level in eV. Assuming that 1/4 of the hydrogen molecules are formed in an even state and 3/4 in an odd state,

$$\beta(vj) = \frac{1}{4}\frac{g(vj)\exp(-E_{vj}/1.493)}{\sum_{vj}^{even} g_{vj}\exp(-(E_{vj}-E_0)/1.493)}(even\ J)$$
$$= \frac{3}{4}\frac{g(vj)\exp(-E_{vj}/1.493)}{\sum_{vj}^{odd} g_{vj}\exp(-(E_{vj}-E_1)/1.493)}(odd\ J), \qquad (C3)$$

where E_0 and E_1 are the energies of the two first rotational levels ($j = 0$ and 1) in the ground vibrational level ($v = 0$).

Appendix D
Properties of the Hydrogen Molecule

In the present section we present a brief description of the notation, selection rules, and energy level distribution of hydrogen molecules. Detailed reviews of the characteristics of this molecule have been presented by Field *et al.* (1966) and Shull and Beckwith (1982). See also the description (discussion) of homonuclear molecules given by Herzberg (1950).

For a molecule such as H_2, whose nuclei are identical fermions, the total wave function must be antisymmetric with respect to the nuclei interchange. Each electronic state possesses a set of vibration-rotation levels, corresponding to the motion of the nuclei. Since molecular hydrogen is homonuclear, it exists in two different states: Ortho-H_2, in which the allowed rotational levels are odd values, *i.e.*, J = 1, 3, 5, ..., and para-H_2, which has even (0, 2, 4, ...) J values. For H_2 the total nuclear spin is $I = 0$ or 1, where 0 corresponds to even states (para-H_2) and 1 to odd states (ortho-H_2). The statistical weight is (2J + 1) (2I + 1), where J is the total angular-momentum quantum number excluding nuclear spin. In analogy with atomic spectroscopic notation, the electronic states $\Lambda = 0, 1, 2, 3, ...$ are denoted by Σ, Π, Δ, Φ, ..., respectively. Here, Λ is the component of electronic orbital angular momentum along the internuclear axis. The various electronic states are labeled alphabetically, with capital letters for singlet states and lower case letters for triplet states. Thus, the ground state of H_2 is $X^1\Sigma_g^+$ and the repulsive lowest triplet state is $b^3\Sigma_u^+$. The subscript g or u and, for Σ states, the superscript + or − are concerned with symmetry properties of the electronic wave function. The left superscript corresponds to the value (2S + 1), where S is the total spin angular-momentum quantum number, which for a molecule with two electrons takes values S = 0 or 1. The first allowed electronic transitions from the ground state ($X^1\Sigma_g^+$) are to the $B^1\Sigma_u^+$ state at ~11.2 eV and to the $C^1\Pi_u$ state at ~12.3 eV, and the first allowed transition from the repulsive state $b^3\Sigma_u^+$ is to the $a^3\Sigma_g^+$ state. For states with $\Lambda \neq 0$, each rotational level J splits into two almost degenerate levels, corresponding to the two possible signs of Λ. This is called Λ *doubling*. For instance, the Π state is a Λ – *doublet*, having Π^+ and Π^- substates.

1. Selection Rules and Line Transitions

The selection rules for electric dipole transitions between electronic states are:

1. $\Delta\Lambda = 0, \pm 1$

2. $\Delta J = -1, 0, +1$, but J=0→J=0 is not allowed and $\Delta J = 0$ is not allowed if Λ=0→Λ=0.

3. Δv = any positive or negative integer,

along with the symmetry rules:

a) $u \leftrightarrow g$, $\Sigma^+ \leftrightarrow \Sigma^+$, and $\Sigma^- \leftrightarrow \Sigma^-$ allowed;

b) $g \leftrightarrow g$, $u \leftrightarrow u$, and $\Sigma^+ \leftrightarrow \Sigma^-$ not allowed.

Transitions forbidden by (1.) and the symmetry rules may be allowed as magnetic dipole or electric quadrupole transitions, but with relatively much smaller probabilities (Field *et al.*, 1966).

Within the ground state of H_2, all rotational-vibrational transitions are forbidden for electric dipole radiation because this molecule does not have a permanent dipole moment and because the symmetry rules are violated. The magnetic dipole moment is also zero for this state, but electric quadrupole transitions can occur. H_2 has a permanent quadrupole moment and the rotational selection rule is $\Delta J = 0, \pm 2$, with the following restrictions

$$\Delta J = \begin{cases} -2, & \text{for } \Delta \text{ v} = 0; \\ 0, \pm 2, & \text{for } \Delta \text{ v} \geq 1; \\ 2, & \text{for J} = 0; \\ 0, 2, & \text{for J} = 1; \\ 0, -2, & \text{for J} = \text{J}_{max} \text{ and } \text{J}_{max}\text{-1}. \end{cases}$$

Because the energies required to excite vibrational modes are much larger than those required to excite rotation, it is unlikely to have a pure vibrational spectrum within transitions between electronic states or within the same electronic level. There is, therefore, what is called a *rotation–vibration* spectrum, in which both the vibrational and rotational

states can change together. This allows a classification of the rotational "fine-structure" according to the change in J as follows

$$\Delta J = \begin{cases} -2: & \text{S branch;} \\ -1: & \text{R branch;} \\ 0: & \text{Q branch (when allowed);} \\ +1: & \text{P branch;} \\ +2: & \text{O branch.} \end{cases}$$

Here ΔJ = J" – J', where J' refers to the upper state, and J" to the lower state. According to the aforementioned transition rules, the O, Q, and S branches can occur for transitions within the ground electronic state, and P, Q, and R branches, between electronic states (the Q branch is not allowed for transitions between the B and X Σ states). Since the Π state is a Λ – *doublet*, the Q branch connects the ground state with the Π^+ while the P and R branches connect the ground state with the Π^- substate.

A common notation to describe a specific line is $v' - v''S(J)$, where S corresponds to the specific branch (in this case the S branch), J refers to the lower rotational state (J = J"), and v' and v'' are the upper and lower vibrational states, respectively. Electronic transitions between the ground X state and the upper B and C states are known as Lyman and Werner bands, with energies from 11 to 14 eV. Rotational-vibrational transitions (within the ground electronic state) where $\Delta v = \pm 1$ have energies $\sim$ 0.5 eV, with wavelengths near 2 μm. Pure rotational lines ($\Delta v = 0$, with $v = 0$) lie between 3 and 28 μm. Because H_2 has a very small inertia momentum, the rotational lines are widely spaced and easily separated by low-resolution spectrometers or isolated by narrowband filters (*e.g.*, $\Delta\lambda/\lambda \sim 1\%$).

2. Vibrational-Rotational Energy levels

2.1. Ground state, X $^1\Sigma_g^+$

The energy E_{vj} of the H_2 vibrational-rotational levels and the transition energies can

be computed according to Herzberg(1950):

$$\frac{E_{vJ}}{hc} = \left[w_e\left(v+\frac{1}{2}\right) - w_e x_e\left(v+\frac{1}{2}\right)^2 - w_e y_e\left(v+\frac{1}{2}\right)^3 - w_e z_e\left(v+\frac{1}{2}\right)^4\right] + B_v J(J+1) - D_v J^2(J+1)^2,\ cm^{-1} \qquad (D1)$$

where

$$B_v = B_e - \alpha_e\left(v+\frac{1}{2}\right)$$

and

$$D_v = D_e + \beta_e\left(v+\frac{1}{2}\right).$$

Here, $w_e = 4395.2$, $w_e x_e = 117.99$, $w_e y_e = 0.29$, $w_e z_e = 0.046$, $B_e = 60.809$, $D_e = 0.04656$, $\alpha_e = 2.993$, and $\beta_e = -1.799 \times 10^{-3}$ (all in cm^{-1}). For the ground vibrational level, a more detailed formula (Jennings, Rahn, and Owyoung 1985) can be used:

$$\frac{E_J}{hc} = B_o J(J+1) - D_o J^2(J+1)^2 + H_o J^3(J+1)^3 + L_o J^4(J+1)^4 + M_o J^5(J+1)^5 + \Delta E_6(J),\ cm^{-1} \qquad (D2)$$

where $\Delta E_6(J) = B[RJ(J+1)]^6/R[1 - RJ(J+1)]$, $B = 59\ cm^{-1}$, and $R = -10^{-3}$. In this case $B_o = 59.334629$, $D_o = 0.0456914$, $H_o = 4.8980 \times 10^{-5}$, $L_o = -6.318 \times 10^{-8}$, $M_o = 7.06 \times 10^{-11}$ (all in cm^{-1}).

2.2. Upper electronic levels, B $^1\Sigma_u^+$ and C $^1\Pi_u$

The energy of the vibrational-rotational levels of each of the excited electronic states can be written as an expansion in the quantum numbers (Dabrowski and Herzberg 1974):

$$\frac{E_{vJ}}{hc} = \nu_0^v + B_v\left[J(J+1) - \Lambda^2\right] + D_v\left[J(J+1) - \Lambda^2\right]^2 + H_v\left[J(J+1) - \Lambda^2\right]^3,\ cm^{-1} \qquad (D3)$$

where the constants of the expansion are usually determined empirically from spectra of the molecule (Fink *et al.* 1965, Beck *et al.* 1979), or calculated from potential curves (*e.g.*, Black and Dalgarno 1976). For the first two excited electronic states, B $^1\Sigma_u^+$ and C $^1\Pi_u$, the coefficients where taken from Herzberg and Howe (1959), Dabrowski and Herzberg (1974), Wilkinson (1968), and Namioka (1964).

REFERENCES

Aannestad, P.A., 1973a, *Ap. J. Suppl.*, **25**, 205.
Aannestad, P.A., 1973b, *Ap. J. Suppl.*, **25**, 223.
Allison, A.C., and Dalgarno, A. 1970, *Atomic Data*, **1**, 289.
Black, J.H., and Dalgarno, A. 1976, *Ap. J.*, **203**, 132.
Black, J.H., and Dalgarno, A. 1977, *Ap. J. Suppl.*, **34**, 405.
Blais, N.C., and Truhlar, D.G. 1982, *Ap. J. (Letters)*, **258**, L79.
Blais, N.C., and Truhlar, D.G. 1981, *in Potential Energy Surfaces and Dynamics Calculations, ed by D.G. Truhlar (New York: Plenum), p. 431-473.*
Brugel, E.W. 1989, *in ESO-Workshop on Low Mass Star Formation and Pre-Main Sequence Objects, ed Bo Reipurth, p. 311-329.*
Dalgarno, A., Black, J.H., and Weisheit, J. 1973, *Ap. Letters*, **14**, 77.
Draine, B.T. 1980, *Ap. J.*, **241**, 1021.
Draine, B.T., Roberge, W.G., and Dalgarno, A. 1983, *Ap. J.*, **264**, 485.
Duley, W.W., and Williams, D.A. 1986, *MNRAS*, **223**, 177.
Field, G.B., Rather, J.D.G., Aannestad, P.A., Orszag, S.A. 1968, *Ap. J.*, **151**, 953.
Field, G.B., Somerville, W.B., and Dressler, K. 1966, *Ann. Rev. Astr. Ap.*, **4**, 207.
Graham, J.R., Wright, G.S., Hester, J.J., and Longmore, A.J. 1991, *A. J.*, **101**, 175.
Hollenbach, D., and McKee, C.F. 1979, *Ap. J. Suppl.*, **41**, 555.
Hollenbach, D., and McKee, C.F. 1980, *Ap. J. (Letters)*, **241**, L47.
Hollenbach, D., and McKee, C.F. 1989, *Ap. J.*, **342**, 306.
Hollenbach, D., and Salpeter, E.E. 1971, *Ap. J.*, **163**, 155.
Hunter, D.A., and Watson, W.D. 1978, *Ap. J.*, **226**, 477.
Jura, M. 1976, *Ap. J.*, **204**, 12.
Leonas, V.B., and Pjarnpuu, A.A. 1981, *Soviet Astr. Letters*, **7**, 19.
Lepp, S., and Shull, J.M. 1983, *Ap. J.*, **270**, 578.
London, R. 1978, *Ap. J.*, **225**, 405.
Neufeld, D.A., and Melnick, G.J. 1987, *Ap. J.*, **322**, 266.
Schofield, K. 1967, *Planet. Space Sci.*, **15**, 643.
Shemansky, D.E., Ajello, J.M., and Hall, D.T. 1985, *Ap. J.*, **296**, 765.
Shemansky, D.E., Ajello, J.M., and Hall, D.T. 1987, *Ap. J.*, **315**, 409.
Shull, J.M., and Beckwith, S. 1982, *Ann. Rev. Astr. Ap.*, **20**, 163.
Shull, J.M., and Hollenbach, D.J. 1978, *Ap. J.*, **220**, 525.
Stephens, T.L., and Dalgarno, A. 1973, *Ap. J.*, **186**, 165.
Stephens, T.L., and Dalgarno, A. 1972, *J. Quant. Spectrosc. Radiant. Transfer.*, **12**, 569.
Sternberg, A., and Dalgarno, A. 1989, *Ap. J.*, **338**, 197.

Shull, J.M., and Beckwith, S. 1982, *Ann. Rev. Astr. Ap.*, **20**, 163.
Shull, J.M., and Hollenbach, D.J. 1978, *Ap. J.*, **220**, 525.

Takayanagi, K., Sakimoto, K., and Onda, K. 1987, *Ap. J. (Letters)*, **318**, L81.
Turner, J., Kirby-Docken, K., and Dalgarno, A. 1977, *Ap. J. Suppl.*, **35**, 281.
Zarur, G., and Rabitz, H. 1974, *J. Chem. Phys.*, **60**, 2057.
Beck, S.C., Lacy, J.H., and Geballe, T.R. 1979, *Ap. J. (Letters)*, **234**, L13.

Drabrowski, I., and Herzberg, G. 1974, Canadian J. Phys, **52**, 1110.
Field, G.B., Somerville, W.B., and Dressler, K. 1966, *Ann. Rev. Astr. Ap.*, **4**, 207.
Fink, U., Wiggin, T.A., and Rank, D.M. 1965, J. Mol. Spectrosc. **18**, 384.
Herzberg, G. 1950, Spectra of Diatomic Molecules (New York: Van Nostrand Reinhold), 658 pp.
Herzberg, G. 1950, Molecular Spectra and Molecular Sructure (New York: Van Nostrand).
Herzberg, G., and Howe, L.L. 1959, Canadian J. Phys, **37**, 636.
Jennings, D.E., Rahn, L.A., and Owyoung, A. 1985, *Ap. J. (Letters)*, **291**, L15.
Namioka, T. 1964, J. Chem. Phys., **40**, 3154.
Wilkinson, P.G. 1968, Canadian J. Phys., **46**, 1228.

Table 1
Radiative Cooling Rates

	Temp / Density = 1 (K) / cm^-3	10	10^2	10^3	10^4	10^5	10^6	LTE
1	1.000E+01	0.000E+00	2.223E-45	0.000E+00	0.000E+00	0.000E+00	0.000E+00	0.000E+00	1.868E-46
2	1.123E+01	0.000E+00	0.000E+00	0.000E+00	0.000E+00	0.000E+00	1.761E-42	1.944E-41	5.051E-44
3	1.262E+01	0.000E+00	0.000E+00	0.000E+00	1.666E-42	1.984E-42	1.019E-41	1.269E-39	7.387E-42
4	1.417E+01	0.000E+00	0.000E+00	7.845E-43	1.030E-41	1.570E-37	6.148E-37	1.763E-35	6.250E-40
5	1.592E+01	0.000E+00	6.479E-41	9.964E-38	7.511E-38	2.531E-37	1.081E-36	8.892E-35	3.248E-38
6	1.789E+01	5.746E-37	1.525E-37	2.326E-36	4.514E-36	4.493E-36	4.054E-36	4.809E-36	1.094E-36
7	2.009E+01	1.074E-36	1.043E-35	5.411E-35	9.206E-35	9.892E-35	9.955E-35	9.418E-35	2.505E-35
8	2.257E+01	1.974E-35	1.808E-34	9.025E-34	1.500E-33	1.606E-33	1.616E-33	1.500E-33	4.067E-34
9	2.535E+01	2.557E-34	2.284E-33	1.104E-32	1.791E-32	1.910E-32	1.922E-32	1.919E-32	4.862E-33
10	2.848E+01	2.461E-33	2.183E-32	1.023E-31	1.619E-31	1.720E-31	1.730E-31	1.733E-31	4.428E-32
11	3.199E+01	1.845E-32	1.623E-31	7.361E-31	1.139E-30	1.204E-30	1.211E-30	1.212E-30	3.166E-31
12	3.594E+01	1.102E-31	9.612E-31	4.214E-30	6.371E-30	6.714E-30	6.751E-30	6.754E-30	1.827E-30
13	4.037E+01	5.356E-31	4.626E-30	1.959E-29	2.895E-29	3.041E-29	3.057E-29	3.058E-29	8.730E-30
14	4.535E+01	2.157E-30	1.844E-29	7.531E-29	1.089E-28	1.141E-28	1.146E-28	1.147E-28	3.543E-29
15	5.094E+01	7.337E-30	6.205E-29	2.441E-28	3.461E-28	3.618E-28	3.635E-28	3.637E-28	1.253E-28
16	5.722E+01	2.148E-29	1.795E-28	6.796E-28	9.479E-28	9.913E-28	9.963E-28	9.968E-28	3.957E-28
17	6.428E+01	5.519E-29	4.552E-28	1.659E-27	2.292E-27	2.410E-27	2.425E-27	2.426E-27	1.144E-27
18	7.221E+01	1.268E-28	1.031E-27	3.623E-27	5.029E-27	5.361E-27	5.406E-27	5.411E-27	3.089E-27
19	8.111E+01	2.655E-28	2.127E-27	7.236E-27	1.033E-26	1.128E-26	1.142E-26	1.144E-26	7.875E-27
20	9.112E+01	5.151E-28	4.061E-27	1.351E-26	2.044E-26	2.314E-26	2.355E-26	2.359E-26	1.904E-26
21	1.024E+02	9.404E-28	7.296E-27	2.408E-26	3.989E-26	4.701E-26	4.808E-26	4.819E-26	4.358E-26
22	1.150E+02	1.637E-27	1.250E-26	4.177E-26	7.734E-26	9.451E-26	9.710E-26	9.737E-26	9.420E-26
23	1.292E+02	2.744E-27	2.066E-26	7.138E-26	1.481E-25	1.859E-25	1.917E-25	1.923E-25	1.921E-25
24	1.451E+02	4.468E-27	3.319E-26	1.208E-25	2.767E-25	3.536E-25	3.656E-25	3.669E-25	3.705E-25
25	1.630E+02	7.097E-27	5.213E-26	2.022E-25	4.989E-25	6.446E-25	6.688E-25	6.715E-25	6.782E-25
26	1.831E+02	1.103E-26	8.025E-26	3.329E-25	8.623E-25	1.125E-24	1.173E-24	1.179E-24	1.187E-24
27	2.057E+02	1.679E-26	1.212E-25	5.360E-25	1.427E-24	1.885E-24	1.983E-24	1.996E-24	2.003E-24
28	2.310E+02	2.505E-26	1.795E-25	8.403E-25	2.264E-24	3.056E-24	3.259E-24	3.287E-24	3.294E-24
29	2.595E+02	3.660E-26	2.608E-25	1.280E-24	3.460E-24	4.836E-24	5.263E-24	5.324E-24	5.333E-24
30	2.915E+02	5.241E-26	3.718E-25	1.893E-24	5.125E-24	7.539E-24	8.424E-24	8.558E-24	8.575E-24
31	3.275E+02	7.356E-26	5.201E-25	2.721E-24	7.411E-24	1.166E-23	1.344E-23	1.372E-23	1.376E-23
32	3.678E+02	1.013E-25	7.147E-25	3.807E-24	1.053E-23	1.795E-23	2.138E-23	2.196E-23	2.209E-23
33	4.132E+02	1.369E-25	9.658E-25	5.198E-24	1.479E-23	2.746E-23	3.386E-23	3.503E-23	3.551E-23
34	4.642E+02	1.819E-25	1.285E-24	6.945E-24	2.060E-23	4.163E-23	5.320E-23	5.561E-23	5.750E-23
35	5.214E+02	2.376E-25	1.684E-24	9.113E-24	2.850E-23	6.236E-23	8.313E-23	9.087E-23	9.493E-23
36	5.857E+02	3.060E-25	2.179E-24	1.177E-23	3.918E-23	9.205E-23	1.285E-22	1.468E-22	1.623E-22
37	6.579E+02	3.888E-25	2.784E-24	1.501E-23	5.342E-23	1.340E-22	1.980E-22	2.477E-22	2.902E-22
38	7.391E+02	4.882E-25	3.515E-24	1.892E-23	7.222E-23	1.925E-22	3.065E-22	4.450E-22	5.383E-22
39	8.302E+02	6.063E-25	4.391E-24	2.370E-23	9.668E-23	2.741E-22	4.809E-22	8.487E-22	1.014E-21
40	9.326E+02	7.458E-25	5.432E-24	2.954E-23	1.282E-22	3.882E-22	7.698E-22	1.662E-21	1.894E-21
41	1.048E+03	9.098E-25	6.661E-24	3.667E-23	1.688E-22	5.486E-22	1.252E-21	3.197E-21	3.438E-21
42	1.177E+03	1.102E-24	8.106E-24	4.539E-23	2.205E-22	7.721E-22	2.025E-21	5.823E-21	6.003E-21
43	1.322E+03	1.326E-24	9.793E-24	5.599E-23	2.855E-22	1.073E-21	3.156E-21	9.821E-21	1.004E-20
44	1.485E+03	1.584E-24	1.174E-23	6.861E-23	3.642E-22	1.450E-21	4.565E-21	1.511E-20	1.606E-20
45	1.668E+03	1.880E-24	1.395E-23	8.341E-23	4.573E-22	1.901E-21	6.186E-21	2.167E-20	2.468E-20
46	1.874E+03	2.226E-24	1.659E-23	1.020E-22	5.812E-22	2.583E-21	9.350E-21	3.400E-20	3.654E-20
47	2.105E+03	2.628E-24	1.967E-23	1.248E-22	7.378E-22	3.502E-21	1.405E-20	5.172E-20	5.235E-20
48	2.364E+03	3.095E-24	2.331E-23	1.526E-22	9.374E-22	4.749E-21	2.100E-20	7.652E-20	7.293E-20
49	2.656E+03	3.639E-24	2.765E-23	1.872E-22	1.195E-21	6.458E-21	3.124E-20	1.104E-19	9.920E-20
50	2.984E+03	4.280E-24	3.290E-23	2.306E-22	1.532E-21	8.833E-21	4.619E-20	1.557E-19	1.322E-19
51	3.352E+03	5.044E-24	3.938E-23	2.861E-22	1.982E-21	1.217E-20	6.766E-20	2.149E-19	1.731E-19
52	3.765E+03	5.970E-24	4.755E-23	3.583E-22	2.590E-21	1.689E-20	9.781E-20	2.902E-19	2.231E-19
53	4.229E+03	7.118E-24	5.811E-23	4.539E-22	3.422E-21	2.357E-20	1.390E-19	3.836E-19	2.832E-19
54	4.751E+03	8.577E-24	7.207E-23	5.828E-22	4.570E-21	3.298E-20	1.935E-19	4.952E-19	3.540E-19
55	5.337E+03	1.050E-23	9.105E-23	7.590E-22	6.161E-21	4.607E-20	2.636E-19	6.228E-19	4.355E-19
56	5.995E+03	1.322E-23	1.182E-22	1.004E-21	8.368E-21	6.403E-20	3.507E-19	7.608E-19	5.270E-19
57	6.734E+03	1.746E-23	1.593E-22	1.354E-21	1.144E-20	8.829E-20	4.556E-19	9.010E-19	6.270E-19
58	7.565E+03	2.414E-23	2.222E-22	1.864E-21	1.572E-20	1.206E-19	5.769E-19	1.035E-18	7.333E-19
59	8.498E+03	3.367E-23	3.113E-22	2.591E-21	2.169E-20	1.630E-19	7.112E-19	1.156E-18	8.436E-19
60	9.545E+03	4.635E-23	4.298E-22	3.587E-21	2.988E-20	2.177E-19	8.527E-19	1.263E-18	9.552E-19
61	1.072E+04	6.304E-23	5.845E-22	4.911E-21	4.092E-20	2.873E-19	9.949E-19	1.357E-18	1.066E-18
62	1.205E+04	8.508E-23	7.869E-22	6.653E-21	5.555E-20	3.739E-19	1.132E-18	1.439E-18	1.173E-18
63	1.353E+04	1.142E-22	1.052E-21	8.942E-21	7.475E-20	4.788E-19	1.260E-18	1.515E-18	1.276E-18
64	1.520E+04	1.528E-22	1.399E-21	1.195E-20	9.980E-20	6.018E-19	1.379E-18	1.587E-18	1.373E-18
65	1.707E+04	2.037E-22	1.853E-21	1.590E-20	1.323E-19	7.409E-19	1.488E-18	1.656E-18	1.464E-18
66	1.918E+04	2.707E-22	2.446E-21	2.108E-20	1.740E-19	8.914E-19	1.589E-18	1.724E-18	1.548E-18
67	2.154E+04	3.584E-22	3.216E-21	2.783E-20	2.269E-19	1.047E-18	1.682E-18	1.791E-18	1.625E-18
68	2.420E+04	4.723E-22	4.211E-21	3.658E-20	2.925E-19	1.203E-18	1.768E-18	1.856E-18	1.695E-18
69	2.719E+04	6.191E-22	5.485E-21	4.779E-20	3.721E-19	1.351E-18	1.848E-18	1.919E-18	1.759E-18
70	3.054E+04	8.060E-22	7.099E-21	6.199E-20	4.654E-19	1.490E-18	1.921E-18	1.979E-18	1.816E-18
71	3.430E+04	1.041E-21	9.120E-21	7.967E-20	5.713E-19	1.616E-18	1.988E-18	2.035E-18	1.868E-18
72	3.854E+04	1.331E-21	1.162E-20	1.013E-19	6.871E-19	1.729E-18	2.049E-18	2.088E-18	1.915E-18
73	4.329E+04	1.684E-21	1.465E-20	1.273E-19	8.094E-19	1.829E-18	2.104E-18	2.137E-18	1.957E-18
74	4.863E+04	2.106E-21	1.828E-20	1.578E-19	9.343E-19	1.917E-18	2.155E-18	2.182E-18	1.994E-18
75	5.462E+04	2.604E-21	2.257E-20	1.930E-19	1.058E-18	1.994E-18	2.200E-18	2.223E-18	2.028E-18
76	6.136E+04	3.182E-21	2.755E-20	2.326E-19	1.178E-18	2.061E-18	2.240E-18	2.260E-18	2.058E-18
77	6.893E+04	3.842E-21	3.326E-20	2.765E-19	1.292E-18	2.120E-18	2.277E-18	2.294E-18	2.085E-18
78	7.743E+04	4.588E-21	3.971E-20	3.242E-19	1.398E-18	2.171E-18	2.309E-18	2.324E-18	2.109E-18
79	8.697E+04	5.419E-21	4.690E-20	3.752E-19	1.497E-18	2.216E-18	2.338E-18	2.351E-18	2.130E-18
80	9.770E+04	6.335E-21	5.484E-20	4.287E-19	1.587E-18	2.256E-18	2.364E-18	2.375E-18	2.149E-18
81	1.097E+05	7.336E-21	6.351E-20	4.842E-19	1.668E-18	2.290E-18	2.387E-18	2.397E-18	2.166E-18
82	1.233E+05	8.421E-21	7.288E-20	5.411E-19	1.742E-18	2.320E-18	2.407E-18	2.416E-18	2.181E-18

83	1.385E+05	9.588E-21	8.294E-20	5.988E-19	1.809E-18	2.347E-18	2.425E-18	2.434E-18	2.194E-18
84	1.556E+05	1.084E-20	9.365E-20	6.567E-19	1.870E-18	2.370E-18	2.441E-18	2.449E-18	2.206E-18
85	1.748E+05	1.216E-20	1.050E-19	7.144E-19	1.924E-18	2.391E-18	2.456E-18	2.462E-18	2.217E-18
86	1.963E+05	1.357E-20	1.169E-19	7.716E-19	1.974E-18	2.409E-18	2.468E-18	2.475E-18	2.226E-18
87	2.205E+05	1.505E-20	1.295E-19	8.281E-19	2.018E-18	2.425E-18	2.480E-18	2.485E-18	2.235E-18
88	2.477E+05	1.662E-20	1.425E-19	8.835E-19	2.059E-18	2.440E-18	2.490E-18	2.495E-18	2.242E-18
89	2.783E+05	1.826E-20	1.561E-19	9.378E-19	2.096E-18	2.452E-18	2.499E-18	2.503E-18	2.249E-18
90	3.126E+05	1.998E-20	1.703E-19	9.908E-19	2.129E-18	2.464E-18	2.507E-18	2.511E-18	2.255E-18
91	3.511E+05	2.178E-20	1.849E-19	1.043E-18	2.160E-18	2.474E-18	2.514E-18	2.518E-18	2.260E-18
92	3.944E+05	2.367E-20	2.000E-19	1.093E-18	2.188E-18	2.483E-18	2.520E-18	2.524E-18	2.265E-18
93	4.431E+05	2.564E-20	2.157E-19	1.142E-18	2.213E-18	2.491E-18	2.525E-18	2.529E-18	2.269E-18
94	4.977E+05	2.770E-20	2.318E-19	1.190E-18	2.237E-18	2.499E-18	2.530E-18	2.534E-18	2.273E-18
95	5.591E+05	2.986E-20	2.485E-19	1.236E-18	2.258E-18	2.505E-18	2.535E-18	2.538E-18	2.276E-18
96	6.280E+05	3.211E-20	2.657E-19	1.281E-18	2.278E-18	2.511E-18	2.539E-18	2.542E-18	2.279E-18
97	7.055E+05	3.446E-20	2.833E-19	1.325E-18	2.297E-18	2.516E-18	2.542E-18	2.545E-18	2.282E-18
98	7.925E+05	3.693E-20	3.016E-19	1.368E-18	2.314E-18	2.521E-18	2.545E-18	2.548E-18	2.284E-18
99	8.902E+05	3.951E-20	3.203E-19	1.410E-18	2.330E-18	2.525E-18	2.548E-18	2.550E-18	2.286E-18
100	1.000E+06	4.221E-20	3.396E-19	1.450E-18	2.344E-18	2.529E-18	2.551E-18	2.553E-18	2.288E-18
101	1.123E+06	4.503E-20	3.595E-19	1.490E-18	2.358E-18	2.533E-18	2.553E-18	2.555E-18	2.290E-18

Table 2
Dissociative Cooling Rates

	Temp / Density = 1 (K) / cm^-3	10	10^2	10^3	10^4	10^5	10^6	LTE
1	1.000E+01	0.000E+00	0.000E+00	0.000E+00	0.000E+00	0.000E+00	0.000E+00	1.868E-46
2	1.123E+01	0.000E+00	0.000E+00	0.000E+00	0.000E+00	0.000E+00	0.000E+00	5.051E-44
3	1.262E+01	0.000E+00	0.000E+00	0.000E+00	0.000E+00	0.000E+00	0.000E+00	7.387E-42
4	1.417E+01	0.000E+00	0.000E+00	0.000E+00	0.000E+00	0.000E+00	0.000E+00	6.250E-40
5	1.592E+01	0.000E+00	0.000E+00	0.000E+00	0.000E+00	0.000E+00	0.000E+00	3.248E-38
6	1.789E+01	0.000E+00	0.000E+00	0.000E+00	0.000E+00	0.000E+00	0.000E+00	1.094E-36
7	2.009E+01	0.000E+00	0.000E+00	0.000E+00	0.000E+00	0.000E+00	0.000E+00	2.505E-35
8	2.257E+01	0.000E+00	0.000E+00	0.000E+00	0.000E+00	0.000E+00	0.000E+00	4.067E-34
9	2.535E+01	0.000E+00	0.000E+00	0.000E+00	0.000E+00	0.000E+00	0.000E+00	4.862E-33
10	2.848E+01	0.000E+00	0.000E+00	0.000E+00	0.000E+00	0.000E+00	0.000E+00	4.428E-32
11	3.199E+01	0.000E+00	0.000E+00	0.000E+00	0.000E+00	0.000E+00	0.000E+00	3.166E-31
12	3.594E+01	0.000E+00	0.000E+00	0.000E+00	0.000E+00	0.000E+00	0.000E+00	1.827E-30
13	4.037E+01	0.000E+00	0.000E+00	0.000E+00	0.000E+00	0.000E+00	0.000E+00	8.730E-30
14	4.535E+01	0.000E+00	0.000E+00	0.000E+00	0.000E+00	0.000E+00	0.000E+00	3.543E-29
15	5.094E+01	0.000E+00	0.000E+00	0.000E+00	0.000E+00	0.000E+00	0.000E+00	1.253E-28
16	5.722E+01	0.000E+00	0.000E+00	0.000E+00	0.000E+00	0.000E+00	0.000E+00	3.957E-28
17	6.428E+01	0.000E+00	0.000E+00	0.000E+00	0.000E+00	0.000E+00	0.000E+00	1.144E-27
18	7.221E+01	0.000E+00	0.000E+00	0.000E+00	0.000E+00	0.000E+00	0.000E+00	3.089E-27
19	8.111E+01	0.000E+00	0.000E+00	0.000E+00	0.000E+00	0.000E+00	0.000E+00	7.875E-27
20	9.112E+01	0.000E+00	0.000E+00	0.000E+00	0.000E+00	0.000E+00	0.000E+00	1.904E-26
21	1.024E+02	0.000E+00	0.000E+00	0.000E+00	0.000E+00	0.000E+00	0.000E+00	4.358E-26
22	1.150E+02	0.000E+00	0.000E+00	0.000E+00	0.000E+00	0.000E+00	0.000E+00	9.420E-26
23	1.292E+02	0.000E+00	0.000E+00	0.000E+00	0.000E+00	0.000E+00	0.000E+00	1.921E-25
24	1.451E+02	0.000E+00	0.000E+00	0.000E+00	0.000E+00	0.000E+00	0.000E+00	3.705E-25
25	1.630E+02	0.000E+00	0.000E+00	0.000E+00	0.000E+00	0.000E+00	0.000E+00	6.782E-25
26	1.831E+02	0.000E+00	0.000E+00	0.000E+00	0.000E+00	0.000E+00	0.000E+00	1.187E-24
27	2.057E+02	0.000E+00	0.000E+00	0.000E+00	0.000E+00	0.000E+00	0.000E+00	2.003E-24
28	2.310E+02	0.000E+00	0.000E+00	0.000E+00	0.000E+00	0.000E+00	0.000E+00	3.294E-24
29	2.595E+02	0.000E+00	0.000E+00	0.000E+00	0.000E+00	0.000E+00	0.000E+00	5.333E-24
30	2.915E+02	0.000E+00	0.000E+00	0.000E+00	0.000E+00	0.000E+00	0.000E+00	8.575E-24
31	3.275E+02	0.000E+00	0.000E+00	0.000E+00	0.000E+00	0.000E+00	0.000E+00	1.376E-23
32	3.678E+02	0.000E+00	0.000E+00	0.000E+00	0.000E+00	0.000E+00	0.000E+00	2.209E-23
33	4.132E+02	0.000E+00	0.000E+00	0.000E+00	0.000E+00	0.000E+00	0.000E+00	3.551E-23
34	4.642E+02	0.000E+00	0.000E+00	0.000E+00	0.000E+00	0.000E+00	0.000E+00	5.750E-23
35	5.214E+02	0.000E+00	3.772E-55	4.703E-53	4.667E-51	4.672E-49	4.605E-47	4.243E-45	9.493E-23
36	5.857E+02	7.869E-55	8.512E-53	8.513E-51	8.428E-49	8.424E-47	8.256E-45	7.396E-43	1.623E-22
37	6.579E+02	8.569E-53	8.939E-51	8.904E-49	8.837E-47	8.830E-45	8.591E-43	7.449E-41	2.902E-22
38	7.391E+02	5.498E-51	5.858E-49	5.799E-47	5.752E-45	5.714E-43	5.507E-41	4.599E-39	5.383E-22
39	8.302E+02	2.043E-49	2.459E-47	2.446E-45	2.420E-43	2.400E-41	2.290E-39	1.834E-37	1.014E-21
40	9.326E+02	6.754E-48	7.110E-46	7.004E-44	6.884E-42	6.858E-40	6.474E-38	4.947E-36	1.894E-21
41	1.048E+03	1.339E-46	1.449E-44	1.429E-42	1.411E-40	1.405E-38	1.287E-36	9.256E-35	3.438E-21
42	1.177E+03	2.089E-45	2.179E-43	2.155E-41	2.127E-39	2.094E-37	1.774E-35	7.156E-34	6.003E-21
43	1.322E+03	2.429E-44	2.543E-42	2.640E-40	2.482E-38	2.424E-36	2.026E-34	8.026E-33	1.004E-20
44	1.485E+03	2.284E-41	2.850E-40	5.698E-39	2.788E-37	2.356E-35	1.963E-33	9.446E-32	1.606E-20
45	1.668E+03	2.878E-39	3.321E-38	4.401E-37	8.123E-36	3.192E-34	2.250E-32	1.899E-30	2.468E-20
46	1.874E+03	2.162E-37	2.465E-36	3.103E-35	4.692E-34	1.127E-32	5.796E-31	7.048E-29	3.654E-20
47	2.105E+03	1.017E-35	1.151E-34	1.417E-33	2.054E-32	4.342E-31	1.890E-29	2.240E-27	5.235E-20
48	2.364E+03	3.155E-34	3.542E-33	4.288E-32	6.056E-31	1.199E-29	4.729E-28	5.044E-26	7.293E-20
49	2.656E+03	6.753E-33	7.526E-32	8.968E-31	1.238E-29	2.328E-28	8.567E-27	8.114E-25	9.920E-20
50	2.984E+03	1.039E-31	1.149E-30	1.351E-29	1.826E-28	3.281E-27	1.150E-25	9.600E-24	1.322E-19
51	3.352E+03	1.191E-30	1.309E-29	1.518E-28	2.012E-27	3.474E-26	1.180E-24	8.596E-23	1.731E-19
52	3.765E+03	1.051E-29	1.147E-28	1.315E-27	1.711E-26	2.851E-25	9.515E-24	5.976E-22	2.231E-19
53	4.229E+03	7.350E-29	7.969E-28	9.041E-27	1.155E-25	1.867E-24	6.172E-23	3.301E-21	2.832E-19
54	4.751E+03	4.177E-28	4.500E-27	5.056E-26	6.351E-25	1.001E-23	3.288E-22	1.479E-20	3.540E-19
55	5.337E+03	1.975E-27	2.113E-26	2.354E-25	2.909E-24	4.498E-23	1.464E-21	5.483E-20	4.355E-19
56	5.995E+03	7.928E-27	8.421E-26	9.308E-25	1.133E-23	1.728E-22	5.533E-21	1.713E-19	5.270E-19
57	6.734E+03	2.753E-26	2.899E-25	3.184E-24	3.823E-23	5.783E-22	1.798E-20	4.599E-19	6.270E-19
58	7.565E+03	8.391E-26	8.765E-25	9.570E-24	1.135E-22	1.713E-21	5.088E-20	1.082E-18	7.333E-19
59	8.498E+03	2.275E-25	2.362E-24	2.564E-23	3.008E-22	4.551E-21	1.268E-19	2.280E-18	8.436E-19
60	9.545E+03	5.555E-25	5.748E-24	6.204E-23	7.212E-22	1.098E-20	2.816E-19	4.378E-18	9.552E-19
61	1.072E+04	1.237E-24	1.277E-23	1.370E-22	1.582E-21	2.432E-20	5.647E-19	7.797E-18	1.066E-18
62	1.205E+04	2.538E-24	2.615E-23	2.790E-22	3.208E-21	4.978E-20	1.036E-18	1.305E-17	1.173E-18
63	1.353E+04	4.842E-24	4.980E-23	5.289E-22	6.065E-21	9.484E-20	1.762E-18	2.073E-17	1.276E-18
64	1.520E+04	8.661E-24	8.894E-23	9.403E-22	1.078E-20	1.690E-19	2.812E-18	3.151E-17	1.373E-18
65	1.707E+04	1.463E-23	1.500E-22	1.580E-21	1.814E-20	2.829E-19	4.257E-18	4.608E-17	1.464E-18
66	1.918E+04	2.347E-23	2.403E-22	2.523E-21	2.906E-20	4.472E-19	6.164E-18	6.514E-17	1.548E-18
67	2.154E+04	3.597E-23	3.678E-22	3.852E-21	4.458E-20	6.709E-19	8.593E-18	8.931E-17	1.625E-18
68	2.420E+04	5.296E-23	5.408E-22	5.653E-21	6.576E-20	9.602E-19	1.160E-17	1.191E-16	1.695E-18
69	2.719E+04	7.520E-23	7.670E-22	8.006E-21	9.362E-20	1.319E-18	1.521E-17	1.551E-16	1.759E-18
70	3.054E+04	1.034E-22	1.053E-21	1.099E-20	1.290E-19	1.748E-18	1.946E-17	1.973E-16	1.816E-18
71	3.430E+04	1.382E-22	1.406E-21	1.466E-20	1.726E-19	2.249E-18	2.437E-17	2.461E-16	1.868E-18
72	3.854E+04	1.800E-22	1.830E-21	1.908E-20	2.247E-19	2.818E-18	2.994E-17	3.015E-16	1.915E-18
73	4.329E+04	2.293E-22	2.328E-21	2.428E-20	2.854E-19	3.454E-18	3.616E-17	3.635E-16	1.957E-18
74	4.863E+04	2.862E-22	2.904E-21	3.028E-20	3.543E-19	4.155E-18	4.302E-17	4.319E-16	1.994E-18
75	5.462E+04	3.508E-22	3.556E-21	3.710E-20	4.311E-19	4.920E-18	5.052E-17	5.067E-16	2.028E-18
76	6.136E+04	4.232E-22	4.287E-21	4.473E-20	5.153E-19	5.745E-18	5.864E-17	5.877E-16	2.058E-18
77	6.893E+04	5.034E-22	5.095E-21	5.316E-20	6.063E-19	6.630E-18	6.736E-17	6.747E-16	2.085E-18
78	7.743E+04	5.911E-22	5.980E-21	6.237E-20	7.038E-19	7.574E-18	7.667E-17	7.678E-16	2.109E-18
79	8.697E+04	6.864E-22	6.939E-21	7.234E-20	8.075E-19	8.574E-18	8.658E-17	8.667E-16	2.130E-18
80	9.770E+04	7.890E-22	7.972E-21	8.304E-20	9.170E-19	9.632E-18	9.706E-17	9.714E-16	2.149E-18
81	1.097E+05	8.989E-22	9.077E-21	9.445E-20	1.032E-18	1.075E-17	1.081E-16	1.082E-15	2.166E-18
82	1.233E+05	1.016E-21	1.025E-20	1.065E-19	1.153E-18	1.192E-17	1.198E-16	1.198E-15	2.181E-18
83	1.385E+05	1.140E-21	1.150E-20	1.193E-19	1.280E-18	1.315E-17	1.320E-16	1.321E-15	2.194E-18

84	1.556E+05	1.271E-21	1.282E-20	1.328E-19	1.412E-18	1.445E-17	1.449E-16	1.450E-15	2.206E-18
85	1.748E+05	1.410E-21	1.421E-20	1.469E-19	1.551E-18	1.580E-17	1.584E-16	1.585E-15	2.217E-18
86	1.963E+05	1.556E-21	1.568E-20	1.617E-19	1.696E-18	1.722E-17	1.726E-16	1.726E-15	2.226E-18
87	2.205E+05	1.709E-21	1.721E-20	1.772E-19	1.848E-18	1.871E-17	1.874E-16	1.875E-15	2.235E-18
88	2.477E+05	1.870E-21	1.883E-20	1.935E-19	2.006E-18	2.028E-17	2.030E-16	2.031E-15	2.242E-18
89	2.783E+05	2.039E-21	2.052E-20	2.105E-19	2.172E-18	2.191E-17	2.194E-16	2.194E-15	2.249E-18
90	3.126E+05	2.216E-21	2.230E-20	2.282E-19	2.346E-18	2.363E-17	2.366E-16	2.366E-15	2.255E-18
91	3.511E+05	2.402E-21	2.416E-20	2.469E-19	2.528E-18	2.544E-17	2.546E-16	2.546E-15	2.260E-18
92	3.944E+05	2.598E-21	2.611E-20	2.664E-19	2.719E-18	2.733E-17	2.735E-16	2.735E-15	2.265E-18
93	4.431E+05	2.803E-21	2.816E-20	2.868E-19	2.920E-18	2.932E-17	2.934E-16	2.934E-15	2.269E-18
94	4.977E+05	3.018E-21	3.032E-20	3.082E-19	3.131E-18	3.142E-17	3.143E-16	3.143E-15	2.273E-18
95	5.591E+05	3.244E-21	3.258E-20	3.307E-19	3.352E-18	3.362E-17	3.363E-16	3.364E-15	2.276E-18
96	6.280E+05	3.481E-21	3.495E-20	3.544E-19	3.585E-18	3.594E-17	3.595E-16	3.595E-15	2.279E-18
97	7.055E+05	3.731E-21	3.745E-20	3.792E-19	3.830E-18	3.838E-17	3.839E-16	3.840E-15	2.282E-18
98	7.925E+05	3.994E-21	4.008E-20	4.053E-19	4.089E-18	4.096E-17	4.097E-16	4.097E-15	2.284E-18
99	8.902E+05	4.270E-21	4.284E-20	4.328E-19	4.361E-18	4.367E-17	4.368E-16	4.368E-15	2.286E-18
100	1.000E+06	4.562E-21	4.576E-20	4.618E-19	4.648E-18	4.654E-17	4.654E-16	4.654E-15	2.288E-18
101	1.123E+06	4.869E-21	4.882E-20	4.923E-19	4.951E-18	4.956E-17	4.956E-16	4.957E-15	2.290E-18

Table 3
Pumping Cooling Rates

	Temp / Density = 1 (K) / cm^-3	10	10^2	10^3	10^4	10^5	10^6	LTE
1	1.000E+01	0.000E+00	0.000E+00	0.000E+00	0.000E+00	0.000E+00	0.000E+00	0.000E+00	0.000E+00
2	1.123E+01	0.000E+00	0.000E+00	0.000E+00	0.000E+00	0.000E+00	0.000E+00	0.000E+00	0.000E+00
3	1.262E+01	0.000E+00	0.000E+00	0.000E+00	0.000E+00	0.000E+00	0.000E+00	0.000E+00	0.000E+00
4	1.417E+01	0.000E+00	0.000E+00	0.000E+00	0.000E+00	0.000E+00	0.000E+00	0.000E+00	0.000E+00
5	1.592E+01	0.000E+00	0.000E+00	0.000E+00	0.000E+00	0.000E+00	0.000E+00	0.000E+00	0.000E+00
6	1.789E+01	0.000E+00	0.000E+00	0.000E+00	0.000E+00	0.000E+00	0.000E+00	0.000E+00	0.000E+00
7	2.009E+01	0.000E+00	0.000E+00	0.000E+00	0.000E+00	0.000E+00	0.000E+00	0.000E+00	0.000E+00
8	2.257E+01	0.000E+00	0.000E+00	0.000E+00	0.000E+00	0.000E+00	0.000E+00	0.000E+00	0.000E+00
9	2.535E+01	0.000E+00	0.000E+00	0.000E+00	0.000E+00	0.000E+00	0.000E+00	0.000E+00	0.000E+00
10	2.848E+01	0.000E+00	0.000E+00	0.000E+00	0.000E+00	0.000E+00	0.000E+00	0.000E+00	0.000E+00
11	3.199E+01	0.000E+00	0.000E+00	0.000E+00	0.000E+00	0.000E+00	0.000E+00	0.000E+00	0.000E+00
12	3.594E+01	0.000E+00	0.000E+00	0.000E+00	0.000E+00	0.000E+00	0.000E+00	0.000E+00	0.000E+00
13	4.037E+01	0.000E+00	0.000E+00	0.000E+00	0.000E+00	0.000E+00	0.000E+00	0.000E+00	0.000E+00
14	4.535E+01	0.000E+00	0.000E+00	0.000E+00	0.000E+00	0.000E+00	0.000E+00	0.000E+00	0.000E+00
15	5.094E+01	0.000E+00	0.000E+00	0.000E+00	0.000E+00	0.000E+00	0.000E+00	0.000E+00	0.000E+00
16	5.722E+01	0.000E+00	0.000E+00	0.000E+00	0.000E+00	0.000E+00	0.000E+00	0.000E+00	0.000E+00
17	6.428E+01	0.000E+00	0.000E+00	0.000E+00	0.000E+00	0.000E+00	0.000E+00	0.000E+00	0.000E+00
18	7.221E+01	0.000E+00	0.000E+00	0.000E+00	0.000E+00	0.000E+00	0.000E+00	0.000E+00	0.000E+00
19	8.111E+01	0.000E+00	0.000E+00	0.000E+00	0.000E+00	0.000E+00	0.000E+00	0.000E+00	0.000E+00
20	9.112E+01	0.000E+00	0.000E+00	0.000E+00	0.000E+00	0.000E+00	0.000E+00	0.000E+00	0.000E+00
21	1.024E+02	0.000E+00	0.000E+00	0.000E+00	0.000E+00	0.000E+00	0.000E+00	0.000E+00	0.000E+00
22	1.150E+02	0.000E+00	0.000E+00	0.000E+00	0.000E+00	0.000E+00	0.000E+00	0.000E+00	0.000E+00
23	1.292E+02	0.000E+00	0.000E+00	0.000E+00	0.000E+00	0.000E+00	0.000E+00	0.000E+00	0.000E+00
24	1.451E+02	0.000E+00	0.000E+00	0.000E+00	0.000E+00	0.000E+00	0.000E+00	0.000E+00	0.000E+00
25	1.630E+02	0.000E+00	0.000E+00	0.000E+00	0.000E+00	0.000E+00	0.000E+00	0.000E+00	0.000E+00
26	1.831E+02	0.000E+00	0.000E+00	0.000E+00	0.000E+00	0.000E+00	0.000E+00	0.000E+00	0.000E+00
27	2.057E+02	0.000E+00	0.000E+00	0.000E+00	0.000E+00	0.000E+00	0.000E+00	0.000E+00	0.000E+00
28	2.310E+02	0.000E+00	0.000E+00	0.000E+00	0.000E+00	0.000E+00	0.000E+00	0.000E+00	0.000E+00
29	2.595E+02	0.000E+00	0.000E+00	0.000E+00	0.000E+00	0.000E+00	0.000E+00	0.000E+00	0.000E+00
30	2.915E+02	0.000E+00	0.000E+00	0.000E+00	0.000E+00	0.000E+00	0.000E+00	0.000E+00	0.000E+00
31	3.275E+02	0.000E+00	0.000E+00	0.000E+00	0.000E+00	0.000E+00	0.000E+00	0.000E+00	0.000E+00
32	3.678E+02	0.000E+00	0.000E+00	0.000E+00	0.000E+00	0.000E+00	0.000E+00	0.000E+00	0.000E+00
33	4.132E+02	0.000E+00	0.000E+00	0.000E+00	0.000E+00	0.000E+00	0.000E+00	0.000E+00	0.000E+00
34	4.642E+02	0.000E+00	0.000E+00	0.000E+00	0.000E+00	0.000E+00	0.000E+00	0.000E+00	0.000E+00
35	5.214E+02	0.000E+00	0.000E+00	0.000E+00	0.000E+00	0.000E+00	0.000E+00	0.000E+00	0.000E+00
36	5.857E+02	0.000E+00	0.000E+00	0.000E+00	0.000E+00	0.000E+00	0.000E+00	0.000E+00	0.000E+00
37	6.579E+02	0.000E+00	0.000E+00	0.000E+00	0.000E+00	0.000E+00	0.000E+00	0.000E+00	0.000E+00
38	7.391E+02	1.832E-94	2.023E-92	2.017E-90	2.000E-88	1.983E-86	1.868E-84	1.320E-82	5.470E-91
39	8.302E+02	6.909E-88	6.422E-86	6.251E-84	6.169E-82	6.104E-80	5.692E-78	3.828E-76	1.281E-82
40	9.326E+02	9.847E-82	4.663E-80	4.040E-78	3.914E-76	3.884E-74	3.578E-72	2.279E-70	3.749E-75
41	1.048E+03	4.981E-76	1.099E-74	6.720E-73	6.215E-71	6.139E-69	5.524E-67	3.299E-65	1.724E-68
42	1.177E+03	1.432E-70	1.422E-69	3.977E-68	2.905E-66	2.762E-64	2.406E-62	1.097E-60	1.519E-62
43	1.322E+03	5.078E-65	1.745E-64	1.891E-63	5.825E-62	4.367E-60	3.711E-58	1.824E-56	3.062E-57
44	1.485E+03	9.602E-60	1.637E-59	8.789E-59	1.155E-57	3.943E-56	2.938E-54	2.181E-52	1.652E-52
45	1.668E+03	5.780E-55	7.373E-55	2.088E-54	1.833E-53	3.509E-52	1.936E-50	2.055E-48	2.741E-48
46	1.874E+03	1.132E-50	1.299E-50	2.302E-50	1.332E-49	2.151E-48	1.075E-46	1.225E-44	1.587E-44
47	2.105E+03	7.967E-47	8.779E-47	1.193E-46	4.280E-46	5.931E-45	2.826E-43	3.079E-41	3.591E-41
48	2.364E+03	2.235E-43	2.418E-43	2.869E-43	6.723E-43	7.468E-42	3.352E-40	3.376E-38	3.513E-38
49	2.656E+03	2.750E-40	2.943E-40	3.251E-40	5.581E-40	4.683E-39	1.924E-37	1.748E-35	1.627E-35
50	2.984E+03	1.617E-37	1.719E-37	1.819E-37	2.554E-37	1.595E-36	5.791E-35	4.620E-33	3.873E-33
51	3.352E+03	4.918E-35	5.193E-35	5.336E-35	6.636E-35	3.170E-34	9.840E-33	6.682E-31	5.096E-31
52	3.765E+03	8.291E-33	8.703E-33	8.739E-33	1.012E-32	3.893E-32	1.007E-30	5.624E-29	3.957E-29
53	4.229E+03	8.249E-31	8.609E-31	8.478E-31	9.430E-31	3.083E-30	6.549E-29	2.911E-27	1.922E-27
54	4.751E+03	5.124E-29	5.317E-29	5.149E-29	5.611E-29	1.634E-28	2.841E-27	9.739E-26	6.154E-26
55	5.337E+03	2.090E-27	2.156E-27	2.059E-27	2.228E-27	5.985E-27	8.541E-26	2.202E-24	1.361E-24
56	5.995E+03	5.857E-26	6.009E-26	5.692E-26	6.168E-26	1.565E-25	1.841E-24	3.505E-23	2.165E-23
57	6.734E+03	1.174E-24	1.199E-24	1.139E-24	1.241E-24	3.012E-24	2.925E-23	4.087E-22	2.574E-22
58	7.565E+03	1.744E-23	1.778E-23	1.718E-23	1.885E-23	4.396E-23	3.518E-22	3.623E-21	2.363E-21
59	8.498E+03	1.981E-22	2.020E-22	2.003E-22	2.220E-22	4.995E-22	3.276E-21	2.529E-20	1.724E-20
60	9.545E+03	1.769E-21	1.805E-21	1.832E-21	2.065E-21	4.523E-21	2.417E-20	1.438E-19	1.027E-19
61	1.072E+04	1.275E-20	1.301E-20	1.341E-20	1.541E-20	3.331E-20	1.446E-19	6.842E-19	5.107E-19
62	1.205E+04	7.589E-20	7.746E-20	8.052E-20	9.424E-20	2.029E-19	7.171E-19	2.794E-18	2.166E-18
63	1.353E+04	3.808E-19	3.886E-19	4.058E-19	4.829E-19	1.039E-18	3.016E-18	9.983E-18	7.973E-18
64	1.520E+04	1.640E-18	1.673E-18	1.752E-18	2.118E-18	4.539E-18	1.098E-17	3.172E-17	2.589E-17
65	1.707E+04	6.162E-18	6.283E-18	6.588E-18	8.095E-18	1.713E-17	3.526E-17	9.083E-17	7.520E-17
66	1.918E+04	2.049E-17	2.088E-17	2.192E-17	2.739E-17	5.656E-17	1.013E-16	2.370E-16	1.978E-16
67	2.154E+04	6.103E-17	6.217E-17	6.538E-17	8.314E-17	1.655E-16	2.640E-16	5.686E-16	4.763E-16
68	2.420E+04	1.648E-16	1.678E-16	1.768E-16	2.288E-16	4.343E-16	6.307E-16	1.265E-15	1.060E-15
69	2.719E+04	4.076E-16	4.149E-16	4.381E-16	5.764E-16	1.035E-15	1.395E-15	2.628E-15	2.200E-15
70	3.054E+04	9.313E-16	9.476E-16	1.004E-15	1.340E-15	2.265E-15	2.878E-15	5.133E-15	4.286E-15
71	3.430E+04	1.982E-15	2.016E-15	2.142E-15	2.891E-15	4.597E-15	5.581E-15	9.482E-15	7.893E-15
72	3.854E+04	3.957E-15	4.024E-15	4.291E-15	5.832E-15	8.736E-15	1.024E-14	1.665E-14	1.382E-14
73	4.329E+04	7.458E-15	7.583E-15	8.117E-15	1.105E-14	1.566E-14	1.786E-14	2.794E-14	2.312E-14
74	4.863E+04	1.335E-14	1.357E-14	1.458E-14	1.980E-14	2.669E-14	2.977E-14	4.497E-14	3.712E-14
75	5.462E+04	2.279E-14	2.316E-14	2.498E-14	3.370E-14	4.345E-14	4.764E-14	6.974E-14	5.744E-14
76	6.136E+04	3.730E-14	3.791E-14	4.101E-14	5.475E-14	6.794E-14	7.349E-14	1.045E-13	8.595E-14
77	6.893E+04	5.876E-14	5.971E-14	6.477E-14	8.533E-14	1.025E-13	1.096E-13	1.519E-13	1.248E-13
78	7.743E+04	8.938E-14	9.083E-14	9.873E-14	1.281E-13	1.496E-13	1.587E-13	2.147E-13	1.762E-13
79	8.697E+04	1.317E-13	1.339E-13	1.457E-13	1.860E-13	2.122E-13	2.234E-13	2.959E-13	2.426E-13
80	9.770E+04	1.887E-13	1.917E-13	2.087E-13	2.620E-13	2.931E-13	3.068E-13	3.983E-13	3.265E-13
81	1.097E+05	2.631E-13	2.673E-13	2.911E-13	3.593E-13	3.954E-13	4.117E-13	5.248E-13	4.302E-13
82	1.233E+05	3.583E-13	3.639E-13	3.960E-13	4.809E-13	5.219E-13	5.410E-13	6.783E-13	5.560E-13

83	1.385E+05	4.772E-13	4.845E-13	5.266E-13	6.295E-13	6.753E-13	6.974E-13	8.611E-13	7.060E-13
84	1.556E+05	6.229E-13	6.323E-13	6.858E-13	8.078E-13	8.580E-13	8.833E-13	1.075E-12	8.819E-13
85	1.748E+05	7.981E-13	8.098E-13	8.763E-13	1.018E-12	1.072E-12	1.101E-12	1.323E-12	1.085E-12
86	1.963E+05	1.005E-12	1.019E-12	1.100E-12	1.262E-12	1.320E-12	1.352E-12	1.604E-12	1.317E-12
87	2.205E+05	1.246E-12	1.263E-12	1.359E-12	1.540E-12	1.601E-12	1.637E-12	1.921E-12	1.578E-12
88	2.477E+05	1.523E-12	1.543E-12	1.654E-12	1.854E-12	1.918E-12	1.957E-12	2.273E-12	1.868E-12
89	2.783E+05	1.835E-12	1.858E-12	1.986E-12	2.204E-12	2.270E-12	2.312E-12	2.659E-12	2.187E-12
90	3.126E+05	2.185E-12	2.211E-12	2.355E-12	2.589E-12	2.657E-12	2.702E-12	3.080E-12	2.534E-12
91	3.511E+05	2.571E-12	2.600E-12	2.760E-12	3.010E-12	3.078E-12	3.126E-12	3.534E-12	2.909E-12
92	3.944E+05	2.993E-12	3.025E-12	3.200E-12	3.463E-12	3.532E-12	3.583E-12	4.019E-12	3.309E-12
93	4.431E+05	3.451E-12	3.484E-12	3.673E-12	3.948E-12	4.017E-12	4.070E-12	4.533E-12	3.735E-12
94	4.977E+05	3.941E-12	3.977E-12	4.178E-12	4.464E-12	4.532E-12	4.587E-12	5.074E-12	4.183E-12
95	5.591E+05	4.463E-12	4.500E-12	4.713E-12	5.006E-12	5.074E-12	5.131E-12	5.640E-12	4.652E-12
96	6.280E+05	5.014E-12	5.051E-12	5.274E-12	5.574E-12	5.640E-12	5.699E-12	6.229E-12	5.139E-12
97	7.055E+05	5.592E-12	5.629E-12	5.860E-12	6.165E-12	6.229E-12	6.289E-12	6.837E-12	5.643E-12
98	7.925E+05	6.194E-12	6.229E-12	6.468E-12	6.775E-12	6.837E-12	6.899E-12	7.462E-12	6.161E-12
99	8.902E+05	6.817E-12	6.850E-12	7.094E-12	7.403E-12	7.463E-12	7.525E-12	8.101E-12	6.691E-12
100	1.000E+06	7.458E-12	7.489E-12	7.736E-12	8.045E-12	8.103E-12	8.166E-12	8.752E-12	7.231E-12
101	1.123E+06	8.116E-12	8.142E-12	8.392E-12	8.699E-12	8.754E-12	8.818E-12	9.413E-12	7.779E-12

Table B1
Analytical coefficients[a] for the H_2 B and C cross sections

	$B\ ^1\Sigma_u^+$ [b]		$C\ ^1\Pi_u^+$ [c]	
V	E_{ij}(Ryd)	C_7	E_{ij}(Ryd)	C_7
0	0.82211	0.7635-2[d]	0.90337	0.1835+0
1	0.83413	0.2580-1	0.92440	0.2744+0
2	0.84581	0.5059-1	0.94420	0.2575+0
3	0.85717	0.7613-1	0.96300	0.1979+0
4	0.86786	0.9643-1	0.98025	0.1376+0
5	0.87716	0.1094+0	0.99649	0.9086-1
6	0.88944	0.1130+0	1.01154	0.5854-1
7	0.89960	0.1105+0	1.02541	0.3733-1
8	0.90948	0.1031+0	1.03803	0.2383-1
9	0.91908	0.9293-1	1.04934	0.1525-1
10	0.92840	0.8149-1	0.05923	0.9792-2
11	0.93470	0.7055-1		
12	0.94621	0.5905-1		
13	0.95471	0.4929-1		
14	0.96378	0.4063-1		
15	0.97184	0.3333-1		
16	0.97870	0.2729-1		
17	0.98692	0.2216-1		
18	0.99342	0.1804-1		
19	1.00045	0.1464-1		
20	1.00722	0.1188-1		

[a] From Shemansky, Ajello, and Hall (1985, 1987).
[b] $C_0/C_7 = -0.6439$, $C_5/C_7 = -0.3560$, $C_n = 0.0$ for n=1-4.
[c] $C_1/C_7 = -2.082$, $C_4/C_7 = 4.6732$, $C_5/C_7 = -0.26316$, $\alpha = 0.8424$, $C_n = 0.0$ for n=0, 2, 3.
[d] The notation 0.7635-2 stands for 0.7635×10^{-2}.

Table B2
The Honl-London Factor S_J

Band	R $J^* = J + 1$	Q $J^* = J$	P $J^* = J - 1$
Lyman	J + 1	0	J
Werner	(J + 2)/2	(2J + 1)/2	(J - 1)/2

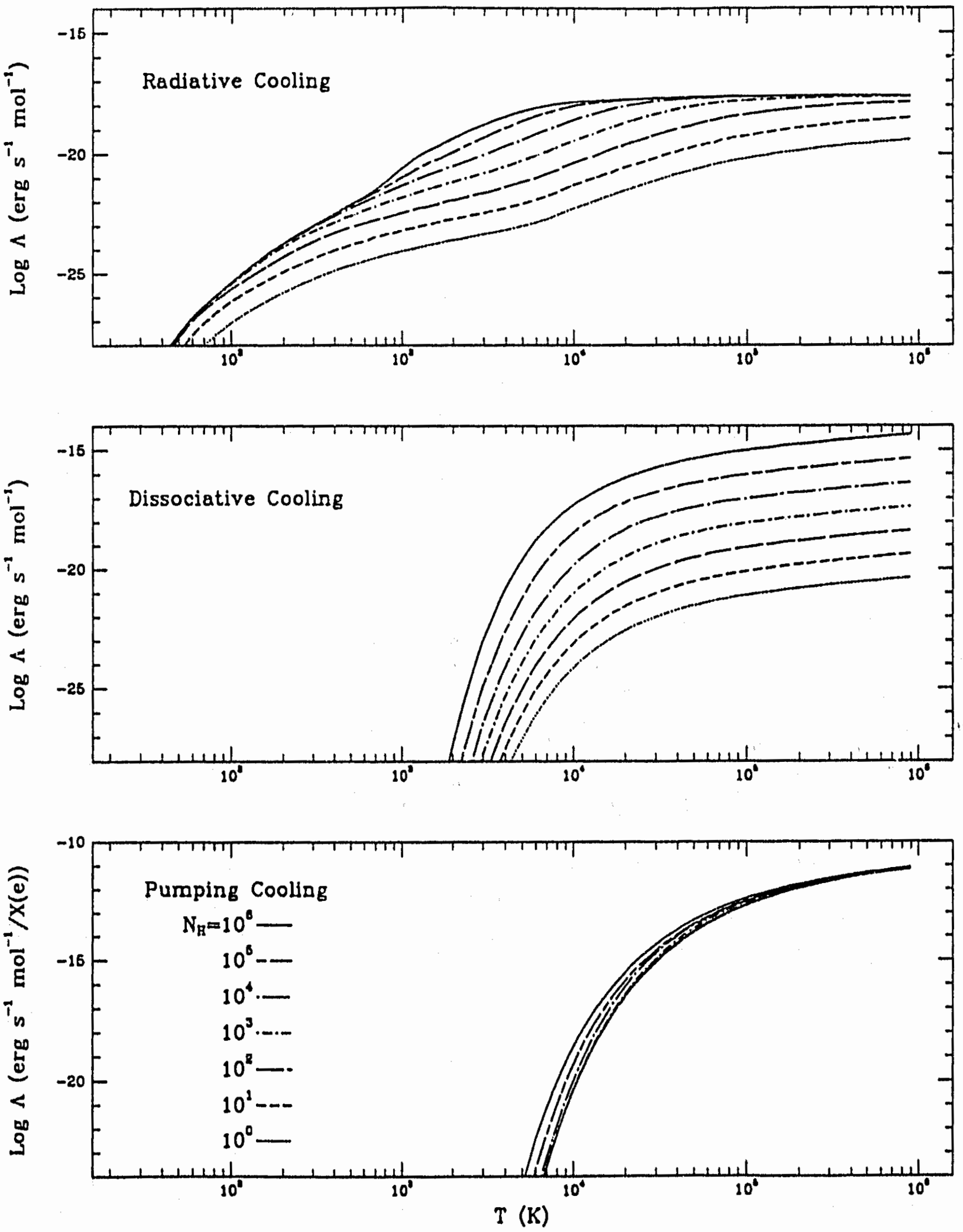

Figure 1. Top: H_2 radiative cooling rates in a molecular cloud. For densities n_H = 10^0–10^6 cm^{-3}, the level populations are solved for equilibrium at each temperature. Middle: dissociative cooling rate for the same densities and conditions. Bottom: Collisional-pumping rate for excitation of the upper H_2 BΣ and CΠ electronic states by collisions with hot electrons. This cooling rate scales with the electron density.

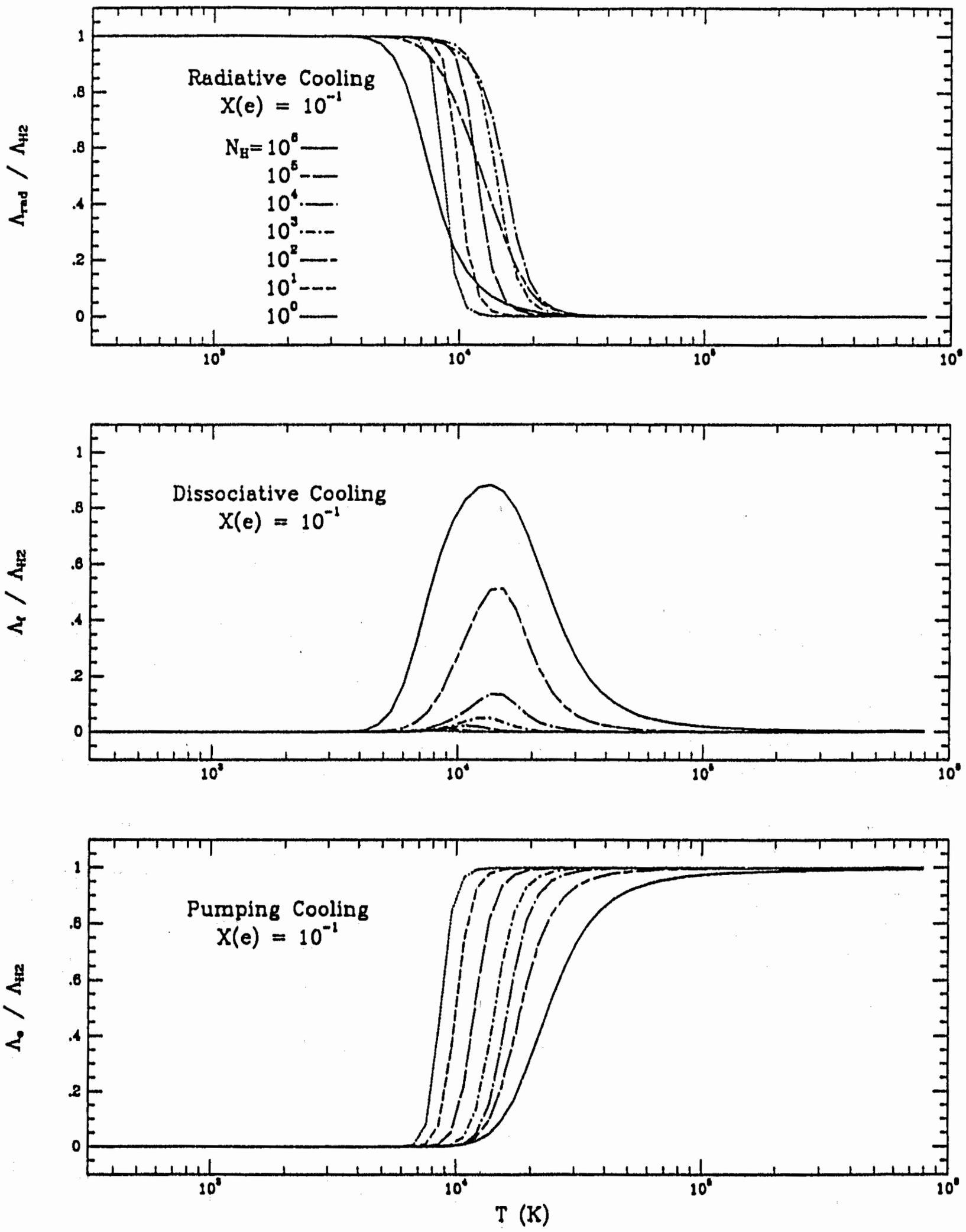

Figure 2. Comparison of the radiative (Λ_{rad}), dissociative (Λ_{diss}) and pumping (Λ_e) cooling fractions for densities $n_H = 10^0$–10^6 cm^{-3} and ionization fractions X(e) = 10^{-1}, 10^{-3} and 10^{-5}.

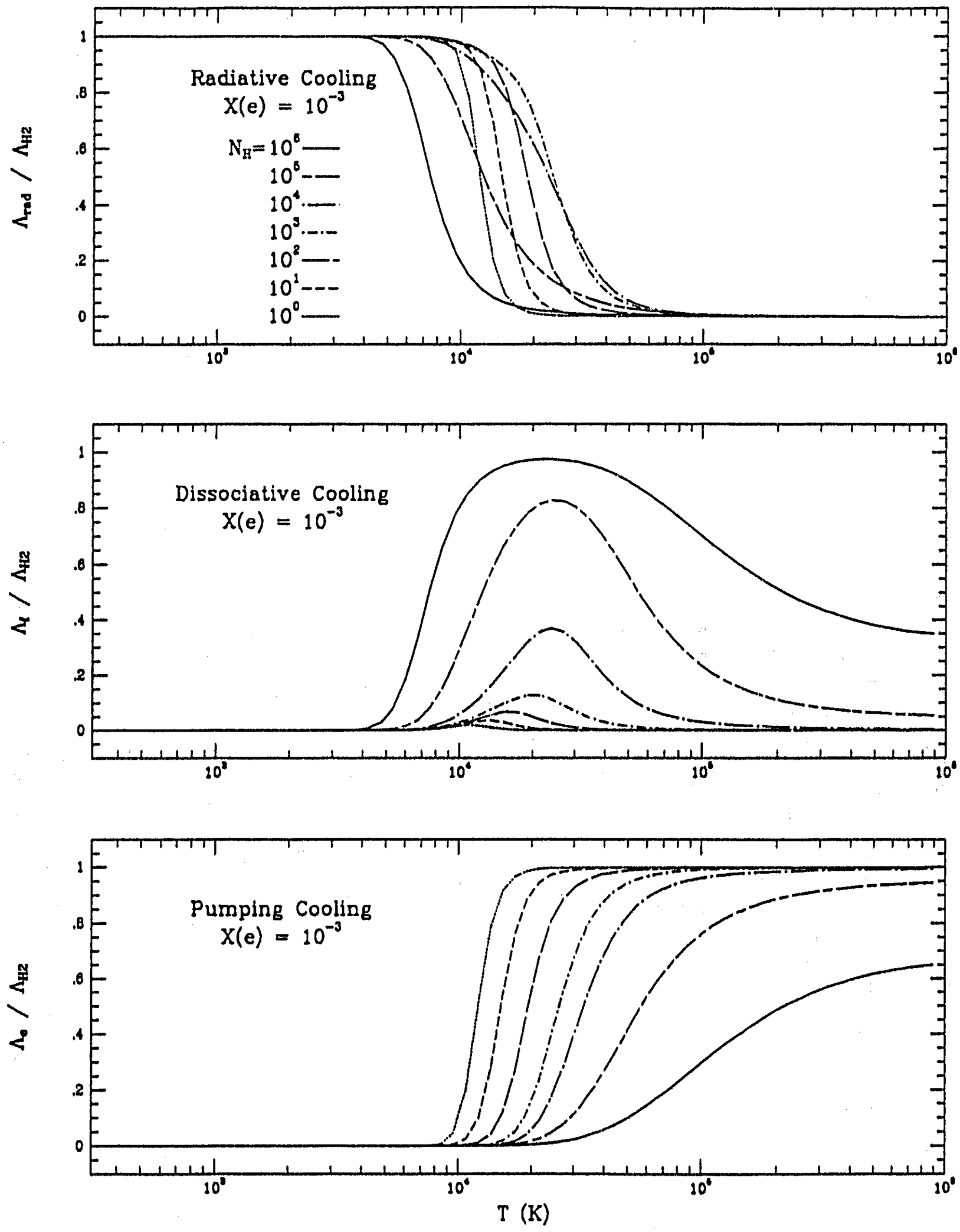
Radiative Cooling
X(e) = 10^-3
N_H= 10^6
10^5
10^4
10^3
10^2
10^1
10^0
Λ_rad / Λ_H2
Dissociative Cooling
X(e) = 10^-3
Λ_d / Λ_H2
Pumping Cooling
X(e) = 10^-3
Λ_e / Λ_H2
0
.2
.4
.6
.8
1
10^2
10^4
10^6
10^8
T (K)

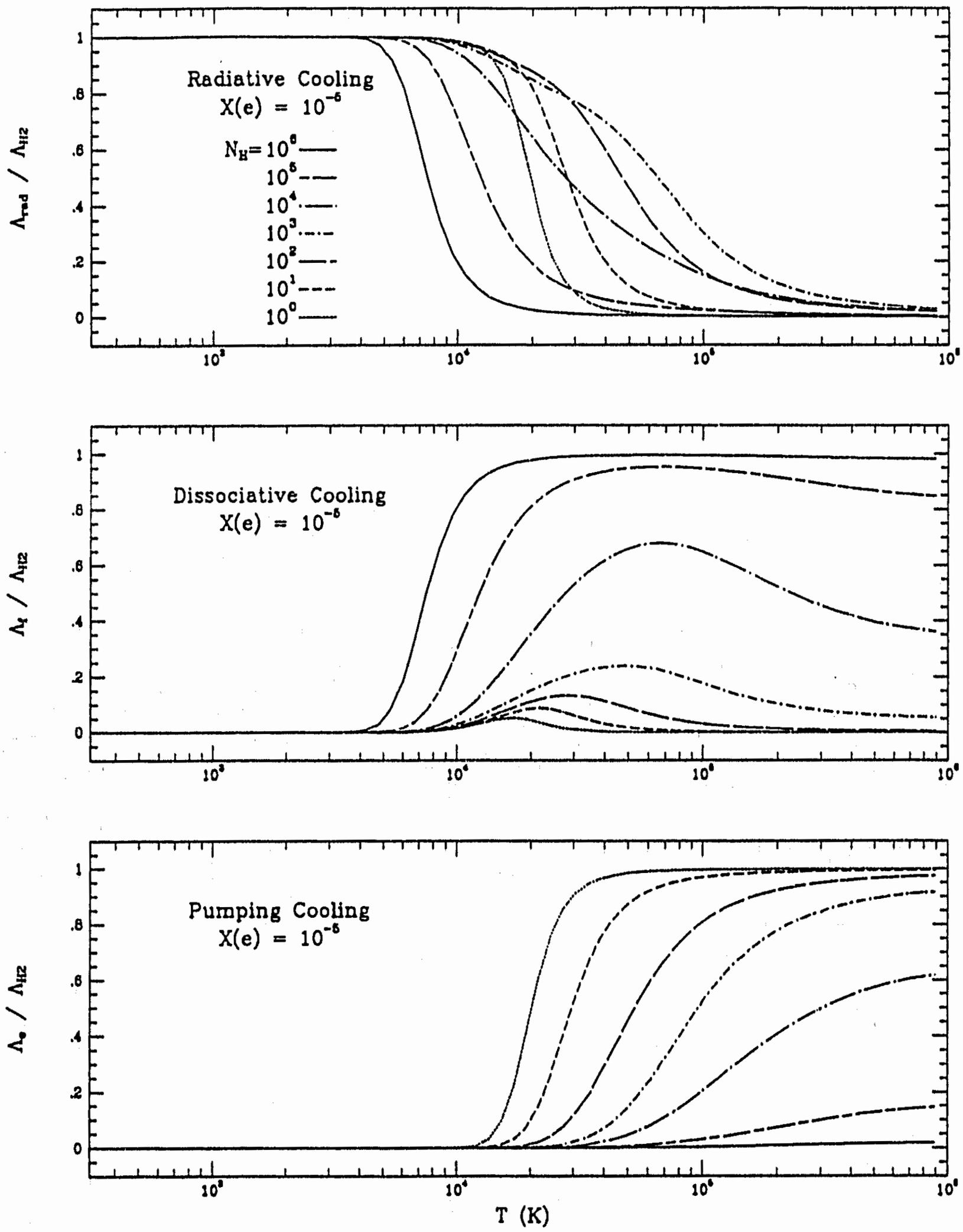
Radiative Cooling
X(e) = 10^-5
N_H= 10^6
10^5
10^4
10^3
10^2
10^1
10^0
Λ_rad / Λ_H2
Dissociative Cooling
X(e) = 10^-5
Λ_d / Λ_H2
Pumping Cooling
X(e) = 10^-5
Λ_e / Λ_H2
0
.2
.4
.6
.8
1
10^3
10^4
10^5
10^6
T (K)

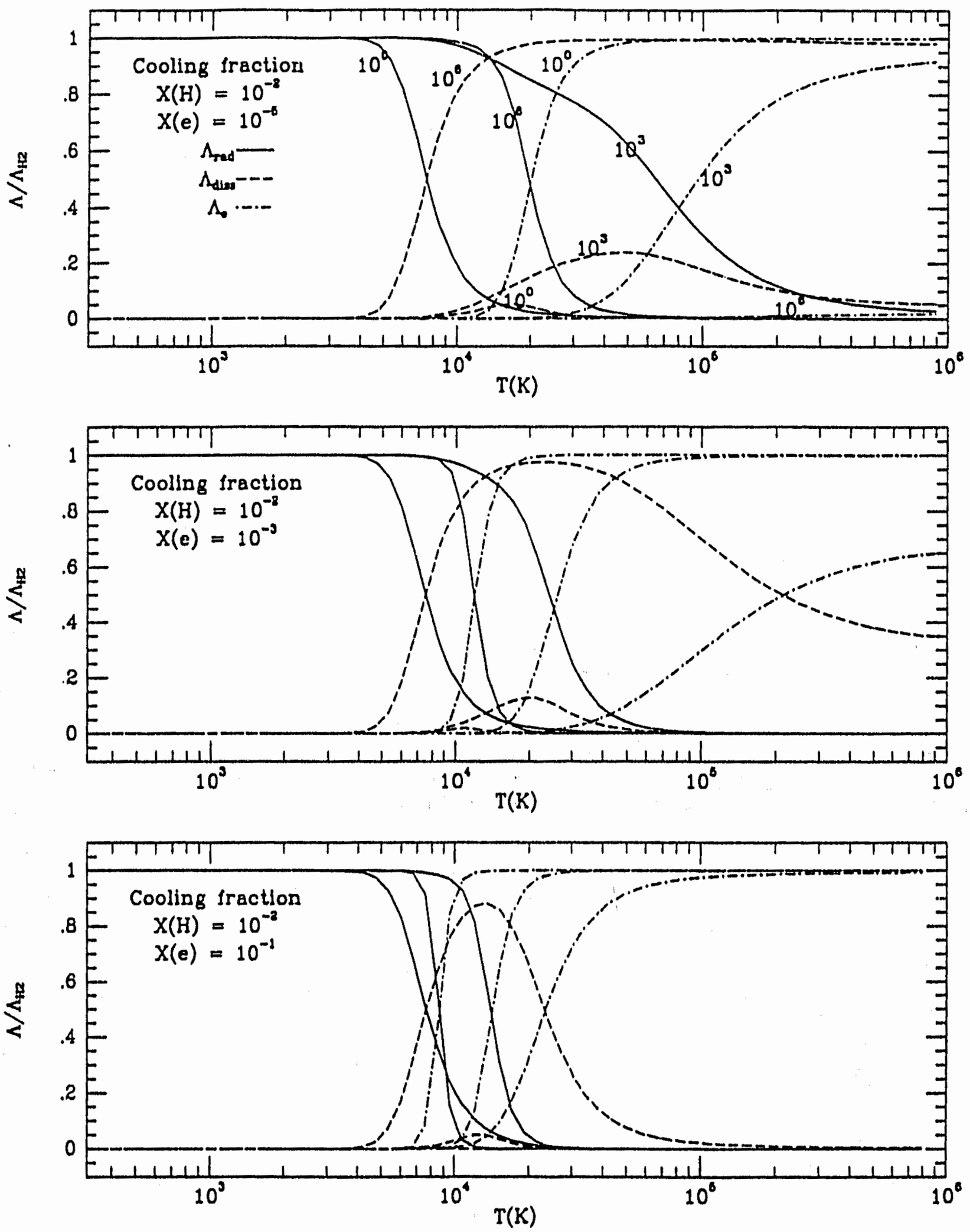

Figure 3. Comparison of the radiative (Λ_{rad}), dissociative (Λ_{diss}) and pumping (Λ_e) cooling fractions for densities $n_H = 10^0$, 10^3 and 10^6 cm^{-3} at given ionization fractions X(e) = 10^{-1}, 10^{-3} and 10^{-5}.

CHAPTER 3

MOLECULAR HYDROGEN AND OPTICAL IMAGES OF HH 7-11

Abstract

We compare flux-calibrated H_2 images of HH 7-11 with Hα and [S II] images taken almost simultaneously. The H_2 and optical images are fairly similar except for HH 11, which is bright in Hα but absent in H_2. HH 7, 8, and 10 are morphologically similar in all the images, suggesting that molecular gas is present in the same shock that produces the optical lines. We conclude that a bow shock with magnetic precursor could explain many of the existing observations of HH 7.

I. Introduction

The formation of stars in our galaxy is a complex process that often involves the ejection of an energetic bipolar wind as the young star emerges from its placental dark cloud (Shu, Adams, and Lizano 1988). When these winds interact with the surrounding medium they form shocks in the outflowing gas and in the ambient molecular cloud. Nebulous emission-line sources known as Herbig-Haro (HH) objects often exist in the vicinity of a young star, and appear to mark the regions where the stronger shocks are cooling radiatively (Schwartz 1983). The line ratios and line profiles observed in HH objects are often complex and difficult to interpret, although simple bow shock and jet models can account for many of the observed properties (e.g. Mundt 1988; Hartigan 1989).

Probably the most enigmatic HH objects are the so-called low-excitation objects, the prototype of this class being HH 7-11 (Böhm, Brugel and Mannery 1980). HH 7-11 have radial velocities and line profiles indicative of shock velocities $\sim$ 100 km s^{-1}(Solf and Böhm, 1987), but their spectra show strong [O I] and [S II] lines characteristic of a low velocity ($\sim$ 30 km s^{-1}) shock. In principle, molecules could radiate much of the kinetic energy lost by gas entering the shock and help to produce a low-excitation spectrum. If

this process is important in low-excitation HH objects, then one would expect H_2 emission to arise from the same shock that produces the optical lines, and be spatially coincident with the optical emission in the low-excitation HH objects. Alternatively, H_2 line emission could form in oblique shocks that are entirely distinct from those exciting the optical lines (for example, if gas is entrained along the edges of an evacuated cavity), or be completely absent if none of the preshock gas is molecular and no molecules are formed on grains in the postshock flow.

Molecular hydrogen is a symmetric molecule and thus, has no dipole moment, so the easiest lines to detect in HH objects are the quadrupole S(0) and S(1) ($v = 1 - 0$) transitions near 2.2μ (e.g. Zealey Willimans, and Sandell 1984), and occasionally the flourescent ultraviolet lines when the extinction is small (e.g. Schwartz, Dopita, and Cohen 1985). Some HH objects (including HH 7-11, Burton *et al.* 1989) have H_2 emission with line ratios indicative of shock excitation. It has been difficult to compare H_2 observations with optical data due to the large ($\sim 8''$) apertures typically used in H_2 work. However, the recent development of near-infrared array detectors makes a detailed comparison of optical and molecular lines possible. Observing with an infrared array, Schwartz (1988) found that the H_2 emission from HH 43 was spatially coincident with the optical emission from that low-excitation object.

In this *Letter* we present nearly simultaneous images of HH 7-11 taken in the light of Hα, [S II], and H_2 S(1). The H_2 images were taken with the new SBRC infrared array at Kitt Peak, with the optical CCD images obtained one month after the IR images. Except for HH 11, the Hα and [S II] images are very similar to the H_2 image, suggesting that molecular gas is involved in the same shocks that produce the higher excitation optical lines. Bellow, we present the images and discuss the calibration procedure as well as possible interpretations for the existing data.

II. Observations and Data Reduction

The H_2, Hα, and [S II] images of HH 7-11 appear in Figures 1 and 2. The optical images were obtained using the TI 2 CCD on the Kitt Peak 2.1-meter telescope on 28-29 Dec, 1988. The CCD (binned to 400 × 400) had a scale of $0.39''$ per pixel, with a field of view of $2.5' \times 2.5'$. The Hα images were taken through a narrow filter that excluded the

neighboring [N II] lines. The [S II] filter was wide enough to include both the 6716 Å and the 6731 Å lines.

The infrared images [S(1) and K] were taken 1988 November 27-28 with the 58 × 62 SBRC array on the 2.1-meter telescope on Kitt Peak. A total of eighteen 5-minute exposures and one 10-minute exposure comprise the final co-added images in Figures 1 and 2. Bad pixels can be eliminated in the co-added image because adjacent exposures were shifted by a few seconds of arc with respect to one another. Various experiments to flatten the IR images indicated that the most uniform backgrounds were obtained by simply subtracting a median-filtered image of the six blank sky frames (with background levels adjusted to the same mean) taken with the same exposure time as the object frame. Photometry of the bright (K=7) stars used for flux calibration (see below) appears to be reproducible to 2% or so between images. The seeing was 1″ for the optical images and 2″ for the IR images.

The scale of 0.73″ per pixel on the array gives a field of view of roughly 45″ square. This is too small to include the entire HH 7-11 field, and care must be taken to combine the images correctly. In all but the extreme northwest image in the composite (where a telescope offset was needed to position the image) at least one of HH 7, SVS 13, or star 6 (see Figure 1) is visible, allowing the small images to be embedded into the composite. Images were shifted by the appropriate fractional pixel amount using the NOAO IRAF package "imshift", and then incorporated (co-added and averaged where they overlap) into the composite using "imcombine (threshold)". The most uncertain alignment was the combination of the images near HH 7 with those near SVS 13. The only way to connect these fields in to use HH 10, a nonstellar image, for alignment. This was accomplished by examining one-dimensional cuts across the images. The stellar images in the composite have seeing profiles indistinguishable from those in the original images. The total integration time for a given position in the final image depends on the number of individual images that have data at that point. The HH 7 area has roughly 45 minutes total exposure; HH 11 has 40 minutes, and the region to the northwest of SVS 13 has 15 minutes in all.

It is important to magnify the H_2 image to put it on the same scale in arcseconds per pixel as the optical images, and to check the rotation between the sets of images. Rotation and scale measurements cannot be done accurately using the HH 7-11 images owing to the

paucity of stars appearing in both the optical and H_2 images. Instead, we measured the scale and rotation of the H_2 and optical images of Cepheus A, which has several stars that can be used for this purpose. The H_2 and optical images coincide when the H_2 images are rotated by 1.9° and magnified by 1.87. We estimate that the final images in Figures 1 and 2 are aligned to ±1.0".

We used photometry of Feige 110 (chosen for its featureless continuum at optical wavelengths) to calibrate the fluxes of the HH objects. The K magnitude of Feige 110 was 12.67 (using Gl 406 as a standard star). This corresponds to flux of 3.39×10^{-16} erg cm^{-2} s^{-1} Å^{-1} (Rydgren *et al.* 1984) at K, which we assume to be the flux at S(1). We calibrated S(1) line fluxes by knowing the filter bandpass and measuring the S(1) counts for Feige 110. The above procedure assumes that the HH objects have no continuum and no lines except S(1) passed by the filter. Since the filter transmission peaks at 2.122μ with FWHM of 0.027μ, other emission lines do not contribute significantly to the observed counts. A large K/S(1) ratio identifies the presence of a continuum component to the flux. Burton *et al.* (1989) found HH 7 to be a pure emission-line source, and the K/S(1) photometry presented in Table 1 suggests that the other HH objects are similar in nature.

We observe 2.0×10^{-13} erg cm^{-2} s^{-1} at S(1) centering a 5″ aperture on HH 7, in excellent agreement with Burton *et al.* (1989), who found an S(1) flux for HH 7 of 1.8×10^{-13} erg cm^{-2} s^{-1} within a 5″ aperture. Zealey *et al.* (1984) observed 2.4×10^{-13} erg cm^{-2} s^{-1} using a 12″ beam centered just south of HH 7. Without correcting for a continuum component (which should be negligible for HH 7-11) they find 9.6×10^{-13} erg cm^{-2} s^{-1} from two overlapping beams that include HH 7. We measure 6.7×10^{-13} erg cm^{-2} s^{-1} within a 12″ aperture centered on HH 7. Systematic errors, such as the assumption of the same magnitude for Feige 110 at K and S(1), the flatness of the IR field, and uncertainties in the filter transmission curve dominate any statistical errors, which are a few percent or less for the HH objects. The fluxes in Table 1 should be good to 10%.

III. Discussion

The optical and H_2 images of HH 7-11 appear in Figures 1 and 2. Except for HH 11, which shows no H_2 (some faint, extended emission is visible in the direction of SVS 13 in Figure 1), the optical and H_2 emission are spatially coincident, implying that the H_2 is

not excited from entrainment along the sides of a cavity evacuated by SVS 13, but that it arises from the same shock that produces the optical lines.

HH 7 is distinctly bow-shaped in all the images, with the H_2 and [S II] images coinciding to within an arcsecond. HH 7 has a bright secondary emission peak within the bow on this [S II] image. This peak is also bright in Hα, but disappears at H_2 making it a much higher excitation object than the remainder of HH 7. HH 8 consists of two distinct knots, which have comparable brightnesses in Hα. However, the southeastern knot is considerably brighter than the northwestern knot in [S II] and H_2. The knots roughly coincide spatially except for HH 8SE, which is displaced 2″ to the east in [S II] (away from the exciting source) with respect to its Hα and H_2 photocenters. A clear gradient in excitation conditions also exists in HH 10, with the northern component bright in Hα and the southern portion bright in [S II]. The [S II] emission is also located to the east of the H_2 emission in this object. HH 11 does not have any H_2 emission although it is the brightest of all the objects in Hα. This knot has a much higher radial velocity than the other HH objects, and is more pointlike (cf. Solf and Böhm 1987).

HH 7 is bow-shaped, oriented in the sense of a bullet or a jet from the exciting star. The lack of any dense HCO^+ condensations near HH 7 argues for a jet interpretation, as does the presence of a second, higher excitation region of emission within the bow shock. This emission could come from jet gas cooling behind the jet's Mach disk. Hartigan (1989) has pointed out that the bow shock and Mach disk of a stellar jet should have comparable brightnesses for a wide range of initial conditions, and Raga (1989) has found Mach disk emission in his nonadiabatic jet models. The line ratios from this region would help to constrain the velocity and density of the putative jet. This information already exists, in principle, in the data presented by Solf and Böhm (1987).

In the absence of a transverse magnetic field, strong UV flux from the apex of a bow shock will dissociate any H_2 entering the shock, and molecular line emission will arise predominantly in the wings of the bow where the shock is more oblique. Such H_2 emission will have small line widths and small radial velocities (compared with the optical lines). However, Draine (1989) and Draine *et al.* (1983) showed that a "magnetic precursor" can heat and compress gas in front of a shock wave moving through a weakly ionized gas with transverse magnetic field B_o. A jet moving through a magnetized molecular medium could produce a substantial amount of H_2 emission from a magnetic precursor (even at

high velocities close to the apex of the bow shock). In this case, the H_2 lines are broader and have higher radial velocities than those expected in a bow shock model without a magnetic precursor, and the H_2 and optical emission should coincide spatially.

We adopted a very simplified jet model with a magnetic precursor in which the temperature and density grow linearly through the precursor from T_o, n_o to $T_m, n_m = 2no$, respectively, and then increase linearly through the shock until they reach their post shock values. Following Draine's (1980) analytical formulation, we find that a shock wave moving with a velocity $v_o = 100$ km s^{-1}in a molecular medium with a density $n_o \sim 600$ cm^{-3}, and ionization fraction $X_e \sim 10^{-5}$, a temperature $T_o \sim 10$ K, and a magnetic field $B_o \sim 70$ μG produces a magnetic precursor with a maximum temperature $T_m \sim 5000$ K and a width $L_m \sim 10^{16}$ cm. For these conditions, the shock front will have a width of $L_{sf} \sim 10^{14}$ cm (corresponding to a mean free path).

In order to get the intensities of the H_2 lines, we calculated the dissociation rates and population of the rotational-vibrational levels including collisions with electrons, and atomic and molecular hydrogen, throughout the precursor and shock front regions. The line ratios in Table 2 obtained with the simple model agree well with the 1-0 S(1) line intensity in Table 1 and the 1-0 S(1), 2-1 S(1) and 1-0 O(7) line intensities obtained by Burton *et al.* (1989). The optical spectrum of a shock with a magnetic precursor will have a lower excitation spectrum than a simple J-shock, since less energy is radiated in the optical lines when a precursor is present. The optical linewidths observed in HH 7 are large, and indicate a shock velocity of 130–150 km s^{-1}although the optical spectrum resembles a 30 km s^{-1}shock (Solf and Böhm 1987; Hartigan, Raymond and Hartmann 1987). The infrared emission and dissociation energy of H_2 cannot account for this discrepancy, but excitation of the ultraviolet Lyman and Werner bands by electrons could carry away enough energy. A detailed model is being developed in order to calculate the emission from a strong J-shock wave (with velocities around 100 km s^{-1}) with a magnetic precursor moving through a molecular medium.

The above model predicts that the gas should already be moving at ~ 50 km s^{-1}with respect to the ambient cloud when it enters the J-shock that produces the optical line. Hence, the velocity for HH 7 should be blue-shifted from the value predicted from shock models with a stationary medium. This removes the discrepancy Solf and Böhm (1987) observed between the radial velocities in HH 7, which are all blue-shifted, and the

predictions of the bow shock model, which include zero radial velocity for all orientation angles (Hartigan, Raymond and Hartmann 1987; Raga and Böhm 1986). A magnetic precursor also predicts a linewidth for HH 7 $\sim$ 50 km s^{-1}in H_2, close to that observed by Zinnecker *et al.* (1989). A J-shock with a magnetic precursor seems to be a promising way to explain the [O I] 63μm fluxes observed by Cohen *et al.* (1988) in HH 7.

Neither HH 8 nor HH 10 can be explained with a simple bow shock, since zero velocity is not included within the line profiles and the high radial velocity material does not occur closer to the star than the low radial velocity gas, as the bow shock models predict. Both objects have HCO^+ and H_2 S(1) emission that concentrate to the south of the objects, with higher excitation material to the north. The simplest explanation seems to be having a stellar wind from SVS 13 impact the side of a cavity, driving a shock into the high-density gas that gives rise to the HCO^+ and H_2 emission. The model is similar to a cloudlet model like that proposed by Rudolph and Welch (1988), but the shock surrounding the 'cloudlet' cannot be a simple bow shock. We see no easy way to understand the spatial separation of [S II] from the H_2 and Hα in these objects.

HH 11 is even more enigmatic. This object cannot be a simple bow shock for the same reasons given for HH 8 and 10. In addition, HH 11 has no associated H_2 emission. We agree with Solf and Böhm (1987) that this object is most easily explained as a second ejection from SVS 13, but the only way we can think of to explain the observed 170 km s^{-1}linewidth and low-excitation spectrum without forming strong H_2 emission would be to have a *very* strong pre-shock magnetic field ($\sim$ 1 mG) for this object.

No bright H_2 emission is visible on the other side of SVS 13. Faint [S II] emission is visible 40″ northwest of SVS 13, near a concentration of HCO^+ (Rudolph and Welch 1988) and a faint wisp of H_2 (see Figure 1). If an object as intrinsically bright as HH 7 were to exist within the area covered by our H_2 image it would have to be reddened by $\sim$ 1.7 magnitudes more than HH 7 at K, so $A_V \sim 20$.

IV. Conclusions

We have presented nearly simultaneous H_2, S(1), [S II], and Hα images of the set of low-excitation HH objects HH 7-11. These images show that H_2 emission occurs in the same shocks that produce the optical lines in HH 7, 8, and 10. The existing data on HH 7

can be explained by a simple Mach disk/bow shock configuration at the end of the stellar jet, provided the preshock medium remains molecular in front of the jet. A magnetic precursor in front the J-shock probably excites the H_2 lines observed in HH 7. This model explains the anomalous blueshifted radial velocities seen in HH 7, and provides a means to reconcile the low-excitation optical spectrum with the large linewidth observed.

The objects HH 8 and HH 10 show peculiar excitation gradients, with the lowest excitation spectrum occurring to the south in both objects where wind from the exciting star appears to shock against the walls of an evacuated cavity. The spatial and velocity characteristics of the emitting gas reveal a geometry more complex than a simple bow shock or planar shock. HH 11 remains an enigma, and could represent a second major ejection from SVS 13. The low-excitation spectrum observed in this object is particularly difficult to explain since HH 11 has no visible H_2 emission.

Acknowledgments

It is a pleasure to acknowledge John Booth and Grace Wolf of the KPNO staff for their assistance with data acquisition, and Mike Merrill and Ron Probst for advise conserning data reduction. We are grateful to Ian Gatley and Williams Zealey for communicating their results prior to publication, and to Emilio Falco for his assistance in obtaining hard copies of the images presented in this paper.

References

Böhm, K.-H., Brugel, E.W., and Mannery, E. 1980. *Ap. J. (Letters)*, **235**, L137.

Böhm, K.-H., Brugel, E.W., and Olmsted, E. 1983. *Astr. Ap.*, **125**, 23.

Brand, P.W.J.L., Moorhouse, A., Burton, M.G., Geballe, T.R., Bird, M., and Wade, R. 1988. *Ap. J. (Letters)*, **334**, L103.

Burton, M.G., Brand, P.W.J.L., Geballe, T.R. and Webster, A.S. 1989. *MNRAS*, **236**, 409.

Cohen, M., Hollenbach, D.J., Hass, M.R., and Erickson, E.R. 1988. *Astrophys. J.* **329**, 863.

Draine, B.T. 1989. *Astrophys. J.* **241**, 1021.

Draine, B.T., Roberge, W.G., and Delgarno, A. 1983. *Astrophys. J.* **264**, 485.

Hartigan, P. 1989. *Astrophys. J.* **339**, 987.

Hartigan, P., Raymond, J., and Hartmann, L. 1987. *Astrophys. J.* **316**, 323.

Mundt, R. 1988. *in Formation and Evolution of Low Mass Stars*, A.K. Dupree and M.T.V.T. Lago eds., (Dordrecht:Kluwer), p. 257.

Raga, A.C. 1989. *Astrophys. J.* , ., in press.

Raga, A.C., and Böhm, K.-H. 1986. *Astrophys. J.* **308**, 829.

Rudolph, A., and Welch, W.J. 1989. *Astrophys. J. Lett.* **326**, L31.

Rydgren, A.E., Schmelz, J.T., Zak, D.S. and Vrba, F.J. 1984. *Publ. U.S.N.O.*, **25**, No. 1.

Schwartz, R.D. 1983. *Ann. Rev. Astron. Ap.* **21**, 209.

Schwartz, R.D., Dopita, M.A., and Cohen, M. 1985. *Astrophys. J.* **90**, 1820.

Schwartz, R.D., Williams, P.M., Cohen, M., and Jennings, D.G. 1988. *Astrophys. J. Lett.* **334**, L99.

Shu, F.H., Adams, F.C., and Lizano, S. 1987. *Ann. Rev. Astron. Ap.* **25**, 23.

Solf, J. and Böhm, K.-H. 1987. *Astron. J.* **93**, 1172.

Zinnecker, H., Mundt, R., Geballe, T.R., and Zealey, W.J. 1989. *Astrophys. J.* **342**, 337..

Table 1

Photometry

Object	[a]K/H_2	S(1) Flux (10^{-13} erg cm^{-2} s^{-1})
Gl 406	12.1	–
Feige 110	15.3	–
HD 1160	12.3	–
HH 7 (12" aperture)	1.9	6.7
HH 7 (5" aperture)	–	6.7
HH 8 (8" aperture)	2.0	1.7
HH 10 (12" aperture)	2.2	2.5

[a] Ratio of counts in the K and H_2 S(1) images. The ratio is about 13 for most continuum sources, and roughly 2 for pure emission line objects.

Table 2

Line Fluxes[a] For HH 7

Line	This Paper	model	Burton *et al.*
1–0 S(1)	2.00(-13)	1.83(-13)	1.80(-13)
1–0 S(0)	–	5.57(-14)	4.38(-14)
2–1 S(1)	–	3.26(-14)	1.84(-14)
1–0 O(7)	–	1.83(-14)	1.94(-14)

[a] The fluxes are in ergs s^{-1} cm^{-2}.

Figure 1. H_2 S(1), [S II], and Hα images of the HH 7–11 region. HH 7, 8, and 10 are clearly visible in all three images. Positions of HCO^+ emission (Rudolph and Welch 1988) are marked with triangles; SSV 13, the bright infrared source in the H_2 image, is marked with a cross in the Hα image.

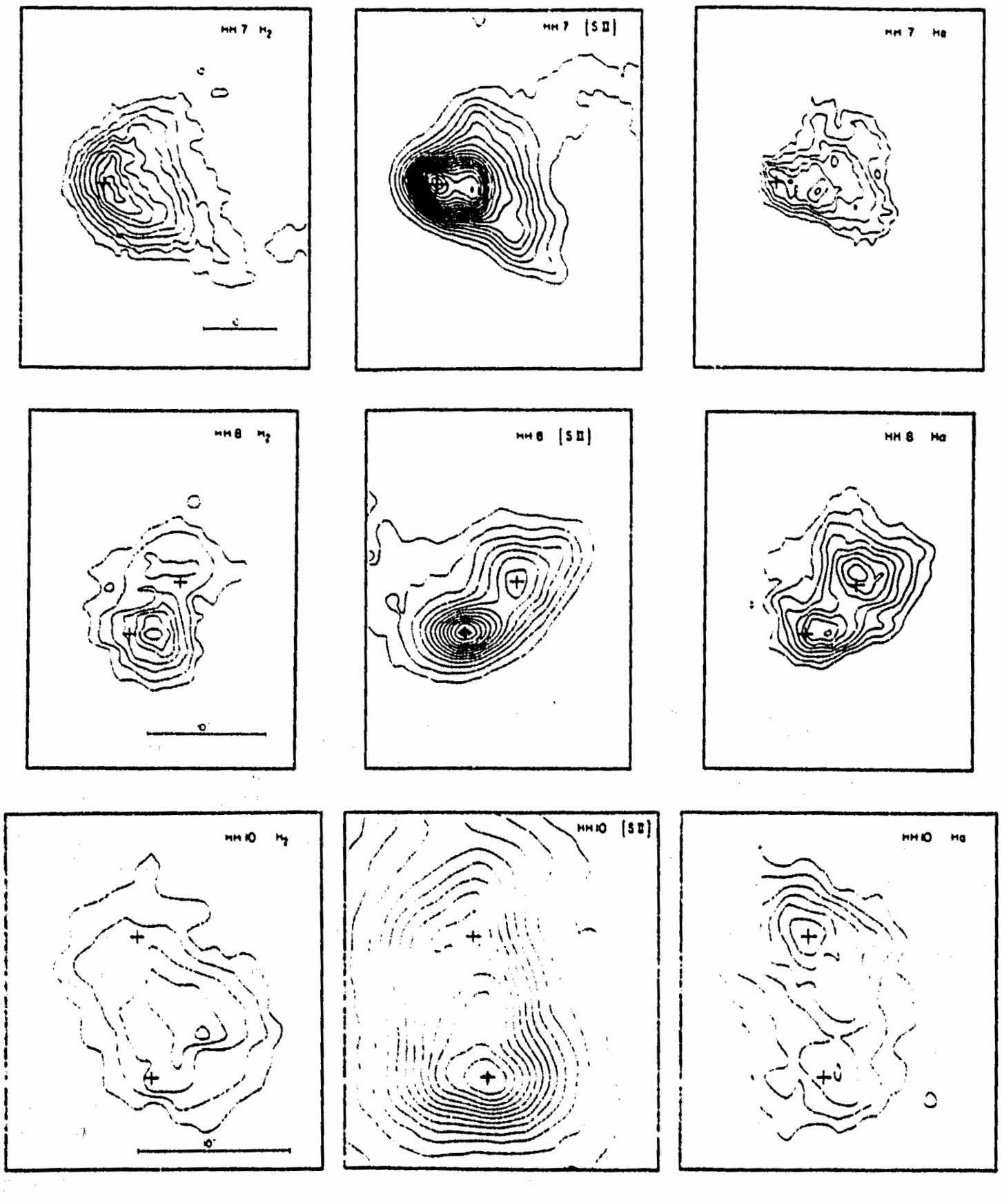

Figure 2. Contour plots of HH 7, 8, and 10 (cf. Figure 1). The contours are linear and range from the surrounding sky level to the maximum intensity in each image. Fiducial marks denote prominent emission peaks in one of the filters. Plots for a given HH object have the same spatial scale.

CHAPTER 4

MODEL FOR J-SHOCK WAVES WITH MAGNETIC PRECURSORS

I. Introduction

Low-excitation Herbig-Haro (HH) objects are a particularly interesting phenomenon due to their peculiar spectral characteristics. HH7-11, for instance, have radial velocities and line profiles indicative of shock velocities ~ 100 km s^{-1}. However, the spectra show strong [O I] and [S II] lines characteristic of a low velocity ($\sim$30 km s^{-1}) shock (*e.g.*, Hartigan *et al.* 1987). In principle, molecules could radiate much of the kinetic energy lost by the gas entering the shock and thus, help to produce a low-excitation spectrum. If this process is important in low-excitation HH objects, then one would expect H_2 emission to arise from the same shock that produces the optical lines, and for it to be apatially coincident with the optical emission in the low-excitation HH object. Alternatively, H_2 line emission could form in oblique shocks that are entirely distinct from those exciting the optical lines (for example, if gas is entrained along the edges of an evacuated cavity), or be completely absent if none of the pre-shock gas is molecular and no molecules are formed on grains in the post-shock flow.

H_2 emission has been detected in a number of low-excitation HH objects such as HH7-11, 43, 47 and 12, as well as several high-excitation HH objects such as HH1-2 and Cepheus A/GGD 37. A review of molecular emission in HH objects is presented in Chapter 1 (Curiel 1992; see also references therein). High-resolution infrared spectral observations of HH objects have shown that H_2 lines are much narrower than optical lines (see Chapter 1, and references therein). In particular, the 1-0S(1) line has typical widths of $\sim$50 km s^{-1} while the width of the H_α line in the same object is typically of the order of 100 km s^{-1} or greater (*e.g.*, Zinnecker *et al.* 1989). Imaging of HH objects with infrared and optical detectors is a very useful technique to establish the shock type and geometry of individual objects. Infrared observations have shown that H_2 line emission in HH objects presents a wide and complex variety of morphologies, being in

most of the cases similar to those observed at optical wavelengths. Since H_2 and optical lines trace different components of the shocked gas, they provide important complementary information which can be compared with predictions of theoretical models for shock waves. From this information, physical parameters can be derived for the gas that yields both H_2 and optical emission from the same object.

Bow-shock models applied to HH7-11, using pre-shock velocities of $\sim$30 km s^{-1}, accurately predict observed optical characteristics (Hartigan *et al.* 1987). However, the observed line widths (100–120 km s^{-1}) are much too large for the 30 km s^{-1} bow shock. Using a combination of J and C-shocks, Cohen *et al.* (1988) were able to explain the [OI] lines at 6300 Å and 63 μm, and the 1–0 S(1) H_2 emission observed in HH7–11, T Tau, HH42A, and HH43. In the case of HH7–11 they used velocities of 40 and 26 km s^{-1}, and densities of 4100 and 10,000 cm^{-3} for the J and C-shocks, respectively. However, the combination of J and C-shocks does not explain the $\sim$50 km s^{-1} width for the 1–0 S(1) line (Zinnecker *et al.* 1989) observed in this low-excitation objects.

Standard models of interstellar shocks produce either strong H_2 emission (magnetically controlled C-shocks) or strong optical and UV emission (J-shocks), but not both. J-shocks with magnetic precursors have the advantage of producing strong optical, UV and infrared emission from the same shock wave; optical and UV lines are emitted mainly in the post-shock region while the H_2 lines arise from the precursor. However, up to now this possibility has not yet been explored. In this paper, we calculate the optical, UV, and infrared emission produced by such shock waves, assuming a very simplified structure for the magnetic precursor and calculating the post-shock region in detail. The simplified dynamical structure allows us to compute not only the intensity of H_2 lines emitted from the magnetic precursor but also to calculate the energy loss in this region, which will play an important role in the excitation of the spectrum emitted by the post-shock region. Furtheremore, as we will show further on Chapter 5, the simplicity of this model will allow us to construct bow-shaped shock waves, and based on them, to predict the infrared and optical morphology, and the spatially resolved and integrated line profiles for a jet moving through a magnetized molecular medium. In the present work, we present the atomic optical and infrared line intensities as well as those for infrared H_2 lines expected from plane-parallel models of J-shocks with magnetic precursors. The plane-parallel model is presented in section II, and the results for a number of initial conditions are given in section

III. Finally the main conclusions are presented in IV.

II. Model

a) Magnetic Precursor

Shock wave models with magnetic precursors were initially developed by Draine (1980). Provided that the gas is largely neutral and the shock velocity is less that the ion-magnetic speed, a precursor of compressed magnetic field and electrically charged particles coupled to it moves through the gas upstream of the main shock transition. Interactions equivalent to friction between the ionized and neutral particles transfer momentum and energy from the charged particles to the neutral ones. As long as the gas is sufficiently cooled by the molecules, the heating and compression of the gas yield infrared spectral lines at wavelengths near 2 μm. Close to the J-shock, H_2 Lyman and Werner bands may be excited by hot electrons producing a substantial amount of H_2 UV emission. Finally when the temperature rises enough to destroy hydrogen molecules, the cooling efficiency drops sharply, the temperature rises quickly, and a rapid transition to the post-shock conditions occurs. Under these conditions, the H_2 emission arises from the magnetic precursor while the optical lines are emitted mainly by the gas behind the shock front.

A necessary condition for a shock wave to occur in an initially quiescent medium is that a compressive disturbance be advancing into the medium at a speed greater than the characteristic "signal speed". Otherwise, the signal will travel ahead of the disturbance and the shock will not be formed. In a partially ionized medium with a magnetic field there are two characteristic speeds at which compressive disturbances may propagate through the gas. In the neutral component of the gas, the disturbances travel at the neutral sound speed, given by

$$C_n = \left(\frac{\gamma k T_n}{\mu_n}\right)^{1/2} = 0.29 \left[\frac{\gamma (T_n/10k)}{\mu_n/m_p}\right]^{1/2} \quad km\ s^{-1}, \tag{1}$$

where T_n, μ_n and γ are the temperature, the mean molecular weight, and the adiabatic exponent of the neutral component, respectively. Compressive disturbances in the charged

component of the gas, propagating perpendicular to the magnetic field B, travel at the Alfvén speed, given by

$$v_{ims} = \left(\frac{B^2}{4\pi\rho_i}\right)^{1/2} = 218\left[\frac{B_{-6}^2}{n_H(x_i/10^{-4})(\mu_i/m_p)}\right]^{1/2} \quad km\ s^{-1}, \tag{2}$$

where B_{-6} is in microGauss (μG), n_H is the number density of hydrogen nuclei, ρ_i and μ_i are the mass density and the mean weight of the ionized gas, and x_i is the ionization fraction in the gas. The magnetosonic speed v_{ims} will be greater than the shock velocity v_s when the magnetic field is stronger than a minimum value B_{min}, given by

$$B_{min} = 0.46\left[n_H v_7^2(x_i/10^{-4})(\mu_i/m_p)\right]^{1/2} \quad \mu G, \tag{3}$$

When a shock wave is "supermagnetosonic", *i.e.*, the shock velocity v_s is greater than both characteristic velocities C_n and v_{ims}, a J-shock occurs and no magnetic precursor is formed, as in the case of a single fluid shock. On the other hand, if the shock wave is "supersonic" ($v_s > C_n$) but "submagnetosonic" ($v_s < v_{ims}$), three types of shock waves may be formed: 1) C-type shock, 2) J-type shock with magnetic precursors (*e.g.*, Draine 1980), and 3) C*-type shock (Chernoff 1987; Roberge and Draine 1990). In all three cases the charged fluid is accelerated upstream from the neutrals, and ion-neutral streaming motions occur throughout a "magnetic precursor" (Mullan 1971; Draine 1980). In the C-type shock, the neutral fluid remains supersonic (in the frame of reference where the shock front is stationary), and no discontinuity is present so that, all the flow variables (neutral and ionized components) vary continuously throughout the shock transition (Draine 1980; Draine, Roberge and Dalgarno 1983; Flower *et al.* 1985). The second class of shock waves resemble single fluid shocks in that there is a "jump" transition in which molecular viscosity effects produce an irreversible change in the variables of the neutral component on a length of the order of the neutral mean free path. However, ahead of the J-shock the neutral gas is accelerated and heated by collisions with the ions forming a magnetic precursor. As in the case of a neutral single shock, the neutral gas is supersonic upstream from the J-shock but subsonic immediately downstream from the shock. Under some circumstances, however, the transition from supersonic to subsonic motions may occur smoothly instead of through

a jump in the flow variables; such transonic shocks have been referred to as C*-type shocks (Chernoff 1987; Roberge and Draine 1990).

The different classes of Magneto-Hydrodynamic (MHD) shocks differ significantly in their degree of computational difficulty. The super-magnetosonic J-type is relatively easy to compute, since the ordinary differential equations describing a steady state, plane-parallel shock can be integrated as an initial value problem (*e.g.*, Raymond 1979; Shull and Hollenbach 1979). The C-type shocks are also relatively easy to compute following a similar method, but in this case, a small perturbation to the pre-shock flow variables is introduced, and the MHD equations are integrated directly through the shock structure (Draine 1980; Flower, Pineau des Forests and Hartquist 1985). In both cases there are no critical points in the flow, and the integration is numerically stable. There can be some difficulties associated to the treatment of the chemistry, heating and cooling, but there are no numerical obstacles presented by the hydrodynamics. C*-type shocks are somewhat more difficult to compute because the neutral flow gas goes from a supersonic to a subsonic state through a sonic point. "Shooting" techniques can be employed to determine the flow structure in the subsonic region (Roberge and Draine 1990). Finally, J-shocks with magnetic precursors are the most difficult ones from a numerical point of view. In this case, the main problem is that the location of the jump front cannot be known ***a priori*** since its position is determined by the flow parameters far downstream in the post-shock region. This problem has been discussed by Chernoff (1987) and Roberge and Draine (1990).

b) Structure of the Magnetic Precursor

In this section, the magnetic precursor structure is calculated following Draine's (1980) analytical formulation. Assuming a strong J shock with $\rho v^2 \gg B_0^2/8\pi$, an ion mass density significantly less than the neutral mass density, and a shock velocity less than the ion magnetosonic speed, the characteristic length scale over which the magnetic field is compressed is the damping length L,

$$L \approx \frac{(\mu_i + \mu_n)B_0^2}{\pi \rho_i \rho_n < \sigma v >_{in} v_s} \quad cm, \tag{4}$$

where μ_i is the ion mass and μ_n is the neutral particle mass, B_0 is the pre-shock field, and

ρ_i and ρ_n are the upstream ion and neutral mass densities, and the rate $< \sigma v >_{in}$ specifies the momentum transfer rate between ions and neutrals (Draine 1980). Using $< \sigma v >_{in} = \mid v_i - v_n \mid \times 10^{-15}$ cm^3 s^{-1}, and $v_i - v_n \approx v_s/2$, which is valid for velocities higher than $\sim$20 km s^{-1} (Draine 1980),

$$L \approx 3.8 \times 10^{16} \frac{B_{-6}^2}{x_{i-4} x_n n_H^2 v_7^2 (\mu_{in}/m_H)} \ cm, \tag{5}$$

where v_7 is the shock velocity in 100 km s^{-1}, $x_{i-4} = x_i/10^{-4}$, and μ_{in} is the ion-neutral reduced mass.

The temperature will increase steadily in the precursor over the length L up to some fraction of the post-shock temperature so that there may be a substantial column of vibrationally excited H_2 ahead of the shock. The heating rate (or energy dissipation rate) of the neutrals gas per unit volume, due to ion-neutral scattering Γ is

$$\Gamma \approx \frac{\rho_i \rho_n < \sigma v >_{in} v_s^2}{2(\mu_i + \mu_n)} \ erg \ cm^{-3} s^{-1}, \tag{6}$$

and the energy dissipation rate per unit area of the shock ΓL is

$$\Gamma L \approx \frac{B_0^2 v_s}{2\pi} \ erg \ cm^{-2} s^{-1}. \tag{7}$$

The maximum temperature of the neutral gas can be calculated assuming that the change in temperature is due to the difference between the heating Γ and the cooling Λ acting over a distance L (or heating timescale L/v_s), *i.e.*,

$$\frac{\rho_n v_s}{\mu_n} \left[\frac{3}{2} k (T_{n,max} - T_{n0}) \right] \approx L \left[\Gamma - \Lambda(T_{n,max}) \right] \ erg \ cm^{-2} s^{-1}. \tag{8}$$

This expression provides an implicit equation for the maximum temperature $T_{n,max}$ in the magnetic precursor:

$$T_{n,max} \approx T_{n0} + \frac{2\mu_n L}{3\rho_n v_s k}\left[\frac{B_0^2 v_s}{2\pi L} - \Lambda(T_{n,max})\right] \quad K, \tag{9}$$

$$T_{n,max} \approx T_{n0} + 772.9\frac{L_{16}}{v_7 n_n}\left[\frac{B_{-6}^2 v_7}{L_{16}} - \frac{\Lambda(T_{n,max})}{1.6\times 10^{-22}}\right] \quad K, \tag{9'}$$

where the damping distance is in units of 10^{16} cm, and the cooling rate Λ is evaluated at $T_{n,max}$. This transcendental equation can be solved when the cooling rate is known as a function of density and temperature. Since only molecular shocks are being taken into account, the cooling rate given in Chapter 2 can be used to calculate the maximum temperature in the precursor.

According to Draine (1980) (Figures 2 and 3), the temperature increases steadily in the precursor, and a linear function for the temperature does not seem to differ much from the detailed calculations. Therefore, the temperature is assumed to grow linearly throughout the precursor from $T_{n,0}$ to $T_{n,max}$.

Since the maximum deceleration (in a frame of reference where the J-shock is at rest) and compression of the ionized and neutral components of the flow in the precursor can only be obtained through detailed calculations, an arbitrary assumption has to be made. We have adopted a maximum compression fraction of two in the precursor, which seems to be a representative value for intense magnetic fields and very low ionization fractions (see Draine 1980). The velocity can be obtained from the mass transfer equation $\rho v = \rho_0 v_0$.

The shock transition in a J-shock is usually taken to be infinitesimally thin. However, significant destruction of molecules and radiation may occur in the shock front. This motivates the inclusion of the shock front in the present calculations. An approximate description of strong collisional shock fronts is provided by the Mott-Smith (1951) model. In this model, two interpenetrating Maxwellian distributions with fixed temperatures, representing the shocked and unshocked fluids, interact via collisions which transfer particles from the unshocked to the shocked distributions. The shock thickness Δ_s is of the order of the mean free path,

$$\Delta_s \approx \frac{1}{n_s \sigma} \ , \tag{10}$$

where n_s is the density of the shocked fluid, and σ is the effective hard sphere cross section. In a weakly ionized gas ($x_e \sim 10^{-2}$) the large ion-atom cross section keeps the ions and atoms at nearly the same velocity (Jaffrin 1965). For instance, $\sigma_{cex} \approx 5{\times}10^{-15} T_4^{-0.16}$ cm^2 for the H-H$^+$ charge exchange cross section when the temperature is in the range $0.1 \lesssim T_4 \lesssim 100$ (Dalgarno 1960), where $T_4 \equiv \mathrm{T}/10^4$ K. However, in a very weakly ionized gas ($x_e \lesssim 10^{-4}$) neutral-neutral collisions predominate over charge exchange processes. In this case, the collision cross section for hydrogen atoms is $\sigma_c = \pi a_0^2 \approx 10^{-16}$ cm^2 (Clausius 1858), where $a_0^2 \approx 0.5{\times}10^{-8}$ is the first Bohr orbit.

The length scale for a chemical process with rate coefficient, κ, may be defined as:

$$L_{chem} \approx \frac{v_s}{n\kappa} \ , \tag{11}$$

where n is the local density of hydrogen nuclei. Under certain conditions the length scale for some chemical processes may be lower than the size of the shock front. For instance, the length scale of the reactions $C + H_2 \rightarrow H + CH$ and $O + H_2 \rightarrow OH + H$ are of the order of 6-7$\times10^{13}$ cm, for $n = 100$ cm^{-3}, $v_s = 100$ km s^{-1}, and $T = 10^4$ K, while $\Delta_s \sim 10^{14}$ cm. Temperatures of this order, and even higher, are expected in the shock front. This indicates that if hydrogen molecules reach the shock front, they may be dissociated in this region via chemical reactions. Likewise, some infrared emission may be produced in this region. The chemical reaction network used in these calculations is similar to that used by Hollenbach and Mckee (1989). The reaction network and rate coefficients are listed in Table 1.

In order to investigate the optical, ultraviolet and infrared emission produced by J-shocks with magnetic precursors, a very simplified plane-parallel shock wave model has been adopted. In the present treatment of molecular shocks, the shock wave is divided in three main regions: 1) magnetic precursor, 2) shock front, and 3) post-shock region. For the first two regions a very simplified model is adopted in which the temperature and density grow linearly through the precursor from initial values T_0, n_0 to their maximum

values n_m, T_m and then increase linearly through the shock front until they reach their post-shock values (T_s and n_s). Here $n_m = 2n_0$ and T_m is given by equation (9). In the third region, the post-shock region, the atomic shock code developed by John Raymond (see Raymond 1976; Raymond 1979) has been used to follow the gas down to a temperature of about 600 K.

c) Calculation of the Line Strengths

In order to calculate the intensity of the H_2 lines, the population of the vibrational-rotational levels of this molecule is calculated in detail, including collisions with electrons, and atomic and molecular hydrogen, throughout the precursor and shock front regions. The processes included in these calculations are described in Chapter 2.

H_2 line and continuum emission processes following both collisional excitation of the $X\Sigma$ state as well as collisional-pumping and fluorescence through the $B\Sigma$ and $C\Pi$ states, contribute to the emission from the precursor and shock front regions. In the present calculations only collisional processes are taken into account. The processes included to calculate the population of the H_2 vibrational-rotational levels are presented in Chapter 2. The wavelengths of the H_2 infrared lines as well as H_2 ultraviolet lines and continuum were calculated as described in Appendix D in Chapter 2.

The intensity of the H_2 infrared lines produced by a magnetic precursor is derived by integrating the equation

$$\frac{dI(vj \rightarrow v'j')}{dx} = \frac{1}{4\pi} n_{vj} A(vj \rightarrow v'j') \Delta E(vj \rightarrow v'j') \ \ ergs\ s^{-1} cm^{-3} sr^{-1}, \qquad (12)$$

where vj and $v'j'$ are the upper and lower rotational-vibrational levels of the transition, n_{vj} is the density of level vj, $\Delta E(vj \rightarrow v'j')$ is the transition energy, and $A(vj \rightarrow v'j')$ is the radiative transition rate given by Turner, Kirby-Docken and Dalgarno (1977). These forbidden transitions in H_2 are so intrinsically weak that self-absorption in a line can be ignored.

The intensity of the H_2 ultraviolet emission lines, in the optically thin limit, produced

by collisions with hot electrons in a magnetic precursor is derived by integrating the equation

$$\frac{dI(v^*j^* \rightarrow v'j')}{dx} = \frac{1}{4\pi}\sum_{vj} n_{vj} n_e P_e(vj \rightarrow v^*j^*) b(v^*j^* \rightarrow v'j') \times \Delta E(v^*j^* \rightarrow v'j') \ \ ergs\ s^{-1}cm^{-3}sr^{-1}, \tag{13}$$

where vj and v^*j^* are the rotational-vibrational levels in the ground $X\Sigma$ and excited $B\Sigma$ and $C\Pi$ electronic state, respectively, n_e is the electron density, n_{vj} is the density of level vj, and the summation extends over all vj levels with permitted transitions to the v^*j^* levels (see Apendix D in Chapter 2). Here, $\Delta E(v^*j^* \rightarrow v'j')$ is the transition energy, $P_e(vj \rightarrow v^*j^*)$ are the collisional excitation rates out of level vj, and $b(v^*j^* \rightarrow v'j')$ is the branching ratio of the transition (see Chapter 2).

The intensity of the H_2 ultraviolet continuum, in the optically thin limit, produced by collisions with hot electrons is derived by integrating the equation

$$\frac{dI(v^*j^* \rightarrow f)}{dx} = \frac{1}{4\pi}\sum_{vj} n_{vj} n_e P_e(vj \rightarrow v^*j^*) \eta(v^*j^*) \times \Delta E(v^*j^* \rightarrow f) \ \ ergs\ s^{-1}cm^{-3}sr^{-1}, \tag{14}$$

where vj and v^*j^* are the rotational-vibrational levels in the ground $X\Sigma$, and excited $B\Sigma$ and $C\Pi$ electronic states, respectively, n_e is the electron density, n_{vj} is the density of level vj, and the summation extends over all vj levels with permitted transitions to the v^*j^* levels (see Apendix D in Chapter 2). Here, $\Delta E(v^*j^* \rightarrow f) = E_{v^*j^*} - E_f$ is the transition energy, $E_f = 4.48$ eV is the the energy of the vibrational continuum ($v > 14$), $P_e(vj \rightarrow v^*j^*)$ are the collisional excitation rates out of level vj, and $\eta(v^*j^*)$ is the dissociation fraction out of level v^*j^* (see Chapter 2).

d) Computational Method

The magnetic precursor is divided into a number of cells, the parameters of the gas (density, temperature, and velocity) being calculated at each cell according to the adopted

linear dependency. At each cell in the precursor, the chemical reactions and the H_2 level population and line emission are calculated in the following sequence. The coupled set of differential equations governing the chemical evolution of the molecular gas is stiff in the sense of having normal modes which decay at a wide range of different rates. They are integrated using the GEAR algorithm (Gear 1971), a predictor-corrector scheme with a variable step-size for which a well-tested computer program has been written and is widely used. After each integration of the chemical equations, the level population of the hydrogen molecule is calculated in detail at equilibrium with the current temperature, using a matrix inversion technique. After the abundance and level populations of H_2 are obtained, the infrared and ultraviolet emission spectra from the current step are calculated and integrated to the previous steps. Once the parameters of the magnetic precursor are calculated, the post-shock structure is computed in detail. First, the post-shock parameters are obtained using the Ranking-Hugoniot conditions for a magnetized medium. Then, the integration of the hydrodynamic equations and the spectrum emitted in this region are obtained as described by Raymond (1976) and Raymond (1979). In the magnetic precursor, the UV radiation from the post-shock region is ignored. This approximation may not be accurate, specially for the higher velocities ($v_s > 100$ km s^{-1}), since UV radiation emitted from the cooling post-shock region may dissociate or even ionize the gas before it reaches the shock front, suppressing the magnetic precursor.

III. Results and Discussion

a) Initial Parameters

The abundances used in the shock models are given in Table 2. These abundances were fixed to have "cosmic" values in all models: [He]=10.93, [C]=8.53, [N]=7.96, [O]=8.82, [Ne]=7.96, [Mg]=7.52, [Si]=7.60, [S]=7.20, [Ar]=6.90, [Ca]=6.30, [Fe]=7.60, and [Ni]=6.30, where the abundance of element X is $10^{[X]-12}$. For the molecular pre-shock region, carbon monoxide and atomic carbon were assumed to have comparable abundances, and about 15% of the carbon is assumed to be in CH molecules. The initial oxygen is taken to be 30% in OI, 20% in CO, and about 50% in OH, O_2, and H_2O, having similar fractions. The fractional ionization in the pre-shock gas depends upon the density in the molecular cloud. In diffuse clouds where the density is $\sim 10^2$ cm^{-3}, ambient ultraviolet radiation ionizes the metals (*e.g.*, Draine 1980). The models given in Table 3 were calculated using

the following pre-shock "standard" initial conditions: a) ambient density of $n_H = 300$ cm^{-3}; b) an ionization fraction of $x_e \equiv n_e/n_H = 10^{-5}$; c) molecular and atomic hydrogen fractions of $x(H_2) \equiv n(H_2)/n_H = 0.489$ and $x(H) = 2.19 \times 10^{-2}$; and e) cloud temperature of $T_0 = 10$ K.

With these "standard" initial conditions we have calculated the shock structure for shock velocities between 10 and 100 km s^{-1}, at 10 km s^{-1} intervals. In these models we also assume the presence of a pre-shock magnetic field of strength $B_{-6} = 0.7\ v_s$, where B is in μG and v_s is in km s^{-1}. The constant is set such that B = 70 μG when v_s = 100 km s^{-1}. This relationship between B and v_s is the expected dependency in a Bow-shock where B is the magnetic field perpendicular to the axis of symmetry. Under these conditions, the width of the precursor ($L \sim 10^{16}$ cm) and the Alfvén Mach number ($M_A = v_{ims}/v_s \sim 6$) remain constant in all models. This set of plane-parallel model is used in Chapter 5 to calculate line intensities and profiles, and morphologies expected from a Bow-Shock Model. In this chapter, the plane-parallel models are presented, and the main results are discussed in the following section.

We also investigate the effects of changing the assumed density, magnetic field, and ionization fraction. Since the shock velocity is restricted to be $C_s < v_s < v_{ims}$, we have chosen the following initial conditions for a second group of models: a) $nv_s = 3\times10^4$ cm^{-3} km s^{-1}; b) $nv_s^2 = 3\times10^6$ cm^{-3} (km s^{-1})^2; c) $B/nv_s = 2.3\times10^{-3}$ μG cm^3 (km s^{-1})$^{-1}$; d) $B^2/x_e = 1.2\times10^8$ μG; and e) v_s, B, and x_e constant. These conditions imply that the width of the precursor and/or the Alfvén Mach number remain constant (see eqs 2 and 5) for different initial parameters within the same group. These models allow a study of the emitted spectra for different parameters staying under the submagnetosonic condition. The initial parameters are chosen such that at least three models are obtained under each condition. These models are presented in Table 4 and the results will be discussed below.

b) Temperature in the Precursor

An approximate temperature profile in the magnetic precursor can be obtained by assuming that the change in temperature in the precursor is due to the difference between the heating of the neutral gas described by eq. (6) and the H_2 cooling, which dominates in molecular gas at low densities ($n_H \lesssim 2000$ cm^{-3}) and relatively high temperatures ($T \gtrsim$ 3000 K) (Hollenbach and McKee 1979). Therefore, the temperature profile is calculated by

using eq. (8) and the H_2 cooling rate given in Chapter 2. The results, shown in Figure 1, indicate that the linear dependence for the temperature adopted in this calculations does not differ substantially from that obtained numerically.

Tables 3 and 4 show that the maximum temperature T_m in the magnetic precursor is highly sensitive to the pre-shock initial conditions. T_m seems to increase with velocity and magnetic fields, and decrease with density. In particular, Table 3 shows that T_m can be fitted well by a power law when v/B is constant. It is found that $T_m \sim 7700\ v_7^{1.6}$ K, where the shock velocity is given in units of 100 km s^{-1}. These temperatures do not seem to have a simple dependence on the other shock parameters.

c) Atomic Lines

Figure 2 shows the effects of the shock velocity in the strength of optical and infrared lines. The UV lines are typically invisible at low velocities ($v_s \lesssim 50$ km s^{-1}) until v_s is high enough to produce the corresponding ion, and then they increase, with higher or comparable strength to the forbidden lines. Tables 3 and 4 show that in reducing the shock velocity, high-excitation UV lines such as SiIII λ1206, SiIII λ1896, and CIII λ1908 drop in strength with respect to H_β, while low-excitation lines such as [OI] λ6300/6363, [NII] λ6583/6548, and [SII] λ6716/6731 increase. This trend reflects the fact that the post-shock temperature drops with reducing shock velocity, diminishing H_β and favoring the emission of lines from atoms and ions with lower excitation energies (increasing the line ratios of [OI]/H_β, [NII]/H_β, [SII]/H_β, etc.). This result shows that low-velocity shock waves have low-excitation spectra and that the excitation of the spectra increases with the shock velocity.

Infrared atomic lines such as [FeII] $\lambda 1.64\mu$, and [SiII] $\lambda 35\mu$ have intensities comparable to H_β when $v_s \sim 100$ km s^{-1}, and increase monotonically with respect to H_β with decreasing shock velocities. For velocities lower than 60 km s^{-1}, these infrared lines are stronger than H_β and H_α, becoming the dominant lines in the spectra of such low velocity shock waves. It is important to mention that the atomic infrared lines may be stronger than the models predict since the integration in the post-shock region is halted when the gas temperature drops to values of the order of 600 K, and a considerable amount of IR emission may arise from the gas at lower temperatures (Hollenbach and McKee 1979).

Changes in the magnetic field and density also produce a substantial variation in the line ratios, reflecting the post-shock temperature dependence on these variables ($T_s \sim A_1 \times v_s^2$ - $A_2 \times B^2/n$, where A_1 and A_2 are constants). For given shock velocity and density, the intensity of the lines will depend mainly on the B^2/n ratio. Increasing the pre-shock density makes all lines brighter (the Hβ flux scales linearly with density) to different extents depending upon the other shock parameters. For instance, the intensity of most of the permitted UV lines with respect to Hβ increases with density when the other parameters are fixed (see models S100, N100 and N600), which reflects the fact that the B^2/n ratio reduces in value, and thus, the post-shock temperature increases, favoring the emission of UV lines. On the other hand, ratios of the forbidden optical and IR lines to Hβ are quite insensitive to this increase in density. Likewise, both permitted or forbidden line ratios to Hβ are insensitive to density when the latter varies simultaneously with either the ionization fraction or the magnetic field (see models S50 and NVV1000, or BNV1000 and BBX110). Increasing the magnetic field, reduces the compression and temperature of the post-shock gas, decreasing the emission of Hβ and UV lines.

d) Molecular Lines

In general, the 1-0S(1) line is stronger than H_β for most of the models considered in this work (see Tables 3 and 4, and Figure 2). As in the case of H_β, this line decreases monotonically when reducing shock velocity. However, the 1-0S(1)/H_β line ratio decreases with the velocity for $v_s \sim 100$ to 50 km s^{-1}, and then increases at lower values, indicating that this infrared line has a stronger dependence in the shock velocity than H_β. Lines emitted from excited vibrational levels exhibit a similar behavior to that observed in the 1-0S(1) line, while rotational lines increase monotonically when reducing shock velocity. The increase of the line strengths with respect to H_β at velocities lower than or about 50 km s^{-1} is due to the fact that the shock front has been taken into account in the present calculations. A characteristic temperature at which the 1-0S(1) line is emitted can be calculated by,

$$T_{1-0S(1)} = \frac{\Sigma T(x) j_{1-0S(1)}(x) \Delta x}{\Sigma j_{1-0S(1)}(x) \Delta x} \quad K, \tag{15}$$

where T(x) and j(x) are the local gas temperature and the emission rate of the 1-0S(1)

line at a cell x in the precursor (including the shock front), and Δx is the cell size. This temperature can be greater than the maximum temperature in the precursor (see Tables 3), indicating that in such case the emission rising from the shock front, for a given line, can predominate over that emitted in the precursor. In fact, the low 1-0S(1)/2-1S(1) line ratio at velocities lower than 50 km s^{-1} reflects the high temperatures in the shock front. Table 3 also shows that this line ratio has a maximum value of ~6 when v_s~70 km s^{-1}, and that if the shock front is not taken into account ($10s1_{s,h}$ and $21s1_{s,h}$), it increases monotonically from being ~3 for a shock velocity of 100 km s^{-1} to higher than 100 for v_s=10 km s^{-1}.

When infrared H_2 lines are compared to the 1-0S(1) line, they present two general behaviours according to their excitation energies with respect to the level from which the 1-0S(1) line is emitted (v=1 and j=3). Lines from lower excitation levels tend to increase monotonically in strength relative to the 1-0S(1) line when reducing shock velocity, reaching a maximum value and then decreasing with the velocity. Since the increase in the intensity of the rotational lines is the result of an increment in the population of these levels (due to the lower temperature in the precursor) and consequently a depopulation of vibrational-rotational levels, lines from high excitation levels decrease monotonically until they reach their lowest values with respect to 1-0S(1), and then increase once more when the contribution from the shock front (with higher temperatures than the precursor) starts diminating the emission. For instance, both 0-0S(3) and 1-0Q(1) lines reach a maximum with respect to 1-0S(1) at about 50 km s^{-1}, while 1-0S(3) and 2-1S(1) lines acquire minimum values at about 60 and 70 km s^{-1}, respectively. The turnover for the high-excitation lines (as well as the low-excitation lines) may occur at different velocities for different lines, depending on their excitation energies. The predicted line ratios at velocities higher than the turnover velocity depend mainly on the temperature in the magnetic precursor, while for lower velocities they depend mainly on the temperature in the shock front and on how fast the H_2 molecules are dissociated. These results show that the inclusion of the shock front region produces considerable changes in the intensity of the infrared H_2 line emission as well as in the relative intensity of rotational lines with respect to vibrational-rotational lines such as 1-0S(1).

Effects in the H_2 line emission due to changes in the pre-shock parameters are different and in general less conspicuous than those produced in the atomic lines. In this case, the

H_2 line fluxes reflect the dependency of the characteristic parameters of the magnetic precursor, such as the damping length L and the maximum temperature $T_{n,max}$, on the shock parameters. For instance, increasing only the density or magnetic field makes all lines weaker or brighter, respectively, but to different extents depending mainly upon the variation of the maximum temperature in the precursor. As mentioned above, higher temperatures produce stronger vibrational and weaker rotational lines, with respect to the 1-0S(1) line. The dependence on n_H and B is due to the fact that $L \propto n_H^{-2}B^2$, and $T_{n,max}$ depends weakly on these variables, while the intensity increases approximately with the density. Tables 3 and 4 show that in particular, the 1-0S(1) flux varies strongly with B, and decreases weakly with density.

The H_2 ultraviolet line and continuum emission expected from this type of shock wave was also calculated. The results indicate that within the span of parameters used in these calculations, the predicted intensity is too weak, by several orders of magnitude, to be detectable. The predicted H_2 UV emission cannot explain neither the UV continuum observed in objects such as HH1 and HH2, nor the H_2 UV lines observed in HH43 and HH47. These results will not be discussed further in this work.

e) Equivalent Shock Velocity and Energy Loss in the Magnetic Precursor

When a shock wave moves through a molecular medium, a considerable fraction of the available energy in the shock is dissipated by excitation and dissociation of the molecules (McKee and Hollenbach 1987). If the shock is strong enough to ionize the gas, a fraction of the energy is also dissipated by excitation and ionization of the atomic gas (Cox and Raymond 1985). This loss of energy reduces the excitation of the spectrum produced by the shocked gas. Therefore, the net result of this energy loss is that the spectrum obtained for a shock wave moving through a neutral medium with velocity v_s applies in reality to a shock moving through a molecular gas of an equivalent velocity v_{eqv} (Cox and Raymond 1985; McKee and Hollenbach 1987), given by

$$v_{eqv}^2 = v_s^2 + 2g_{H2}(0)v_{H2}^2, \tag{16}$$

where the velocities are given in km s^{-1}, $g_{H2}(0) = n(H_2)/n_H$, and v_{H2} is given by

$$\left[\frac{v_{H2}}{km\ s^{-1}}\right] \simeq 9.78 \left[\frac{R_{H2} + I_{H2}}{eV}\right]^{1/2}. \qquad (17)$$

Here, $I_{H2} = 4.48$ eV is the energy required to dissociate hydrogen molecules, and R_{H2} is the energy loss by excitation of H_2. This energy loss in the magnetic precursor and the equivalent velocity are given in Table 3, which shows that for the parameters considered here, v_{eqv} is typically about 10–15% greater than the assumed shock velocity. For instance, the expected atomic spectrum for a molecular shock wave moving at 100 km s^{-1} will be similar to that calculated for a 80–90 km s^{-1} shock wave (see models S90 and S80), while the corresponding H_2 spectrum will be that of the 100 km s^{-1} shock wave (see model S100). These results indicate that the characterictic spectrum observed in low-excitation HH objects and their high radial velocities might be the result of the energy loss by molecules in magnetic precursors. However, some objects such as HH7-11 exhibit high radial velocities of $\sim$ -60 to -180 km s^{-1}, while their extremely low-excitation spectra are characteristic of shocks with velocities of 20-30 km s^{-1}. The energy loss in the magnetic precursor can not take account of both, the extremely low-excitation spectra and the radial velocities, simultaneously. For instance, a shock wave moving at 100 km s^{-1} can explain the -60 km s^{-1} radial velocity observed in HH7, but the resultant spectrum (similar to that of a 80–90 km s^{-1} shock) is still far from explaining its extremely low-excitation spectrum. Since a bow-shaped shock wave has a variety of high and low-velocity shock waves, its spectrum will have a mixture of high and low-excitation lines. Therefore, a bow-shaped shock wave moving through a magnetized molecular medium could explain the characteristic spectrum observed in low-excitation HH objects. This possibility will be explored in Chapter 5.

f) Application to HH7 and The Cygnus Loop

The plane-parallel model has been used by Hartigan, Curiel and Raymond (1989; Chapter 3) to explain the intensity of H_2 lines observed in HH7. They obtain that a 100 km s^{-1} shock wave moving through a magnetized molecular medium can account for the observed H_2 line intensities. They have also proposed that the morphology and line profiles observed in this object at both optical and infrared wavelengths, could be explained by this type of model. This interpretation has recently been supported by new and independent

observations (Carr 1990; Stapelfeldt *et al.*1991). Based on morphological appearance and spatial distribution of optical and infrared emission, Stapelfeldt *et al.* (1991) have concluded that a magnetic precursor seems to be the origin of the infrared emission. Likewise, Carr (1990) concluded that the spatial distribution of the H_2 1-0S(1) line within this object is consistent with a bow-shaped shock wave morphology, and that the integrated line profile can be explained by a magnetic precursor preceding the bow-shock. A model based on this plane-parallel results will be used in Chapter 5 to study the morphological and line characteristics expected from a bow-shaped shock wave moving through a magnetized molecular medium, and the results will be applied in particular to the case of HH7.

Recently, Graham *et al.* (1991) detected faint infrared emission lines from vibrationally excited H_2 associated with the bright optical shock-excited filaments (both radiative and non-radiative) to the NE of the Cygnus Loop. They find that the H_2 level populations inferred from the 1-0S(2), 1-0S(1), 1-0S(0) and 2-1S(1) lines are consistent with a single rotational and vibrational excitation temperature $T_{ex} \simeq 2500$ K. This result implies that the excitation mechanism is collisional excitation in a shock wave (ruling out UV fluorescence and post-shock molecular formation as possible mechanisms). Graham *et al.* used a model similar to the one presented here to explain the observed H_2 surface brightness, level populations, and relation to optical emission in the Cygnus Loop. Likewise, they propose that a magnetic precursor can also account for the otherwise unexplained 20-30 km s^{-1} width of the narrow component of H_α from non-radiative shocks observed by Hester and Raymond (1988). Using parameters similar to those derived by Graham *et al.* (1991), we obtain similar surface brightness but with some important differences. Table 5 shows a comparison between the calculated surface brightness and those observed and calculated in the filament MH1 by Graham *et al.*. This table shows that for the 87 km s^{-1} shock velocity, both models predict the same 1-0S(1) surface brightness, whereas the 173 km s^{-1} model differs by an order of magnitude. This discrepancy might be due to differences in the calculations. For instance, this table shows that the maximum temperature obtained in the precursor by these authors is substantially higher than that obtained in the present calculations. They suggest that the 87 km s^{-1} model seems to be appropriate for the MH1 filament and that this model can account for the H_2 emission with a geometrical enhancement factor of about 30. The present results support the results of Graham *et al.*. However, the line ratios obtained with these calculations, are quite different from those observed. Further calculations will be needed to better explain

the H_2 line rations observed in these filaments of the Cygnus Loop.

IV. Summary and Conclusions

A plane-parallel model for J-shock wave with a magnetic precursors has been presented. It has been shown that this type of shock waves may produce a substantial amount of both molecular and atomic line emission from the same shock wave. This type of shock waves produces infrared H_2 line emission with comparable or even higher strength than atomic optical lines such as Hβ.

It has also been shown that when the shock front region is taken into account, the infrared H_2 lines can be considerably stronger than those expected when it is not considered. Likewise, ratios of H_2 lines to the 1-0S(1) line can change considerably when including the shock front.

The energy emitted by hydrogen molecules considerably reduces the "excitation" of the shock wave, *i.e.*, the atomic spectra will be equivalent to that of a lower shock wave. However, this alone is not enough to explain the extremely low-exciation character of HH7.

The line intensities predicted by this plane-parallel model can account for the observed H_2 line intensities in HH7. In the case of the Cygnus Loop, a geometric enhancement factor of about 30 is needed to explain the intensities observed in the filament MH1.

In a future paper (Chapter 5), the predicted infrared and optical morphology, and spatially resolved and integrated line profiles for a jet moving through a magnetized molecular medium will be presented. In particular, this model will be applied to the case of HH7.

REFERENCES

Curiel, S. 1992, in the Astrochemistry of Cosmic Phenomena (IAU Symposium No. 150), edited by P.D. Sing, *Submitted.*

Chernoff, D.F. 1987, *Ap. J.*, **312**, 143.

Cohen, M., Hollenbach, D.J., Haas, M.R., and Erickson, E.F. 1988, *Ap. J.*, **329**, 863.

Dalgarno, A. 1960, *Proc. Phys. Soc.*, **75**, 374.

Draine, B.T., 1980, *Ap. J.*, **241**, 1021.

Draine, B.T., Roberge, W.G., and Dalgarno, A. 1983, *Ap. J.*, **264**, 485.

Flower, *Ap. J. Suppl.*, **25**, 205.

Graham, J.R., Wright, G.S., Hester, J.J., and Longmore, A.J. 1991, *A. J.*, **101**, 175.

Hartigan, P. 1989, *Ap. J.*, **339**, 987.

Hartigan, P., Curiel, S., and Raymond, J. 1989, *Ap. J. (Letters)*, **347**, L31.

Hartigan, P., Raymond, J., and Hartmann, L. 1987, *Ap. J.*, **316**, 323.

Hollenbach, D., and McKee, C.F. 1979, *Ap. J. Suppl.*, **41**, 555.

Hollenbach, D., and McKee, C.F. 1989, *Ap. J.*, **342**, 306.

Jaffrin, M.Y. 1965, *Phys. Fluids*, **8**, 606.

Lang, K.R. 1980, *Astrophysical Formulae, Springer-Verlag Berlin Heidelberg*, pp 224

Mott-Smith, H. 1951, *Phys. Rev.*, **82**, 885.

Mullan, D.J. 1971, *MNRAS*, **123**, 145.

Raga, A.C. 1988, *Ap. J.*, **335**, 820.

Raga, A.C., and Böhm, K-H 1986, *Ap. J.*, **308**, 829.

Raymond, J.C. 1979, *Ap. J. Suppl.*, **39**, 1.

Raymond, J.C. 1976, *Ph.D. Thesis, University of wisconsin, Madison.*

Roberge, W.G., and Draine, B.T. 1990, *Ap. J.*, **350**, 700.

Shull, J.M., and McKee, C.F. 1979, *Ap. J.*, **227**, 131.

Stapelfeldt, K.R., Beichman, C.A., Hester, J.J., Scoville, N.Z., and Gautier III, T.N. 1991, *Ap. J. (Letters), in press.*

Zinnecker, H., Mundt, R., Geballe, T.R., and Zealey, W.J. 1989, *Ap. J.*, **342**, 337.

Table 1
(a) Neutral–Neutral Reactions

Reaction (1)	A[a] (2)	B[a] (3)	C[a] (4)
$H + H \rightarrow H^+ + H + e$	3.000(-13)	0.500	1.490(+5)
$He + H \rightarrow He^+ + H + e$	8.630(-14)	0.430	2.850(+5)
$He + H_2 \rightarrow He^+ + H_2 + e$	8.630(-14)	0.430	2.850(+5)
$C + H \rightarrow C^+ + H + e$	5.900(-13)	0.400	1.310(+5)
$C + H_2 \rightarrow C^+ + H_2 + e$	5.900(-13)	0.400	1.310(+5)
$C + H_2 \rightarrow CH + H$	4.500(-11)	0.500	1.560(+4)
$C + OH \rightarrow CO + H$	1.110(-10)	0.500	0
$C + H_2O \rightarrow CH + OH$	1.430(-10)	0.500	2.400(+4)
$C + O_2 \rightarrow CO + O$	1.800(-11)	0.500	0
$O + H \rightarrow O^+ + H + e$	3.040(-13)	0.490	1.580(+5)
$O + H_2 \rightarrow O^+ + H_2 + e$	3.040(-13)	0.490	1.580(+5)
$O + CH \rightarrow CO + H$	9.530(-11)	0.500	0
$O + CH \rightarrow C + OH$	1.730(-11)	0.500	4.000(+3)
$O + OH \rightarrow O_2 + H$	4.330(-11)	-0.500	3.000(+1)
$O + H_2O \rightarrow OH + OH$	1.350(-12)	1.750	7.860(+3)
$O + CO \rightarrow C + O_2$	2.900(-11)	0.500	6.930(+4)
$CH + H \rightarrow C + H_2$	1.800(-11)	0.500	4.000(+3)
$CH + H \rightarrow CH^+ + H + e$	8.830(-14)	0.500	1.290(+5)
$CH + H_2 \rightarrow CH_2 + H$	3.600(-10)	0	3.900(+3)
$CH + H_2 \rightarrow CH^+ + H_2 + e$	8.830(-14)	0.500	1.290(+5)
$CH + OH \rightarrow H_2O + C$	1.000(-10)	0	0
$CH_2 + H \rightarrow CH + H_2$	3.600(-10)	0	2.650(+3)
$CH3 + H \rightarrow CH_2 + H_2$	5.300(-12)	0	1.080(+4)
$OH + H \rightarrow O + H_2$	6.600(-13)	1.530	2.970(+3)
$OH + H \rightarrow OH^+ + H + e$	8.830(-14)	0.500	1.530(+5)
$OH + H_2 \rightarrow H_2O + H$	8.800(-13)	1.950	1.420(+3)
$OH + H_2 \rightarrow OH^+ + H_2 + e$	8.830(-14)	0.500	1.530(+5)
$OH + OH \rightarrow H_2O + O$	4.200(-12)	0	2.420(+2)
$H_2O + H \rightarrow OH + H_2$	7.440(-12)	1.570	9.130(+3)
$H_2O + H \rightarrow H_2O^+ + H + e$	7.550(-14)	0.450	1.470(+5)
$H_2O + H_2 \rightarrow H_2O^+ + H_2 + e$	7.550(-14)	0.450	1.470(+5)
$CO + H \rightarrow C + OH$	1.110(-10)	0.500	7.770(+4)
$CO + H \rightarrow CH + O$	9.530(-11)	0.500	8.830(+4)
$CO + H \rightarrow CO^+ + H + e$	1.130(-13)	0.600	1.630(+5)
$CO + H_2 \rightarrow CO^+ + H_2 + e$	1.130(-13)	0.600	1.630(+5)
$O_2 + H \rightarrow OH + O$	1.630(-09)	-0.900	8.750(+3)
$O_2 + H \rightarrow O_2^+ + H + e$	2.370(-15)	1.040	1.400(+5)
$O_2 + H_2 \rightarrow O_2^+ + H_2 + e$	2.370(-15)	1.040	1.400(+5)
$H_2 + H \rightarrow H + H + H$	3.400(-09)	0	4.390(+4)
$H_2 + H_2 \rightarrow H_2 + H + H$	5.500(-09)	0	5.190(+4)

[a] The reaction rate coefficients have the form $A(T/300\ K)^B e^{-C/T}\ cm^3\ s^{-1}$.

Table 1
(b) Ion–Neutral Reactions

Reaction (1)	A[a] (2)	B[a] (3)	C[a] (4)
$He + H^+ \rightarrow He^+ + H^+ + e$	8.630(-14)	0.430	2.850(+5)
$C + H^+ \rightarrow C^+ + H^+ + e$	5.900(-13)	0.400	1.310(+5)
$CH + H^+ \rightarrow CH^+ + H^+ + e$	8.830(-14)	0.500	1.290(+5)
$O + H^+ \rightarrow H + O^+$	7.000(-10)	0	2.320(+2)
$O + H^+ \rightarrow O^+ + H^+ + e$	3.040(-13)	0.490	1.580(+5)
$H_2 + H^+ \rightarrow H + H_2^+$	6.400(-10)	0	2.130(+4)
$CH + H^+ \rightarrow H + CH^+$	1.900(-09)	0	0
$OH + H^+ \rightarrow H + OH^+$	2.100(-10)	0	0
$OH + H^+ \rightarrow OH^+ + H^+ + e$	8.830(-14)	0.500	1.530(+5)
$H_2O + H^+ \rightarrow H + H_2O^+$	8.200(-09)	0	0
$H_2O + H^+ \rightarrow H_2O^+ + H^+ + e$	7.550(-14)	0.450	1.450(+5)
$CO + H^+ \rightarrow H + CO^+$	1.900(-10)	0	4.660(+3)
$CO + H^+ \rightarrow CO^+ + H^+ + e$	1.130(-13)	0.600	1.630(+5)
$O_2 + H^+ \rightarrow H + O_2^+$	1.200(-09)	0	0
$O_2 + H^+ \rightarrow O_2^+ + H^+ + e$	2.370(-15)	1.040	1.400(+5)
$H + He^+ \rightarrow He + H^+$	1.900(-15)	0	0
$H_2 + He^+ \rightarrow H + H^+ + He$	1.100(-13)	0	0
$H_2O + He^+ \rightarrow H + OH^+ + He$	2.860(-10)	0	0
$H_2O + He^+ \rightarrow OH + H^+ + He$	2.030(-10)	0	0
$H_2O + He^+ \rightarrow He + H_2O^+$	6.500(-11)	0	0
$CO + He^+ \rightarrow O + C^+ + He$	1.700(-09)	0	0
$O_2 + He^+ \rightarrow O + O^+ + He$	1.100(-09)	0	0
$H_2 + C^+ \rightarrow CH_2 +$	4.000(-16)	-0.200	0
$H_2 + C^+ \rightarrow H + CH^+$	2.000(-10)	0	4.640(+3)
$OH + C^+ \rightarrow H + CO^+$	7.700(-10)	0	0
$H_2O + C^+ \rightarrow H_2 + CO^+$	2.700(-09)	0	0
$O_2 + C^+ \rightarrow O + CO^+$	3.760(-10)	0	0
$O_2 + C^+ \rightarrow CO + O^+$	6.140(-10)	0	0
$H + O^+ \rightarrow O + H^+$	7.000(-10)	0	0
$H_2 + O^+ \rightarrow H + OH^+$	1.600(-09)	0	0
$H + H_2^+ \rightarrow H_2 + H^+$	1.000(-10)	0	0
$O + H_2^+ \rightarrow H + OH^+$	1.500(-09)	0	0
$H_2 + H_2^+ \rightarrow H + H_3+$	2.100(-09)	0	0
$H_2 + H_2^+ \rightarrow H_2 + H^+ + H$	4.170(-11)	0.500	3.070(+4)
$OH + H_2^+ \rightarrow H_2 + OH^+$	7.600(-10)	0	0
$H_2O + H_2^+ \rightarrow H_2 + H_2O^+$	3.900(-09)	0	0
$H_2O + H_2^+ \rightarrow H + H_3O^+$	3.400(-09)	0	0
$O_2 + H_2^+ \rightarrow O_2^+ + H_2$	2.700(-09)	0	0
$CO + H_2^+ \rightarrow H_2 + CO^+$	2.800(-09)	0	0

[a] The reaction rate coefficients have the form $A(T/300\ K)^B e^{-C/T}$ $cm^3\ s^{-1}$.

Table 1
(b) Ion–Neutral Reactions (cont.)

Reaction (1)	A[a] (2)	B[a] (3)	C[a] (4)
$H + H_3+ \rightarrow H_2 + H_2^+$	2.080(-09)	0	1.880(+4)
$H_2 + H_3+ \rightarrow H_2 + H_2^+ + H$	3.410(-11)	0.500	7.160(+4)
$H_2 + H_3+ \rightarrow H_2 + H^+ + H_2$	3.410(-11)	0.500	5.040(+4)
$O + H_3+ \rightarrow H_2 + OH^+$	8.000(-10)	0	0
$OH + H_3+ \rightarrow H_2 + H_2O^+$	1.300(-09)	0	0
$H_2O + H_3^+ \rightarrow H_2 + H_3O^+$	5.900(-09)	0	0
$CO + H_3^+ \rightarrow H_2 + CO^+$	1.700(-09)	0	0
$C + H_3+ \rightarrow H_2 + CH^+$	2.000(-09)	0	0
$H + OH^+ \rightarrow OH + H^+$	2.100(-09)	0	2.800(+3)
$H + OH^+ \rightarrow O + H_2^+$	1.600(-09)	0	2.260(+4)
$H + OH^+ \rightarrow H_2 + O^+$	4.900(-10)	-0.030	1.970(+3)
$H_2 + OH^+ \rightarrow OH + H_2^+$	7.600(-10)	0	2.360(+4)
$H_2 + OH^+ \rightarrow O + H_3+$	8.000(-10)	0	2.900(+3)
$H_2 + OH^+ \rightarrow H + H_2O^+$	1.100(-09)	0	0
$H + H_2O^+ \rightarrow H_2 + OH^+$	1.700(-09)	0.290	1.400(+4)
$H + H_2O^+ \rightarrow H_2O + H^+$	8.200(-09)	0	1.150(+4)
$H + H_2O^+ \rightarrow OH + H_2^+$	7.600(-10)	0	4.000(+4)
$H_2 + H_2O^+ \rightarrow OH + H_3+$	1.300(-09)	0	2.030(+4)
$H_2 + H_2O^+ \rightarrow H_2O + H_2^+$	3.900(-09)	0	3.270(+4)
$H_2 + H_2O^+ \rightarrow H + H_3O+$	6.100(-10)	0	0
$H + H_3O^+ \rightarrow H_2 + H_2O+$	6.000(-09)	0.390	1.980(+4)
$H + H_3O^+ \rightarrow H_2O + H_2^+$	3.400(-09)	0	5.250(+4)
$H_2 + H_3O^+ \rightarrow H_2O + H_3^+$	5.900(-09)	0	3.280(+4)
$H + CH^+ \rightarrow H_2 + C^+$	6.000(-10)	-0.250	0
$H_2 + CH^+ \rightarrow H + CH_2^+$	1.000(-09)	0	0
$H + CH_2^+ \rightarrow H_2 + CH^+$	1.000(-09)	0	1.200(+4)
$H_2 + CH_2^+ \rightarrow CH + H_3^+$	1.200(-09)	0	4.220(+4)
$O + CH_2 \rightarrow H + CO^+$	7.500(-10)	0	0
$H + CO^+ \rightarrow CO + H^+$	1.900(-10)	0	0
$H + O_2^+ \rightarrow O_2 + H^+$	2.800(-10)	-0.040	1.780(+4)

[a] The reaction rate coefficients have the form $A(T/300\ K)^B e^{-C/T}$ $cm^3\ s^{-1}$.

Table 1
(c) Electron Reactions

Reaction (1)	A[a] (2)	B[a] (3)	C[a] (4)
$e + H_2^+ \rightarrow H + H$	8.000(-08)	-0.500	0
$e + H_3^+ \rightarrow H_2 + H$	5.000(-09)	-0.500	0
$e + H_3^+ \rightarrow H + H + H$	5.000(-09)	-0.500	0
$e + OH^+ \rightarrow O + H$	2.000(-07)	-0.500	0
$e + H_2O^+ \rightarrow OH + H$	2.000(-07)	-0.500	0
$e + H_2O^+ \rightarrow O + H_2$	2.000(-07)	-0.500	0
$e + H_3O^+ \rightarrow H_2O + H$	1.000(-06)	-0.500	0
$e + H_3O^+ \rightarrow OH + H$	3.000(-07)	-0.500	0
$e + O_2^+ \rightarrow O + O$	2.000(-07)	-0.500	0
$e + CO^+ \rightarrow C + O$	1.800(-07)	-0.500	0
$e + CH^+ \rightarrow C + H$	3.000(-07)	-0.400	0
$e + CH_2^+ \rightarrow C + H_2$	2.500(-07)	-0.500	0
$e + CH_2^+ \rightarrow CH + H$	2.500(-07)	-0.500	0
$e + H \rightarrow H^+ + e + e$	1.000(-09)	0.500	1.580(+5)
$e + H_2 \rightarrow H_2^+ + e + e$	6.800(-11)	0.370	1.810(+5)
$e + H_2 \rightarrow H + H + e$	3.200(-09)	0.350	1.020(+5)
$e + He \rightarrow He^+ + e + e$	5.100(-10)	0.430	2.850(+5)
$e + O \rightarrow O^+ + e + e$	1.790(-09)	0.490	1.580(+5)
$e + C \rightarrow C^+ + e + e$	3.400(-09)	0.400	1.310(+5)
$e + OH \rightarrow OH^+ + e + e$	5.200(-10)	0.500	1.500(+5)
$e + H_2O \rightarrow H + OH + e$	9.200(-09)	-0.500	6.960(+4)
$e + H_2O \rightarrow H_2O^+ + e + e$	4.400(-10)	0.450	1.470(+5)
$e + O_2 \rightarrow O + O + e$	2.300(-09)	-0.500	6.960(+4)
$e + O_2 \rightarrow O_2^+ + e + e$	1.400(-11)	1.040	1.400(+5)
$e + CH \rightarrow CH^+ + e + e$	5.200(-10)	0.500	1.500(+5)
$e + CO \rightarrow CO^+ + e + e$	6.700(-10)	0.600	1.630(+5)
$e + CO \rightarrow C + O + e$	8.100(-10)	-0.500	1.140(+5)
$e + H^+ \rightarrow H$	6.000(-12)	-0.750	0
$e + C^+ \rightarrow C$	1.800(-12)	-0.620	0
$e + O^+ \rightarrow O$	1.800(-12)	-0.620	0
$e + He^+ \rightarrow He$	1.800(-12)	-0.620	0
$e + H \rightarrow H^-$	3.800(-16)	0.700	0
$H^- + H^+ \rightarrow H + H$	4.040(-08)	-0.500	0
$H^- + H \rightarrow H_2 + e$	1.810(-09)	-0.100	0

[a] The reaction rate coefficients have the form $A(T/300\ K)^B e^{-C/T}$ $cm^3\ s^{-1}$.

Table 2
Abundance Fractions

Element	fraction	Element	fraction	Element	fraction
H	2.19(-02)	H^+	1.00(-06)	H^-	1.00(-07)
H_2	4.89(-01)	H_2^+	1.00(-06)	H_3^+	0.00(+00)
He	1.00(-01)	He^+	1.00(-06)	C	1.40(-04)
C^+	1.00(-05)	CO	1.40(-04)	CO^+	1.00(-07)
CH	5.00(-05)	CH^+	0.00(+00)	CH_2	1.00(-07)
CH_2^+	0.00(+00)	O	2.00(-04)	O^+	0.00(+00)
O_2	1.50(-04)	O_2^+	0.00(+00)	OH	1.50(-04)
OH^+	0.00(+00)	H_2O	1.50(-04)	H_2O^+	0.00(+00)
H_3O^+	0.00(+00)	e	1.00(-05)		

Table 3
Shock Wave Models

	S100	S90	S80	S70	S60	S50	S40	S30	S20	S10
V_s (km s^{-1})	100	90	80	70	60	50	40	30	20	10
N_H $(cm-3)$	300	300	300	300	300	300	300	300	300	300
B_0 (μG)	70	63	56	49	42	35	28	21	14	7
X_e (10^{-5})	1	1	1	1	1	1	1	1	1	1
M_{A0}	6.23	6.23	6.23	6.23	6.23	6.23	6.23	6.23	6.23	6.23
L (10^{16} cm)	1.66	1.66	1.66	1.66	1.66	1.66	1.66	1.66	1.66	1.66
T_{max} (K)	7695	6749	5559	4749	3738	2735	1842	1102	557	196
T_{10S1} (K)	6486	6120	5724	5889	7147	10766	14920	14030	9093	2306
T_S (10^4 K)	27.17	22.01	17.39	13.31	9.78	6.79	4.35	2.45	1.09	0.27
E_{IR} (eV/part)	27.94	22.98	10.96	6.04	4.34	3.32	2.78	2.80	1.38	0.04
v_{H2} (km s^{-1})	55.69	51.25	38.43	31.72	29.05	27.31	26.35	26.39	23.67	20.79
v_{equ} (km s^{-1})	114.46	103.57	88.75	76.85	66.66	56.97	47.90	39.95	31.00	23.07
Hβ(flux)	12.5	8.98	6.03	3.77	2.15	1.05	.396	.079	7.0(-4)	6.0(-6)
1-0S(1)(flux)	38.7	29.6	11.7	4.35	1.99	1.04	.787	.820	0.882	5.8(-3)
I_{H2}(flux)	607	456	197	95.5	57.9	37.3	26.1	20.9	16.9	.239
SiIII 1206	12.4	1.65	.665	.307	.145	.064	.025	.006	0	0
Ly$_\alpha$	6401	6737	7051	7483	8073	9167	11469	19260	73505	3267
SiIII 1896	20.1	1.82	.676	.340	.195	.120	.076	.043	0	0
CIII 1908	20.1	3.99	1.77	.920	.485	.232	.087	0	0	0
CII 2325	50.4	22.9	21.1	23.3	29.5	44.1	87.3	317	6870	.010
MgII 2800	22.6	10.9	9.59	10.2	12.5	18.5	34.0	166	4820	.019
[OII] 3727	164	79.0	61.2	52.6	47.0	41.9	36.6	28.9	63.7	.072
[SII] 4072	6.51	4.98	5.31	6.00	7.21	9.70	16.9	55.7	1390	1.82
Hβ	100	100	100	100	100	100	100	100	100	100
[NI] 5200	2.22	2.18	2.89	4.44	7.97	17.5	53.0	275	7650	17.0
[OI] 6300	7.99	14.9	23.4	35.2	54.8	94.2	205	775	19700	201
Hα	313	322	331	344	357	381	425	542	1081	405
[NII] 6560	59.9	44.6	45.4	50.1	58.4	70.7	86.0	104	1570	369
[SII] 6725	39.0	39.5	51.8	72.4	109	183	392	1448	36200	1656
2 phot	1038	1236	1405	1639	1973	2571	3843	8140	39722	0
[OII] 7322	17.6	5.74	3.48	2.39	1.70	1.18	.790	.507	1.30	0
[FeII] 8617	5.96	7.55	9.06	11.4	15.6	24.3	49.3	183	4622	369
CI] 9810	28.1	30.0	33.4	39.2	49.0	67.5	112	196	238	19.5
[FeII] 1.64μ	62.4	76.5	93.0	119	163	254	508	1836	43448	28401
[FeII] 26.0μ	26.7	31.7	39.1	50.5	70.0	108	210	697	14800	237619
[SiII] 35μ	69.5	87.4	122	182	296	558	1340	5130	111000	1700000
[OI] 63μ	11.0	14.7	20.9	30.9	47.9	83.0	189	1020	358000	4.13(+7)
[CII] 156μ	1.09	1.10	1.60	2.77	5.68	15.5	73.2	1230	637000	1.06(+7)

[a] The fluxes are in 10^{-4} ergs s^{-1} cm^{-2}.

Table 3 (continuation)

	S100	S90	S80	S70	S60	S50	S40	S30	S20	S10
20s1 1.16μ	66.0	62.6	29.1	15.7	15.5	25.1	67.5	363	36986	3962
20q1 1.23μ	53.0	50.4	24.0	13.4	13.1	20.2	52.7	282	28460	4051.0
10s5 1.84μ	108	108	53.1	26.8	22.8	32.7	87.7	500	61079	12710
10s4 1.89μ	62.1	64.2	35.0	19.7	17.7	24.2	57.3	296	34251	10120
10s3 1.96μ	258	268	148	81.0	64.9	77.0	177	982	124500	54650
10s2 2.04μ	108	116	68.1	40.6	34.9	42.6	90.8	450	53004	27150
21s3 2.08μ	70.6	66.2	30.3	16.5	17.1	29.1	80.0	430	43505	3126
10s1 2.12μ	310	330	195	115	92.5	99.2	199	1044	133280	95550
$10s1_{,h}$	310	326	186	101	67.2	42.0	20.3	5.51	0.619	20.0
10s0 2.22μ	89.2	97.5	60.3	37.3	31.9	35.7	67.6	317	38142	30230
21s1 2.25μ	87.7	83.1	38.6	20.9	20.6	33.3	89.8	482	49143	5264
$21s1_{,h}$	87.5	80.8	33.1	12.1	6.08	2.40	0.416	0.017	0.143	7.35
10q1 2.41μ	279	299	184	117	99.4	106	190	912	113430	112520
10q142.42μ	656	704	426	262	219	240	456	2249	282040	228400
10q3 2.43μ	218	232	137	81.2	65.1	69.8	140	735	93805	67250
10q5 2.46μ	126	131	72.2	39.6	31.7	37.6	86.6	480	60794	26690
21q1 2.55μ	82.5	78.5	37.4	20.9	20.4	31.4	82.1	438	44295	6306
21q3 2.57μ	63.7	60.4	28.0	15.2	15.0	24.2	65.2	350	38237	3825
10o2 2.63μ	157	179	122	82.0	72.5	76.7	118	472	57071	86240
21o2 2.79μ	52.3	51.9	26.7	16.8	15.6	22.3	52.2	257	25924	5062
10o3 2.80μ	237	254	156	99.4	84.4	90.3	161	774	96274	95490
21o3 2.97μ	71.2	67.7	32.3	18.0	17.6	27.1	70.9	378	38237	5443
10o4 3.01μ	76.2	83.3	51.5	31.9	27.2	30.5	57.8	271	32578	25820
10o5 3.24μ	123	131	77.2	45.8	36.7	39.4	78.9	414	52892	37920
10o7 3.81μ	33.9	35.3	19.4	10.7	8.54	10.1	23.3	129	16374	7187
00s7 5.51μ	43.5	52.4	45.4	36.1	26.3	18.9	28.2	162	26914	55570
00s6 6.11μ	34.4	45.2	47.3	44.2	37.5	28.4	26.5	101	16000	81970
00s5 6.91μ	165	231	283	313	316	279	209	322	48712	709900
00s4 8.03μ	66.6	96.7	131	164	195	218	215	245	15329	424900
00s3 9.67μ	142	210	306	432	602	838	1141	1718	34692	1278000
00s2 12.3μ	18.9	28.3	43.0	65.3	102	172	315	755	17828	217800
00s1 17.0μ	9.25	14.0	21.9	35.3	61.0	119	269	995	49126	294900
00s0 28.2μ	.119	.181	.289	.483	.884	1.89	5.14	24.7	2205	56420

[a] The fluxes are in 10^{-4} ergs s^{-1} cm^{-2}.

Table 4
Shock Wave Models II

	N100	N600	NV1000	NV90	NVV1000	NVV10000	NVV90	BNV1000	BNV90	BBX110	BBX11
V_s (km s^{-1})	100	100	30	333	55	17	183	50	90	50	50
N_H ($cm-3$)	100	600	1000	90	1000	10000	90	1000	90	300	300
B_0 (μG)	70	70	70	70	70	70	70	117	19	110	11
X_e (10^{-5})	1	1	1	1	1	1	1	1	1	10	0.1
M_{A0}	10.79	4.40	11.37	3.42	6.20	6.35	6.22	11.41	3.41	6.19	6.19
L (10^{16} cm)	14.94	0.42	1.66	1.66	0.49	0.05	5.51	1.67	1.66	1.64	1.64
T_{max} (K)	8331	6512	1747	26547	3420	584	15527	3821	4049	9185	457
T_S (10^4 K)	23.70	28.04	2.08	314.78	8.22	0.78	91.02	5.77	23.00	2.94	7.18
E_{IR} (eV/part)	51.74	6.56	5.64	5.74	3.84	11.16	15.26	11.62	2.92	35.62	3.46
v_{H2} (km s^{-1})	73.33	32.50	31.11	31.27	28.21	38.68	43.45	39.24	26.60	61.93	27.56
v_{eqv} (km s^{-1})	124.01	105.15	43.22	334.46	61.81	42.25	82.39	63.56	93.85	79.60	57.09
Hβ(flux)	3.44	25.9	0.191	33.6	5.27	5.3e-4	9.67	2.82	2.95	0.585	1.20
1-0S(1)(flux)	25.8	16.9	3.71	6.44	5.44	37.4	11.4	21.9	0.382	25.4	1.478
I_{H2}(flux)	388.1	276.3	109.7	116.4	139.9	1216.4	180.7	472.9	13.2	391.2	31.8
SiIII 1206	2.34	52.4	0.005	35.0	0.095	–	59.6	0.046	2.63	0.033	0.072
Ly$_\alpha$	6680.23	6239.38	20939.24	5041.67	8457.31	133257.52	4943.12	9406.96	6735.59	10406.84	9136.21
SiIII 1896	2.64	65.6	0.035	34.8	0.150	–	44.2	0.096	3.35	0.080	0.142
CIII 1908	5.42	51.7	–	122	0.333	–	133	0.180	6.17	0.124	0.27
CII 2325	22.8	108.0	385	127	35.7	7.51×10^4	106	49.5	27.5	63.0	48.2
MgII 2800	9.17	37.1	207	353	17.3	1.21×10^5	189	21.5	12.6	20.0	25.9
[OII] 3727	109.20	185.80	25.10	688	37.60	246	577	35.90	114.40	34.8	47.20
[SII] 4072	2.65	14.1	70.3	12.5	12.7	3.30×10^4	13.9	12.8	4.11	11.1	13.7
Hβ	100	100	100	100	100	100	100	100	100	100	100
[NI] 5200	2.62	1.59	345	9.70	9.11	1.892×10^5	12.24	20.57	2.72	32.50	18.12
[OI] 6300	10.7	9.72	967	79.8	76.4	5.54×10^5	63.4	114	12.2	141	107
Hα	320.06	306.18	565.48	267.86	366.03	1215.98	278.18	386.01	321.69	405.13	379.57
[NII] 6560	44.0	79.2	109	353	63.3	4.99×10^4	283	74.3	47.5	83.9	72.1
[SII] 6725	41.70	37.50	1802	104.2	123.8	1.24×10^6	163.60	211	43.90	278	193.1
2 phot	1174.42	945.95	9114.72	395.83	2201.14	76315.79	383.66	2705.97	1216.95	3230.77	2566.45
[OII] 7322	4.22	24.9	0.44	39.60	1.99	2.98	26.20	1.133	3.49	0.725	1.66
CI] 9810	20.6	27.7	303	5.51	73.4	1.19×10^5	21.1	83.0	29.5	55.8	104
[SiII] 35μ	129.0	50.1	6.59×10^3	114	288	5.90×10^6	197	619	101	1.10×10^3	444
[OI] 63μ	10.4	12.4	1.54×10^3	21.5	68.8	1.77×10^7	27.9	107	12.8	123	96.6
[CII] 156μ	3.53	0.954	1.05×10^3	3.45	3.38	2.05×10^6	8.08	13.2	1.62	112	6.97
[FeII] 1.64μ	93.40	101.29	3393.53	338.26	336.51	3378039.75	349.92	479.66	101.91	552.94	427.44

[a] The fluxes are in 10^{-4} ergs s^{-1} cm^{-2}.

Table 4 (continuation)
Shock Wave Models II

	N100	N600	NV1000	NV90	NVV1000	NVV10000	NVV90	BNV1000	BNV90	BBX110	BBX11
20q1 1.23μ	122.215	8.552	453.748	4.135	14.779	2.214×10^{6}	22.308	65.014	2.792	720.905	32.291
10s5 1.84μ	175.430	24.200	1036.129	5.527	36.974	9.100×10^{6}	30.020	224.755	3.119	1447.068	55.836
10s4 1.89μ	119.365	14.604	532.742	4.346	22.425	4.012×10^{6}	20.590	142.204	4.181	843.460	33.873
10s3 1.96μ	546.811	56.757	1867.205	14.858	85.499	1.306×10^{7}	88.098	611.739	9.174	3549.154	113.530
10s2 2.04μ	242.207	25.118	748.776	8.350	38.551	4.560×10^{6}	40.786	273.392	8.210	1494.690	53.053
10s1 2.12μ	749.964	65.112	1940.879	19.152	103.273	1.078×10^{7}	117.919	777.154	12.963	4334.861	123.150
10s0 2.22μ	231.485	19.678	524.152	7.332	30.561	2.496×10^{6}	37.661	229.107	7.254	1254.249	38.134
21s1 2.25μ	185.354	14.694	783.733	6.856	24.826	4.133×10^{6}	35.375	106.956	4.370	1183.096	55.217
10q1 2.41μ	754.468	55.829	1763.902	17.679	94.953	7.838×10^{6}	113.855	707.398	15.314	3944.442	107.027
10q142.42μ	1673.943	137.479	4128.710	43.943	223.018	2.074×10^{7}	261.338	1660.811	37.057	9219.326	265.572
10q3 2.43μ	527.858	45.829	1366.078	13.480	72.688	7.588×10^{6}	82.996	546.996	9.124	3051.070	86.679
10q5 2.46μ	267.007	27.715	911.753	7.255	41.749	6.376×10^{6}	43.018	298.711	4.480	1733.047	55.436
21q1 2.55μ	190.216	13.311	706.218	6.436	23.002	3.446×10^{6}	34.720	101.189	4.346	1122.027	50.257
21q3 2.57μ	134.674	10.676	569.440	4.982	18.038	3.003×10^{6}	25.702	77.712	3.175	859.607	40.120
10o2 2.63μ	485.665	34.023	896.508	12.322	58.882	2.556×10^{6}	70.673	460.022	14.656	2270.604	56.120
21o2 2.79μ	130.076	9.020	356.161	4.727	13.811	1.421×10^{6}	22.926	67.225	5.446	720.848	30.208
10o3 2.80μ	640.331	47.383	1497.056	15.005	80.588	6.652×10^{6}	96.632	600.381	12.998	3347.722	90.836
21o3 2.97μ	164.201	11.490	609.630	5.556	19.856	2.975×10^{6}	29.972	87.350	3.752	968.568	43.384
10o4 3.01μ	197.718	16.808	447.695	6.262	26.103	2.132×10^{6}	32.167	195.687	6.196	1071.291	32.572
10o5 3.24μ	297.630	25.840	770.250	7.601	40.985	4.278×10^{6}	46.797	308.421	5.144	1720.329	48.873
10o7 3.81μ	71.913	7.464	245.564	1.954	11.244	1.717×10^{6}	11.586	80.452	1.207	466.765	14.931
00s7 5.51μ	41.279	23.597	607.208	1.171	77.684	5.703×10^{6}	6.469	678.140	1.007	568.166	17.619
00s6 6.11μ	48.643	17.661	498.649	1.298	70.665	1.793×10^{6}	7.010	590.181	2.020	470.909	11.374
00s5 6.91μ	365.291	73.168	3641.247	5.246	386.510	3.391×10^{6}	43.672	3012.037	19.788	2391.283	30.212
00s4 8.03μ	224.229	25.536	2417.823	3.210	157.890	6.708×10^{5}	25.071	1156.054	18.171	1009.138	10.376
00s3 9.67μ	733.634	44.998	8387.827	6.133	339.095	8.951×10^{5}	71.427	2324.965	79.973	2248.414	15.983
00s2 12.3μ	139.112	5.290	1615.320	1.207	44.204	1.264×10^{5}	13.027	290.594	18.641	308.655	5.542
00s1 17.0μ	89.867	2.356	1119.880	0.537	22.675	1.092×10^{5}	7.712	143.347	13.986	154.768	17.640
00s0 28.2μ	1.285	0.030	19.756	0.008	0.321	3.137×10^{3}	0.107	1.982	0.219	1.998	1.005

[a] The fluxes are in 10^{-4} ergs s^{-1} cm^{-2}.

Table 5
The Cygnus Loop

	Graham *et al.*[a]		Model[a]		
	G87	G173	M87	M173	Observed
B(μG)	10	10	10	10	—
$n_H 2(cm^{-3})$	4	1	4	1	—
v_S(km s^{-1})	87	173	87	173	—
T_{max}(K)	21800	64500	12200	16900	—
L(10^{16} cm)	2.1	8.4	3.15	12.7	—
$F^b_{1-0S(1)}$	5.14	32.9	6.7	2.2	187
1-0S(2)	—	—	73	172	42
1-0S(1)	—	—	100	100	100
1-0S(0)	—	—	76	191	27
2-1S(1)	—	—	33	35	12

[a] Graham *et al.* (1991).
[b] Fluxes in units of 10^{-7} erg cm^{-2} s^{-1} sr^{-1}.

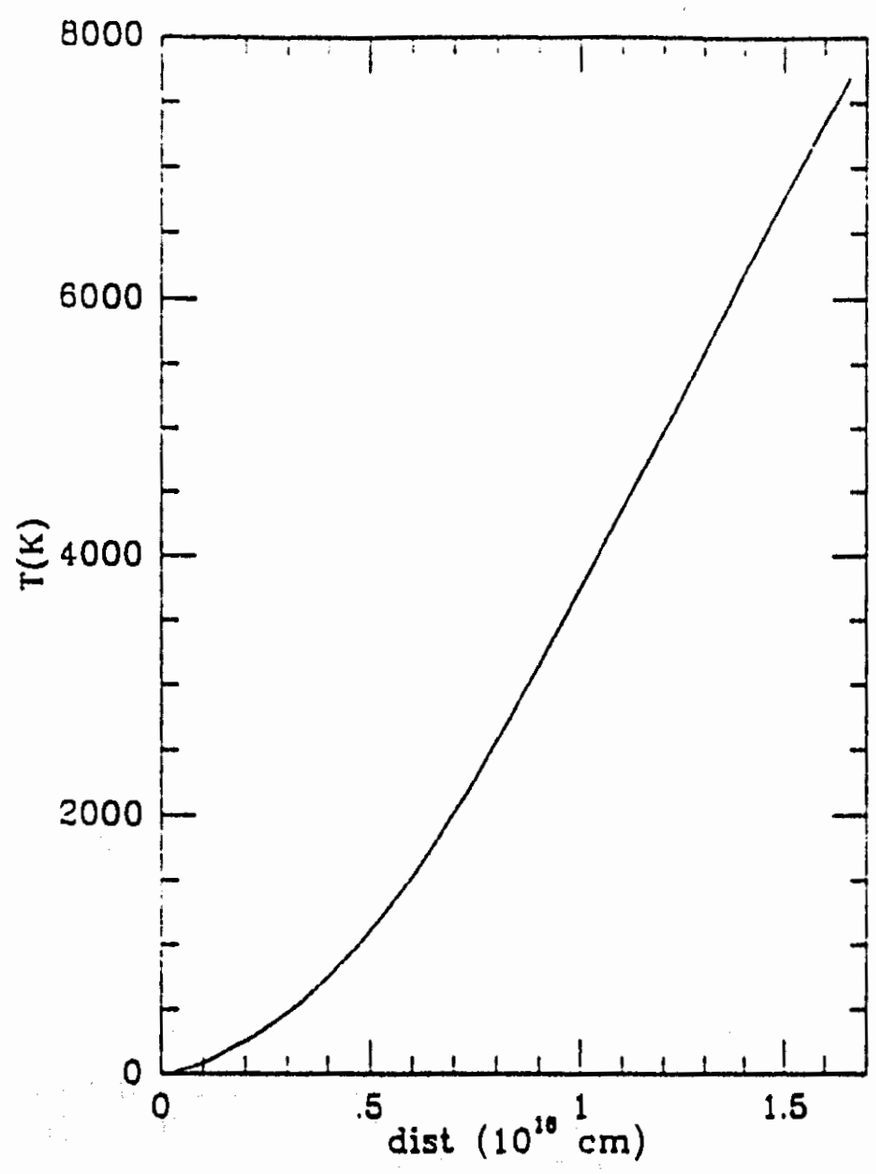

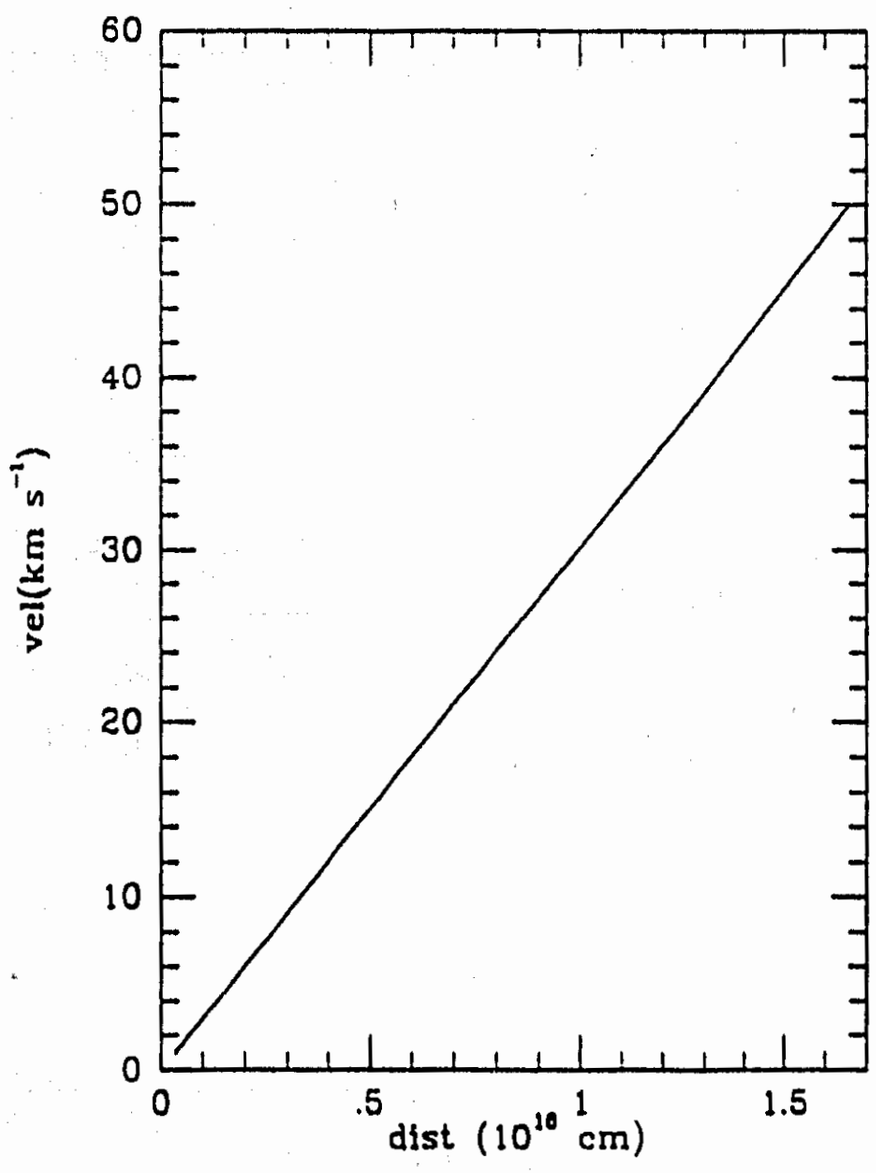

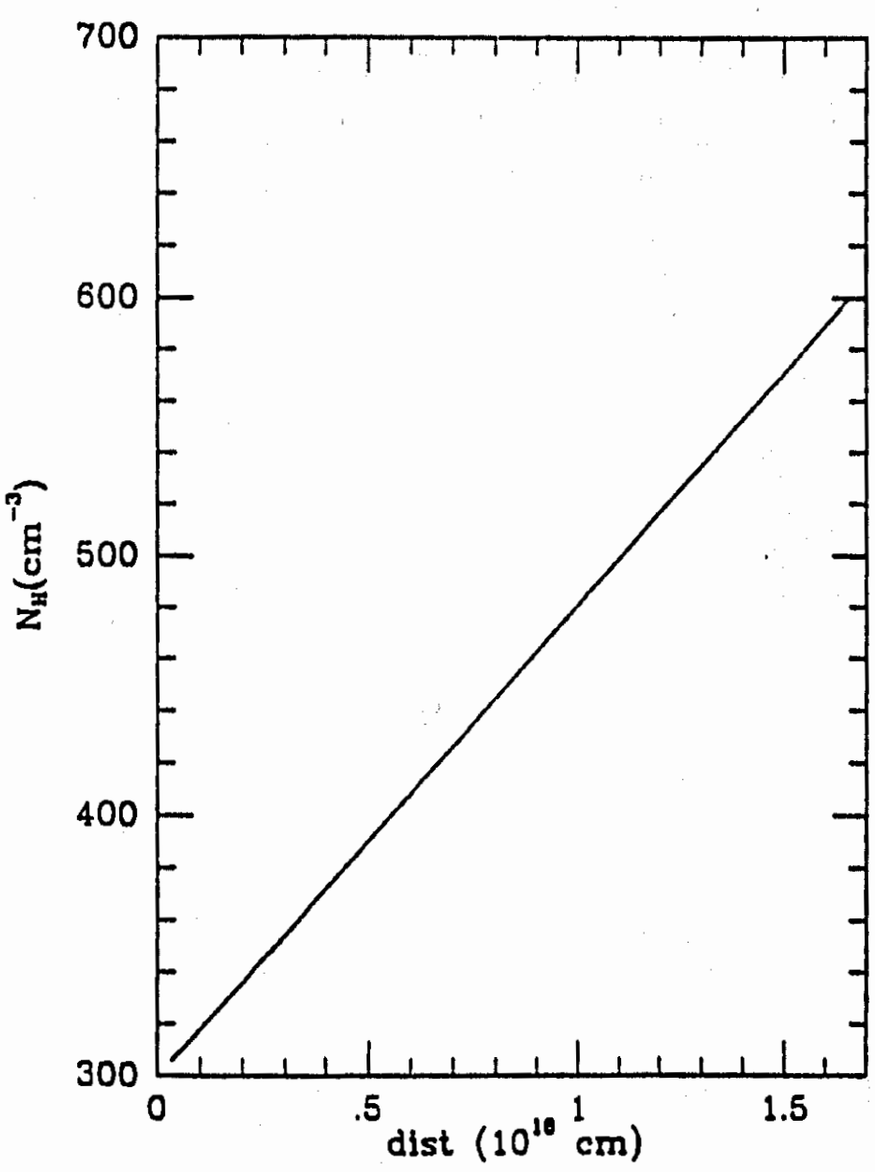

Figure 1. Temperature, density and velocity profiles in the magnetic precursor. The density and velocity are assumed to change linearly throughout the precursor, while the temperature is calculated by using eq. (8).

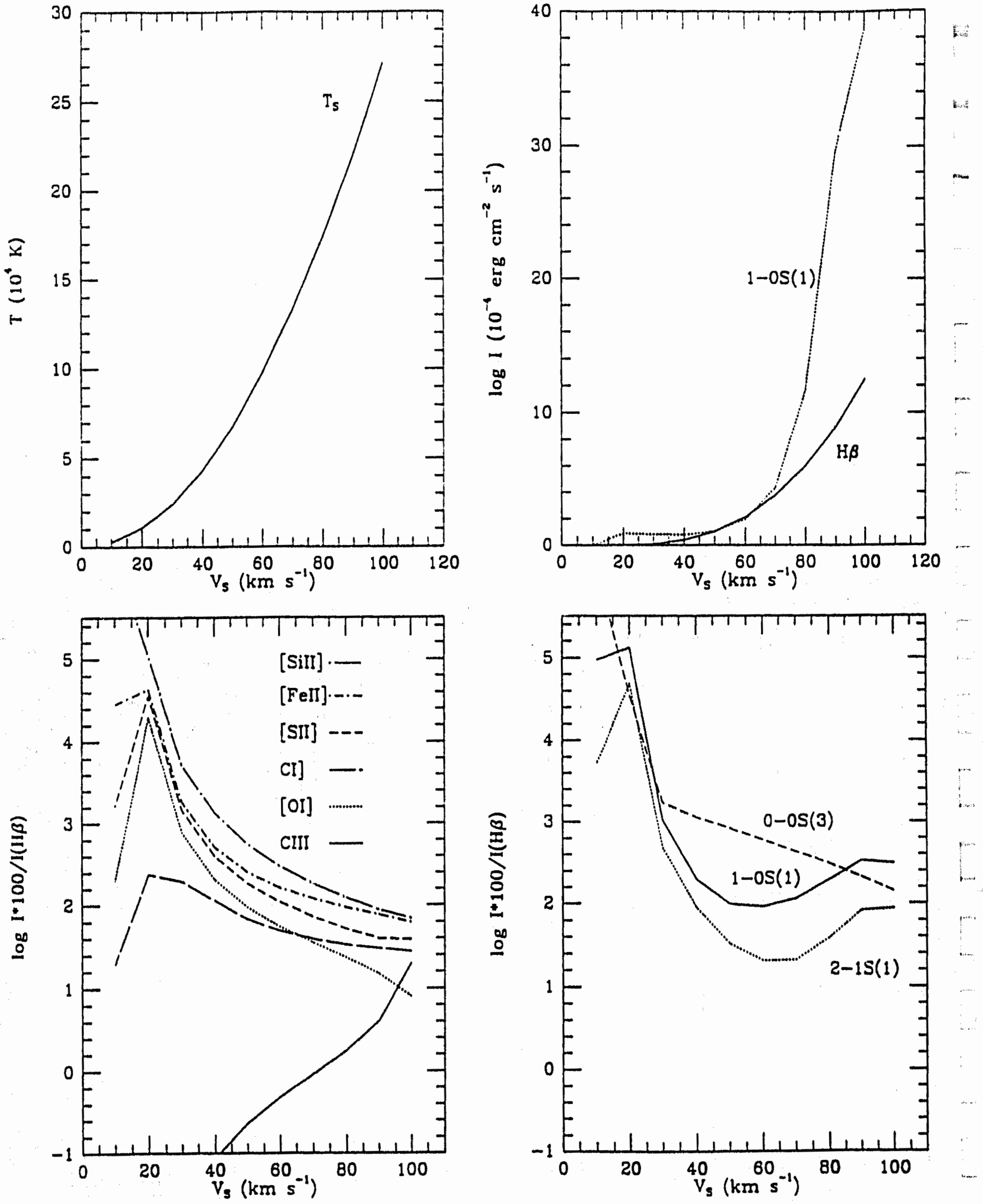

Figure 2. Top: Post-shock gas temperature (left) and intensity of the Hα and H_2 1–0S(1 lines (right) as function of the shock velocity. Bottom: Optical and infrared ratios for atomic (left) and H_2 (right) lines with respect to Hβ as a function of the shock velocity. The wavelengths of these lines are given in the text and Table 3.

CHAPTER 5

MODEL FOR BOW J-SHOCKS WITH MAGNETIC PRECURSORS

I. Introduction

Herbig-Haro (HH) objects are compact knots of shock-excited gas seen in regions of star formation, which arise as a supersonic, bipolar wind from a newly-formed star interactes with the surrounding environment. The nature of the shocks present in HH objects remains controversial. In some regions a simple bow shock formed around a dense obstacle in the flow (the 'cloudlet' model) or around a dense obstacle ejected from the star (the 'bullet' model) seems to explain the observed data. In other regions, however, the HH objects apparently outline the positions of radiative shocks in an outflowing jet. Imaging with infrared and optical detectors is a very useful technique to establish the shock type and geometry of individual HH objects. Infrared observations have shown that H_2 line emission in these objects presents a wide and complex variety of morphologies, being in most of the cases similar to those observed at optical wavelengths. Since H_2 and optical lines trace different components of the shocked gas, they provide important complementary information which can be compared with predictions of theoretical models for shock waves in order to derive physical parameters for the gas that yields both H_2 and optical emission from the same HH object. In a jet model where a collimated flow moving through a molecular medium forms a bow shock at its end, the external H_2 entering the bow shock will usually be dissociated near its apex and H_2 line emission will therefore predominantly arise from the wings of the bow shock. This H_2 emission will have small line widths and small radial velocities (compared to the optical lines). These characteristics have been observed in a number of Herbig-Haro objects such as HH1 and Cepheus A/GGD 37, which have an optical bow-shaped morphology, and where the H_2 line emission is observed mainly from the wings (for more detail see Chapter 1). On the other hand, as Draine (1980) and Draine *et al.*(1983) showed, when a shock wave moves through a partially ionized gas with a transverse magnetic field B_0, it may be preceded by a "magnetic precursor" which heats and compresses the medium before it goes through the main shock. Under these

conditions, a considerable fraction of the available "free energy" is dissipated throughout the precursor. Thus, when a jet is moving through a molecular medium and is preceded by a magnetic precursor, a substantial amount of H_2 emission may be produced before the molecules are dissociated (even at high velocities close to the bow shock apex). In this case, the H_2 lines will be broader and with higher radial velocities than those expected in a bow shock model without a magnetic precursor, and the H_2 and optical emission should nearly coincide spatially, having similar morphologies. These characteristics have been observed in HH7, where the optical and infrared emission have bow-shaped morphologies, coinciding within an arc-second. Further information can be obtained by calculating infrared line intensities and profiles from bow-shaped shock waves with magnetic precursors, similar to those calculated for optical lines by Hartigan, Raymond and Hartmann (1987), Raga and Böhm (1986), and Hartmann and Raymond (1984).

Theoretical line profiles expected from bow-shocks have been calculated either for optical (Hartigan, Raymond and Hartmann 1987) or for H_2 infrared lines (Smith and Brand 1990) but not simultaneously for both. In the former case, the bow shock was constructed using plane-parallel atomic shock waves, while in the latter, C-type shock waves were used for molecular emission. Likewise, theoretical position-velocity diagrams of optical lines from bow-shocks have been calculated by Raga and Böhm (1986), and Hartigan, Raymond and Meaburn (1990). The purpose of this work is to calculate theoretical spatially resolved infrared and optical emission-line spectra from a bow shock moving through a magnetized molecular medium. These calculations are to some extent, based on extension of previous ones carried out by Hartigan, Raymond and Hartmann (1987), which were restricted to the case of a bow shock moving through an atomic medium. In the present work, the role played by infrared H_2 line emission from a magnetic precursor is studied. Line intensities and profiles, as well as position-velocity diagrams and contour maps are calculated for a number of optical and infrared lines. The bow shock model is discussed in section II, and the predictions for the optical and infrared lines are presented in section III. The model is then applied to HH7 in section IV, where the model predictions are compared with high-resolution observations (both spectral and angular) of this object. Finally the main conclusions are presented in V.

II. Description of the Bow Shock Model

In the present work we calculate theoretical line intensities and profiles, position-velocity diagrams, morphologies and local velocity profiles of both optical and infrared line emissions from bow-shaped J-shock waves with magnetic precursors (or bow JMP-shock waves). We follow the bow shock model presented by Hartigan, Raymond and Hartmann (1987). However, since these authors were more concerned about atomic lines emitted in the post-shock region, a number of changes and extensions have been made to calculate the infrared emission from the pre-shock region (*i.e.*, from the magnetic precursor).

a) Geometry

Figure 1 presents a schematic diagram of a bow-shock and its characteristic parameters. This figure shows the parameters defining the bow shock, the direction of the observer and the adopted orientation of the magnetic field B, which is assumed to be in a direction perpendicular to the axis of symmetry of the bow-shock. The observer views the bow-shock at an angle ϕ from its main axis. In this frame of reference, the pre-shock gas moving with a velocity v_s enters the bow-shock at an angle ξ from the vertical, which is determined once the bow shape is known. The radiation emitted by a bow-shaped shock wave is calculated by dividing the bow shock into a number of concentric annuli (typically 200 annuli) of constant $d\xi$. Each annulus is then divided into segments with azimuthal angle Ψ which are treated as single plane-parallel shocks with constant shock velocity $v_\perp$ and magnetic field $B_\parallel$. These plane-parallel models were presented in Chapter 4 and will not be discussed further at present. To calculate the line profiles and position-velocity diagrams, the local velocity v_2 and angle θ of the emitting gas have to be known. Once the local velocity v_2 is known, the emission from each segment is taken to be that of a plane-parallel shock wave with velocity $v_\perp$ and $B_\parallel$ weighted by the area of the segment, and the contribution of each segment to the line profile is binned into intervals of 5 km s^{-1} in the observer's frame. Zero velocity corresponds to the ambient molecular cloud velocity.

The predicted line ratios and profiles are obtained by co-adding the segments in each annulus and then co-adding the annuli over the entire bow. Position-velocity diagrams are obtained assuming that the bow-shock is observed with a theoretical spectrograph having its slit centered on and parallel to the axis of symmetry of the bow-shock. In this case,

the emission from each annulus is calculated by co-adding the segments within the slit, and then, equal-intensity contours in the (z,v_y)-plane are calculated by interpolating the intensities obtained for each annulus as a function of velocity. Finally, three-dimensional IRAF files for each line are constructed with the integrated emission of each segment (integrating along the line-of-sight) and its contribution to the line profile. The first two dimensions contain information about the spatial distribution of the emission while the third one contains the velocity distribution of the line. Contour maps of the bow-shock are then obtained by calculating equal-intensity contours in the (x,z)-plane, and local line profile diagrams are constructed by obtaining the line profile at each (x,z) position within the area of the bow.

b) Velocity and Temperature

The parallel component $v_{\parallel}$ of the incident velocity remains constant across the shock while the perpendicular component $v_{\perp}$ diminishes by approximately a factor of two in the precursor (see Chapter 4) and by a higher factor, that depends on the jump shock conditions ($\sim$4 for a strong shock), immediately behind the J-shock. In the post-shock region, the optical and infrared lines are predominantly emitted when the gas temperature has dropped to about 10^4 K. While the temperature drops, the density increases and consequently the v_{perp} decreases. On the other hand, in the pre-shock region, H_2 lines are emitted in a wide region where the molecular gas is being accelerated and heated. In this case, since there is a steep gradient of temperatures, molecular lines are emitted throughout the precursor. However, most of the emission seems to be produced close to the J-front (see Chapter 4), where the molecular density is higher, and the gas temperature (typically of about 5000 K) is appropriate to excite vibrational-rotational H_2 states. A complete analysis of the atomic and molecular emission and line profiles would require a two-dimensional magnetohydrodynamic flow problem outside (the precursor) and inside (the shocked region) the volume bounded by the bow shock, including radiative cooling, and photodissociation and photoionization in the precursor. This problem has not been studied in detail. A number of approaches have been taken to calculate the evolution of the gas behind the J-front of the bow-shock (*e.g.*, Sandford and Whitaker 1983; Rózyczka and Tenorio-Tagle 1985a,b; Raga and Böhm 1985; Blondin, Köning and Fryxell 1989). However, these studies have not been carried out taking the precursor into account. Therefore, the following approximations have been used to calculate the optical and infrared emission from a bow-shaped shock wave.

In the present calculations, an overall velocity $v_s = 100$ km s^{-1} for the bow-shock is adopted, which is approximately the required velocity to match the optical line widths. The emitting pre-shock region and the cooling distance in the post-shock region are taken to be small compared to the size of the bow shock (Hartigan *et al.* 1987; Chapter 4), so that the radiation arises from a narrow shell around the bow. Results from plane-parallel models suggest that a fixed temperature for the line of interest (typically 10^4 K for optical lines, and 5000 K for H_2 infrared lines) can be used. Since most of the H_2 emission is produced close to the shock front (see Chapter 4), the expected $v_\perp$ in this region is of the order of that of the material before it goes through the shock front (typically $\sim v_{\perp 0}/2$). On the other hand, the expected post-shock velocity $v_\perp$ can be calculated by taking into account the deceleration in the shock front and that due to cooling effects (the velocity typically decreases by a factor greater than 10). Taking $v_\parallel$ to be unchanged by heating and cooling effects, the velocity of the emitting gas v_2 and its deflection angle θ can be calculated. Hence, the local and integrated line profiles can be obtained by integrating over the line-of-sight, in the first case, and then co-adding over all annuli. The final line profiles are obtained first by smoothing the velocity of the local profiles with a Gaussian distribution, the width of which contains thermal and instrumental broadening, and then by spatially smoothing the emission distribution, assuming a given seeing (typically between 1 and 2"). Once the local line profiles are obtained, the total line profile, position-velocity diagrams and contour maps are obtained as mentioned above.

c) Shape of the Bow Shock

As suggested by the morphology observed in some HH objects, bow-shocks are often approximated as hyperbolic or parabolic geometries. More complicated shapes have been studied by Choe, Böhm and Solf(1985), and Raga and Böhm (1986). A simplified form of these shapes has been used by Hartigan, Raymond and Hartmann (1987). In this work, the latter approach has been used. The shape of the shock is given by

$$z(r) = \alpha r^2 + \alpha^3 \beta r^4 \ , \qquad (1)$$

where α and β are constants, and r is the radius of a given annulus (Hartigan, Raymond and Hartmann 1987). To obtain this equation, the radius and height of the bow have been normalized by a constant R_0 which may be chosen to be the radius of a high-density

condensation (*e.g.*, in the "bullet" or "cloudlet" models), or the radius of the bow-shock (*e.g.*, in the jet model), or in units of one arcsecond for a more general case. Under this normalization, $z = Z/R_0$, $r = R/R_0$, and α depends upon the choice of the normalization constant. For given α and β, there is a critical radio r_c at which the fourth order and the quadratic terms are equal. This critical value is $r_c = \alpha^{-1}\beta^{-1/2}$, and it occurs at an incident angle of $\xi_c = tan^{-1}(6\beta^{-1/2})$. This critical angle represents the point where a quadratic shape gives way to the steeper quartic shape. In the present work, the latter case (the general case) has been chosen, with $\alpha = 0.07$ and $\beta = 26.24$, which nearly reproduces the parabolic-like shape observed in HH7.

d) Magnetic Field

Infrared observations of HH7 have revealed that H_2 line emission arises from all of the bow-shaped object, including its apex. A pure J-shock produces H_2 line emission that is far less than that emitted from a magnetic precursor (*e.g.*, Hollenbach and McKee 1989), so a magnetic field must moderate the shock even at the tip. In terms of a magnetic precursor, this observational result could be explained if a magnetic field is aligned mainly perpendicularly to the axis of symmetry of this object. This is because only the parallel component of the magnetic field (*i.e.*, oriented in a direction parallel to the plane of the shock), $B_{\|}$, gives origin to the magnetic precursor of a shock wave. Likewise, the size of the precursor L and the Alfvén Mach number M_A ($M_A = v_s/v_A$, where $v_A = (B^2/4\pi\rho_i)^{1/2}$ is the Alfvén velocity) are proportional to B^2/v_s^2 and v_s/B, respectively. Therefore, infrared emission from a region close to the apex of the bow shock (as observed in HH7) can be expected only if $B_{\|}$ is stronger closer to the apex, where the shocks are less oblique and thus stronger, so that the velocities of the shocks remain sub-alfvénic, producing a precursor of considerable size. This suggests that if the infrared emission is arising from a magnetic precursor, the magnetic field must be oriented perpendicular (or almost perpendicular) to the axis of symmetry of the bow-shock. Under these circumstances, the size of the precursor and the Alfvén Mach number remain constant throughout the whole bow-shock, *i.e.*,

$$\frac{v_\perp}{B_{\|}} = \frac{v_s}{B} \,. \tag{2}$$

However, ultraviolet radiation emitted in the post-shock region could increase the pre-

ionization fraction in the precursor (mainly close to the apex where the UV emission is stronger) and thus, L and M_A would change throughout the bow shock. This possibility should be investigated but it is beyond the scope of the present work. Here, it has been assumed that there is no UV radiation coming from the post-shock region and therefore, equation (1) is valid everywhere in the bow. A molecular medium of density n(H) = 300 cm^{-3}, a uniform magnetic field B = 70 μG, and an ionization fraction of 10^{-5} are taken. This yields an Alfvén Mach number of ~6, and a width for the magnetic precursor of ~10^{16} cm.

III Results and Discussion

a) Theoretical Line Profiles

Figures 2 to 5 show the results of the theoretical line profiles obtained with the bow JMP-shock model described above, using a one arcsecond wide slit in the optical, a five arcsecond wide slit in the infrared, and a 2 arcsecond seeing at both optical and infrared wavelengths. Figure 2 shows the $H\alpha$ line profiles at several viewing angles ϕ from 0° to 90°, where $\phi = 90°$ corresponds to a bow shock moving on the plane of the sky and $\phi = 0°$ represents a bow shock moving toward the observer. The Hα line profile is symmetrical in velocity with a characteristic *plateau* feature when the bow shock moves on the plane of the sky ($\phi = 90°$). As the orientation angle ϕ decreases, the profile becomes increasingly asymmetric, with a main peak rising in intensity at higher negative radial velocities while a second "peak" (or plateau), at lower radial velocities, decreases in intensity. The second peak disappears at low angles ($\phi \lesssim 45°$) leaving the main peak with an extended wing. When $\phi = 0°$, Hα has a highly asymmetric single peak, with a radial velocity similar to that of the bow shock and wings extending to velocities close to zero. This shape indicates that the emission with high radial velocity arises from near the apex, whereas that at lower velocities it is emitted from the wings of the bow-shock. The plateau observed when $\phi = 90°$ is due to to the fact that at this orientation, the front and the back sides of the bow shock have opposite radial velocities but have the same strength, contributing equally to the line emission. When instrumental resolution is not taken into account (see Figure 5), the line remains symmetric in velocity but in this case, a triple peak feature arises from the plateau. The separation between the outer peaks is of about 80 km s^{-1}, similar to the 100 km s^{-1}shock velocity. The third peak coincides with the zero radial velocity (the ambient velocity). Figures 2 and 5 also show that the full width half maximum (FWHM) of an

emission line does not change appreciably when instrumental broadening is not taken into account. This indicates that the line width depends mainly on the macroscopic motions (*i.e.*, on $v_\perp$) having a small thermal broadening contribution. However, as discussed by Hartigan *et al.* (1987), the full width zero intensity (FWZI) is somewhat larger than the shock velocity due to thermal and instrumental broadening (see Figure 5).

Figures 3 and 4 compare the line profiles calculated for a number of optical and infrared lines. The lines chosen are $H\alpha$, [SII] λ6716/6731, [OII] λ3726/3729, and CII λ2326 in the optical, and [FeII] at 1.64μ and H_2 1-0S(1) at 2.12μ, 2-1S(1) at 2.25μ and 0-0S(3) at 9.67μ in the infrared. These figures show that for a given viewing angle high-excitation atomic lines exhibit similar profiles to Hα but with some important differences. High excitation lines such as [OII] and CII are significantly narrower than Hα, being more evident at small inclination angles ϕ. This indicates that these lines arise mainly from regions closer to the bow apex than Hα, where the shocks are stronger and thus, have higher temperatures. On the other hand, low-excitation lines such as [SII] and [FeII] present a characteristic two peak feature, independently of the inclination angle. Both peaks have comparable strengths and similar separation at different angles. The stronger peak corresponds to the negative and highest velocity because the orientation angles that have been chosen ($0° \lesssim \phi \lesssim 90°$). In this case, a considerable fraction of the emission arises from the wings of the bow-shock, where the shocks are oblique and thus weaker (having lower post-shock temperatures and low radial velocities), giving origin to the double peak. A general characteristic is that the FWZI of an emission line remains constant as ϕ varies.

H_2 infrared line profiles do not show a double peak feature as obtained for the low-excitation atomic line profiles. These infrared lines are much narrower and have lower asymmetry than the atomic lines. Because the H_2 lines are emitted during the acceleration of the molecular gas in the magnetic precursor and the velocity increases from zero to a fraction of the local shock velocity $v_\perp$, the expected separation between peaks would be just a few km s^{-1}, depending upon the velocity of the molecular gas and the spatial distribution of the emission. If the separation between peaks is small enough, the two peaks could be masked by the thermal broadening and/or by the instrumental resolution used in the calculations (*i.e.*, 25 km s^{-1} for all the line profiles shown). Figure 5 shows that when instrumental resolution is not taken into account, a double peak appears in the rotational line 0-0S(3), having a separation between peaks of about 30 km s^{-1}, which

is substantially lower than the shock velocity. In the case of the vibrational-rotational H_2 lines 1-0S(1) and 2-1S(1), the double peak remains unresolved, indicating a separation between peaks of $\lesssim$ 10 km s^{-1}. Another characteristic observed in the H_2 lines is that the profile changes little with the inclination angle, having similar widths but higher negative radial velocities for smaller angles. This model predicts that H_2 lines will have radial velocities from 0 to $\sim$ 50 km s^{-1}, depending on the inclination angle of the bow-shock. As in the case of the optical lines, the highest velocity will occur when the bow-shock is moving towards the observer (*i.e.*, $\phi = 0°$). Likewise, the FWZI of these lines remains constant as ϕ varies. However, the FWZI of the H_2 lines is only $\sim$100 km s^{-1} which is much smaller than the $\sim$160 km s^{-1} obtained for the atomic lines. This difference is due to the fact that the atomic lines are emitted in the post-shock region where the gas velocity is $\sim v_\perp$ whereas the molecular gas in the precursor has only been accelerated to a fraction of $v_\perp$ (in the pre-shock region, $v \lesssim v_\perp/2$). Rotational lines tend to have lower radial velocities and be broader than vibrational lines, indicating that a considerable fraction of their emission arises from the wings of the bow, where the shock velocity is lower favoring their excitation. As in the case of atomic lines, the FWHM in H_2 lines does not change when instrumental broadening is not taken into account (see Figure 5), indicating that the width of the line is mainly due to macroscopic motions and thermal broadening.

b) Theoretical Position-Velocity Diagram

Figures 6 to 9 show the results of the theoretical position-velocity diagrams obtained with this bow JMP-shock model using the initial conditions mentioned above. These figures display the effects of varying orientation angles while keeping the other parameters fixed. The lines chosen are the same used in the previous section to calculate the line profiles, and the results are plotted for the same angles ϕ. For both optical and infrared lines, the profiles are symmetrical with respect to the position of the apex when $\phi = 0°$ (having a *boomerang*-like shape), as expected for an axially symmetrical bow-shaped shock like the one considered here. The profiles are symmetrical in velocity when $\phi = 90°$, and have a triangular shape which is more evident in the low-excitation atomic lines. This characteristic shape is due to the fact that, at this orientation, along a line-of-sight the gas moving at both sides of the bow has opposite radial velocities of equal magnitude. At intermediate angles the shape of the profile changes, obtaining a *hook*-like shape when $\phi \sim 45°$. These distinctive shapes are less evident in the H_2 lines because the velocity span of the H_2 emission is lower than that of atomic lines, and also because the velocity resolution

used in these calculations is not high enough to resolve the expected two peaks, especially at high angles as observed in atomic lines (see previous section). The *boomerang*-like shape is the only one clearly observed (especially in the rotational lines), although, it is not as evident as in the atomic lines.

As in the case of the line profiles, the position-velocity diagrams exhibit two main peaks in the low-excitation atomic lines while only one peak is evident in the H_2 and high-excitation lines. Both peaks have similar strength; one of them at high and the other at low radial velocities. A general characteristic is that low-excitation atomic lines (*e.g.*, [SII], [FeII]) appear more extended into the tail/wings of the bow-shock while the high-excitation lines (*e.g.*, [OII], CII) are more constrained to regions closer to the apex. Similarly, rotational lines appear more extended into the wings than vibrational lines. When instrumental broadening is not taken into account, optical and infrared lines decrease in velocity dispersion and secondary peaks start to appear (see Figure 9).

c) Theoretical Contour Maps

Figure 10 shows Hα and 1-0S(1) contour maps predicted for a number of angles between 15 and 90° with respect to the line-of-sight. Figure 11 compares the predicted morphology at a given angle for a number of atomic and H_2 lines. It is evident that the predicted morphology changes drastically with the orientation angle of the bow shock. Two main changes that are observed when ϕ varies are the variation in position of the main peak, and the size of the observable wings. These figures show that the bow-shock exhibits a circular morphology when $\phi = 0°$, as expected for an axially symmetrical bow-shock. As the angle increases, the source appears more and more elongated until reaches a parabolic shape with a steeper quartic tail (*i.e.*, cometary-like morphology) when $\phi = 90°$. The peak of the emission appears at the center of the object when $\phi = 0°$, and moves closer to the tip of the source for larger angles.

Figure 11 shows that for a given angle, different lines show a similar general morphology but have wings with different extension and emission distributions. Low-excitation atomic lines and rotationally excited H_2 lines have long and relatively strong tails while high-excitation and vibrational H_2 lines appear more compact and with fainter wings. This figure clearly shows that high-excitation lines arise from regions with the highest velocity (around the apex of the bow-shock), and that the emission of low-excitation lines

extends to much lower velocities. Likewise, it shows that this type of model predicts that the optical and H_2 emission will present similar morphology and will coincide spatially. An important consequence of this morphological behavior is that the excitation of the object decreases from the apex to the wings of the bow (*e.g.*, the ratio [SII]/Hα increases in this direction), reflecting the lower excitation predicted for the lower velocities in the wings (*e.g.*, Hartigan *et al.* 1987; Chapter 4). Likewise, the ratio between H_2 and Balmer lines (*e.g.*, the 1-0S(1)/Hα line ratio) increases in the same direction, as predicted by plane-parallel models (see also Chapter 4).

d) Theoretical Line Ratios

As discussed in Chapter 4, when a bow shock moves through a magnetized molecular medium, a considerable fraction of the "free energy" is dissipated by excitation and dissociation of the molecules. This loss of energy reduces the excitation of the post-shock region, producing a spectrum similar to that expected for a lower velocity shock wave (Cox and Raymond 1985; Mckee and Hollenbach 1987; see Chapter 4). According to the results of Chapter 4 we estimate that a 100 km s^{-1} bow-shock model will have the corresponding H_2 spectrum but with an atomic spectrum (emitted in the post-shock region) similar to that expected for a ~80 km s^{-1} bow-shock. Table 1 lists line ratios for two bow JMP-shock models, one with $v_s = 100$ km s^{-1} (MODEL 100) and the other with $v_s = 80$ km s^{-1}(MODEL 80). In the 100 km s^{-1} bow-shock model, the energy lost in the precursor is not taken into account when the post-shock spectrum is calculated. The 80 km s^{-1} model (the corrected model) in Table 1 corresponds to the same 100 km s^{-1} bow-shock model, in this case taking into account the energy loss by excitation and dissociation of H_2 molecules in the magnetic precursor. It is important to point out that along with the lower-excitation spectrum less UV radiation is produced in the post-shock region, and therefore, H_2 molecules in the precursor are less likely to be photo-dissociated.

Both models show a mixture of high and low-excitation lines, as expected from an object containing a variety of shock velocities. Since the bow-shock model includes only velocities $\leq$100 km s^{-1}, very high-excitation lines such as [OIII] λ5007 are not expected, and other lines such as [SiIII] λ1206/1896, [CIII] λ1908 appear very weak. Moderate-excitation lines such as [OII] λ3726/3729 and CII λ2325 appear relatively strong, being comparable to Hβ. On the other hand, low-excitation lines such as [SII] λ6716/6731 and [OI] λ6300 as well as infrared [FeII], [OI] and [SiII] appear with similar or higher strength

than Hβ. As mentioned above, the high-excitation UV lines such as [OII], [MgII], [CIII] and [SiIII] are emitted close to the apex where $v_\perp$ is higher ($\sim$ 100 km s^{-1}), while low-excitation lines such as [SII], [OI] and [NI] arise from regions that extent into the wings of the bow-shock, where the shock velocity is low. This table also shows that a bow JMP-shock model produces relatively strong rotational and vibrational H_2 lines, several of them being stronger than Hβ.

When the energy lost in the precursor is taken into account (80 km s^{-1} model), the model has a substantially lower excitation spectrum than that obtained in the 100 km s^{-1} model. The high-excitation UV lines decrease in strength while low-excitation optical forbidden lines (*e.g.*, [OI], [SII], [NII]) and infrared atomic lines (*e.g.*, [FeII], [OI], and [SiII]) increase relative to Hβ, reducing the excitation of the spectrum. This behavior reflects the lower temperature in the post-shock region, reducing $H\beta$ and favoring the emission of low-excitation lines.

There seems to be a direct correlation between the spectra observed in HH objects and the spatial coincidence of their optical and infrared emission in individual objects. Low-excitation objects such as HH7, HH43 and HH12, where the optical and infrared emission exhibit similar morphologies with their main peaks coinciding spatially, have spectra with strong low-excitation lines (*e.g.*, [SII], [OI] and [NI]) with respect to Hβ, which are characteristic of shock waves with very low velocities $\sim$20-30 km s^{-1}(*e.g.*, Hartigan, Raymond and Hartmann 1987). On the other hand, the spectra of high-excitation objects such as HH1 and Cepheus A/GGD 37, where the H_2 emission appears mainly on the wings of the bow-shaped optical object, have very weak low-excitation and relatively strong high-excitation lines (*e.g.*, [OIII], [CIII], [SiIII]), which are characteristic of high-velocity shock waves (v_s > 100 km s^{-1}). This suggests that H_2 emission plays an important role in the excitation appearance of individual HH objects. However, more observations will be needed to confirm this correlation between H_2 emission and the excitation of the spectra of HH objects.

e) Comparison with Observations and other Models

The results presented in the previous sections show that a bow JMP-shock wave will have several characteristics that differ from those predicted by other bow-shock models and that could be observable. A comparison of this model with observations of HH objects,

as well as other models that have been proposed to explain this observation is briefly presented below.

Optical and infrared H_2 line profiles have been obtained for several HH objects (*e.g.*, Solf and Böhm 1987; Zinnecker *et al.* 1989; see also Chapter 1). A general result of these observations is that optical lines are wider and have higher radial velocities than H_2 lines. In several objects, the observed FWHMs of the Hα lines are in the range of 50-120 km s^{-1}, while the H_2 1-0S(1) lines have widths between 30 and 50 km s^{-1} (Zinneker *et al.*1989). Typically the width of the 1-0S(1) line is only half of that of the Hα line in the same object, and the observed central velocities of the H_2 lines are also lower than those of the optical lines. The bow JMP-shock model predicts a FWHM up to ~100 km s^{-1} for the atomic lines and ~50 km s^{-1} for the infrared H_2 lines, which are similar to those observed. Likewise, the radial velocities predicted are in the range of 0 to about −100 km s^{-1} for the optical lines and between 0 and −50 km s^{-1} for the H_2 lines (depending on the viewing angle), which are also similar to those observed.

The position-velocity diagrams show a distinctive triangular shape when $\phi = 90°$, which has been seen in long slit optical spectra for some HH objects such as HH1 (*e.g.*, Choe *et al.* 1985; Böhm and Solf 1985), and predicted by bow shock models (*e.g.*, Raga and Böhm 1986; Choe *et al.* 1985). An approximately triangular shape has also been observed in HH7 by Carr (1990) but in this case in the H_2 1-0S(1) infrared line. An outstanding high velocity, low brightness feature is seen in this H_2 PVD which also appears in the line integrated profile as an extended negative wing. This shape is not predicted by the present models without including a high velocity post-shock component in the emission (see below). The hook-like shape, expected when $\phi \sim 45°$, has been observed in HH47 in Hα emission by Hartigan, Raymond and Meaburn (1990), and predicted by these authors using a bow-shock model.

The model developed in this work, predicts that a bow-shaped shock wave moving through a magnetized molecular medium will present similar optical and infrared bow-shaped morphologies when observed at an angle other than along the line-of-sight (in this direction a circular shape would be observed), having a better defined shape for angles closer to 90° (see Figures 10 and 11). Likewise, the object will have its main optical and infrared peaks spatially coinciding and an extended but a fainter tail at both wavelengths. These characteristics have been observed in some HH objects. Optical and

infrared observations of HH objects have revealed that the H_2 line emission exhibits a wide variety of morphologies, being similar to those observed at optical wavelengths but with some differences (see review presented in Chapter 1; Curiel 1992). In some cases such as HH43 (Schwartz *et al.* 1988) and HH7 (Hartigan, Curiel and Raymond 1989; Stapelfeldt *et al.* 1991) the optical and infrared emission coincide spatially, while in others such as HH1 and Cepheus A (see Chapter 1) the H_2 emission arises from the wings/tails of a bow-shaped optical object. The bow JMP-shock wave can explain the shapes and the spatial optical and infrared emission distribution observed in objects such as HH7 and HH43 but not those observed in objects such as HH1 and Cepheus A/GGD 37. However, as mentioned above if the strong shocks close to the apex produce enough UV emission to dissociate the H_2 molecules before they reach the shock front, the magnetic precursor would not be formed close to the apex, and therefore, H_2 emission would be observed only from the wings of the bow shock, as observed in HH1 and Cepheus A. Recently, bow C-shock models have been proposed by Smith (1991) and Smith and Brand (1990) to explain the spatial coincidence between optical and H_2 emission in HH objects. They calculated the H_2 line emission from a bow-shock based on plane-parallel C-type shock waves. They indicate that the resultant morphology is similar to those observed at optical and infrared wavelengths. This model predicts that the H_2 emission will arise from the wings of the optical bow-shock, as observed in HH1 and Cepheus A. However, it does not predict the spatial coincidence of the main optical and infrared peaks observed in HH7 and HH43. Since C-shocks can predict strong H_2 and weak optical emission, in a bow C-shock the optical emission will be produced mainly from regions close to the apex, where C-shocks are not expected, whereas the H_2 lines will be emitted from the wings, where very weak optical emission will be expected. Figure 11 shows that a bow shock naturally predicts a decrease in the excitation level (*e.g.*, the [SII]/Hα ratio increases) and an increase in the H_2/Hα ratio (*e.g.*, 1-0S(1)/Hα increases) from the apex to the wings of the bow, because lower velocities in the wings produce a lower excitation spectrum (*e.g.*, Hartigan *et al.* 1987) and stronger H_2 lines relative to Hβ (see Chapter 4). A similar behavior has been observed in HH43 by Schwartz *et al.* (1988), where the [SII]/Hα ratio decreases from NW to the SE position of the object while the 1-0S(1)/Hα ratio increases along the same direction. The multiple knot structure observed in this object suggests that the bow-shock may be breaking up into several pieces as seems to be occurring in HH2.

Results of this bow JMP-shock model differ from those obtained by Smith and Brand

(1990) and Smith (1991) using a bow-shock model based on C-type plane-parallel shock waves. Their model predicts that the H_2 line will have radial velocities similar to those of the pre-shock gas, line widths of about about 30-40 km s^{-1} (for an instrumental resolution of about 15 km s^{-1}), and that the infrared emission will be produced on the wings of the bow-shock. This results do not change appreciably for a wide range of initial conditions (Smith and Brand 1990). The intrinsic FWHM widths of about 10 km s^{-1} predicted by this model are much smaller than the $\sim$ 50 km s^{-1} widths obtained with the bow JMP-shock model (see section IIIa). It is remarkable that this model predicts such low radial velocities and line widths even when C-shocks are expected to occur at velocities as high as 40-60 km s^{-1} (Draine, Roberge and Dalgarno 1983), and therefore can accelerate molecules to such velocities. The differences in the predictions of these two models seem to be related to the fact that in the bow C-shock model the H_2 emission is dominated by the warm gas which has not been substantially accelerated (Smith and Brand 1990), while in the bow JMP-shock wave model the H_2 emission arises mainly from the region close to the shock front, where the molecules have been accelerated to a considerable fraction of the shock velocity (see above and Chapter 4).

Individual models would be needed to determine whether this type of bow-shock models can reproduce the characteristics (morphology, line profile, etc.) observed in an individual HH object. In the following section, a detailed comparison between observations and numerical predictions are shown for the HH7 object.

IV. Application of the Bow Shock Model to HH7

With the new infrared array detectors, it is now possible to study the H_2 emission distribution at resolutions comparable to optical CCD images. A brief review on molecular emission in Herbig-Haro objects has been presented in Chapter 1 (Curiel 1992), and observational results on HH7 have been presented in Chapters 1 and 3 (Curiel 1992; Hartigan, Curiel and Raymond 1989). Recent optical and infrared observations of HH7 have revealed that this HH object exhibits a bow-shaped morphology at both optical and infrared wavelengths, which coincide within an arcsecond (Hartigan, Curiel and Raymond 1989; Stapelfeldt *et al.* 1991). Likewise, high-resolution spectral observations of this object have shown that the optical Hα and [SII] lines have FWHM of $\sim$90 km s^{-1} and $v_{rad} \sim$ $-$58 km s^{-1}, whereas the H_2 1-0S(1) line has a width of $\sim$45 km s^{-1} and a radial velocity

of $\sim$–11 km s^{-1} (Zinneker *et al.* 1989; Solf and Böhm 1987). The results presented in previous sections indicate that a bow-shaped shock wave with a magnetic precursor (bow JMP-shock) moving at a velocity of $\sim$ 100 km s^{-1} and with an inclination angle of $\sim$ 60° with respect to the line-of-sight can reproduce most of the observations of this object. In the following, a comparison between observational and theoretical results is presented.

a) Contour Maps

Figure 12 compares the observed integrated Hα, [SII], and H_2 maps obtained by Hartigan, Curiel and Raymond (1989) with those calculated with this bow JMP-shock model. As it can be seen, the calculated contour maps have a bow-shaped morphology at optical and infrared wavelengths, with the main peak of the emission coinciding spatially. Similar morphologies are obtained when this object is observed through the light of [FeII] at 1.64μ, and H_2 2-1S(1) and 1-0Q(3) lines (Stapelfeldt *et al.* 1991). Although the observed and predicted contour maps are quite similar, the observed shape varies from line to line whereas those calculated basically exhibit the same shape, as expected from such an idealized model. This model does not predict the second bright peak within the bow that appears in the [SII] images. However, it has been proposed that this second peak could come from jet gas cooling behind the jet's Mach disk (Hartigan, Curiel and Raymond 1989; Chapter 3), a consideration that has not been taken into account in the present calculations.

b) Line Profiles and Position-Velocity Diagrams

Figures 13 and 14 show a comparison between observed and calculated line profiles and position-velocity diagrams (PVD) obtained for HH7. It is important to notice that in these figures the observed line profiles and position-velocity diagrams are plotted with respect to the LSR radial velocity while those calculated are plotted with respect to the ambient molecular cloud velocity, which is about +7.0 km s^{-1} (Edwards and Snell 1983), and thus, the calculated values are shifted –7 km s^{-1} with respect to those observed. To obtain the calculated line profiles and PVDs, the line profiles were smoothed using instrumental resolutions, seeings and slits similar to those obtained observationally. Table 2 summarizes the properties (FWHM, FWZI, and v_{rad}) derived both observationally and theoretically for the Hα, [SII] and 1-0S(1) lines. These results show a striking similarity between the observed and calculated line profiles and position-velocity diagrams. In

particular, the radial velocities obtained for the three lines as well as the width of the 1-0S(1) are in excellent agreement with those observed. One main difference between the observed and calculated shapes is that the predicted [SII] line profile has a positive low-velocity secondary peak, which does not appear in the observed profile. This difference may be due to the fact that the emission produced by the second bright peak, observed in the [SII] images and that seems to correspond to a Mach disk, may be increasing the strength of the primary peak in the [SII] line profile and thus, increasing the relative intensity between this and the secondary peak. Furthermore, as pointed out by Hartigan (1989), in a stellar jet both the bow-shock and the Mach disk should have comparable brightnesses and therefore, the velocity distribution of the emission from the Mach disk will play an important role in the final shape of the observed lines. Another main difference is the high negative velocity wing that appears in the 1-0S(1) line and that is not predicted by this model. Carr (1990) has proposed that the high velocity component may be emitted behind the J-front, where the gas moves at velocities comparable to that of the shock. This second component could explain the high velocity emission observed in the line profile and the position-velocity diagram. Using a simple model, he finds that if about 15% of the emission comes from this region the high thermal width will be similar to that observed.

c) Line Ratios

A number of optical, ultraviolet and infrared line ratios obtained by integrating over a theoretical slit, the widths of which are similar to those used in the observations, are given in Tables 3 and 4. These line ratios were taken from the more extended list given in Table 1 in order to easily compare with those obtained from observations. The most striking numbers in these tables are the large [OII], [NII], MgII, [FeII], and H_2 line fluxes and the relative weakness of the other lines. The strong UV and optical lines are in agreement with the observed fluxes whereas the low-excitation lines such as [OI], [CI] and [SII] are substantially weaker than those observed. As mentioned in previous sections, when the energy loss in the magnetic precursor is taken into account to calculate the post-shock spectrum (MODEL 80), the UV and optical line ratios show a lower excitation spectrum (*i.e.*, lines such as [SII], [OI] and [CI] are stronger relative to Hβ) than that obtain in MODEL 100, being closer to those observed. However, this does not solve the extremely low-excitation nature of this object derived from the optical line ratios (*e.g.*, Böhm and Solf 1990; Solf and Böhm 1987). For instance, while the predicted intensity for the Hα line is similar to that observed, those predicted for the [SII] and [CI] lines are only about one

tenth of their observed value. If the energy loss in the magnetic precursor is higher than that calculated here (*e.g.*, due to the emission of molecules other than H_2), the optical emission will be similar to that of an even lower shock, and relatively closer to those observed. For comparison, Table 1 lists the optical and infrared emission from a number of velocities for the bow-shock. For a given velocity, the H_2 spectrum will be that listed at that velocity, whereas the optical spectrum will be that listed for a 10–15% lower velocity (see Chapter 4), or lower if the energy loss were higher.

Since the strength of low-excitation lines relative to Balmer lines increases at lower velocity shocks, they are very sensitive to the shape of the wings. In the present model, a steep quartic shape has been adopted for the wings of the bow. More extended wings (*e.g.*, quadratic wings) would produce stronger low-excitation lines relative to Hβ. However, these extended wings would be evident in low-excitation line images such as [SII], and they are not observed in HH7 (see Figure 12, and images in Chapter 3). Another possibility is that the magnetic field in this region is stronger than the 70 μG used in the present calculations. If this is the case, the post-shock temperature will be lower, increasing the emission of low-excitation lines relative to Hβ, and thus, reducing the excitation of the object. A third possibility is that the low-excitation lines were increased by emission from a Mach disk. A high density jet moving through a lower density molecular medium will produce a bow-shock and a Mach disk with comparable surface brightnesses (Hartigan 1989). If the jet velocity is only slightly larger than that of the bow-shock ($v_j \gtrsim v_s$), the shock in the Mach disk will be of low-velocity, producing strong low-excitation lines. An approximate velocity for the shock in the Mach disk can be obtained by balancing the ram pressure of the jet and bow-shock, which can be given by $\beta n_j(v_j - v_s)^2 = n_a v_s^2$ (Norman, Winkler and Smarr 1983), where v_j and v_s are the jet flow and bow-shock velocities respectively, n_a and n_j are the ambient and jet densities, and β is a factor that expresses the efficiency with which momentum is transferred from the jet to the working surface. Adopting $\beta = 0.7$, the shock velocity in the Mach disk is $\sim$ 20–30 km s^{-1} for n_a/n_j = 0.03–0.06 (here, $v_s = 100$ km s^{-1} is used). According to the Hartigan, Raymond and Hartmann (1987) models, this is the required velocity to produce a [SII]/Hβ line ratio similar to the observed in HH7. There is some observational evidence that seems to support the Mach disk explanation. A bright secondary emission peak within the bow is observed in high resolution [SII] images of this object (*e.g.*, Hartigan, Curiel and Raymond 1989; see Chapter 3) as well as in the [CI] λ9823/50 image obtained by Susan

E. Durham (private communication). This second peak could explain not only the strong low-excitation lines observed in HH7 but also the single peak feature observed in the [SII] line profile. The emission of the Mach disk would have a predominantly high negative radial velocity distribution, increasing the relative intensity between the low and high-velocity features predicted for the bow-shock (see Figures 13 and 14). The effects of this high velocity component from the Mach disk could in principle be observable by obtaining high-resolution velocity maps of this object (see below).

The calculated infrared line ratios are in good agreement with those observed. In particular, the 1-0S(1) line is one of the least accurately predicted. The calculated flux for this line is about 70% of that observed when a 5" wide slit is used, and this difference increases when the fluxes are obtained with a wider slit. It is important to notice that the calculated 1-0S(1)/2-1S(1) line ratio is about 4, while the observed value is about 10. The low line ratio obtained in this calculation is a result of: a) a substantial amount of the H_2 line emission comes from regions close to the apex, where the shocks are stronger and thus with higher temperatures, and b) most of the H_2 emission is produced close to the J-front where the temperature is higher. The proposed Mach disk will not modify the H_2 emission predicted for the bow-shock. Observations indicate that the wind emanating from SVS13, the presumed energy source of this system, is largely neutral atomic gas (*e.g.*, Lizano *et al.* 1988) and therefore, the shock in the Mach disk is also expected to be neutral, *i.e.*, lacking of H_2 emission.

The rotational-vibrational H_2 fluxes are similar to those calculated previously by Hartigan, Curiel and Raymond (1989; Chapter 3) using a plane-parallel JMP-shock model. The plane-parallel model predicts stronger 1-0 lines than the bow-shock model, and weaker rotational lines (see Chapter 4). These differences are due to the fact that the fluxes calculated by these authors were based on a single 100 km s^{-1} shock-wave, which produces strong vibrational and weak rotational lines (see Chapter 4), whereas in the present case, the fluxes are calculated by integrating over a multi-velocity bow-shock, where strong rotational emission is produced by the low-velocity shocks in the wings.

d) Comparison with other Models

A simple hyperbolic bow-shaped shock model has been used by Carr (1990) to calculate the H_2 1–0 S(1) line profile. He assumes that the H_2 emission is produced

in a molecular magnetic precursor, and that a second high velocity component comes from behind the J-front at a velocity of 120 km s^{-1}, which is the adopted shock velocity. The second component is needed for the high-velocity feature observed in the negative wing of this line, the width of which seems to be largely thermal in nature. He finds that for an inclination angle of 40° from the line of-sight, the calculated profile for the 1-0S(1) line is similar to the spatially integrated line profile for HH7. Recently, Smith (1991) has found that according to his morphology simulations a bow-shock moving at ~120 km s^{-1} with an inclination angle of 30°-40° reproduces the morphology observed in this object. However, these calculations require of extremely high densities (n(H2) ~ 10^6 cm^{-3}) and magnetic fields (B ~ 10^{-3} Gauss), which are much higher than those expected in the outer parts of molecular clouds (typically, n ~ 10^2-10^4 cm^{-3} and B ~ 1–100 μGauss), where HH objects are observed. Likewise, a bow-shock moving at such velocities and inclination angles would produce optical lines with radial velocities of about 90–100 km s^{-1}(*e.g.*, Hartigan *et al.* 1987; see above), which are much higher than those observed in this object (v_{rad} = –58 km s^{-1} for Hα and [SII]). Our model indicates that an angle of ~ 60° reproduces quite accurately not only optical and H_2 radial velocities and profiles but also the optical and infrared morphology observed in HH7.

e) Spatial Line Profile Maps (Velocity Mapping)

Recently, detailed H_2 1-0S(1) velocity mapping of HH7 with a spatial resolution of the order of 1″ has been obtained combining a two-dimensional infrared detector array (using IRCAM at UKIRT) with a Fabry-Perot spectrophotometer (Carr 1990). Based on the systematic changes in the line profiles, Carr (1990) concluded that the spatial distribution of the line profiles is consistent with the emission being produced by a bow shock. To compare with the observed spatial distribution and profile shape of the 1-0S(1) line, the profile of this line is calculated at different points across the bow-shock. The calculations presented in this section were carried out by making use of numerical codes developed by Pat Hartigan, Gerald Cecil, Joss Bland-Hawthorn and Jon Morse. Figure 15 shows a comparison between the observed line profile map obtained for HH7 by Carr (1990) with that calculated for a bow JMP-shock wave. Although there are some differences between the observed and calculated velocity maps, this figure shows that the calculated spatial distribution and profiles of the lines are similar to those observed in this object, supporting the idea of HH7 being a bow-shock. In both cases, the stronger and wider lines are observed close to the apex of the bow. The lines are weaker on the wings and decrease in strength

in regions farther from the apex. The line profiles behind the apex along the main axis of symmetry are dominated by the emission coming from the higher velocity wings (*i.e.*, the side closer to the observer has a higher contribution to the emission line). Finally, the profiles along the shock limb (top and bottom) are narrower and have lower central velocities. One of the main differences between the velocity maps is that the observed line profiles have wings that extend to higher velocities than those calculated. This difference also appears when the observed and calculated integrated profiles are compared (see Figure 12). This high velocity component has been interpreted as emission coming from the post-shock region (see above). Another main difference is that the observed line profiles remain observable far behind the apex whereas those calculated decline in strength faster, which could be due to different contrasts between the apex regions and the wings.

Since this technique can be used not only in the infrared but also in the optical, similar local line profile maps are calculated for a number of optical and infrared lines and are shown in Figure 16. The lines chosen have already been detected and could presumably be mapped. This Figure shows that a similar line profile distribution is expected at different lines. The characteristics described above for the 1-0S(1) line are even more outstanding in the atomic low-excitation lines such as [SII], [CI] and [FeII]. In these lines, the double peak feature predicted for the integrated line profile also appears in the local line profiles. The relative intensity between both peaks changes along the bow, and as mentioned above, the low-velocity component is more prominent along the shock limb whereas the high velocity wings dominate behind the apex along the main axis.

This new type of observation will be very useful to establish the shock type and geometry of individual HH objects and optical jets. Mapping low-excitation lines seems to be a particularly useful way to define a bow-shock geometry, because of the characteristic double peak feature predicted for this type of lines. In particular, [SII] could be used in the optical and [FeII] in the infrared when these lines are strong enough to be mapped.

Finally, the existence of the proposed Mach disk in HH7 could be tested by obtaining high-resolution velocity maps of low-excitation lines such as [SII] and [FeII], and comparing them to lines expected to be emitted mainly by the bow-shock such as H_2 1-0S(1) and Hα. A detailed study of the systematic changes in the profiles of these lines across this HH object, and their comparison to those predicted for a bow-shock, could lead to the identification of the Mach disk. However, this identification could only be possible if the

projected distance between the proposed Mach disk and the bow-shock is higher than the spatial resolution obtained by combining a two-dimensional detector with a Fabry-Perot spectrophotometer (typically of 1"). This test could also be applied to other HH objects where Mach disks seem to be playing an important role in the spectral characteristics observed in the object. Time-dependent hydrodynamic results indicate a high complexity in the changing morphology of the bow-shock, and that the distance between the latter and the Mach disk oscilates with periods of $\sim$ 20 years (Blondin, Königl and Fryxell 1989). This evolution of the bow-shock migth be observable with several years span observations.

V. Summary and Conclusions

A model for bow J-shock waves with magnetic precursors has been presented. Theoretical line intensities and profiles, as well as position-velocity diagrams, contour maps and velocity maps have been calculated for a number of optical and infrared lines. This is the first time that numerical simulations have been done to simultaneously predict optical and infrared emission lines from bow-shaped shock waves. The main results from the model are listed below.

i) Spectrum. The results indicate that a mixture of high and low-excitation lines as well as relatively strong H_2 lines are expected from a bow J-shock with a magnetic precursor. This model predicts an excitation level decrease from the apex towards the wings of the bow-shock. A similar correlation is expected for the relative intensity of H_2 lines with respect to Hβ ratio (*i.e.*, $H_2/H\beta$ increases from the apex to the wings). The energy loss in the magnetic precursor considerably reduces the excitation of the predicted spectrum. However, this spectrum is still far from that observed in low-excitation HH objects.

ii) Line profiles and PVDs. The predicted optical line profiles and position-velocity diagrams have shapes that change with the orientation of the bow-shock. Low-excitation lines exhibit a characteristic double peak feature, whereas high-excitation lines have only one main peak with a low velocity extended wing. The predicted radial velocity also changes with the angle, being similar to the velocity of the shock when it moves toward the observer. At each angle, the FWHM is different for low and high-excitation lines and similar for lines within each category, whereas the FWZI is similar for all the atomic lines. On the other hand, the H_2 profiles are single-peaked and narrower than optical lines, with

FWHM of $\sim$ 50 km s^{-1} , widths at 10% of the peak of $\sim$ 80 km s^{-1}, and radial velocities that vary from 0 to $\sim$50 km s^{-1}. Instrumental broadening does not change the widths of optical and infrared lines appreciably, indicating that they are mainly due to velocity dispersion and thermal broadening.

iii) Contour maps. This model predicts similar morphologies for the optical and H_2 emission of a bow-shock, coinciding spatially. It is found that the atomic low-excitation and rotational H_2 lines will have extended and relatively strong wings whereas high-excitation and vibrational H_2 lines will be more compact and with fainter wings. This result indicates that the object will present a decrease in excitation from the apex toward the wings.

iv) With the recent development of optical and infrared two-dimensional array detectors, it is now possible to study the morphology of HH objects, and the local line profile distribution within them by combining two-dimensional detectors with Fabry-Perot spectrophotometers. Comparing results from this new type of observations with those obtained from theoretical models, such as the one presented here, will be a very useful way to establish the shock type and geometry of individual HH objects and optical jets. This model predicts a characteristic line profile distribution for a bow shock that could be identified observationally. It is found that the stronger lines with wider profiles and higher radial velocities will appear close to the apex, whereas weaker lines with low radial velocities will appear along the shock limb, and the lines along the axis of symmetry will be dominated by emission from the side of the bow-shock closer to the observer. The mapping of low-excitation lines may be a particularly useful way to define a bow-shock geometry, because of the characteristic double peak feature predicted for this type of lines. In particular, [SII] could be used in the optical and [FeII] in the infrared when these lines are strong enough to be detected.

v) HH7. These results indicate that a bow J-shock with a magnetic precursor can reproduce most of the observational results obtained for the HH7 object. We find that a bow-shock moving with $v_s \sim 100$ km s^{-1} through a magnetized molecular medium of $n_H \sim 300$ cm^{-3}, and with an inclination angle of $\sim 60°$ with respect of the line-of-sight reproduces quite accurately not only optical and infrared line profiles and radial velocities but also position-velocity diagrams, and contour and velocity maps observed in this object. However, the calculated optical spectrum is still far from explaining the extremely low-excitation spectrum observed in this object. It has been proposed that a bow-shock with

more extended wings, even higher magnetic fields, a larger molecular loss, or emission from a Mach disk could account for such a low-excitation spectrum. Likewise, the negative high velocity wing observed in the 1-0S(1) line profile is not reproduced by this model. However, it is proposed that this high velocity component may be due to emission produced in the shock front, where the high temperatures and velocities will produce an extended negative wing. This possibility was not included in the present calculations. It is important to notice how this simple model can reproduce most of the HH7 observations, and several observational results of other HH objects.

vi) Although J-shocks with magnetic precursors may be an important class of shock wave, little work has been done in this direction. This type of shock wave seems to be a very promising way to explain the spatial coincidence of optical and infrared emission, and the line profiles observed in HH7 and other objects. Detailed calculations will be needed to improve the results obtained with this simplified model.

REFERENCES

Blondin, J.M., Königl, A., and Fryxell, B.A. 1989, *Ap. J. (Letters)*, **337**, L37.
Böhm, K.H., Brugel, E.W., and Olmstead, E. 1983, *Astr. Ap.*, **125**, 23.
Böhm, K.H., and Solf, J. 1985, *Ap. J.*, **294**, 533.
Böhm, K.H., and Solf, J. 1990, *Ap. J.*, **348**, 297.
Carr, J.S. 1990, *Bull. AAS*, **21**, 1086.
Choe, S.U., Böhm, K.H., and Solf, J. 1985, *Ap. J.*, **288**, 338.
Cox, D.P., and Raymond, J.C. 1985, *Ap. J.*, **298**, 651.
Curiel, S. 1992, in the Astrochemistry of Cosmic Phenomena (IAU Symposium No. 150), edited by P.D. Sing, *Submitted.*
Draine, B.T. 1980, *Ap. J.*, **241**, 1021.
Draine, B.T., Roberge, W.G., and Dalgarno, A. 1983, *Ap. J.*, **264**, 485.
Edwards, S., and Snell, R.L. 1983, *Ap. J.*, **270**, 605.
Hartigan, P. 1989, *Ap. J.*, **339**, 987.
Hartigan, P., Curiel, S., and Raymond, J.C. 1989, *Ap. J. (Letters)*, **347**, L31.
Hartigan, P., Raymond, J., and Hartmann, L. 1987, *Ap. J.*, **316**, 323.
Hartigan, P., Raymond, J.C., and Meaburn, J. 1990, *Ap. J.*, **362**, 624.
Hartmann, L., and Raymond, J.C. 1984, *Ap. J.*, **276**, 560.
Hollenbach, D., and McKee, C.F. 1989, *Ap. J.*, **342**, 306.
Lizano, S., Heiles, C., Rodríguez, L.F., Koo, B., Shu, F.H., Hasegawa, T., Hayashi, S., and Mirabel, I.F. 1988, *A. J.*, **328**, 763.
McKee, C.F., and Hollenbach, D.J. 1987, *Ap. J.*, **322**, 275.
Norman, M.L., Winkler, K.H.A., and Smarr, L. 1983, *Astrophysical jets*, ed. A. Ferrari and A.G. Pacholczyk (Dordrecht: Reidel), P. 227.
Raga, A.C., and Böhm, K.H. 1985, *Ap. J. Suppl.*, **58**, 201.
Raga, A.C., and Böhm, K-H 1986, *Ap. J.*, **308**, 829.
Rózyczka, M., and Tenorio-Tagle, G. 1985a, *Astr. Ap.*, **147**, 220.
Rózyczka, M., and Tenorio-Tagle, G. 1985b, *Acta Astr.***35**, 213.
Sandford, M.T., and Whitaker, R.W. 1983, *MNRAS*, **205**, 105.
Schwartz, R.D., Williams, P.M., Cohen, M., and Jennings, D.G. 1988, *Ap. J. (Letters)*, **334**, L99.
Smith, M.D. 1991, *MNRAS*, **252**, 378.
Smith, M.D., and Brand, O.W.J.C. 1990, *MNRAS*, **245**, 108.
Solf, J., and Böhm, K.H. 1987, *A. J.*, **93**, 1172.
Stapelfeldt, K.R., Beichman, C.A., Hester, J.J., Scoville, N.Z., and Gautier III, T.N. 1991, *Ap. J. (Letters)*, *in press.*
Zinnecker, H., Mundt, R., Geballe, T.R., and Zealey, W.J. 1989, *Ap. J.*, **342**, 337.

Table 1
Line Ratios for a number of Bow-Shock Models

Line	BS100	BS90	BS80	BS70	BS60	BS50
Hβ[a]	5.25(-14)	3.63(-14)	2.36(-14)	1.42(-14)	7.71(-15)	3.54(-15)
SiIII 1206	4.4	0.8	0.4	0.2	0.1	0.0
Lyα	7407.0	7749.1	8161.8	8723.7	9544.0	10930.1
SiIII 1896	6.9	0.9	0.4	0.2	0.1	0.1
CIII 1908	7.7	2.1	1.0	0.6	0.3	0.2
CII 2325	43.3	37.4	41.7	50.5	66.3	97.7
MgII 2800	20.5	18.0	20.0	24.2	31.9	47.7
[OII] 3727	93.2	61.4	52.4	47.2	43.1	39.2
[SII] 4072	8.0	8.1	9.2	10.9	13.7	19.2
Hβ	100.0	100.0	100.0	100.0	100.0	100.0
[NI] 5200	13.7	16.5	21.0	28.4	41.6	69.2
[OI] 6300	52.2	65.0	82.8	109.0	152.2	234.8
Hα	336.6	345.1	355.1	367.9	384.3	410.6
[NII] 6560	55.9	52.9	56.3	62.1	70.4	81.8
[SII] 6725	110.9	129.9	161.4	209.8	290.2	444.3
2q	1600.4	1792.3	2018.3	2328.6	2784.4	3548.2
[OI] 7322	7.9	3.6	2.4	1.8	1.4	1.0
[FeII] 8617	15.8	18.6	22.4	28.2	38.0	56.9
CI] 9810	40.3	44.1	49.8	58.2	71.2	93.1
[FeII] 1.64μ	161.2	189.2	228.6	288.3	387.2	577.4
[FeII] 26.0μ	70.9	82.3	100.2	126.4	170.3	253.1
[SiII] 35μ	363.6	433.9	551.3	729.9	1041.7	1656.7
[OI] 63μ	1287.2	1401.5	1834.6	2381.6	3484.0	5688.8
[CII] 156μ	600.1	687.7	887.3	1170.0	1705.4	2807.6
20S1 1.16μ	70.5	66.6	60.6	69.5	95.5	154.2
20Q1 1.23μ	56.1	52.9	48.0	54.7	74.7	119.8
10S5 1.84μ	115.0	109.2	97.3	107.8	145.7	233.9
10S4 1.89μ	68.5	66.3	60.2	66.2	88.1	138.9
10S3 1.96μ	268.8	256.1	224.7	238.2	309.3	482.3
10S2 2.04μ	118.1	114.9	103.3	110.3	142.4	219.3
21S3 2.08μ	78.0	74.3	69.1	80.6	111.8	181.4
10S1 2.12μ	321.3	307.8	269.4	278.8	351.3	532.8
10S1 (shf)	321.3	307.8	269.4	278.8	351.3	532.8
10S0 2.22μ	95.6	93.0	82.8	86.1	108.1	162.1
21S1 2.25μ	93.6	88.4	80.5	92.4	126.9	204.9
21S1 (shf)	93.6	88.4	80.5	92.4	126.9	204.9
10Q1 2.41μ	292.1	281.8	249.7	259.0	322.2	478.4
10Q142.42μ	691.4	667.4	590.9	615.1	773.0	1162.8
10Q3 2.43μ	226.0	216.5	189.6	196.4	247.3	375.0
10Q5 2.46μ	131.3	125.1	109.7	116.3	151.1	235.6

[a] The fluxes are in ergs s^{-1} cm^{-2}.

Table 1 (Continuation)

Line	BS100	BS90	BS80	BS70	BS60	BS50
21Q1 2.55μ	87.3	82.4	74.8	85.2	116.2	186.4
21Q3 2.57μ	69.2	65.7	60.3	69.6	95.8	154.7
10O2 2.63μ	170.9	169.0	151.9	154.2	186.4	266.1
21O2 2.79μ	55.7	53.1	48.2	54.0	71.8	112.9
10O3 2.80μ	248.1	239.3	212.0	219.9	273.6	406.1
21O3 2.97μ	75.4	71.1	64.6	73.5	100.3	160.9
10O4 3.01μ	81.7	79.5	70.7	73.5	92.3	138.5
10O5 3.24μ	127.5	122.1	106.9	110.7	139.4	211.4
10O7 3.81μ	35.4	33.7	29.5	31.3	40.7	63.4
00S7 5.51μ	57.9	60.9	60.7	63.0	72.8	102.9
00S6 6.11μ	50.3	55.2	57.7	59.6	64.5	80.5
00S5 6.91μ	277.8	317.2	353.3	380.4	407.0	453.3
00S4 8.03μ	138.9	163.6	193.0	223.1	257.9	302.3
00S3 9.67μ	400.8	482.4	596.8	741.9	941.9	1232.1
00S2 12.3μ	81.7	99.5	126.3	164.9	226.3	333.6
00S1 17.0μ	81.5	99.1	127.1	170.1	244.6	390.2
00S0 28.2μ	3.4	4.0	5.2	6.8	10.0	16.4

[a] The fluxes are in ergs s^{-1} cm^{-2}.

Table 2
Comparison between Observed and Calculated Line Profiles

Line	FWHM (km s^{-1})	FWZI (km s^{-1})	V^a_{rad} (km s^{-1})	Aperture (")/(km s^{-1})	Reference
Hα	92	145	-58	2.2 / 20	Solf and Böhm
Hα	55	130	-55	2.2 / 20	This Model
[SII]	83	150	-58	2.2 / 20	Solf and Böhm
[SII]	60	125	-55	2.2 / 20	This Model
H_2 1-0S(1)	45	—	-11	11 / 35	Zinnecker *et al.*
H_2 1-0S(1)	50	90	-15	11 / 35	This Model
H_2 1-0S(1)	—	~150	-10	3 / 25	Carr
H_2 1-0S(1)	40	75	-25	3 / 25	This Model

[a] Velocity of the center of the line with respect to the molecular cloud.
[b] Solf and Böhm (1987), Zinnecker *et al.* (1989), Carr (1990).

Table 3
Optical Line Rations

Line	M80	M100	Observed	Aperture	Reference
Hβ[a]	2.30	5.09	2.91	—	Böhm *et al.*
MgII 2795/2802	20.0	20.5	19.6	—	Cameron and Liseau
[OII] 3726/29	52.4	93.2	89	—	Böhm *et al.*
[SII] 4068/76	9.2	8.0	135	—	Böhm *et al.*
Hβ	100	100	100	—	Böhm *et al.*
[OI] 6300	82.8	52.2	421	—	Böhm *et al.*
Hα 6563	355	337	370	—	Böhm *et al.*
[NII] 6548/84	56.3	55.9	17	—	Böhm *et al.*
[SII] 6717/31	161.4	110.9	1369	—	Böhm *et al.*
[OII] 7319/30	2.4	7.9	29	—	Böhm *et al.*
FeII 8616	22.4	15.8	32	—	Böhm and Solf
[CI] 9824/48	49.8	40.3	647	—	Böhm *et al.*

[a] Velocity of the center of the line with respect to the molecular cloud.
[b] Solf and Böhm (1987), Zinnecker *et al.* (1989), Carr (1990).

Table 4
Infrared Line Fluxes

Line	M100 (10^{-14} erg cm^{-2} s^{-1})	Observed	Aperture (")	Reference[b]
Hβ[a]	5.09	2.91	—	Böhm *et al.*
1-0S(1)	16.4	67	12	Hartigan *et al.*
1-0S(1)	16.4	67	12	Stapelfieldt *et al.*
1-0S(1)	13.1	20	5	Hartigan *et al.*
1-0S(1)	13.1	18	5	Burton *et al.*
2-1S(1)	4.8	5.9	12	Stapelfieldt *et al.*
2-1S(1)	3.6	1.8	5	Burton *et al.*
1-0O(7)	1.4	1.9	5	Burton *et al.*
1-0S(0)	3.9	4.4	5	Burton *et al.*
1-0Q(3)	9.2	65	12	Stapelfieldt *et al.*
[a][FeII] 1.64μ	8.3/5.3	10.3	12	Stapelfieldt *et al.*

[a] Fluxes for two models: 80 and 100 km s^{-1}.
[b] Böhm, Brugel and Olmsted (1983), Hartigan, Curiel and Raymond (1989).

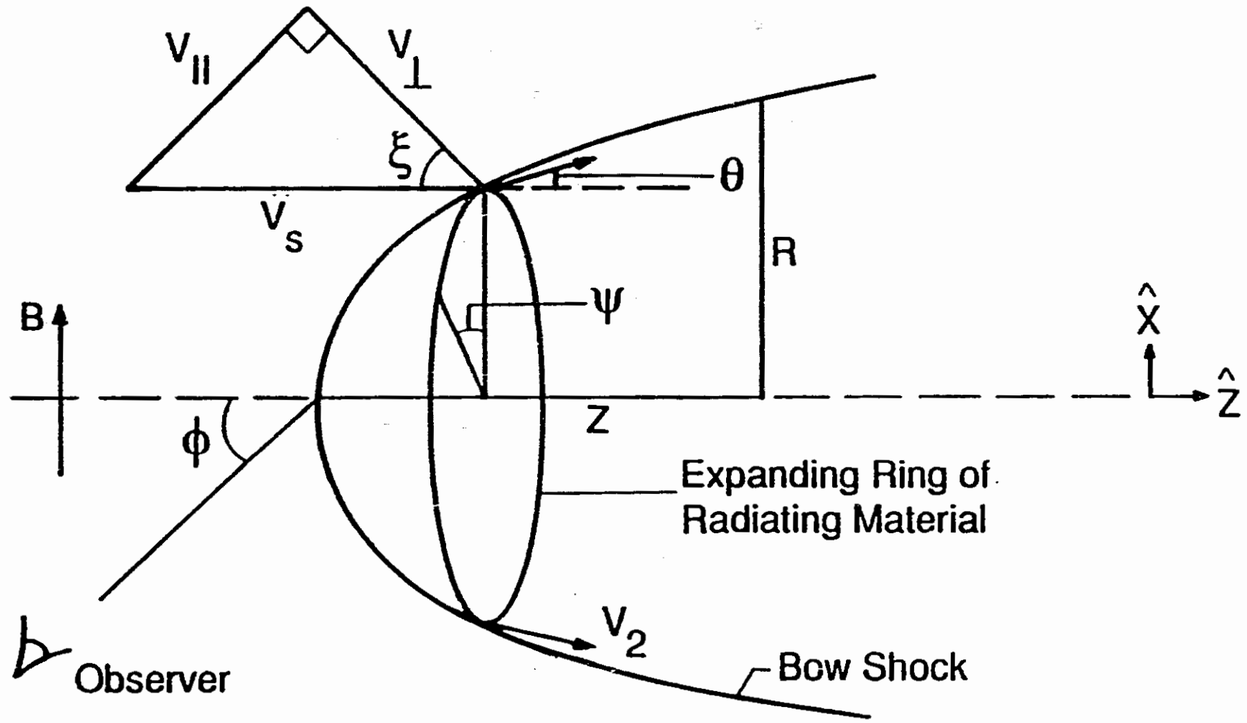

Figure 1. Bow shock geometry.

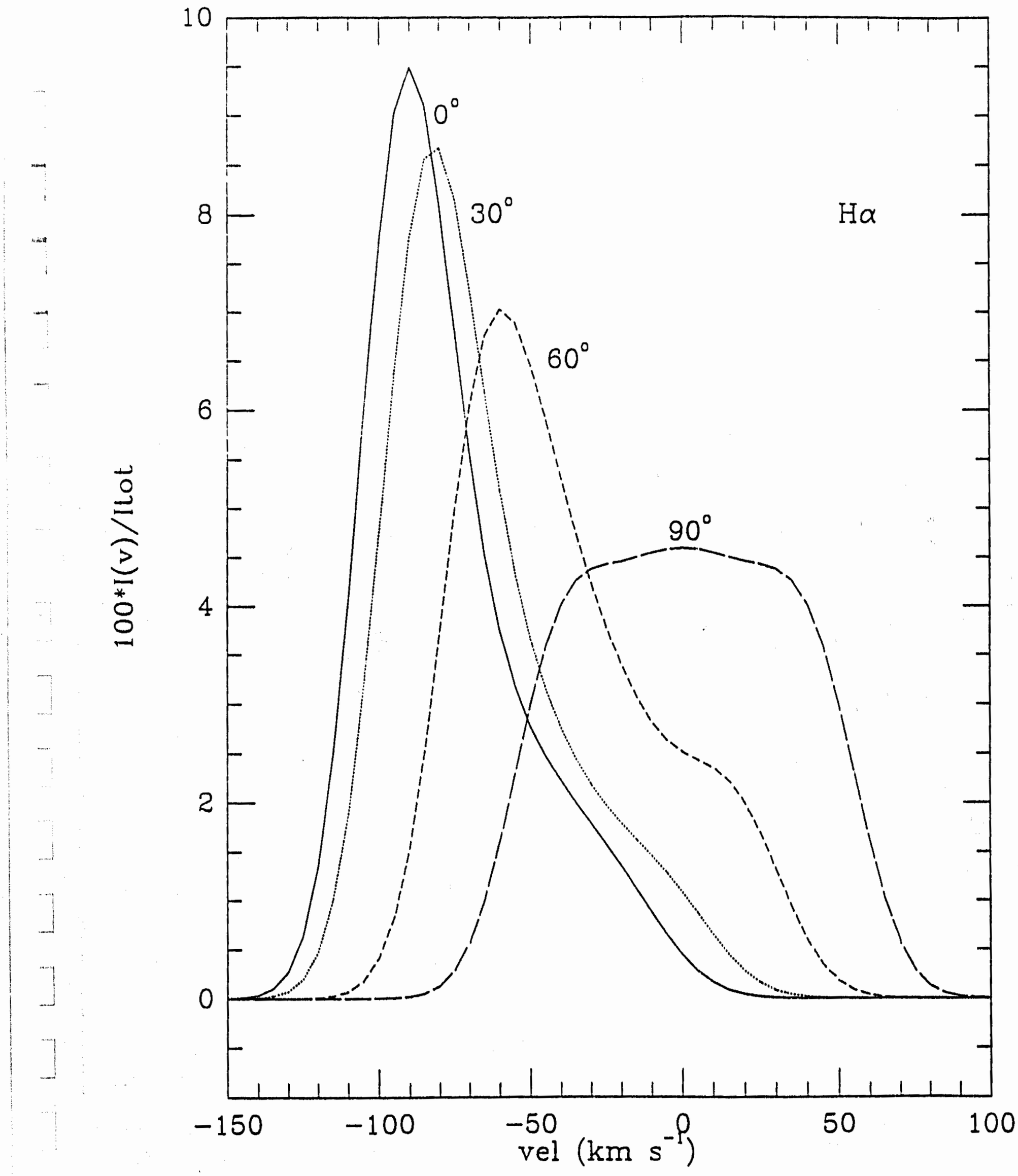

Figure 2. H_α line profiles for viewing angles ϕ between 0° and 90° from the line-of-sight.

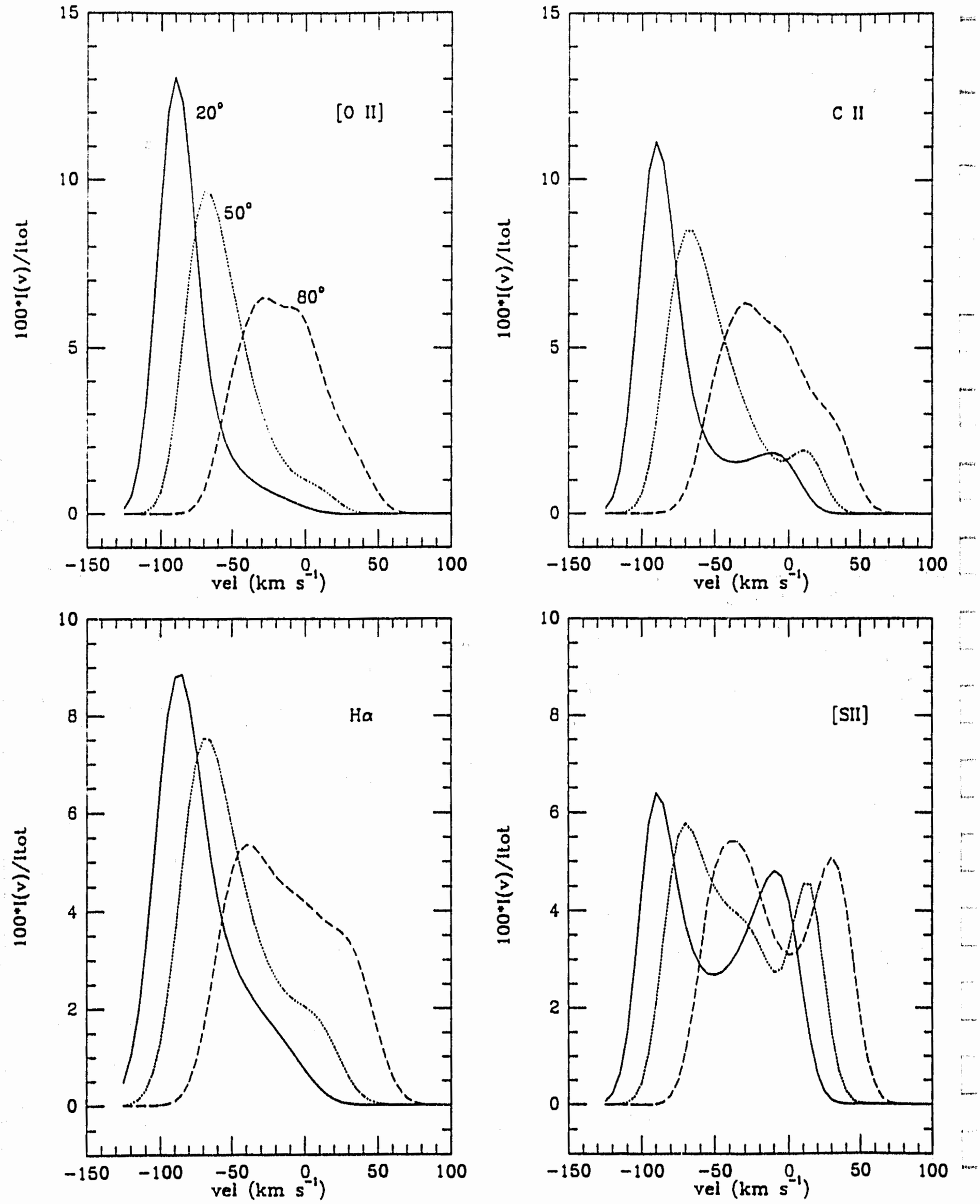

Figure 3. Optical and ultraviolet line profiles obtained for orientation angles $\phi = 20°$, 50 and 80° with respect to the line-of-sight. The lines shown in this figure are Hα, [SII] λ6716/31, [OII] λ3726/29 and CII λ2326.

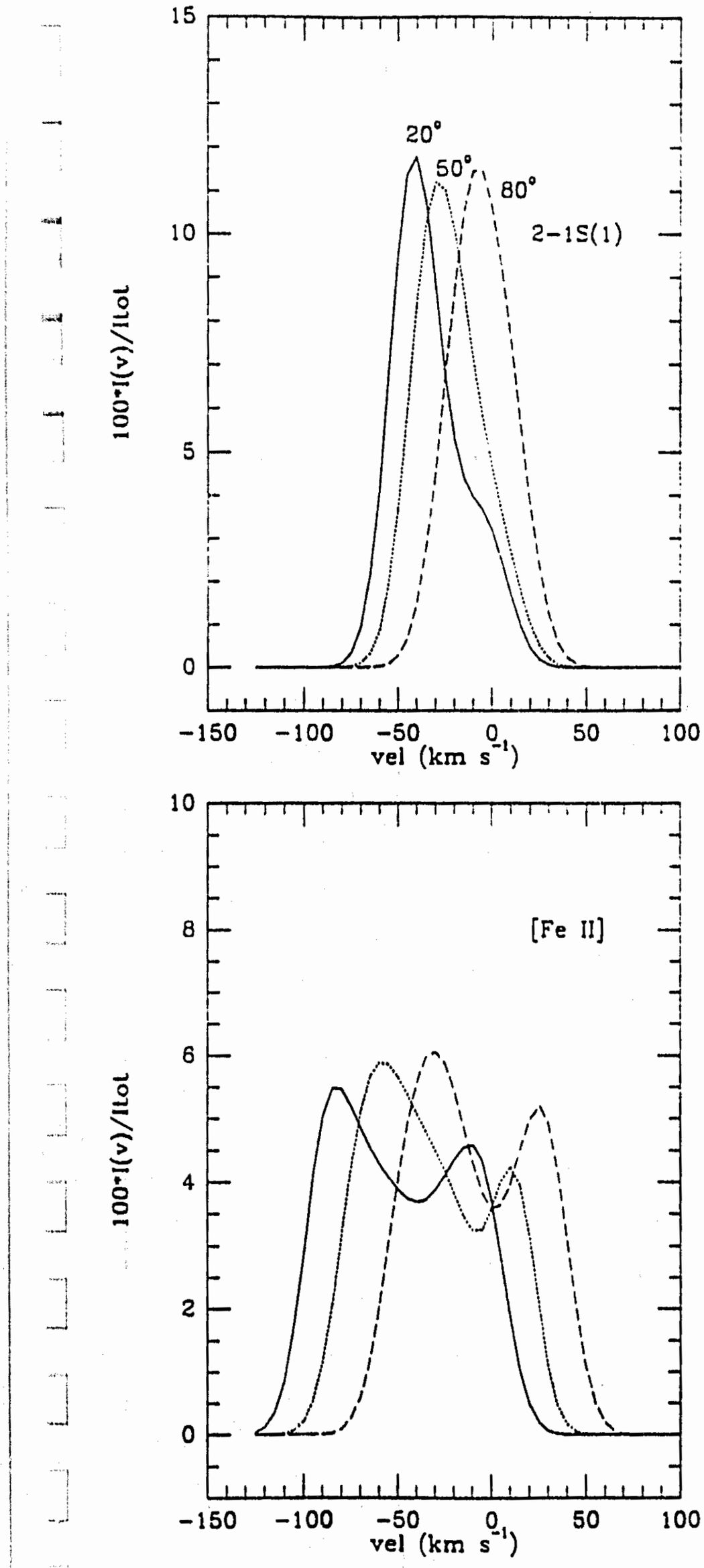

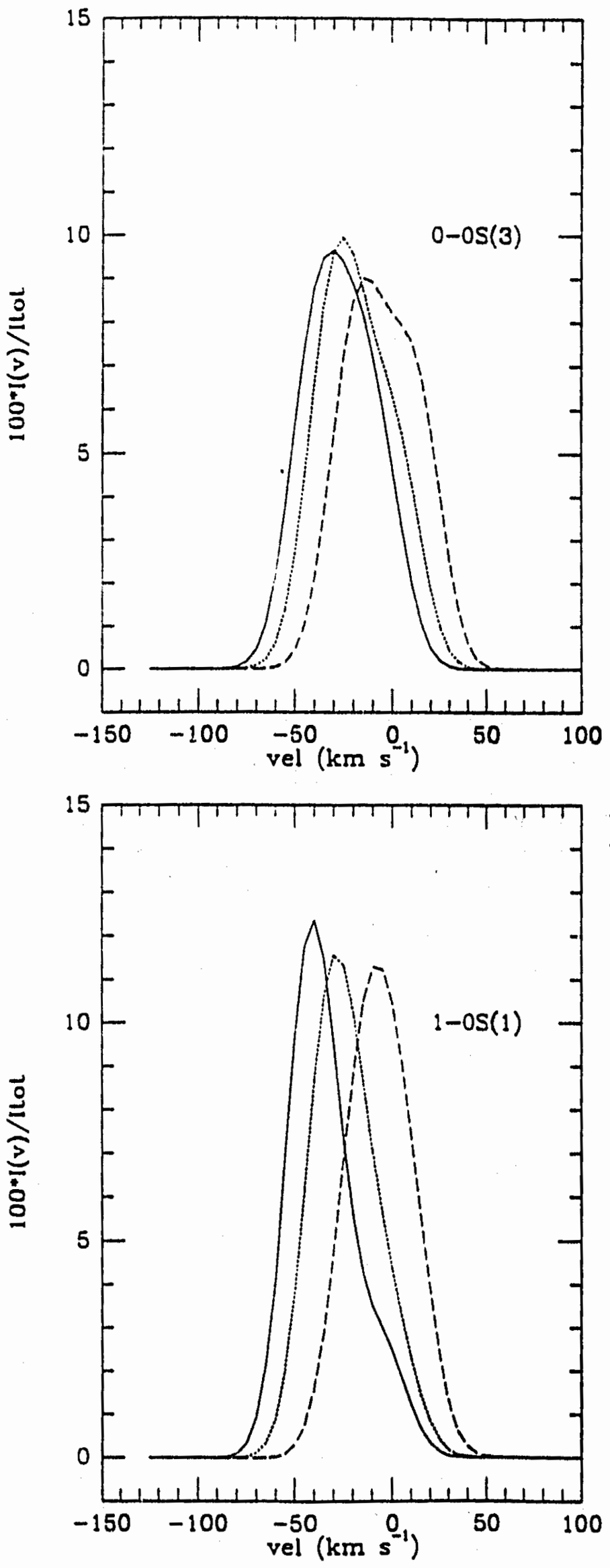

Figure 4. Atomic and H_2 infrared line profiles obtained for orientation angles $\phi = 20°$, 50° and 80° with respect to the line-of-sight. The lines shown in this figure are [FeII] at 1.64μ, 1–0S(1) at 2.12μ, 2–1S(1) at 2.25μ and 0–0S(3) at 9.67μ.

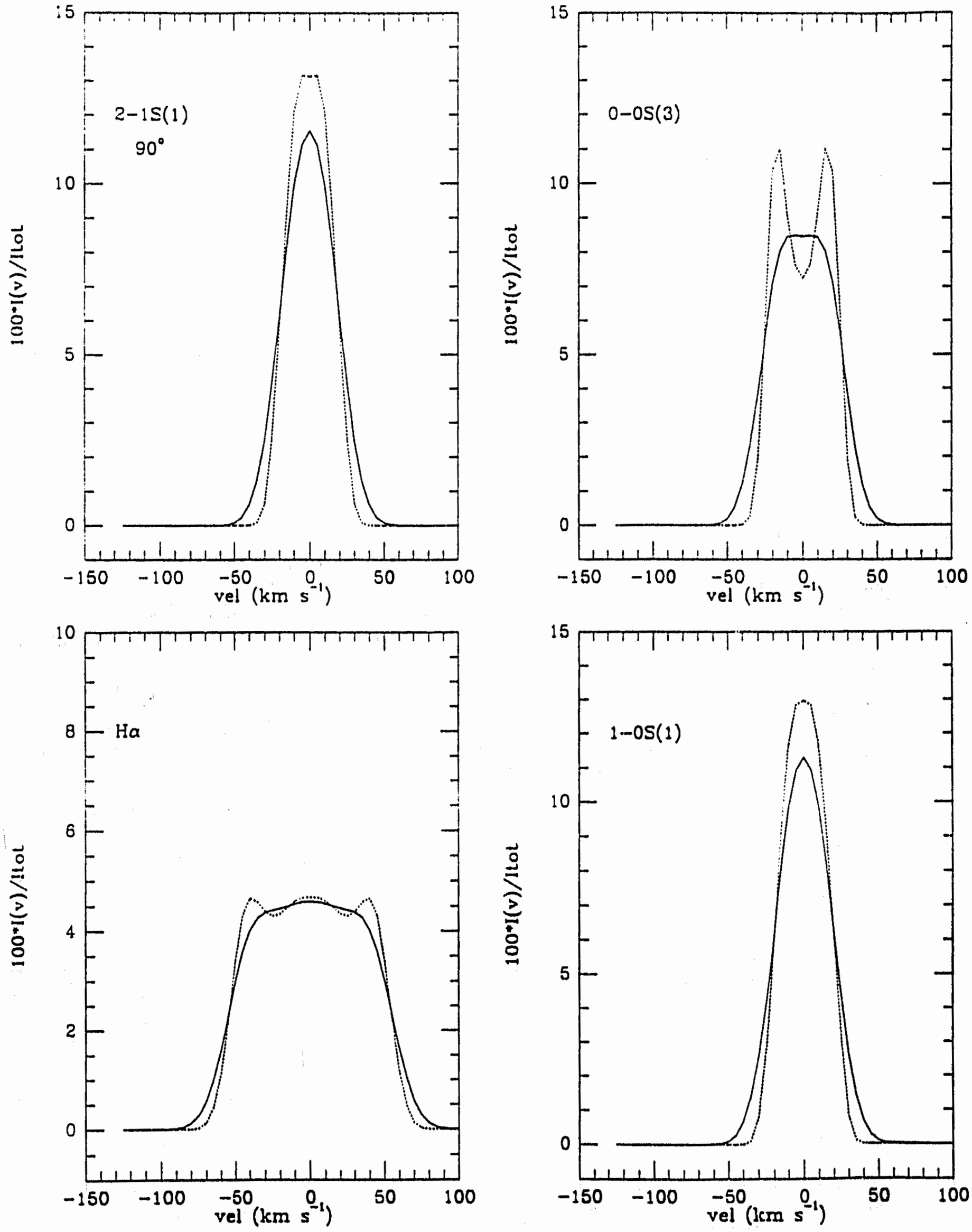

Figure 5. Optical and infrared lines calculated for an inclination angle of 90° from the line-of-sight. This figure shows the effects of the instrumental broadening in the line profile. The solid and dotted lines correspond to line profiles in which instrumental broadening was and was not taken into account respectively.

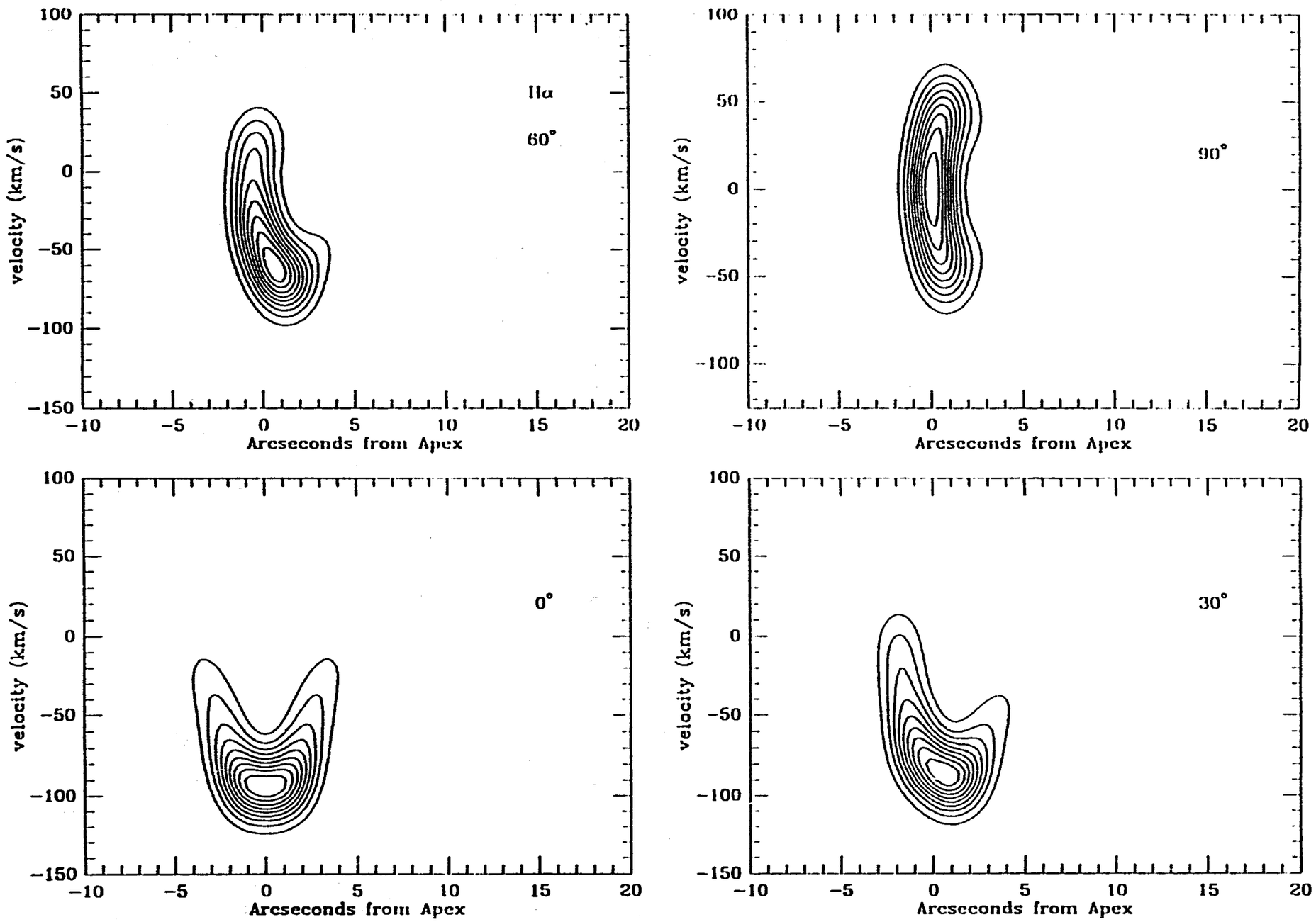

Figure 6. H_α position-velocity diagrams for viewing angles ϕ between 0° and 90° from the line-of-sight. The contours in this and the next three figures are plotted in units of 0.1 of the peak intensity.

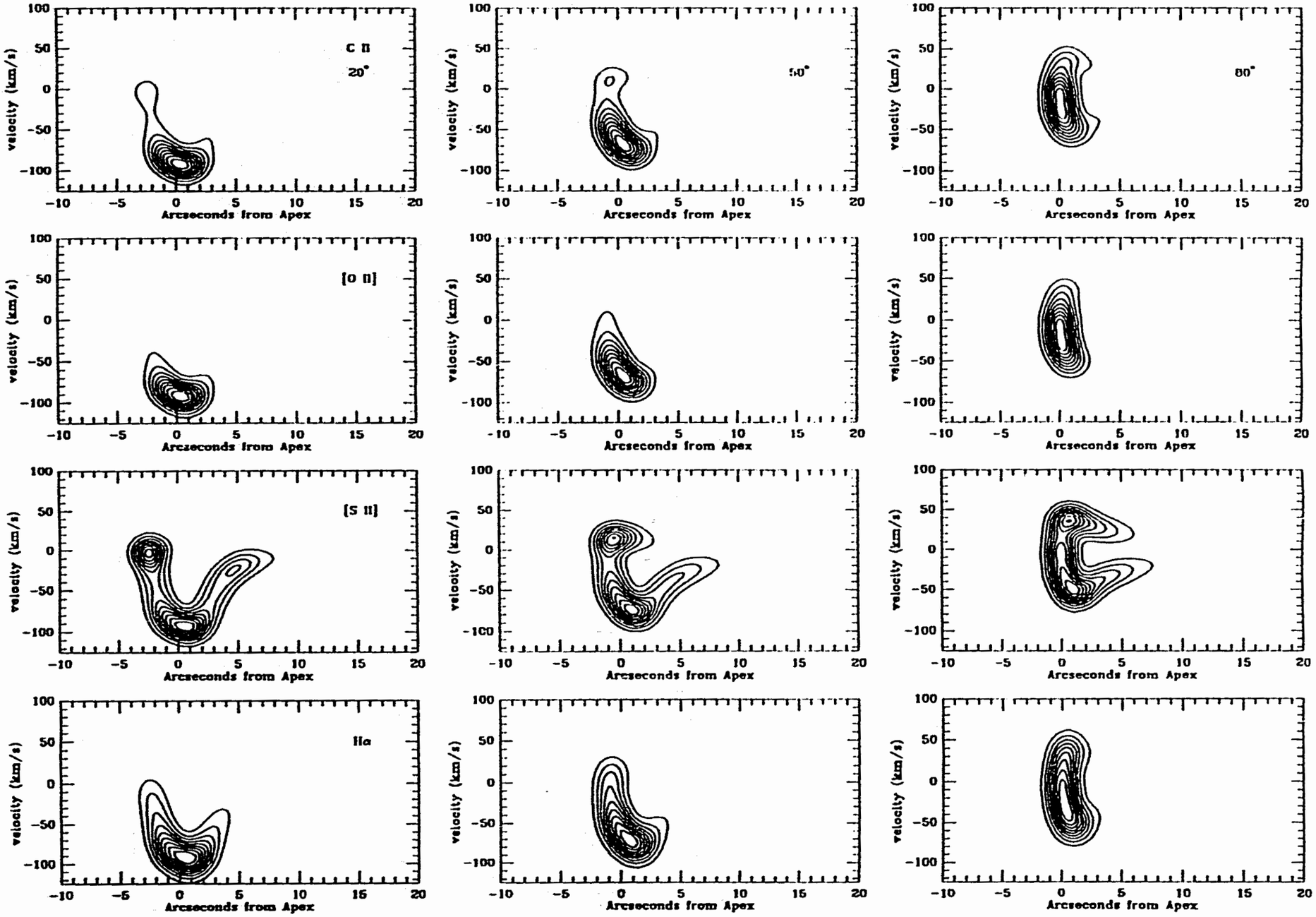

Figure 7. Optical and ultraviolet position-velocity diagrams obtained for orientation angles $\phi = 20°$, 50° and 80° with respect to the line-of-sight. The lines shown in this figure are Hα, [SII] λ6716/31, [OII] λ3726/29 and CII λ2326.

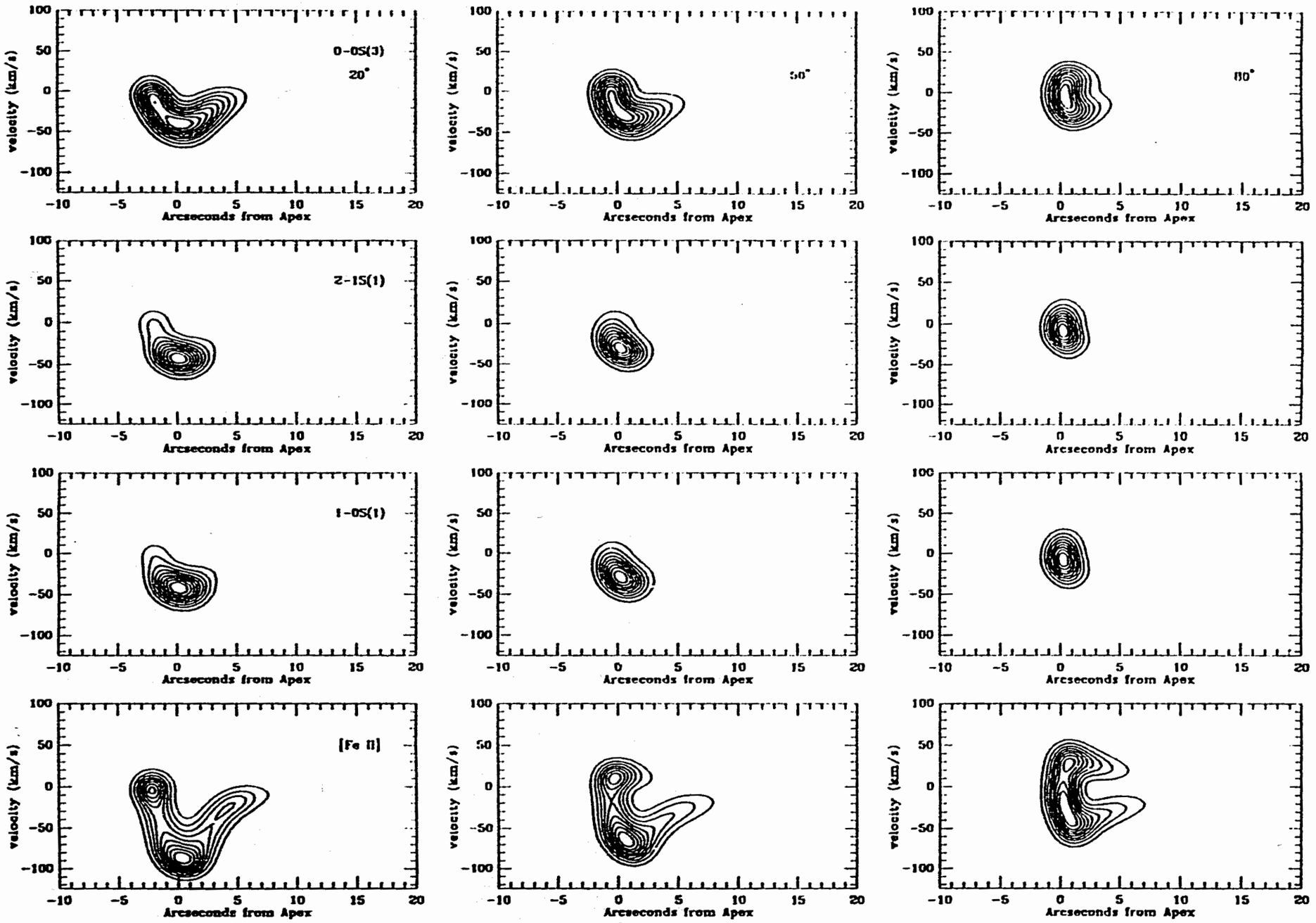

Figure 8. Atomic and H_2 infrared position-velocity diagrams obtained for orientation angles $\phi = 20°$, 50° and 80° with respect to the line-of-sight. The lines shown in this figure are [FeII] at 1.64μ, 1-0S(1) at 2.12μ, 2-1S(1) at 2.25μ and 0-0S(3) at 9.67μ.

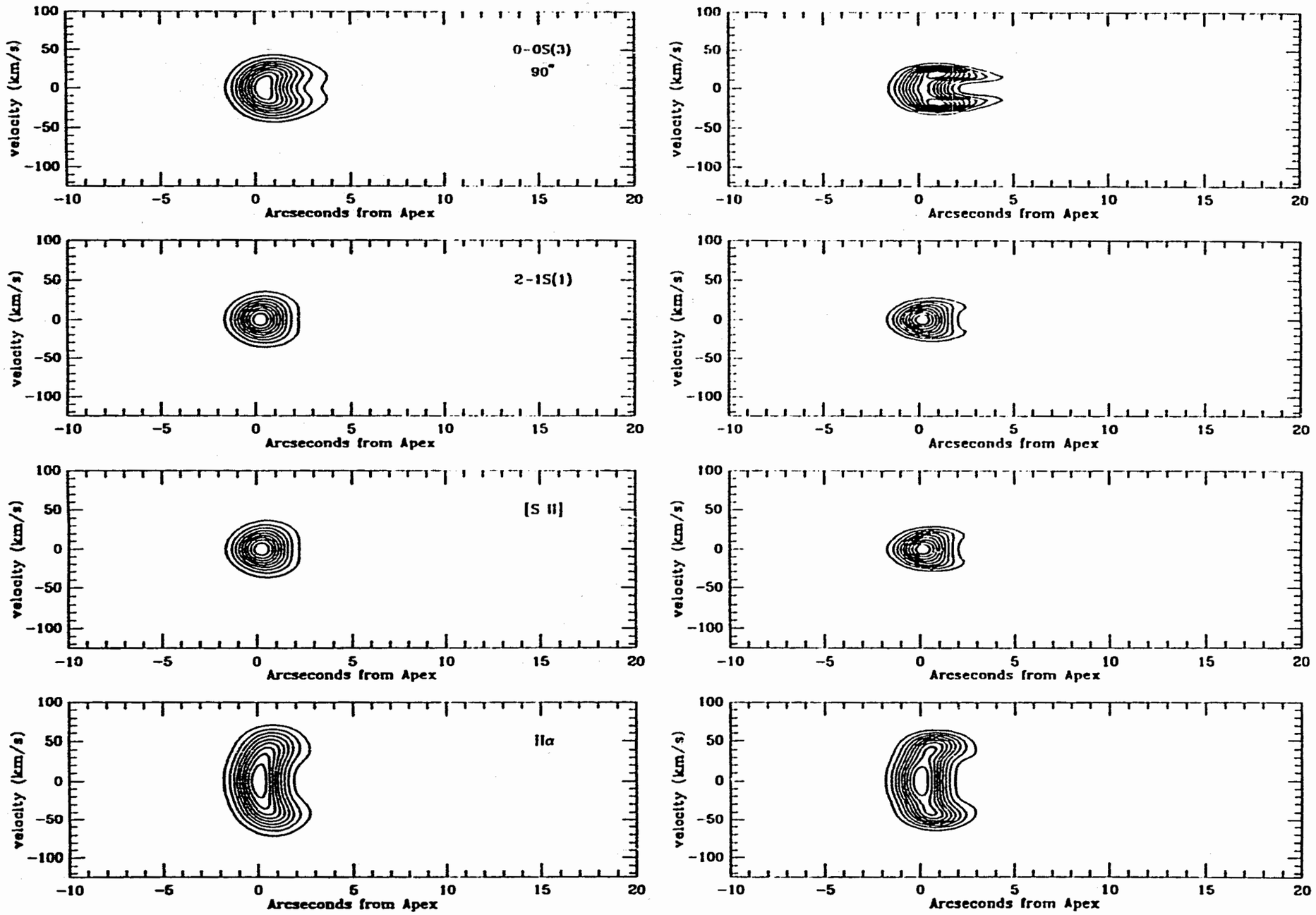

Figure 9. Effects of the instrumental broadening in the position-velocity diagram of optical and infrared lines for an inclination angle of 90°. The left and right panels correspond to diagrams in which instrumental broadening [illegible] and [illegible] not [illegible] respectively

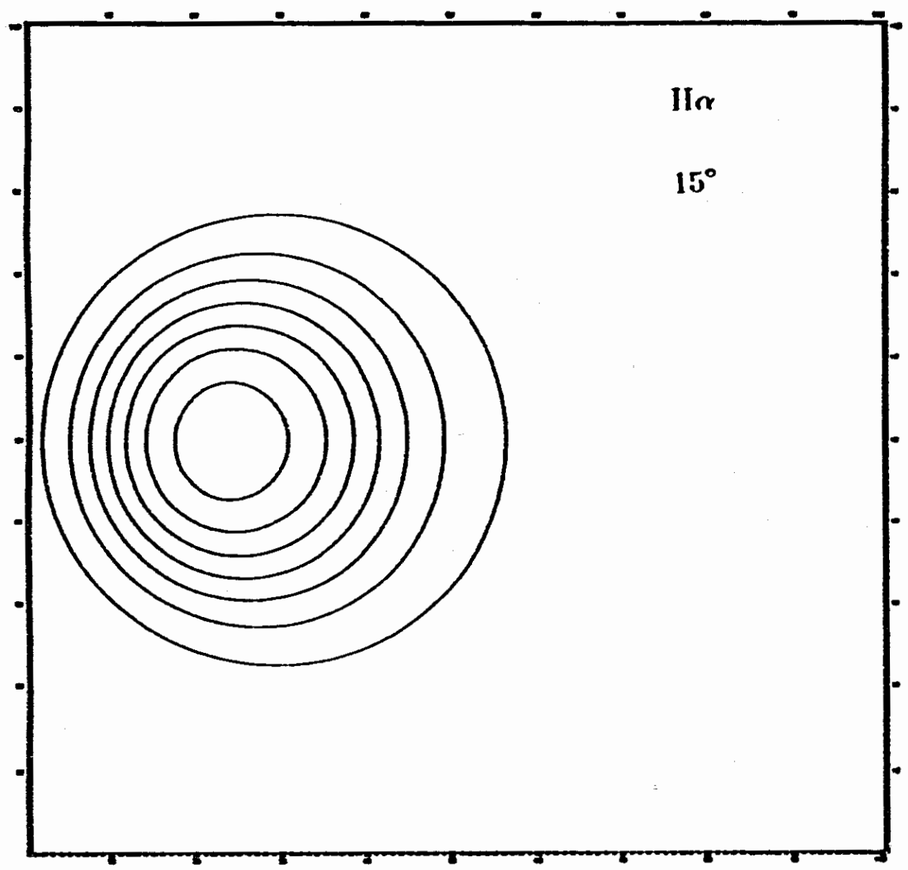

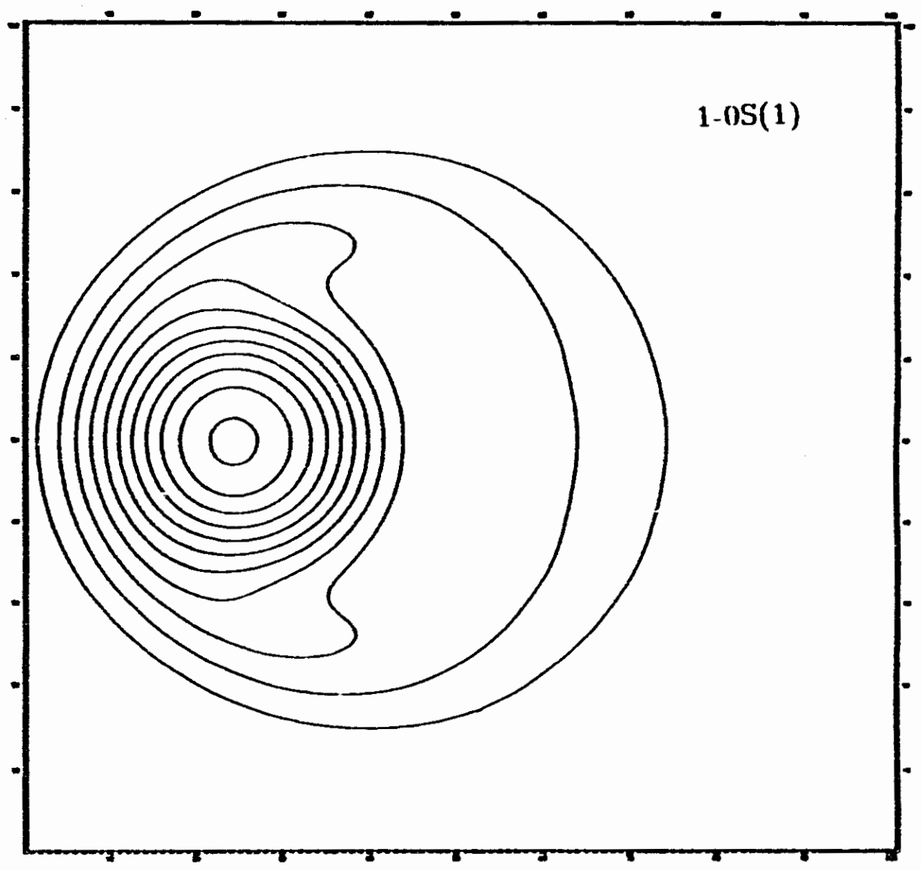

Figure 10. Predicted Hα and 1–0S(1) contour maps for a bow-shock moving through a magnetized molecular medium with inclination angles between 0° and 90° from the line-of-sight. The contours in this and the next figure are plotted in units of 0.1 of the square root of the peak intensity.

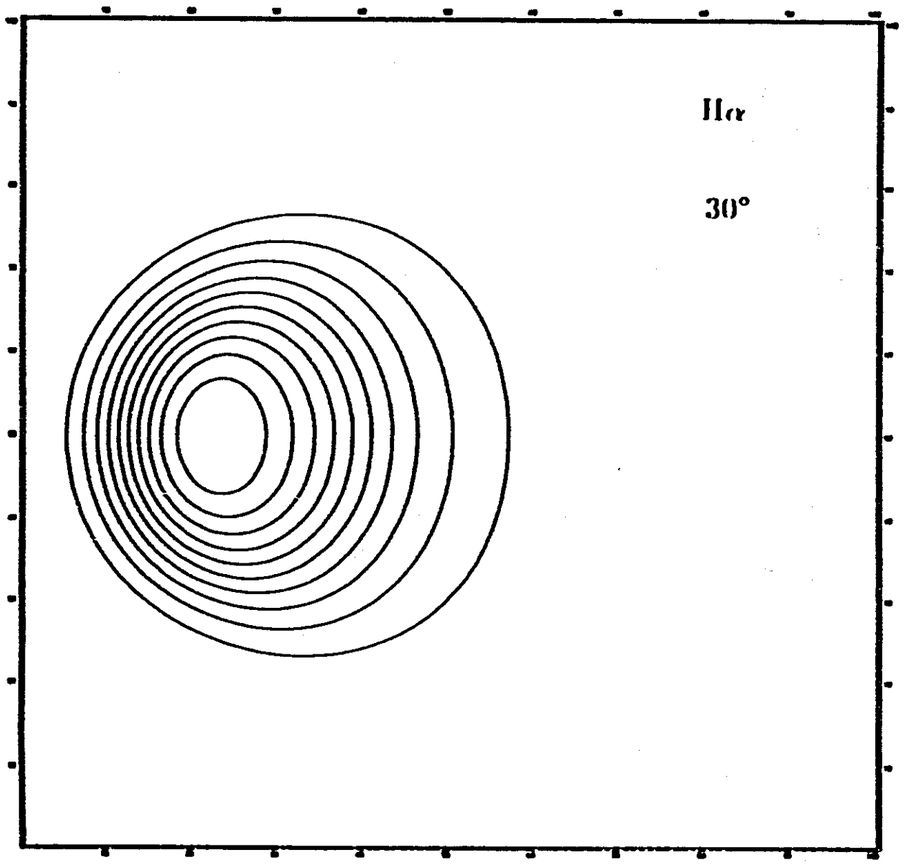
Hα
30°

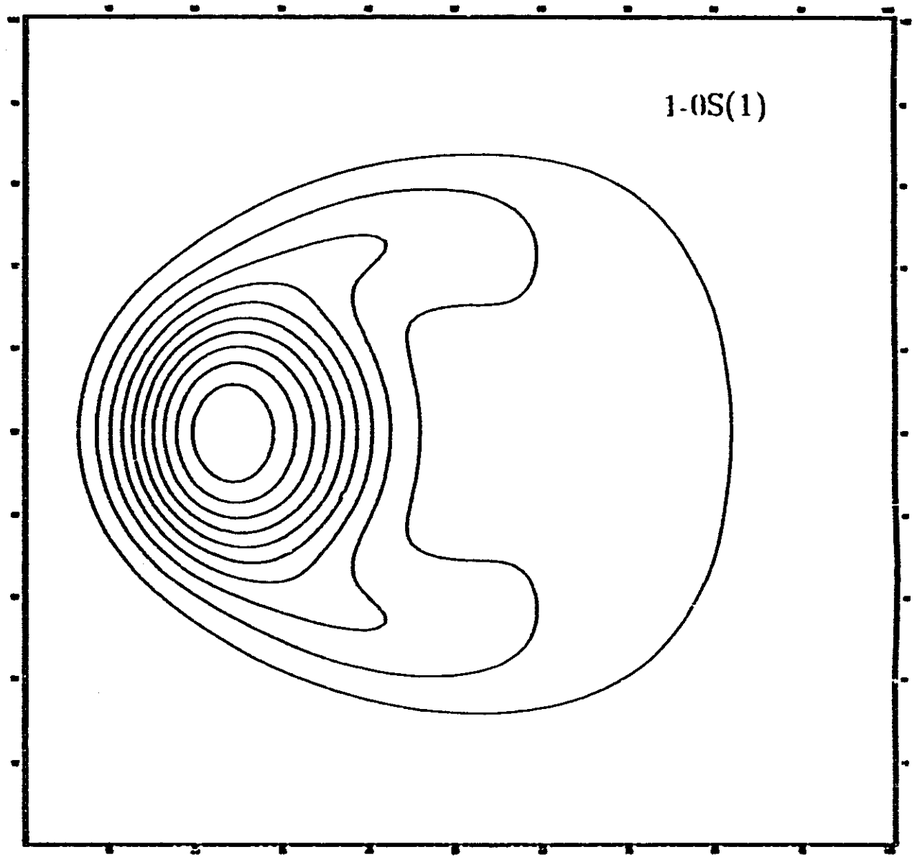
1-0S(1)

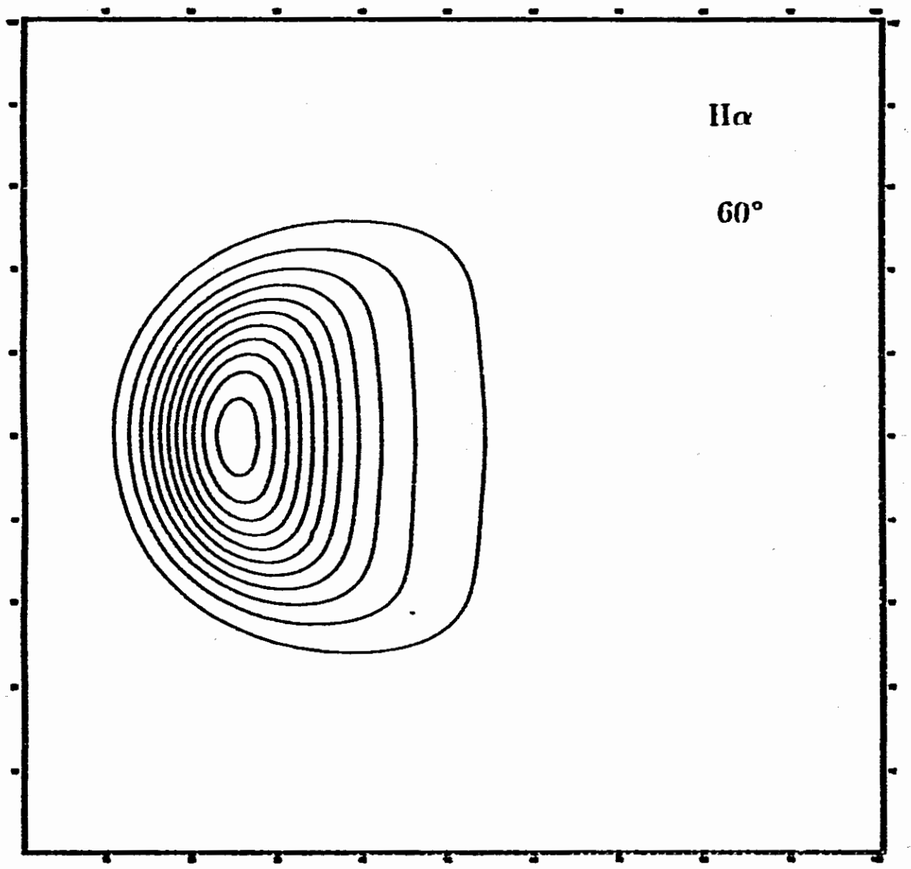
Hα
60°

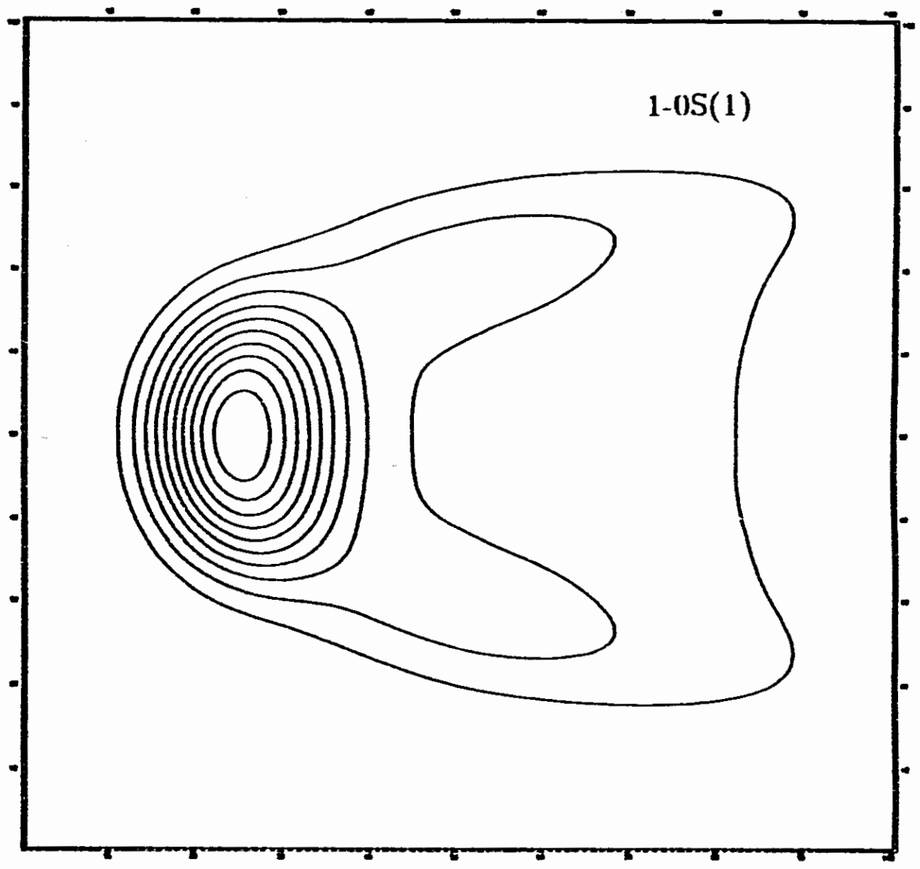
1-0S(1)

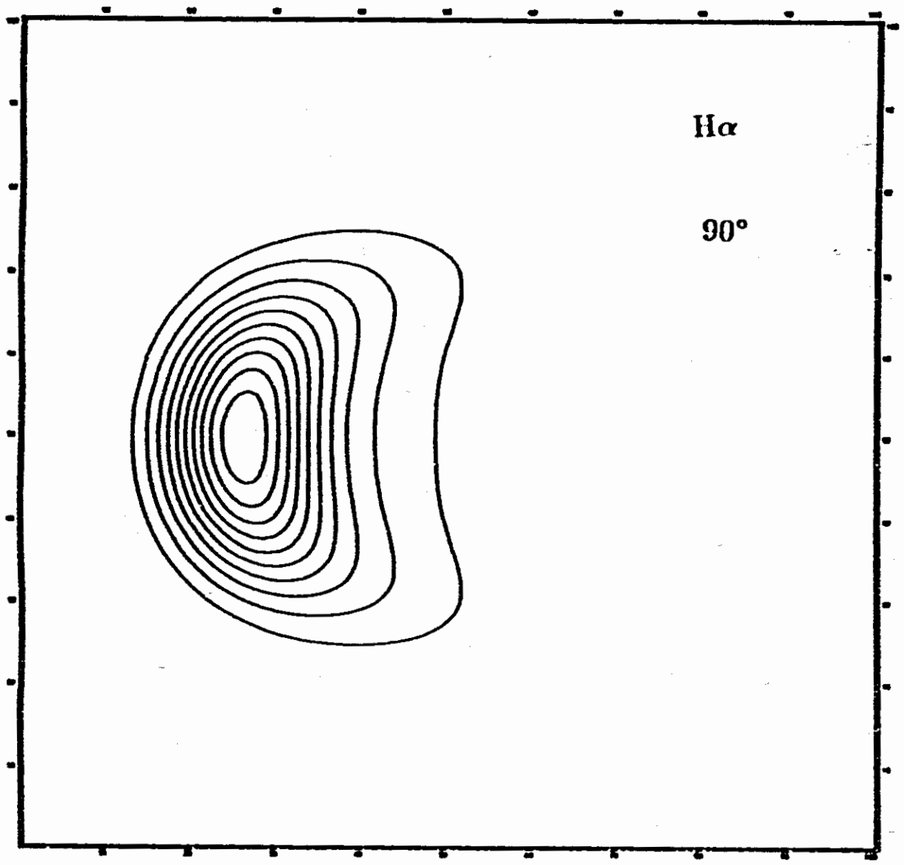
Hα
90°

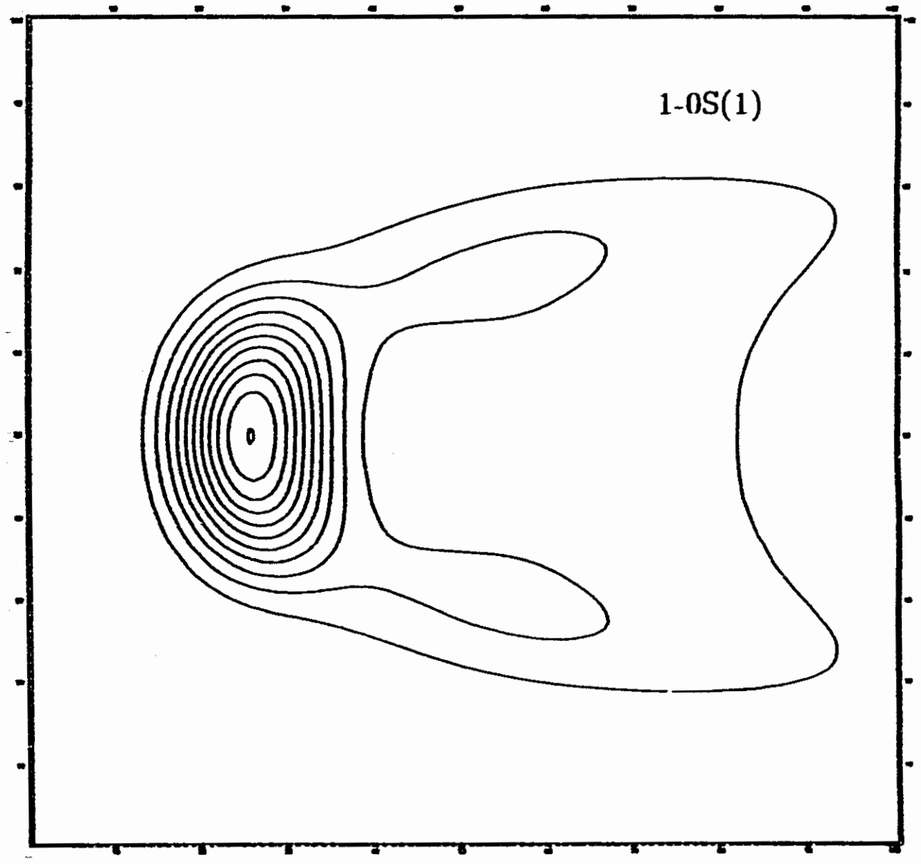
1-0S(1)

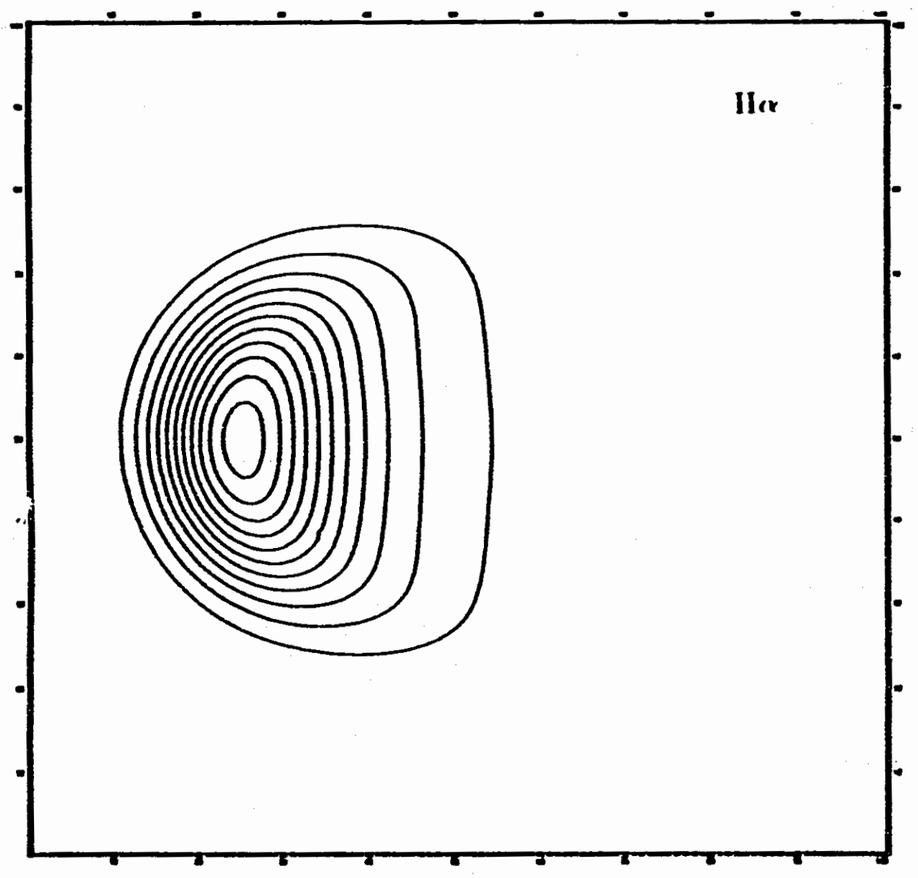

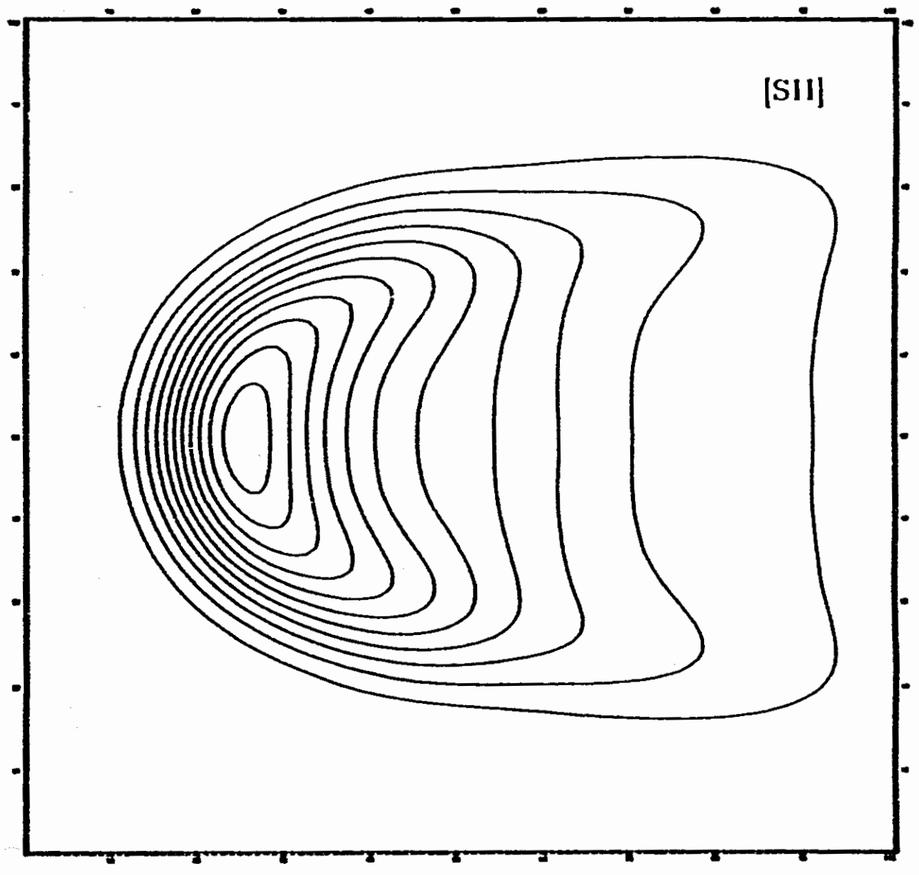

Figure 11. Predicted contour maps for a number of optical and infrared lines for a bow-shock moving through a magnetized molecular medium with an inclination angle of 60°.

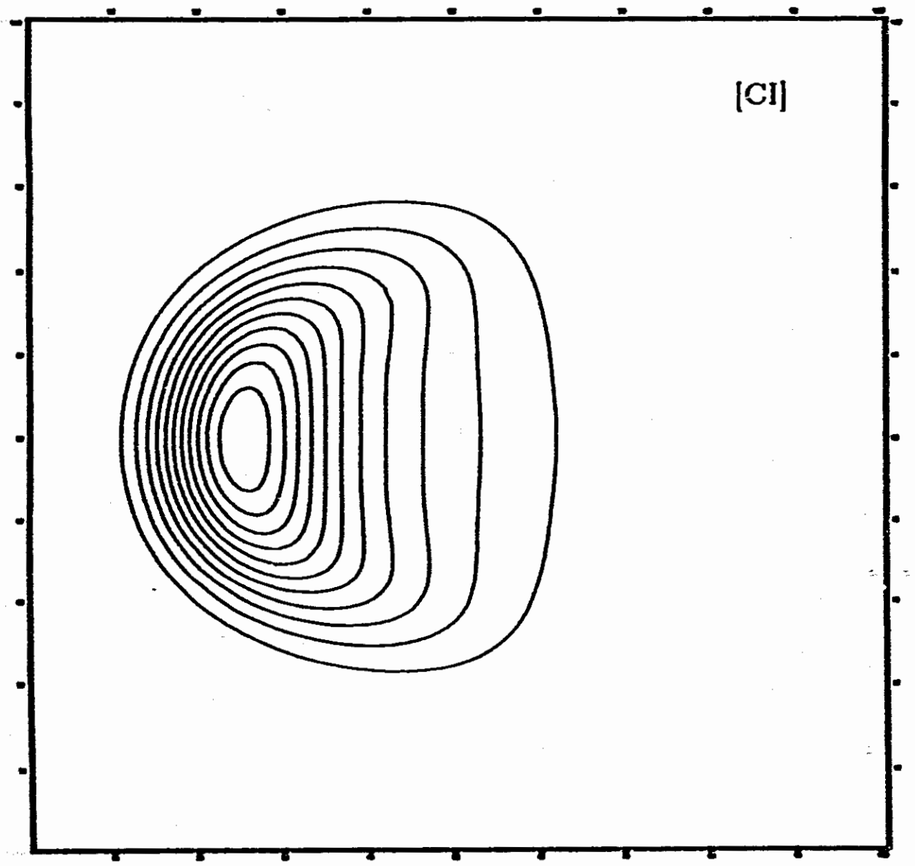
[CI]

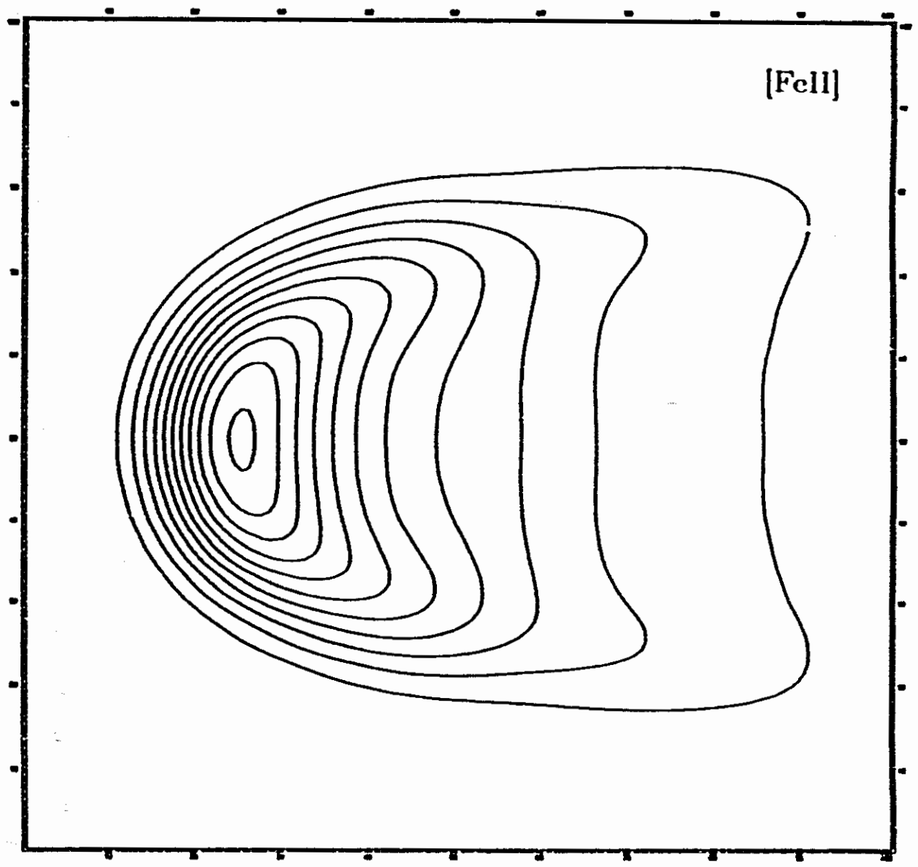
[FeII]

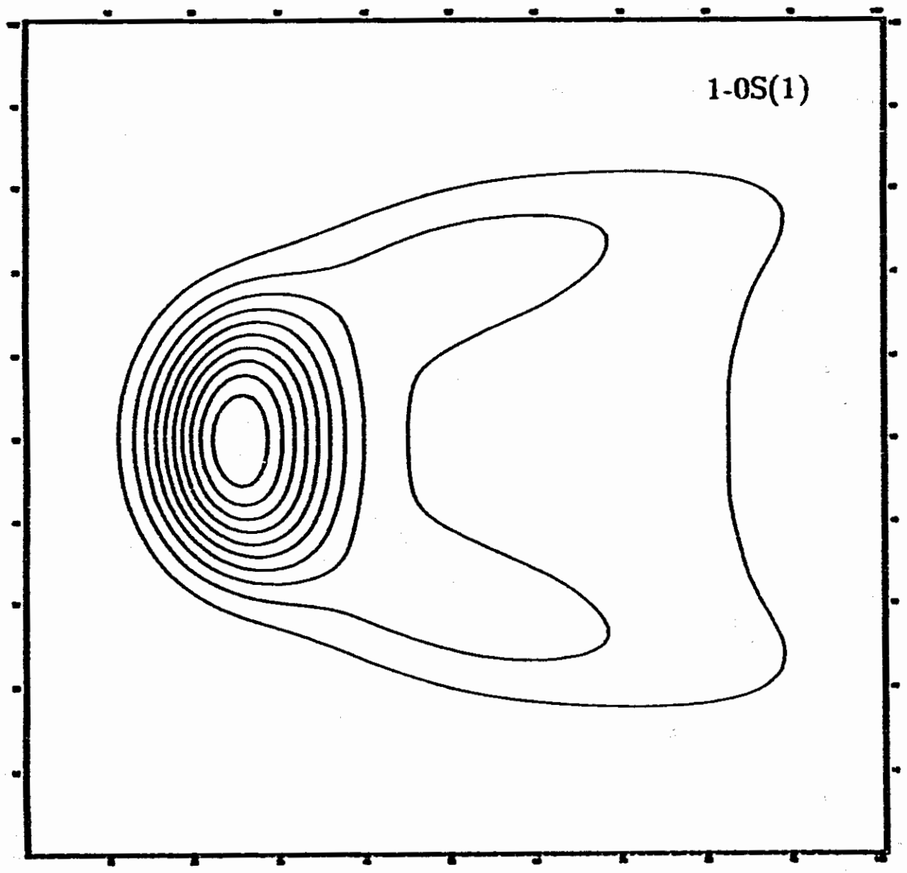
1-0S(1)

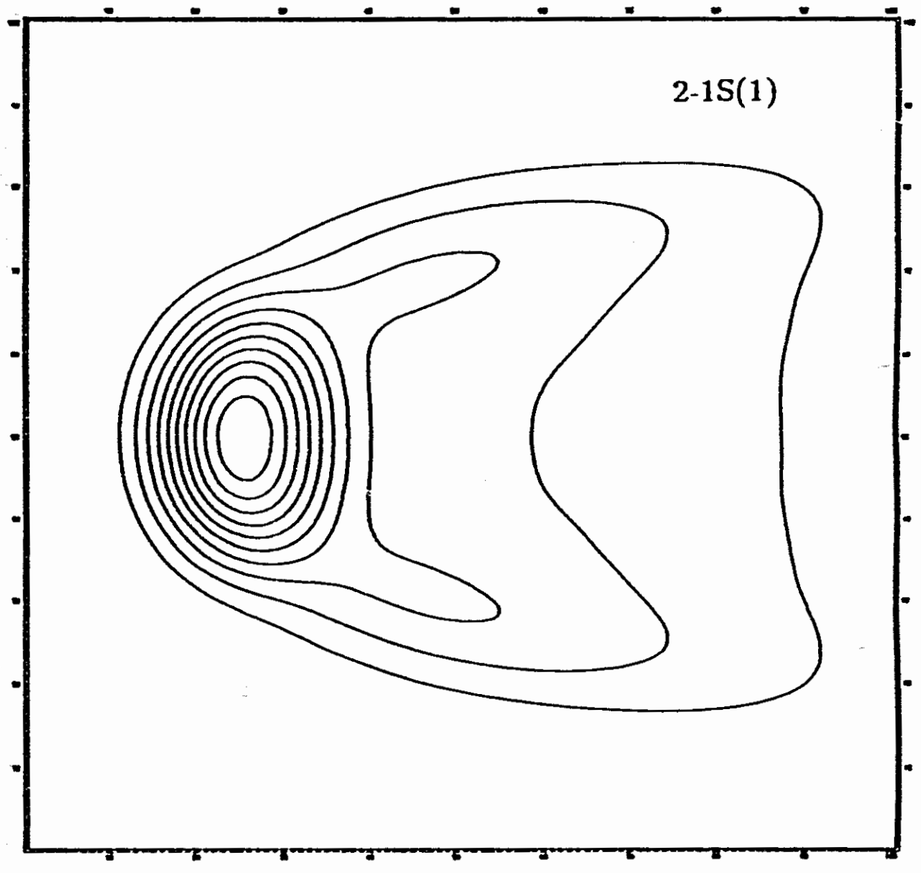
2-1S(1)

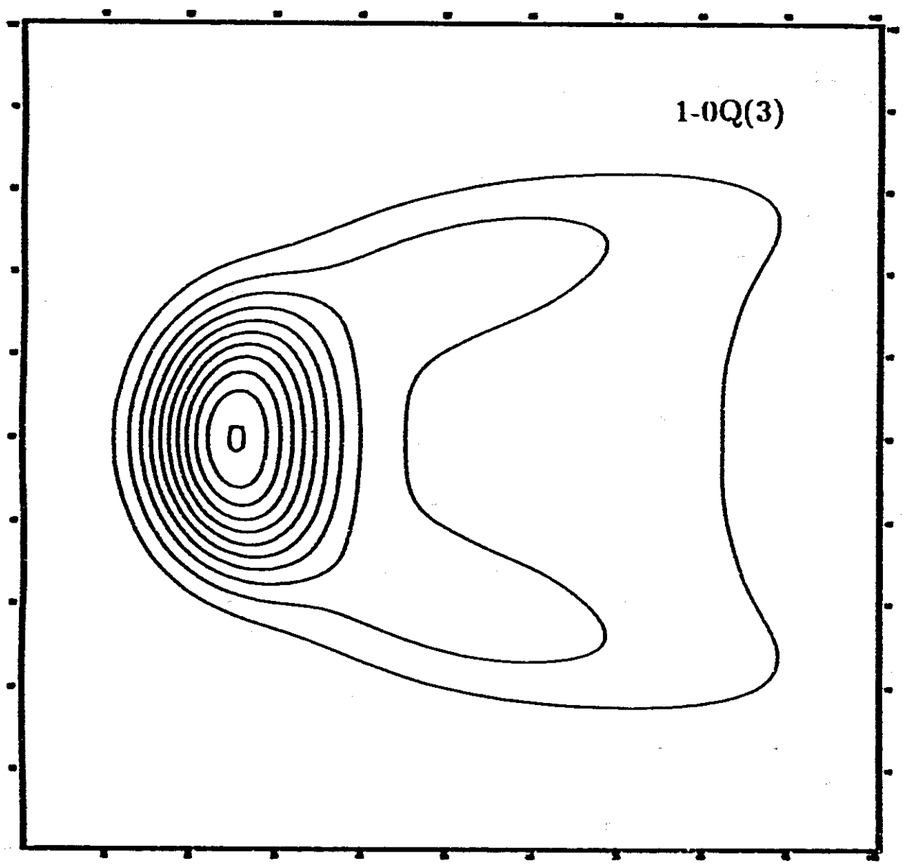
1-0Q(3)

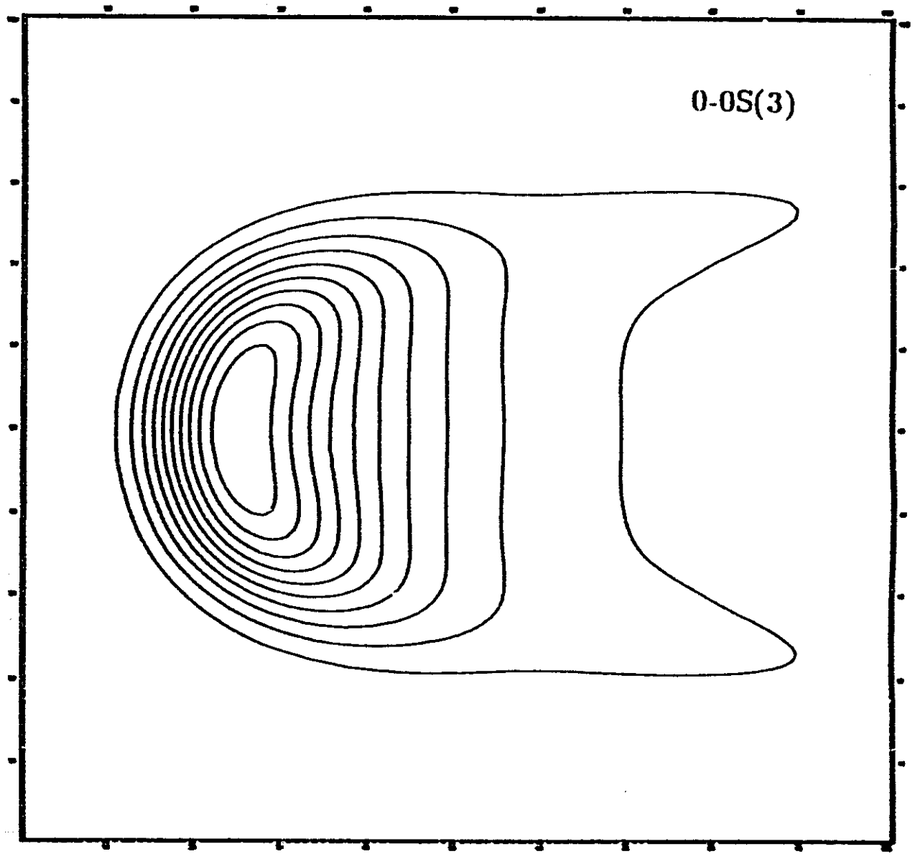
0-0S(3)

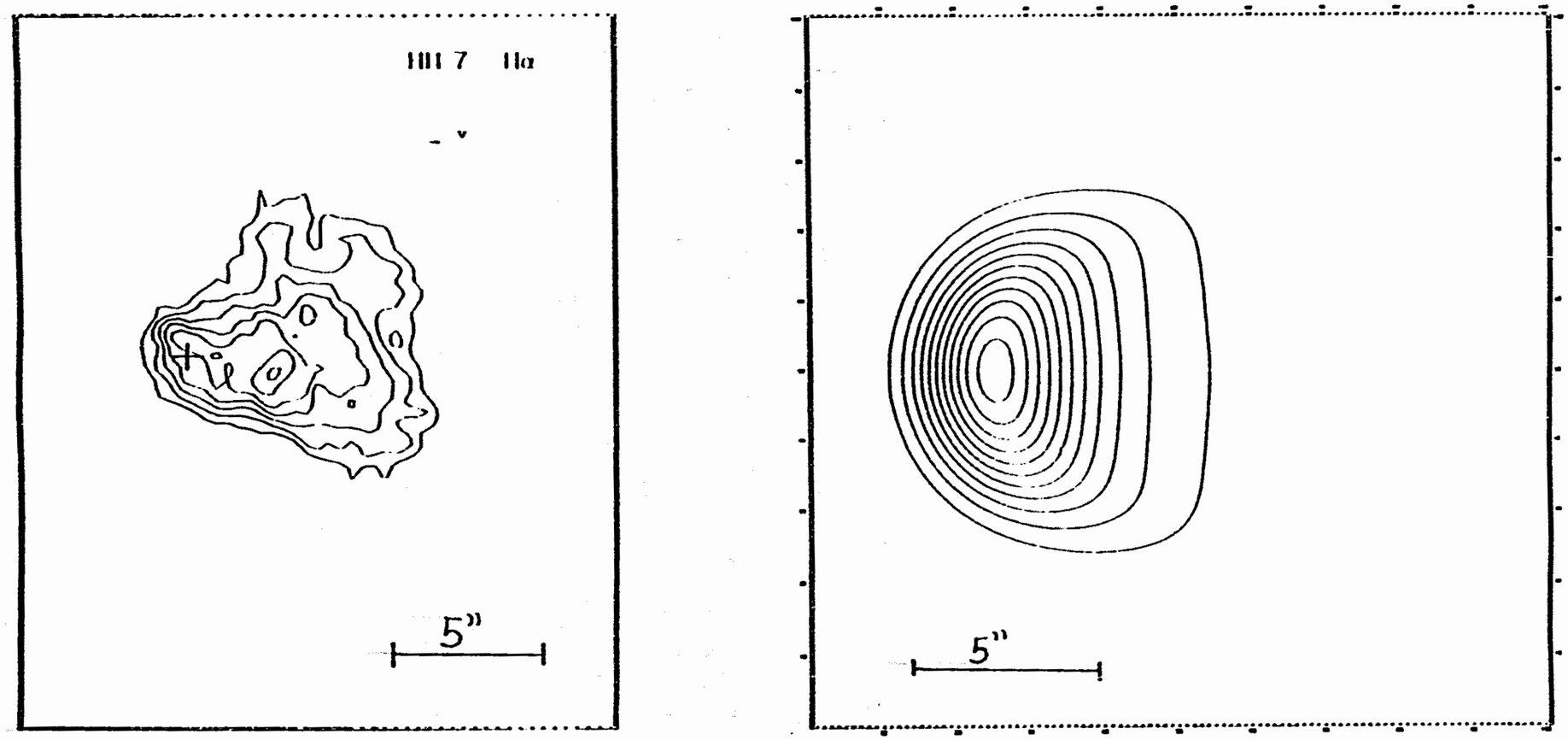

Figure 12. Comparison between observed Hα, [SII] and H_2 1-0S(1) contour maps (left) for the HH7 object by Hartigan, Curiel and Raymond (1989), and those calculated for a bow-shock moving with an inclination angle of 60° (right). The observed contours are linear and range from the surrounding sky level to the maximum intensity in each image, while the calculated ones are plotted in units of 0.1 of the square root of the peak intensity.

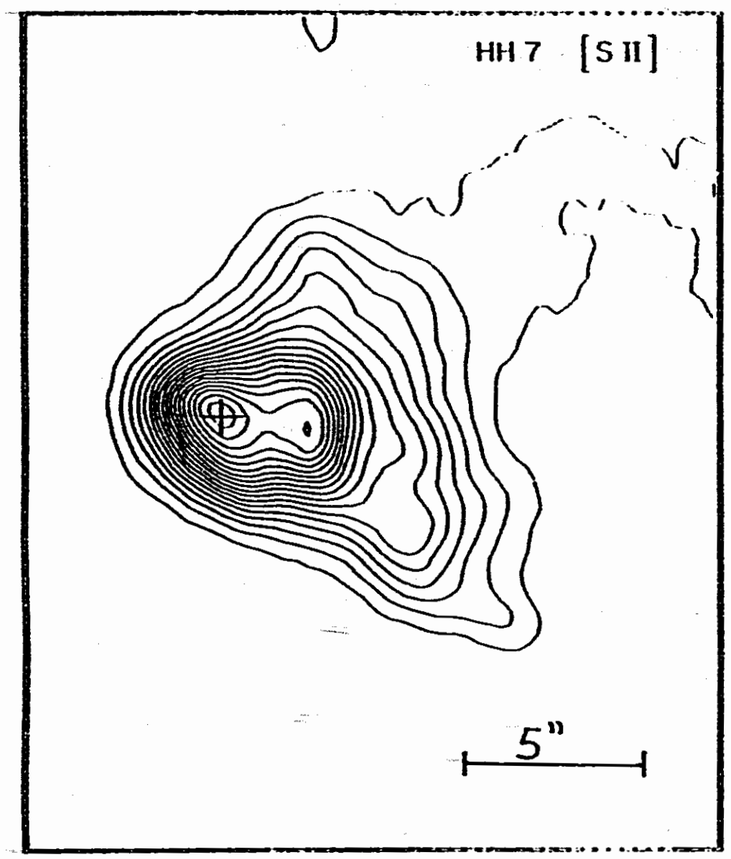
HH 7 [S II]
5"

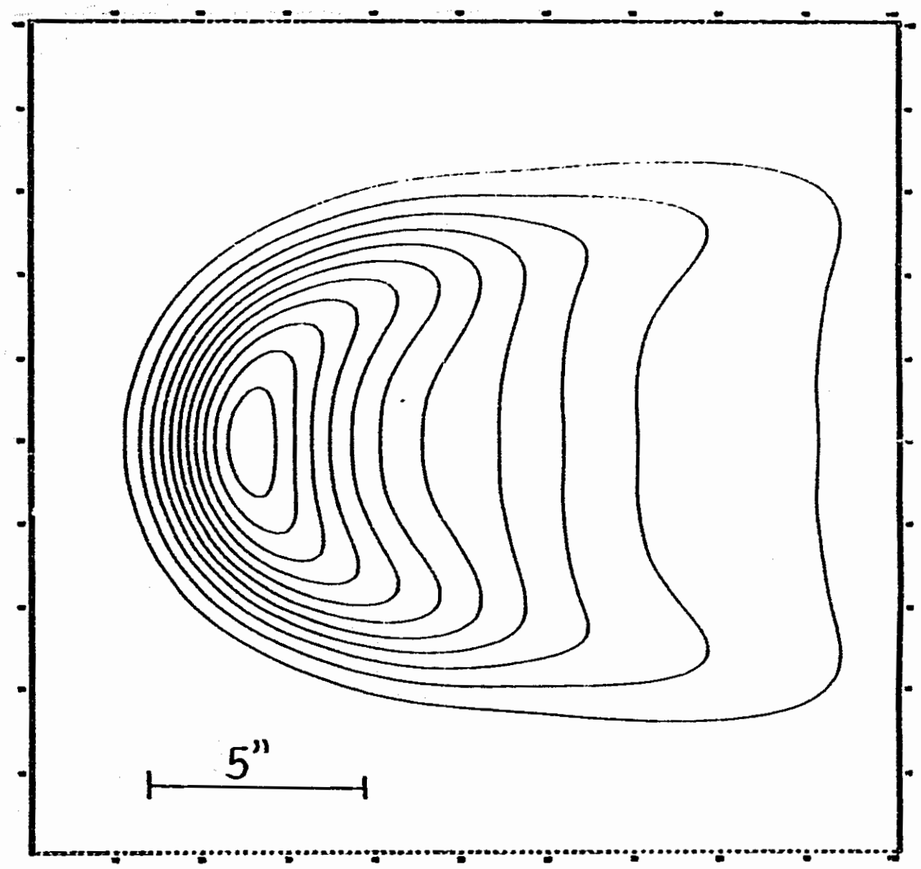
5"

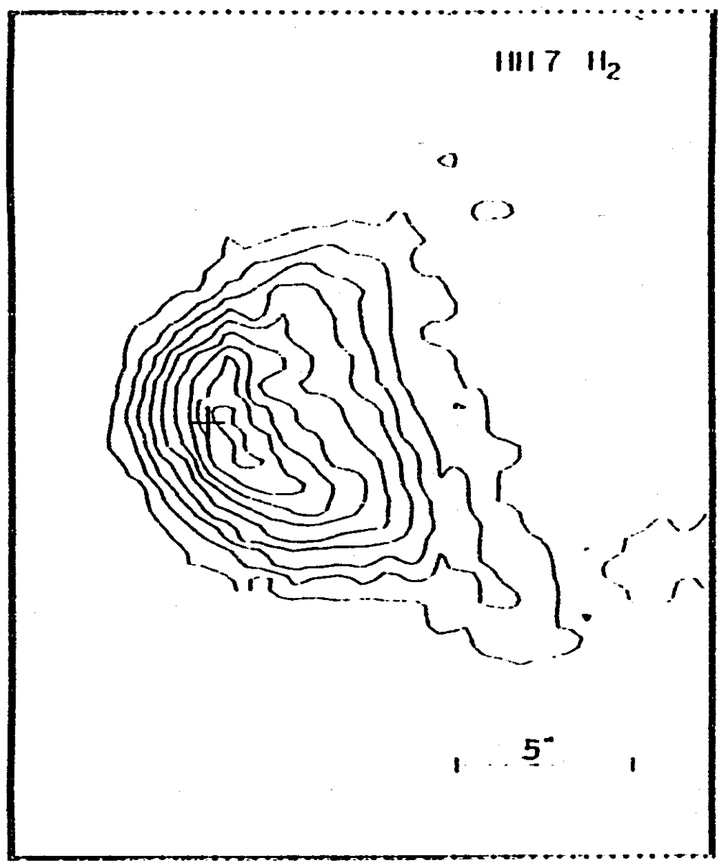
1117 H2
5"

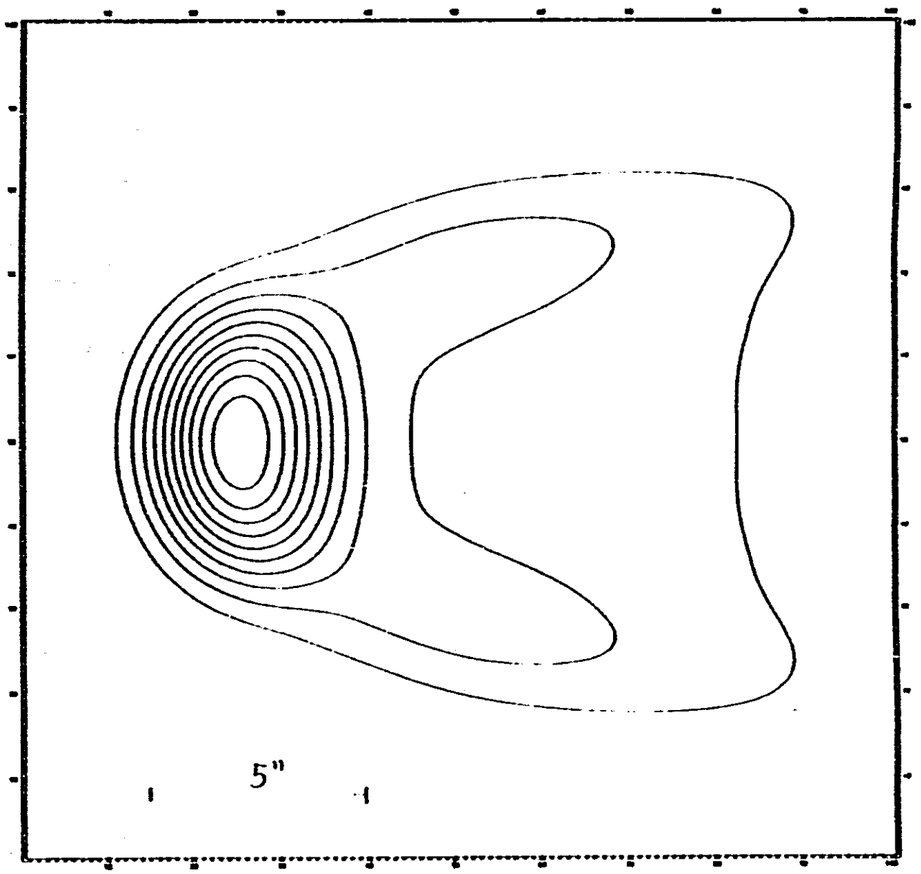
5"

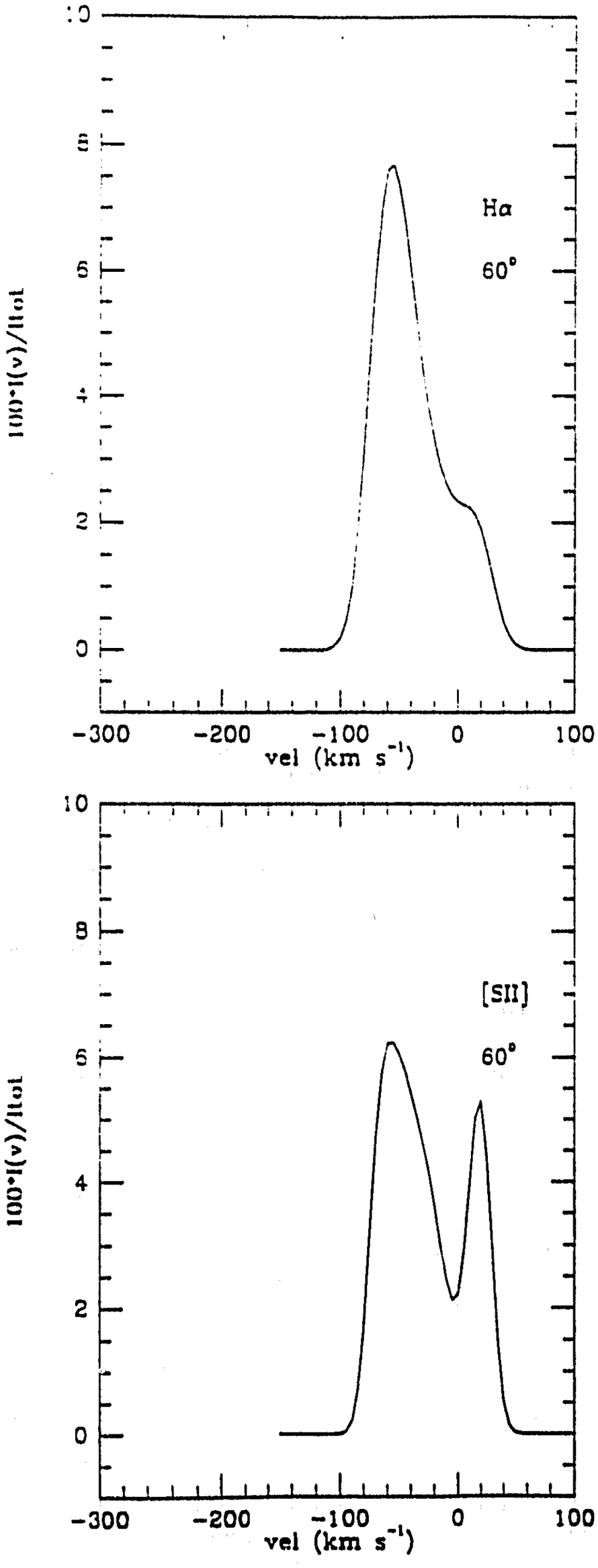

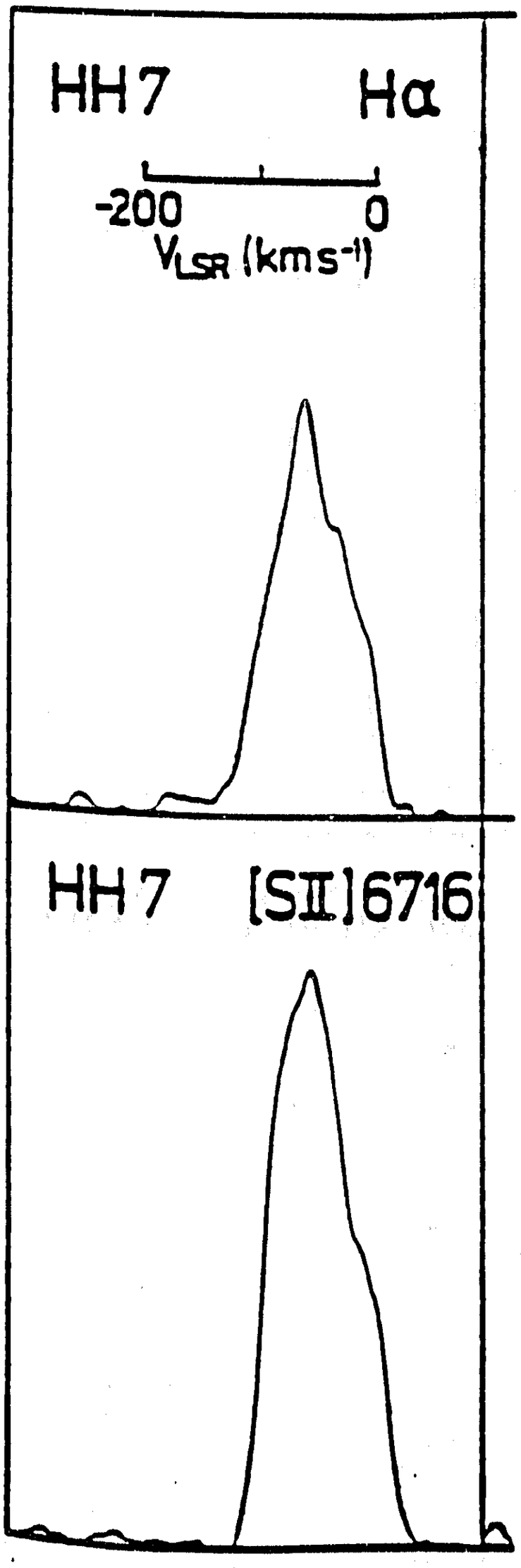

Figure 13. Comparison between observed (right) and calculated (left) Hα, [SII] and 1–0S(line profiles for the HH7 object. The line profiles were calculated using the parameters given in Table 2.

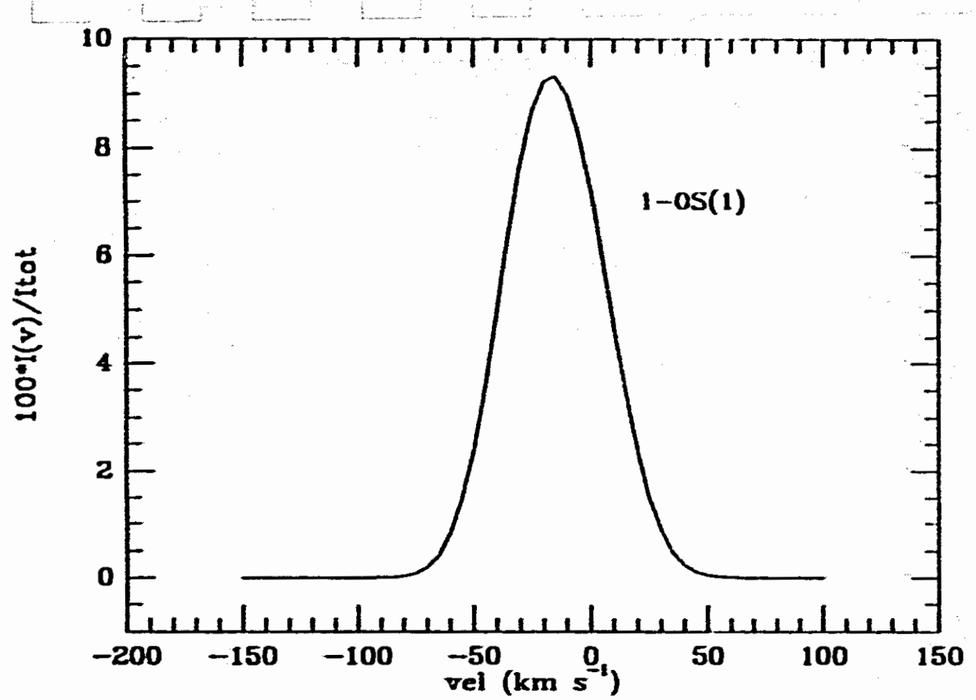
100*I(v)/Itot
1-0S(1)
vel (km s^{-1})

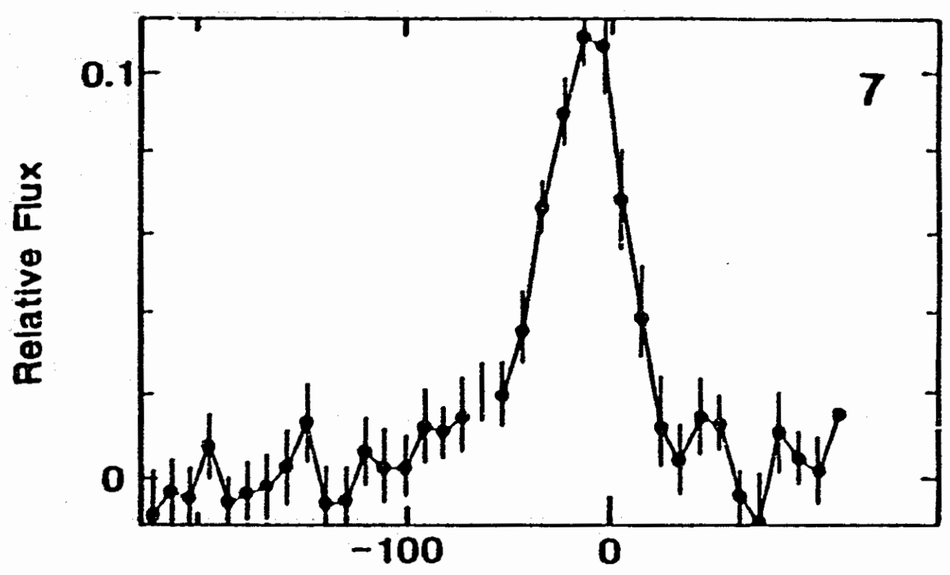
Relative Flux
7

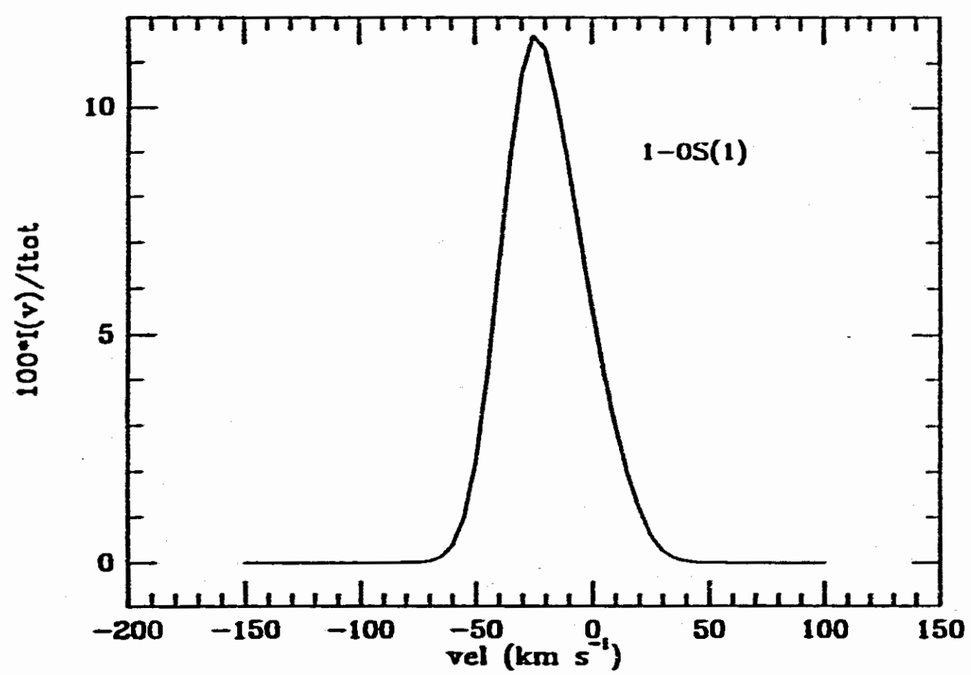
100*I(v)/Itot
1-0S(1)
vel (km s^{-1})

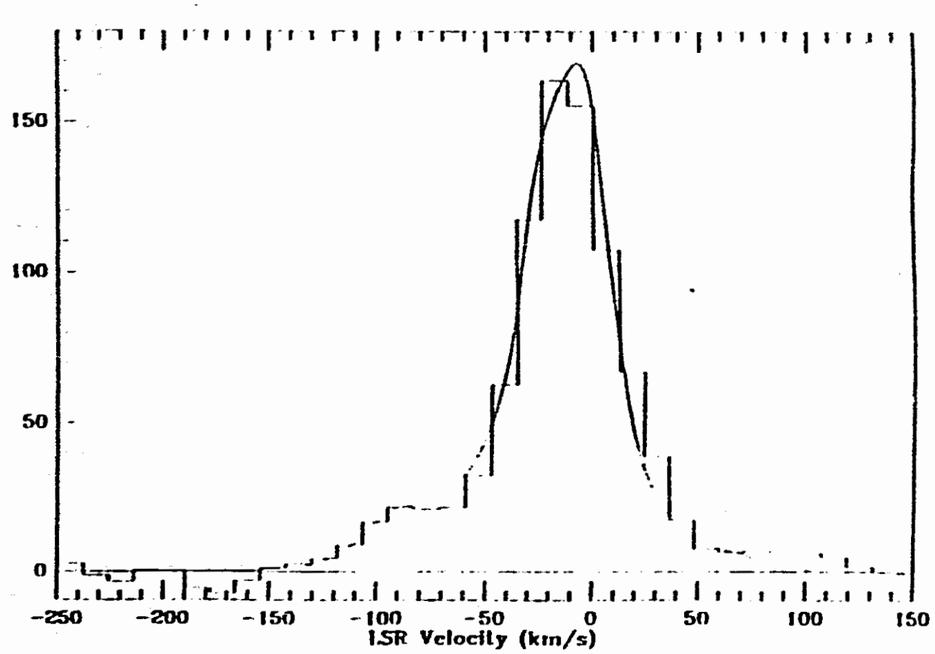
LSR Velocity (km/s)

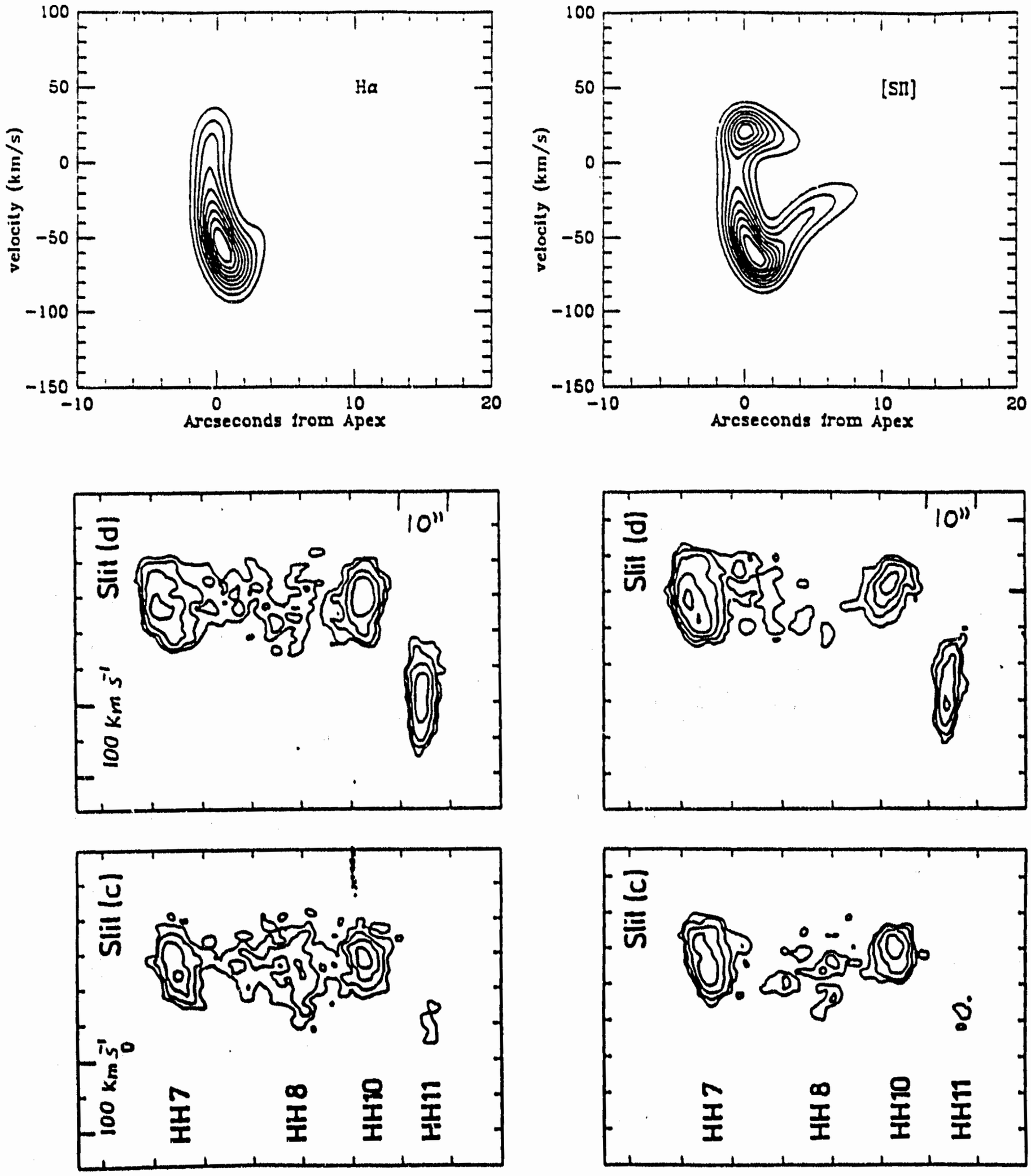

Figure 14. Comparison between observed (right; see Table 2) and calculated (left) Hα, [SII] and 1–0S(1) position-velocity diagrams for HH7. The observed Hα and [SII] contour spacing is logarithmic, corresponding to a factor of $2^{1/2}$ in intensity. The calculated ones are plotted in units of 0.1 of the square root of the peak intensity.

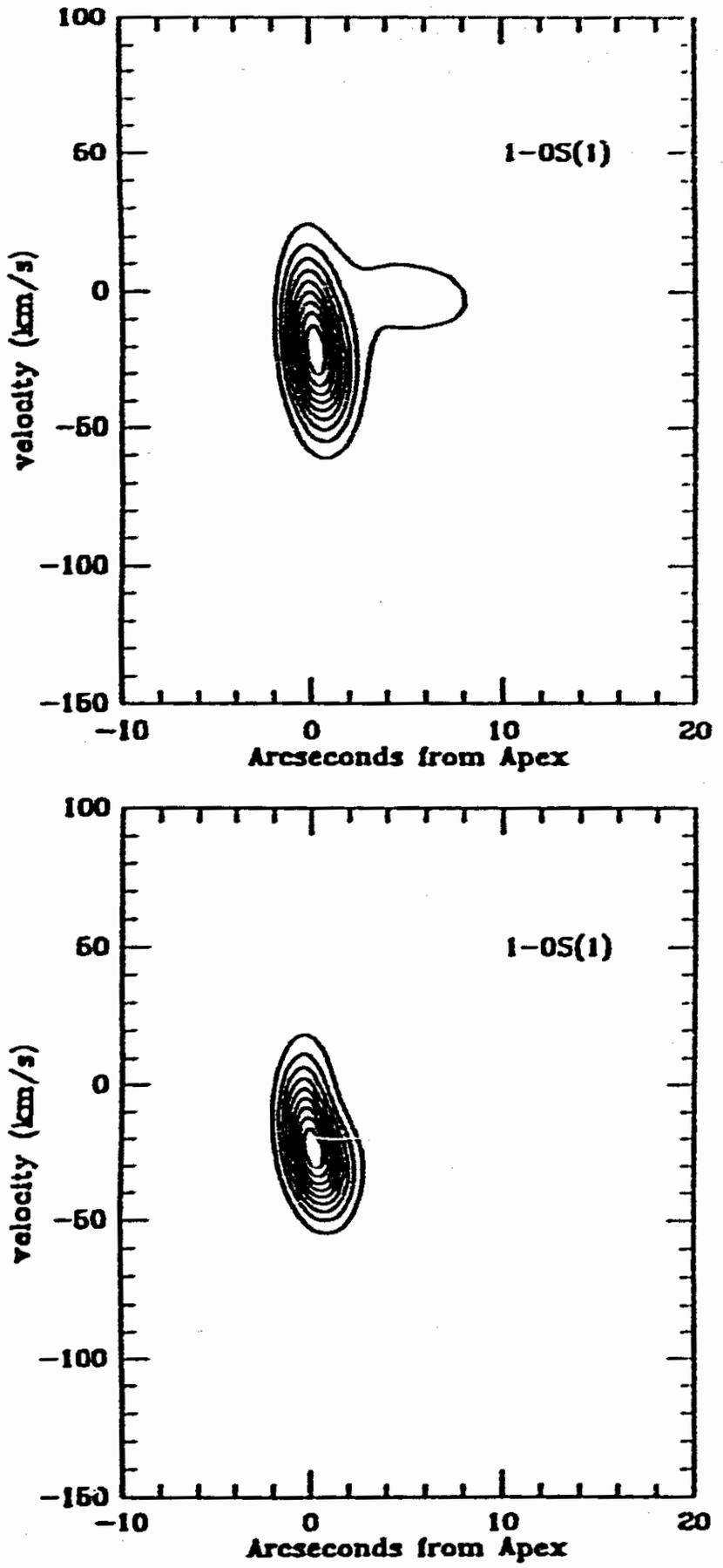
1-0S(1)
velocity (km/s)
100
50
0
-50
-100
-150
-10
0
10
20
Arcseconds from Apex
1-0S(1)
velocity (km/s)
100
50
0
-50
-100
-150
-10
0
10
20
Arcseconds from Apex

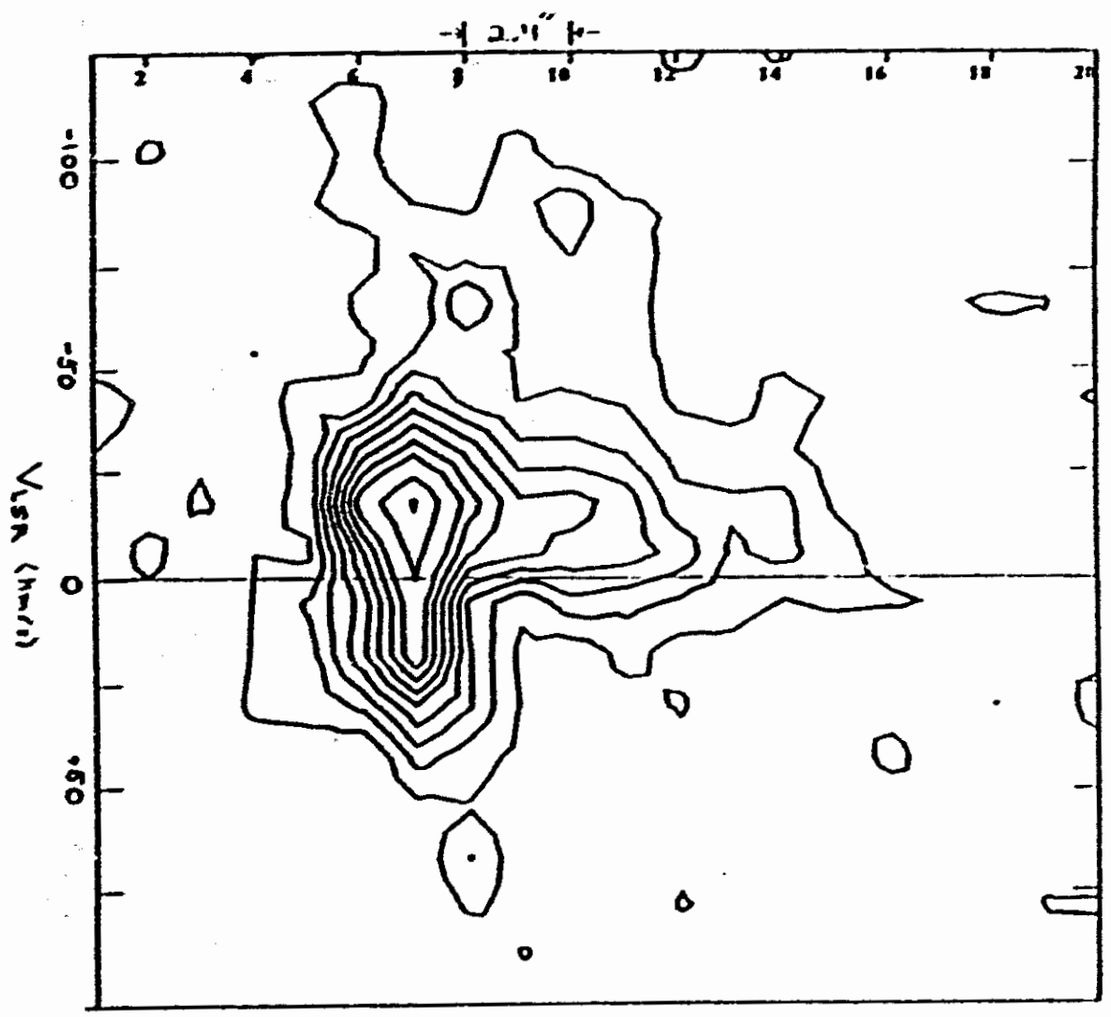
0.1"
0.5"
0.0"
V_LSR (km/s)

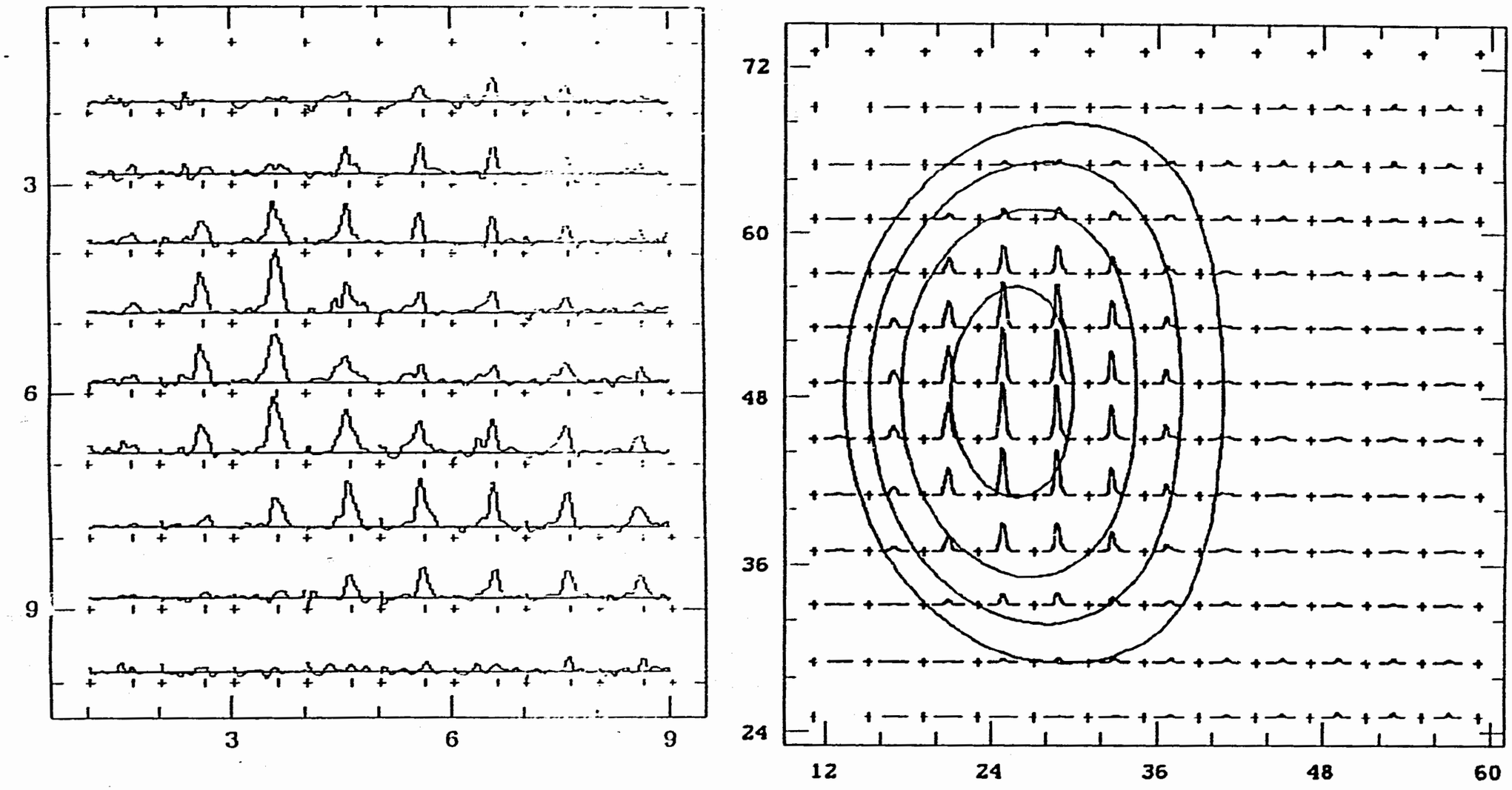

Figure 15. Comparison between the observed (left) grid of the H_2 line profiles (velocity map) in the central region of HII7 by Carr (1990) and that calculated (right) for a bow-shock moving through a magnetized molecular medium with an inclination angle of 60°. The pixel spacings in the observed and calculated maps are 1.2" and 0.8", respectively. The velocity extent in each observed and calculated spectrum is 330 km s^{-1}. In the observed map, the tick mark indicates $V_{LSR} = 0$ km s^{-1}, while in the calculated one, the center between each two marks corresponds to the molecular cloud velocity. The peak of the lines are normalized to the peak of the most intense line.

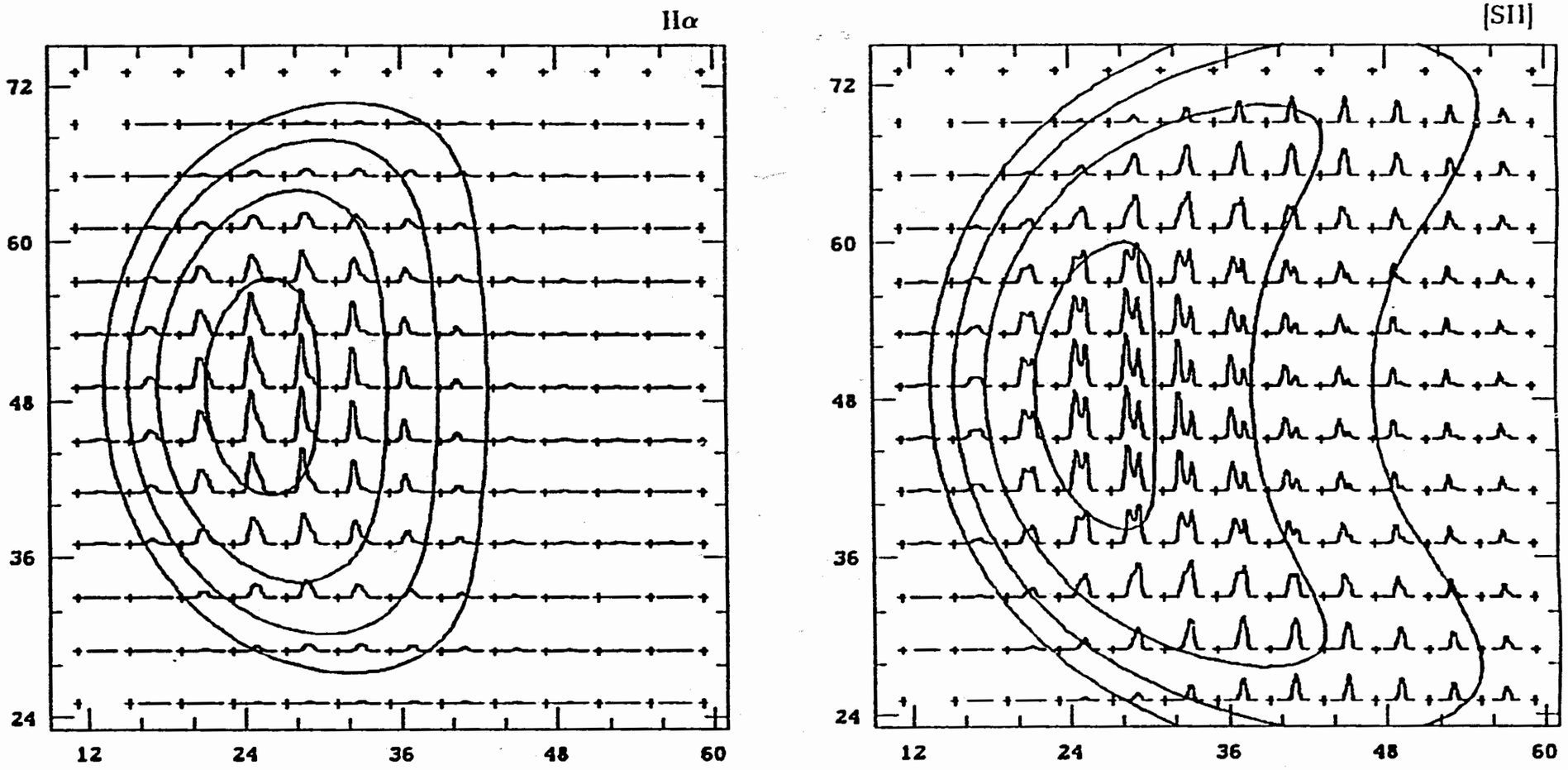

Figure 16. Predicted velocity maps for a number of optical and infrared lines. The description of these maps is as in Figure 15.

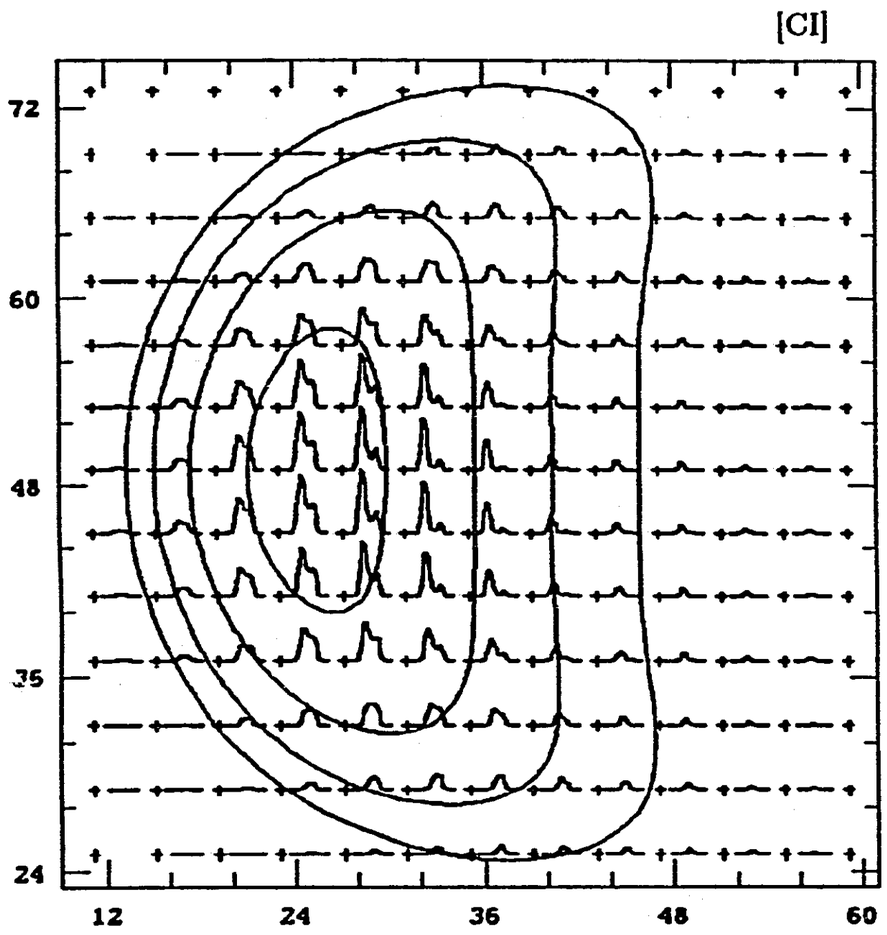
[CI]
72
60
48
36
24
12
24
36
48
60

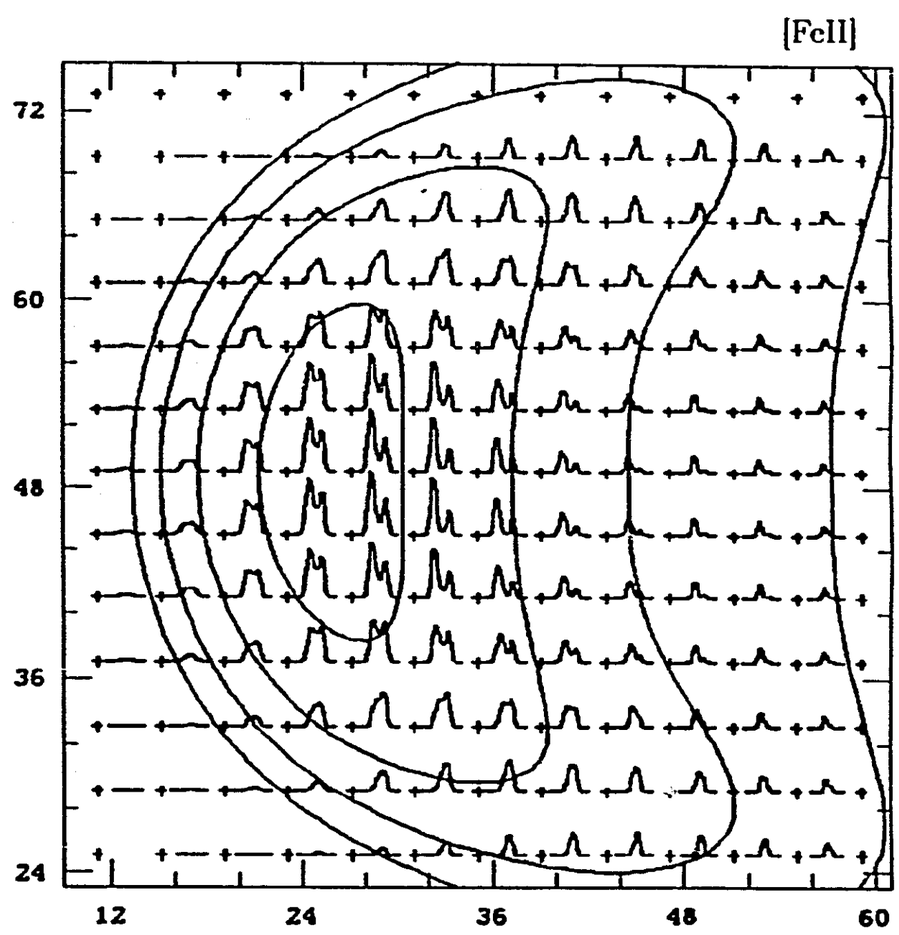
[FeII]
72
60
48
36
24
12
24
36
48
60

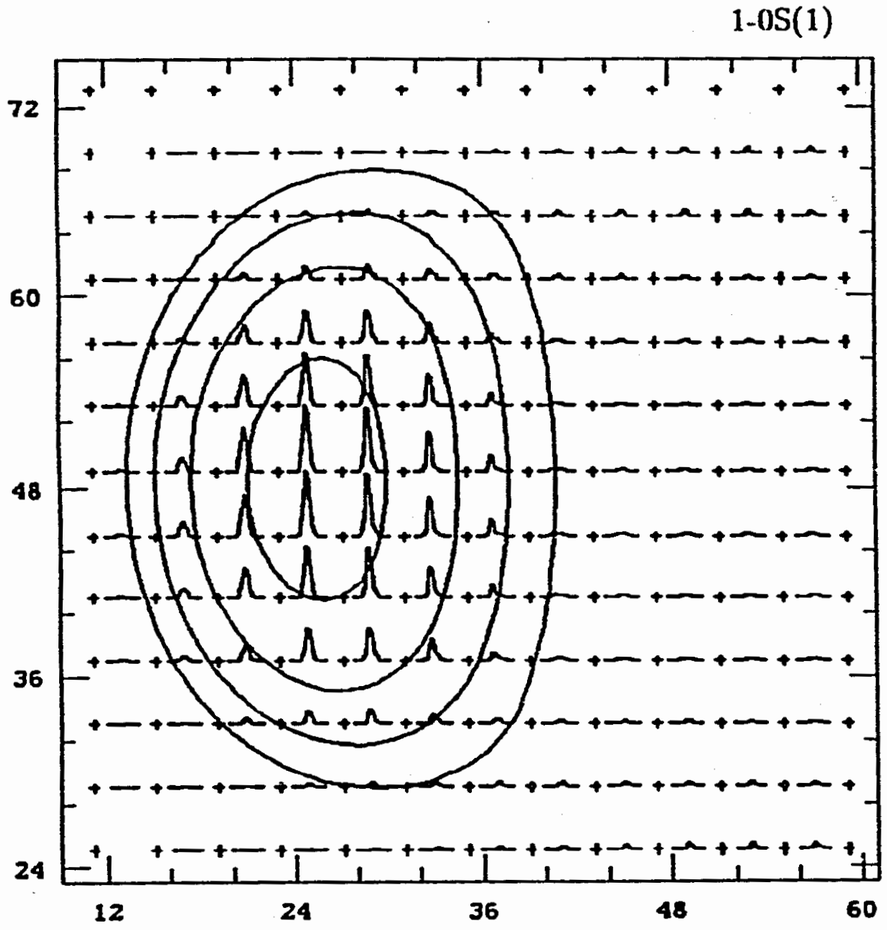
1-0S(1)
72
60
48
36
24
12
24
36
48
60

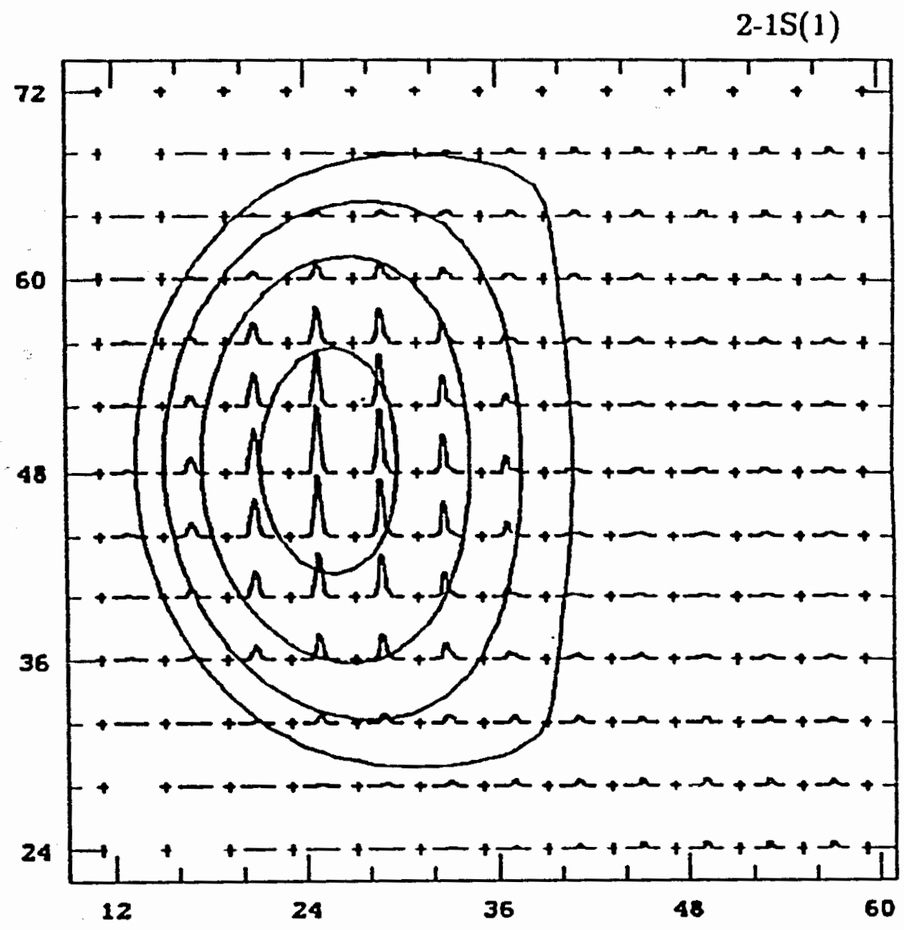
2-1S(1)
72
60
48
36
24
12
24
36
48
60